DEPARTAMENT DE FÍSICA ATÒMICA MOLECULAR I NUCLEAR

VNIVERSITAT ⓖ ID VALÈNCIA

(ESTUDI GENERAL)

Time Calibration and Point Source Analysis with the ANTARES Neutrino Telescope

PhD Thesis

Francisco Salesa Greus

July 2010
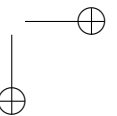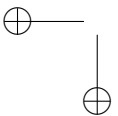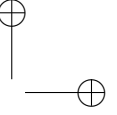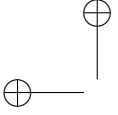
D. JUAN de DIOS ZORNOZA GÓMEZ, Contractat Juan de la Cierva pel C.S.I.C. i D. JUAN ZÚÑIGA ROMÁN, Professor Titular de la Universitat de València,

CERTIFIQUEN:

Que la present memòria, **Time Calibration and Point Source Analysis with the ANTARES Neutrino Telescope**, ha sigut realitzada baix la seua direcció en el Institut de Física Corpuscular (Centre Mixt Universitat de València - CSIC) per D. Francisco Salesa Greus i constitueix la seua Tesi Doctoral en el Departament de Física Atòmica Molecular i Nuclear de la Universitat de València per a optar al grau de Doctor en Física.

I per a que conste, en cumplimient de la legislació vigent, signem el present Certificat a Paterna, a 1 de juliol de 2010.

Signat: Juan de Dios Zornoza Gómez

Signat: Juan Zúñiga Román
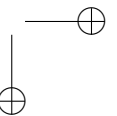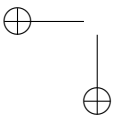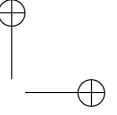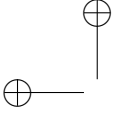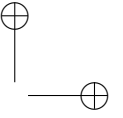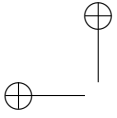
Als meus pares
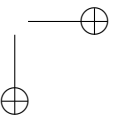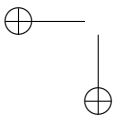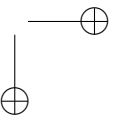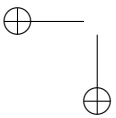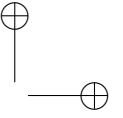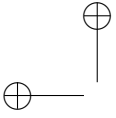
Agraïments

Després de tot el treball realitzat durant quasi set anys en el grup ANTARES per fi aquesta tesi ix a la llum. Durant tot aquest temps he conegut a moltes persones que m'han ajudat, en diferents aspectes, per tal que aquest treball haja sigut possible. En primer lloc m'agradaria donar les gràcies a Juanjo com a responsable del grup per haver confiat en mi des del principi fent-me partícip d'aquest projecte. He d'agrair la seua preocupació i seguiment en tot moment del meu treball. D'ell he après moltes coses com a físic i com a persona.

He d'agrair molt també, com no, als meus directors de tesi Juande i Juan. Ells han donat un salt qualitatiu molt important a aquest treball amb les seues correccions al detall, bon ambient de treball i fructíferes discussions.

La resta del grup ANTARES també han contribuït d'una o altra forma: Juan Pablo, Ciro, Salvatore, Umberto, Harold, Joaquin, Agustín, Damien, Diego, Fernando. I els que ara no estan però que en el passat formaren part com Juanan, Simona, Victor o Emiliano. Aquesta tesi no seria possible sense les seues contribucions. D'ells també he apreciat molt el tracte personal que m'han donat, que han anat més enllà que el simple companyerisme laboral.

Done les gràcies als membre de la col·laboració ANTARES en especial els que han contribuït directament a aquesta tesi com José Busto, Antoine Kouchner, Dmitry Zaborov, Heide Constantini o Jean Pierre Ernenwein entre d'altres.

Vull agrair l'ajuda donada per tot el personal de l'IFIC des de la gent de secretaria fins al tècnics, els quals sempre s'han mostrat accessibles i disposats a solucionar-me qualsevol tipus de problema.

Com no, agrair als companys de l'IFIC: Carlos, Mercedes, Regina, Tito, Emma, Santi, Joan, Ricardo, Pancho, Pablo, Vera, Alex i un llarg etc. Als que ja no estan a l'IFIC com Ximo, Arantxa i Jose. I els que han estat de pas com Leo, Ana i Jose. Ells m'han fet sentir a gust de veritat i m'han fet gaudir de bons moments tant a l'IFIC com fora. Han fet que anar a cada dia a treballar fora un plaer. Guarde molt bons records de tots ells i espere conservar la seua amistat.

També als meus amics del poble, que a pesar de les diverses ocupacions de cadascú s'han preocupat de no perdre el contacte amb mi, m'han animat en els moments difícils i m'han fet passar-ne de bons.

Finalment, i no per això menys important, vull agrair als meus pares i a la meua germana el suport que m'han donat sempre. Si he arribat fins ací, de ben cert que és gràcies al seu suport. Òbviament la meua gratitud cap a ells no es pot expressar només en paraules.
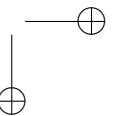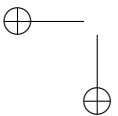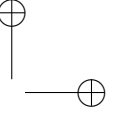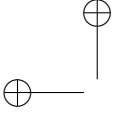
"We are a way for the cosmos to know itself."
Carl Sagan.

Contents

CONTENTS

CONTENTS

CONTENTS

2   Introduction

Preface

The exploration of the Universe has fascinated the human being since ancient times. This exploration has been carried on mainly with the observation of the light, that is photons, arriving to the Earth from extraterrestrial sources. The improvement of our knowledge in particle physics as well as the big advances in the development of our experimental techniques are allowing us to extend our Universe exploration to the most energetic phenomena. For instance, photons exceeding 10 TeV have been observed with current detectors, leading to the discovery of sources without counterpart in other wavelengths. Apart from photons, cosmic rays reaching the Earth can also bring us important knowledge improving our understanding of the Universe. Cosmic rays bombard our atmosphere continuously from the space with energies up to 10^{20} eV. Presently, we have measured quite well the cosmic ray energy spectrum but, almost one hundred years after its discovery, their origin is still unknown. However, recent observations of very high-energy cosmic rays have started to clear up this mystery. Correlation of the most energetic cosmic rays ($> 10^{18}$ eV) with nearby extragalactic Active Galactic Nuclei (AGN) has been observed. Both, cosmic rays and photons, will complement each other in the exploration of the Universe, in what has been called "multi-messenger approach".

This multi-messenger approach needs to be completed with the neutrino. The main advantage of neutrinos with respect to cosmic rays is that the former, being neutral stable particles, can reach the Earth without being deflected by magnetic fields. Thus, they point back to their sources. This magnetic field deflection is negligible only for the most energetic cosmic rays, since they are charged particles. However, at those energies their spectrum starts to fall down critically due to the interaction of the cosmic rays with the relic photons from the cosmic microwave background (CMB). This effect is known as the GZK cutoff. The mean free path predicted in this case is about 50 Mpc, so only nearby sources can be detected. Neutrinos are also advantageous with respect to photons because these are absorbed by the intergalactic medium when interacting with the extragalactic background light (EBL), mainly with optical/infrared radiation. Thus, it is not expected to detect high-energy photons

Introduction

(> 10 TeV) from sources farther than 100 Mpc.

The feasibility of neutrino astronomy was confirmed by the detection of neutrinos emitted by the Sun and the supernova SN 1987A. The observation of neutrinos coming from the Sun meant an important breakthrough, since their flux showed a deficit with respect to what is expected according to the Solar Standard Model. This deficit was confirmed studying atmospheric neutrinos. The best solution to fix the problem is to assume that neutrinos have mass and so change the flavour by the process known as neutrino oscillations. This effect brought the first hint of physics beyond the Standard Model of particle physics.

The main drawback when performing astronomy with neutrinos is that huge volumes are required to detect them because they interact only weakly with matter. The best way to obtain such big volumes is to use a natural medium as water or ice. That was the idea conceived by Markov [1] for constructing what is called a neutrino telescope. Some projects have taken on the challenge of constructing such neutrino telescopes. They aim to detect the Cherenkov light induced by the charged particles produced by the interaction of a high-energy neutrino in the matter surrounding the detector. This light travels in a transparent optical medium, as water or ice, and then it is recorded by a three-dimensional array of photomultipliers. Finally, with the charge time and position information of the hits produced in the detector, the track can be deduced and thus the position of the event in the sky map is obtained.

ANTARES [2] is one of the projects which has recently achieved the completion of one of this huge neutrino detectors. It consists on an array of almost 900 photomultipliers distributed in 12 strings deployed at 2475 m depth in the vicinity of the Toulon coast in the Mediterranean Sea. It is currently taking data steadily. ANTARES is the biggest neutrino telescope deployed underwater and also the biggest at the northern hemisphere.

This thesis work is divided in two main parts. The first one is devoted to the time calibration of the ANTARES detector and the results obtained using the Optical Beacon calibration system. In the second part, the analysis to search for point sources with the data of the first five lines deployed of ANTARES is presented.

The first chapter summarizes the current status of the astroparticle physics field, specially focused on what concerns to high-energy neutrino astronomy. In the second chapter, a detailed description of the ANTARES detector is given. The third chapter is dedicated to the detector time calibration, with a detailed explanation of the systems used to this end. The fourth chapter contains the results of the studies performed by the Optical Beacon system. The fifth chapter describes the Monte Carlo simulation and data processing used for the analysis of point-like sources. Finally, the sixth chapter presents the first results of point source search with the data from the detector.

4

Chapter 1

Neutrino astrophysics

Neutrino astronomy has reached great advances during the last years. For the first time, neutrinos from extraterrestrial sources (the Sun and SN1987A) have been detected. The challenge is to extend this detection to high-energy cosmic neutrinos (above several GeV), which will let us explore the Universe in an unprecedented way. This chapter is a review of the present status of the astroparticle physics mainly focused on neutrino astrophysics, discussing its relation with particle physics and astronomy.

1.1 Neutrino discovery

The neutrino is an elementary particle postulated by Wolfang Pauli in 1930. It was necessary[1] in order to save the energy and momentum conservation in β-decay experiments (see Equation 1.1). In a beta decay, the radioactive nucleus decays to a state with one additional unit of positive charge plus a single electron. The energy conservation law implies that the electron should have a fixed energy. Instead, it is detected with a continuous spectrum of energies up to the expected value. The solution proposed by Pauli was to add a new particle to the decay products: the neutrino[2].

$$(N, Z) \rightarrow (N - 1, Z + 1) + e^{-} + \bar{\nu}_e \qquad (1.1)$$

The neutrino is a neutral particle having a very small mass[3]. It only un-

---

[1]Pauli called it "desperate remedy".

[2]In fact, the missing particle in the β-decay is what we call now anti-neutrino, the antiparticle of the neutrino.

[3]Actually it could turn out that one of the neutrino flavour has no mass at all, but the other two flavours have mass.

Chapter 1. Neutrino astrophysics

dergoes from weak interaction, so it has a very small total cross-section. This is the reason why it is very difficult to detect them. Around 3×10^{12} neutrinos pass through every square centimeter of Earth's surface every second coming from the Universe (mostly from the Sun), but only 1 out of 10^9 interacts with matter.

The first experimental detection of the neutrino was performed by Clyde Cowan, Frederick Reines et al. in 1953 [3]. The idea was to detect some anti-neutrinos coming from the Handford nuclear reactor, where a high flux ($\sim 10^{13}$ cm^{-2}s^{-1}) of them, from the fission reaction, was produced. The detector consisted of a cylindrical tank containing 300 liters of liquid scintillator, large enough to produce some few anti-neutrino interactions. The detector reaction was an inverse beta-decay where an anti-neutrino is captured by a proton creating a positron and a neutron. The positron was promptly annihilated after encountering an electron, producing a pair of back-to-back photons of 0.5 MeV. The neutron excited the cadmium nuclei present in the detection volume yielding another photon. The three photons provided a distinctive signal which proved the neutrino interaction. The final confirmation came after detecting a difference in the number of events when the reactor was switched off. Since then, neutrino physics has became a very exciting field for particle physicists.

There are three neutrino flavours associated to three charged leptons: electron (e), muon (μ), and tau (τ). During years there was no agreement about whether the neutrinos were massless or not. Now, all the experimental evidences point to the existence of neutrino oscillations which is an indirect evidence that at least, two of the neutrino flavours should have mass (see section 1.3).

1.2 Start of neutrino astronomy

As it has been said before, detecting cosmic neutrinos is not an easy task. Apart from the secondary neutrinos produced by cosmic ray interactions in the atmosphere, the only extraterrestrial neutrino sources confirmed at the moment are the Sun and the SN 1987A. Neutrino telescopes aim to extend the survey to more distant sources.

1.2.1 Solar neutrinos

Solar neutrinos are the product of the fusion reactions which take place in the Sun's core. They were detected for the first time by Davis jr. et al. in 1968 [4] by means of a big tank containing 390 m^3 of a chlorine solution (C$_2$Cl$_4$) placed deep underground in the Homestake Gold Mine (South Dakota, USA). The experiment led to the observation of a deficit in the number of detected

neutrinos with respect to the Solar Standard Model (SSM) theory predictions. This disagreement was known as the "solar neutrino problem". The solar neutrino deficit was confirmed by subsequent experiments as SAGE [5] and GALLEX [6], and also by more recent experiments as Super-Kamiokande [7] and SNO [8]. The controversy lasted for more than 40 years. Finally, the SNO collaboration confirmed that the solution to this puzzle comes from neutrino oscillations. Actually, neutrinos produced in the Sun (ν_e) oscillate to other flavours. Thus, the flux detected is not the expected one. However, if the all-flavours neutrino flux is considered, there is a quite good agreement with the SSM prediction. With a detector sensitive to the three neutrino flavours, the SNO collaboration was able to prove that the missing neutrinos were not really missing but invisible to the other detectors which were designed to detect only electron neutrinos (ν_e) and not the two other flavours (ν_μ and ν_τ).

1.2.2 Atmospheric neutrinos

Atmospheric neutrinos are produced after the hadronic interactions of the cosmic rays (mainly protons) with the nuclei of the atmosphere. The primary products are mesons which produce the subsequent decays leading to the neutrino production, as it is shown in the following reactions:

$$
\begin{aligned}
\pi^\pm(K^\pm) \;\;&\rightarrow\;\; \mu^\pm + \nu_\mu(\bar{\nu_\mu}), \\
&\Downarrow \\
&\mu^\pm \rightarrow e^\pm + \nu_e(\bar{\nu_e}) + \bar{\nu_\mu}(\nu_\mu).
\end{aligned}
\tag{1.2}
$$
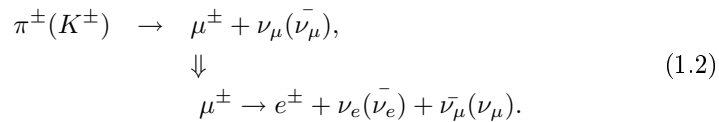
As the solar neutrino experiments did, the experiments devoted to detect atmospheric neutrinos also observed a disagreement with the theoretical expected neutrino flux [9]. According to the reaction 1.2, the ratio between muon and electron neutrino fluxes must be ~ 2. However, Super-Kamiokande observed a deficit in the muon neutrino flux mainly for large zenith angles. Moreover, a larger flux of upward tau-neutrinos was observed too. The most solid explanation is to assume the oscillation of the ν_μ into ν_τ [10]. Neutrino oscillations are not predicted by the Standard Model, therefore, they are an evidence for physics beyond it.

As we will see in the next chapter, atmospheric neutrinos represent an irreducible background for a neutrino telescope.

1.2.3 SN 1987A neutrinos

Apart from the Sun, the only extraterrestrial neutrino source detected up to now is the supernova SN 1987A. It was the result of the explosion of a supergiant star in the Large Magellanic Cloud on February 23rd, 1987. This is

Chapter 1. Neutrino astrophysics

the closest supernova ($\sim$50 kpc) recorded since the invention of the telescope. Its apparent magnitude was around 3, so it could be seen by naked eye in the night sky. A neutrino burst lasting around 13 s was independently detected by three experiments: Kamiokande-II [11] detected eleven anti-neutrinos of which the first two pointed back to the source, Irvine-Michigan-Brookhaven (IMB) [12] detected 8 anti-neutrinos, and Baksan [13] detected 5 neutrinos. All the 24 events accumulated at energies of the order of 10 MeV. The results were remarkably in agreement with the models of supernovae collapse and neutron-star formation, where the 99% of the energy is supposed to be released in neutrinos of all flavours ($\sim$10^{58} neutrinos) with an average energy of 10 MeV.

1.3 Neutrino oscillations

Suggested for the first time by Pontecorvo in 1957 [14], neutrino oscillations are a phenomenon in which one massive neutrino change to another one of different flavour. This flavour changing process has been used to explain the solar electron neutrino deficit and the missing atmospheric muon neutrino flux. Oscillations from one flavour to another are due to the fact that the flavour states produced by the weak interaction (ν_α) are not eigenstates of the mass matrix (ν_i) but a linear combination of them:

$$|\nu_\alpha\rangle = \sum_{i=1}^{3} U_{\alpha i}|\nu_i\rangle$$

where $\alpha = e$, μ, τ (flavours) and i = 1, 2, 3 (mass eigenstates).

Adding the time evolution:

$$|\nu_\alpha(t)\rangle = \sum_{i=1}^{3} U_{\alpha i}\,|\nu_i(t)\rangle = \sum_{i=1}^{3} U_{\alpha i}\;e^{-iE_i t}|\nu_i\rangle$$

If for simplicity we consider only two neutrino states, the oscillation probability between them as a function of the source distance is given by:

$$P_{\alpha\beta} = \sin^2(2\theta)\,\sin^2\left(1.27\frac{L}{E}\,\Delta m^2\right)$$

where $\Delta m^2 = (m_\alpha^2 - m_\beta^2)$ in eV^2, L is the distance between the neutrino source and our detector in meters and E is the neutrino energy in MeV. As it is shown in the previous equation, oscillations can take place only if $\Delta\text{m}^2 \neq 0$. Therefore, at least two of the neutrino states should have mass.

1.4 Cosmic rays

Cosmic rays are all stable charged particles and nuclei which strike continuously the Earth from the outside space. The discovery of this phenomenon was done in 1912 by Victor Hess[4] who observed that the flux of these particles increased when he ascended in a balloon [15]. Therefore, he could confirm that their origin was extraterrestrial and discard an Earth-crust origin, as was thought at the moment. Presently we know that, up to a few TeV, these cosmic rays are light nuclei, protons (89%), helium (10%), and heavier nuclei (1%). A large amount of them are absorbed by the atmosphere, which is the reason why the flux decreases for increasing zenith angles.

One of the most interesting aspects of cosmic rays is that they are the most energetic particles ever observed, reaching in some cases energies up to 10^{20} eV. That means seven orders of magnitude greater than the energies reachable by the current particle accelerators as the LHC. Particle physicists took advantage of this fact during the last century and a lot of new particles, as the positron (1932), which was the first antimatter particle detected, the muon (1936) or the pion (1947) were discovered.

Cosmic rays are particles produced and accelerated in astrophysics sources. Afterwards, they can interact with the interstellar gas which can also accelerate them. They arrive at the Earth with a flux following a power law spectrum (Equation 1.3).

$$\frac{dN}{dE} \propto E^{-\gamma},\qquad(1.3)$$

where γ is the so-called spectral index.

The cosmic ray spectrum ranges from $\sim 10^9$ eV to $\sim 10^{20}$ eV. Its shape has been studied in detail by many experiments. In Figure 1.1 the high energy part (above 10^{13}) of the spectrum is shown. As it can be seen, it follows a broken law in which some characteristic features appear from several TeV up to the 100 EeV. Below the TeV region, at the GeV range, the Sun shields the solar system from charged particles due to the outward-flowing solar wind. Therefore, the flux arriving at the Earth is anti-correlated with the solar activity (solar cycles). This effect is known as solar modulation.

For energies up to $\sim 5 \times 10^{15}$ eV the spectrum follows a power law with $\gamma=2.7$. This power law is well described by the acceleration mechanism originated in the shock-waves of the expanding supernovas in our galaxy (see section 1.5.2). Afterwards, the spectral index changes from ~ 2.7 to ~ 3.0 in the region known as the "knee". The origin of the knee is still an open question. The maximum energy produced in the supernova shock acceleration processes is around 10^{15} eV according to recent estimations, which hints that the knee

---

[4]Although his work is less known, Domenico Pacini gave also a significant contribution to the discovery of cosmic rays in an independent way, using different techniques.

Chapter 1. Neutrino astrophysics
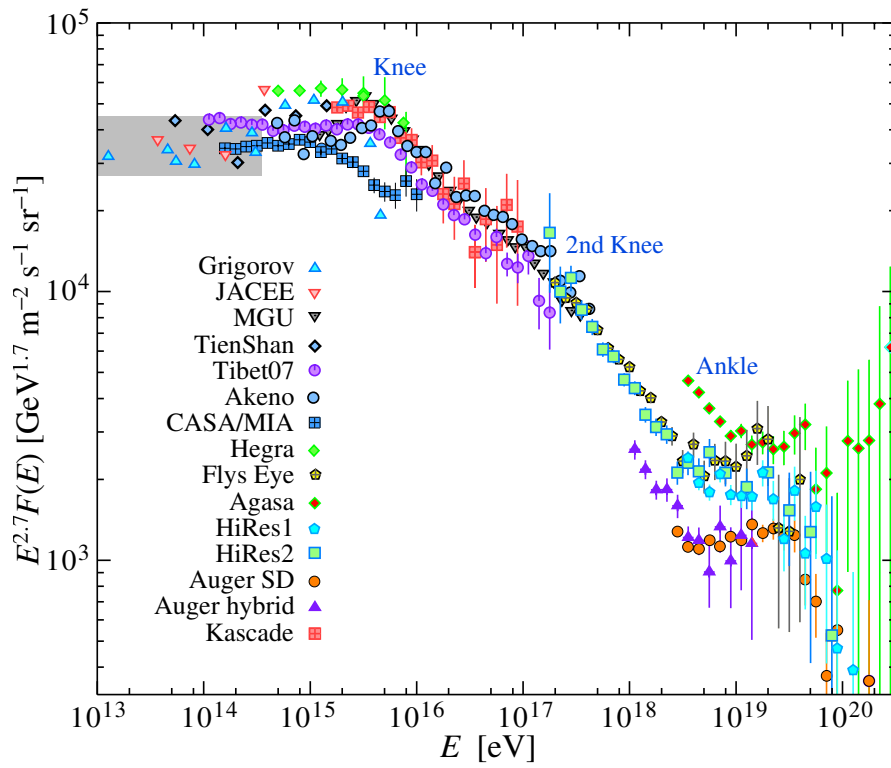
Figure 1.1: *The all-particle cosmic ray spectrum from air shower measure-ments [16]. The shaded area shows the range of the direct cosmic ray spectrum measurements mainly provided by satellites.*

could be reflecting the end of the galactic cosmic ray spectrum.

Currently, the efforts on understanding the cosmic rays, and their features along their energy spectrum, are based on measuring their chemical composition. In this sense, after the KASKADE results [17], some physicists suggest that the drop at the knee may start at different energies depending on the element involved, i.e., $Z \times 3 \times 10^{15}$ eV being Z the atomic number of the element [18]. With this argument this feature should extend up to $25 \times 3 \times 10^{15}$ eV $\sim 8 \times 10^{16}$ eV, for the heaviest common nuclei, the iron.

At higher energies, a new change occurs at $\sim 3 \times 10^{17}$ eV where the flux fall becomes softer and the slope moves from ~ 3.0 to ~ 3.2. This feature in the cosmic ray spectrum has been reported by several experiments with a good consensus. It is commonly known as the "second knee". A detailed review of the experimental results can be found in [19].

Going to energies above the second knee, the energy spectrum changes again. This feature is know as the "ankle" and appears at $\sim 5 \times 10^{18}$ eV. The energy spectrum becomes less steep again, being the spectral index now around 2.8. Presently, the most accepted theory about the ankle origin considers it as the transition of cosmic rays from galactic to extra-galactic origin. Considering that the radius of the circular motion of a charged particle when a magnetic field is present is given by

$$R_L = \frac{cp}{ZeB} \approx 100pc \; \frac{3\mu G}{B} \; \frac{E}{Z \times 10^{18}eV} \tag{1.4}$$

where R_L is the so-called Larmor radius, E is the maximum energy attainable in our galaxy, Ze is the charge of the particle and B is the intensity of the magnetic field, the radius and/or the magnetic field of our galaxy is not enough to accelerate and confine charged particles above 10^{18} eV. Therefore, the origin of cosmic rays above the ankle has been generally thought to be of extra-galactic nature [20]. Other authors state that the transition from galactic to extra-galactic cosmic rays is produced at lower energies. They explain the shape of the ankle region as induced by the electron-positron production when the CR interact with the cosmic microwave background (CMB) [21]. In this scenario the second knee could be the result of the disappearance of the heavy nuclei galactic component and the appearance of a proton extra-galactic component [22].

Even with a good agreement among experiments on finding the special features in the region from the knee to the ankle, the explanation for these is still unknown and so it is the transition point from galactic to extra-galactic origin. Understanding the cosmic ray composition on this region seems to be a key point to throw some light on this mystery. In this sense, some experiments as for instance KASKADE-Grande, TALE, TUNKA have been constructed (or are being constructed) in order to perform a precise measurement of the cosmic ray composition.

Chapter 1. Neutrino astrophysics

After the ankle, at energies above 6×10^{19} eV, the spectrum falls down very steeply due to the Greisen-Zatsepin-Kuzim (GZK) effect [23] [24]. This effect states that the ultra high energy cosmic rays (UHECR)[5] suffer inelastic interactions with the photon gas of the CMB (see Eq. 1.5). The primary protons have enough energy to produce pions which decay into high energy neutrinos (the so-called GZK neutrinos). The GZK leads to an important decrease on the cosmic ray flux and therefore, lead to a sharp end of the cosmic ray spectrum. The mean free path above the energy threshold is around 17 Mpc[6], which is comparable with the distance of the closest galaxy clusters.

$$p + \gamma_{CMB} \rightarrow \Delta^+ \rightarrow p + \pi^0,$$

$$(1.5)$$

$$p + \gamma_{CMB} \rightarrow \Delta^+ \rightarrow n + \pi^+.$$
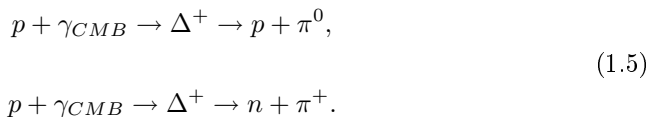
Though the initial disagreement between AGASA, which reported a flux not compatible with the cutoff predicted by the GZK effect, and HiRes, whose data supported the existence of such a cutoff, the AUGER collaboration has finally confirmed its existence. The detection area of AUGER is 30 times bigger than the area of AGASA. It consists of an hybrid detector that employs two independent methods to detect and study high-energy cosmic rays. One technique detects high energy particles through their interaction with the water tanks placed on ground. The other technique tracks the development of air showers by observing the ultraviolet light emitted by the nitrogen fluorescence produced by charged particles.

An alternative hypothesis states that the end of the cosmic ray spectrum is due to the fact that the accelerators have reached their maximum energy and not to the GZK effect.

Cosmic rays are, almost 100 years after their discovery, still a mystery. However, physicists are making big efforts to understand their spectrum and its particular features. With the recent experimental techniques and the next generation of devised detectors in the near future, this enigma is expected to be settled in the incoming years.

1.5 High-energy cosmic rays

From the cosmic ray spectrum, we know that UHECR compatible with the energy of the GZK cutoff exist. They are supposed to be of the extragalactic origin, but the details of their energy spectrum, their composition, and where they come from are still open questions. We want to understand which

---

[5]There is no standard definition, but typically ultra high-energy are cosmic rays with more than 10^{18} eV.

[6]Our galaxy has a diameter of 30 kpc.

are the acceleration processes and the astrophysical sources of such a high-energy events. Due to the fact that neutrinos should be created in the same astrophysical scenarios, a direct link between high-energy cosmic ray sources and high-energy neutrino sources can be established. Meson production is possible when the very energetic hadrons interact with matter at the source. Therefore, the subsequent meson decays should produce neutrinos. In order to understand the acceleration processes and the high-energy extraterrestrial sources, the physicists need as many pieces of information as possible, and cosmic neutrinos can bring some.

1.5.1   Sources of high-energy cosmic rays

The quest for the sources of cosmic rays is still an open issue. It is broadly accepted that the acceleration of cosmic rays up to 10^{15}-10^{17} eV is due to the shock acceleration in supernovae remnants (SNR). However, above this energy range there is no complete agreement among physicists. Being the cosmic rays charged particles, we cannot point back to the emitter. According to Eq. 1.4 the galactic and extra-galactic magnetic fields deflect their trajectories, as:

$$\frac{R}{1pc} \approx 0.01 \frac{E/1TeV}{B/1\mu G} \qquad (1.6)$$

therefore, at a distance of 8 kpc (distance to the galactic center) no directional information can be inferred from protons with energies lower than 300 PeV.

Knowing that the cosmic rays can reach energies of EeV, some attempts have been done in order to constrain the candidate sources for these high-energy particles. In this sense, Hillas argued that the Larmor orbit of accelerated particles have to fit inside the accelerator size (R_S). Therefore, the maximal achievable energy according to Equation 1.4, should be $E_{max} = \beta eBR_s$, where the term β is the velocity of the shock wave in the Fermi model or in any other acceleration mechanism. It can be interpreted as the efficiency of the acceleration mechanism. This argument can be seen graphically in Figure 1.2, where extraterrestrial sources are represented in a graph according to their magnetic field and size. The sources above the two diagonal lines are sources which can accelerate particles up to $E > 10^{12}$ eV or $E > 10^{20}$ eV respectively. The objects that satisfy the conditions for acceleration up to 10^{20} eV are neutron stars with a very strong magnetic field, jets of AGNs, GRBs, radio galaxies, and clusters of galaxies. However, above this energy there are no so many candidates.

A different scenario to explain very high-energy cosmic rays is based on the so-called top-down models. The difference with the previous ones (bottom-up models) is that the particles do not acquire energy gradually but they are the decay products of super-massive particles or topological defects associated,

Chapter 1. Neutrino astrophysics
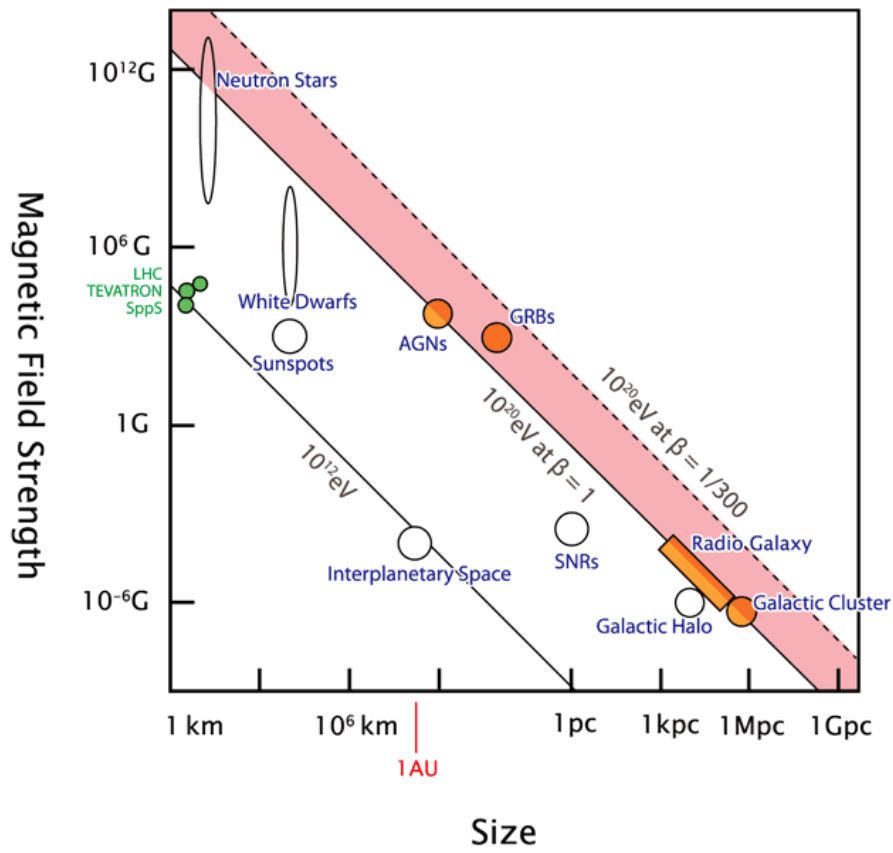
Figure 1.2: *Hillas diagram where cosmic ray sources candidates are classified according to their magnetic field and size. The diagonal lines represent the upper limits of the energy of the particles emitted in such objects. $\beta = 1$ means the maximum attainable energy.*

for instance, with Grand Unified Theory (GUT). Several theories have been postulated (e.g. [25]), mainly triggered by the observation of the AGASA evens over the GZK cutoff. Nevertheless, the recent results from AUGER disfavour this scenario since they confirm the existence of a cutoff. Moreover, the main production in the top-down models would be photons, and not cosmic rays. Therefore, even assuming top-down models, the events over 10^{19} eV are difficult to explain.

Very high-energy cosmic rays (above 10^{19}eV) are not deflected by magnetic fields, allowing the possibility of doing astronomy with them. The drawback in this case is the lack of statistics because of the reduction of the cosmic ray flux (power law) and, in addition, the reduction of the range due to the GZK effect. A huge detector able to accumulate enough statistics can mitigate this situation. Nowadays, the only experiment able to perform astronomy in this way is the AUGER detector. They have published results where they claim correlations between high-energy events (E > 57 EeV) and nearby Active Galactic Nuclei (AGNs) located within a distance of 71 Mpc from us [26]. AUGER was able to collect 27 of such events, having 20 of those an angular distance lower than 3.2° with respect to a list of 44 AGNs (see Figure 1.3). Only 6 coincident events were expected from an isotropic distribution, which means a confidence level larger than 99%. It is important to note that the AUGER angular resolution is better than one degree for the energy range considered in the analysis.
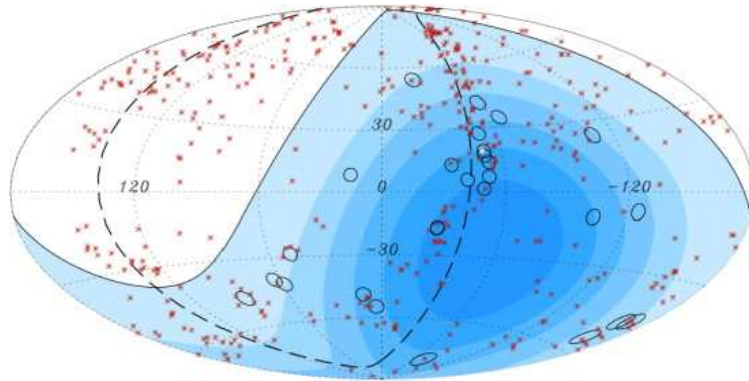
Figure 1.3: *Sky map in galactic coordinates with the nearby AGNs (points) and the 3.2°cone centered at the AUGER events (circles).*

This analysis was recently updated with more data [27] containing 44 selected events of more than 55 EeV. In this sample 17 of these 44 events correlate with the source list. That means a less than 1% probability to occur by chance.

Chapter 1. Neutrino astrophysics

However, the correlation is not so strong as it was found in the first analysis.

1.5.2 Acceleration mechanisms of cosmic rays

The acceleration process of the cosmic rays in the expanding supernova shock-waves is usually known as the Fermi acceleration mechanism because the original theory was proposed by Fermi in 1949 [28]. Actually, we can distinguish between the second order (original theory) and first order Fermi acceleration mechanism. In the second order acceleration mechanism, a parti-
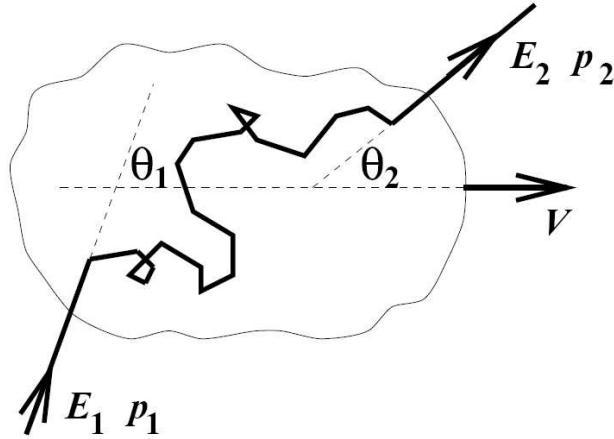
Figure 1.4: *Second order Fermi acceleration mechanism. A particle with energy E_1 and momentum p_1 enters in a moving magnetic cloud and exits with E_2 and p_2 gaining energy.*

cle enters in a magnetic cloud which moves with a certain velocity V. Inside the cloud, the particle suffers collisionless elastic scattering with the magnetic irregularities (see Figure 1.4). After several interactions, the particle goes away with an average energy gain proportional to the square of the cloud velocity β ($\beta = V/c$):

$$\frac{\langle \Delta E \rangle}{E} \backsimeq \frac{4}{3}\beta^2 \qquad (1.7)$$

Being β^2 positive by definition, the energy increases in average, and thus the cosmic rays are accelerated. However, the energy gain is only of second order and the acceleration mechanism rather inefficient.

The first order Fermi acceleration mechanism is a modification of the second order to be more efficient. In this case, a particle enters in a region with magnetic irregularities separated by a non-relativistic planar shock-wave (see
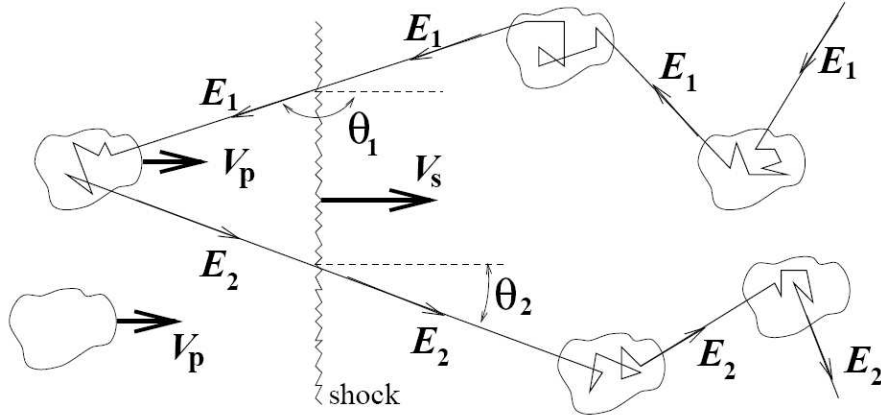
Figure 1.5: *First order Fermi acceleration mechanism. The main difference with respect to the second order mechanism is the shock-wave which produces a more efficient acceleration.*

Figure 1.5). These shock-waves are produced by the mass ejected during a supernovae explosion or other astrophysical scenarios. The mass ejected, traveling faster ($\sim 10^4$ km/s) than the interstellar medium (~ 10 km/s), produces a shock-wave. The particles crossing the shock are accelerated with an average energy gain of:

$$\frac{\langle \Delta E \rangle}{E} \simeq \frac{4}{3}\beta \tag{1.8}$$

where $\beta = V/c$, V being the speed of the supernovae ejected mass. Comparing with the second order mechanism the dependence on β is linear. This is why it is called "first" order Fermi acceleration mechanism.

Both, second and first order mechanisms, can reproduce the power law spectrum of the cosmic rays. Assuming that after each encounter with the magnetic plasma, the kinetic energy of the particle increases by $\Delta E = \xi E$, and the energy of a particle after n acceleration cycles is:

$$E_n = E_0(1 + \xi)^n \tag{1.9}$$

Then, the number of particles with energy above a given value of E is given by:

$$N(> E) \propto \frac{1}{P_{esc}} \left(\frac{E}{E_0}\right)^{-\gamma} \tag{1.10}$$

being the γ obtained:

Chapter 1. Neutrino astrophysics

$$\gamma = \ln\left(\frac{1}{1 - \mathrm{P}_{esc}}\right) / \ln(1 + \xi) \approx \mathrm{P}_{esc}/\xi \qquad (1.11)$$

with the assumption of $\xi \ll 1$ and $\mathrm{P}_{esc} \ll 1$. For more details on Fermi acceleration processes see [29].

The Fermi acceleration is able to explain quite well the energy spectrum of cosmic rays up to $\sim 10^{15}$ eV, assuming they have a galactic origin and that they are accelerated at the outer shock boundaries of expanding SNRs. However, the sources of UHECR which are supposed to have extra-galactic origin remain still unknown. The results aforementioned from AUGER provides a hint about possible sources but the situation is far to be completely understood.

As it was said before, the most promising objects from the numerous candidates suggested as extra-galactic cosmic ray accelerators are AGNs and GRBs.

Active Galactic Nuclei

The present standard model of AGNs states that they are composed by an internal supermassive black hole (10^6 - 10^{10} M$_\odot$) with an accretion disk where dust and gas are accumulated. The black hole accretes matter and produces the jet emission from its centre. The AGNs are commonly classified by their emission properties, like luminosity or main wavelength emission (Seyfert Galaxies, Quasars, LINERs, Blazars, etc.) It is thought that all of them are the same phenomenon seen from different relative angles and at different ages (see Figure 1.6). For instance, blazars are thought to be a subset of AGNs where one of the jets points towards the Earth.

The CR should be accelerated thanks to the shock acceleration processes lead by the large magnetic fields created in the accretion process where a big amount of gravitational energy is released.

Gamma Ray Bursts

Discovered accidentally by US military satellites in 1967, GRBs are extremely luminous sources of electromagnetic radiation. They have luminosities ranging from $\sim 10^{51}$ erg s^{-1} to 10^{54} erg s^{-1} assuming isotropic emission. However, if the burst is beamed in a particular direction, as is nowadays presumed, the energy outflow is lower. They emit very fast (from milliseconds to several minutes of duration) flashes of γ-rays, followed typically by several days of X-ray, optical and radio emission (the so called afterglow of the GRB). They occur at apparently random positions in the sky at a rate of several per day, so it is not possible to predict when or where they will occur. GRBs can be divided into short hard-spectrum bursts (SHB), with a duration shorter than two seconds, and long soft bursts lasting more than two seconds. Although our knowledge on GRBs has increased meaningfully in the last years thanks
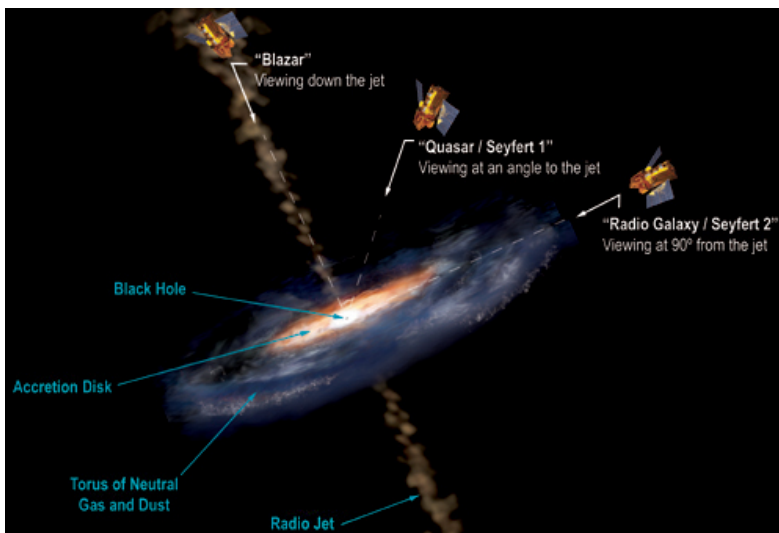
Figure 1.6: *Schematic view of an AGN. Different types of AGNs are related to the different points of view from the observer [30].*

to the Swift satellite (NASA's multi-wavelength observatory dedicated to the study of GRBs), the origin of the GRBs is still unclear. The short duration GRBs are supposed to be the result of the merge of compact objects, e.g. neutron stars in binary systems [31]. The long GRBs, which are two thirds of the total GRBs, are associated to supernova with extremely massive stars which collapse to a black hole [32]. Presently, the most accepted model is the *fireball* model [33], where in the star collapse a fireball of electromagnetic plasma expands at relativistic energy, being powered by the central engine. The GRB takes place in internal shock-waves produced when faster shells in the expanding material overtakes early and slower shells. In this picture, protons should be accelerated. However, the amount of energy transferred to protons is unknown.

A different theory suggest that the cosmic rays acceleration in GRBs is due to the interaction of the protons and nuclei with a "cannonball" during their travel in the interstellar medium. A cannonball is a non-relativist spherical shell emitted after the explosion of a supernovae. According to the authors, this model explains all the observed properties of the cosmic rays for any energy range. An updated review on this theory can be found in [34].

Chapter 1. Neutrino astrophysics

1.6   High-energy photons

Protons are the most abundant component of the cosmic ray flux. However, they cannot give any directional information since are deflected by magnetic fields. In this sense, photons, being neutral particles, allow the possibility of doing astronomy. Nonetheless, their mean free path is considerably reduced due to the interaction with the extra-galactic background light (EBL) and CMB. Therefore, the most energetic sources become opaque (see Fig 1.7). This reduction vanishes at higher energies ($\sim 10^{20}$ eV) but the fluxes are very low at these energies to be detectable by the current experiments.
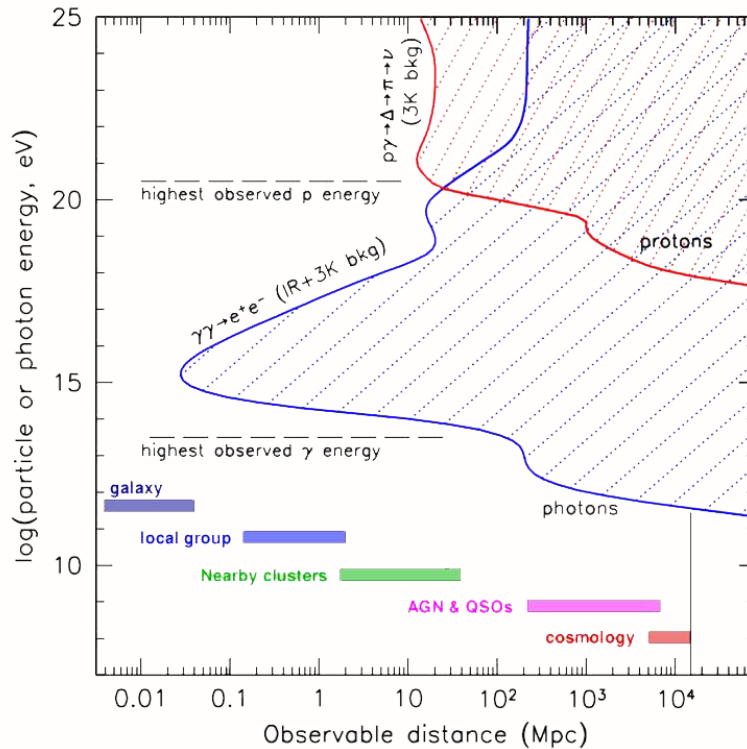
Figure 1.7: *Pair production mean free path for high-energy protons and pho-tons. In the case of photons, the reduction is clear for energies above 100 TeV.*

High-energy photons do not arrive at the Earth surface since they interact with the upper layers of the atmosphere. The way to detect them depends on

the photon energy. Space satellites are used tu detect directly primary photons in the MeV-GeV energy range. At higher energies, the only way to detect them is by collecting the Cherenkov light induced by the charged particles produced when photons interact with the atmosphere. This is the detection principle of the Imaging Atmospheric Cherenkov Telescopes (IACTs) as H.E.S.S., MAGIC or VERITAS. Other ground-based detectors as MILAGRO, catch the light produced by means of a Water Cherenkov Extensive Air Shower Array (EAS), where the detector takes advantage of the larger density and number of photons created with respect to the IACTs. With these experiments, photons up to $\sim$ 100 TeV have been detected.

Satellite-based detectors are limited by their small effective area (~ 1 m^2). The most fruitful experiment was the Compton Gamma Ray Observatory (CGRO), which took data for 9 years (1991-2000) with four different experiments covering six decades of the electromagnetic spectrum. The one covering the most energetic part was the Energetic Gamma Ray Experiment Telescope (EGRET) reaching energies up to 30 GeV. It completed a full sky map of 271 gamma-ray sources with less than one degree of pointing accuracy. However, this accuracy was not enough to correlate 172 of the detected sources with known objects, so they remain still unidentified.

Nowadays, the leading satellite project is the Fermi Gamma-ray Space Telescope (former GLAST) which was launched in June 2008. It covers an energy range from 30 MeV to 300 GeV, which includes the energy gap between previous satellites and ground-based detectors. It is able to locate objects with a resolution better than one arcminute. The sky map of the first source catalog with the Large Area Telescope (LAT) on Fermi for eleven months is shown in Figure 1.8. It represents the deeper and better resolved map of the γ-ray sky.

Several collaborations have worked constructing different kinds of γ-ray detectors which has lead to an enormous development of the detection techniques. Hundreds of sources have been detected and studied bringing out exciting results which have allowed a better understanding of the physical processes at the sources. The proper knowledge of these processes is crucial since the objects producing high-energy gamma-rays are clear candidates for cosmic neutrino emission.

1.6.1 Acceleration mechanisms of gamma rays

The main sources of high energy photons are supposed to be also high energy cosmic ray sources (see section 1.5.2). In many cases, the photon production can be explained by the self-synchrotron Compton (SSC) mechanism. In this model, photons are created by synchrotron radiation of ultra-relativistic electrons accelerated by magnetic fields in the source. This gives a spectrum peaked at infrared/X-rays. By means of inverse Compton scattering with their own parent electron population, the energy of these photons is increased. This

Chapter 1. Neutrino astrophysics
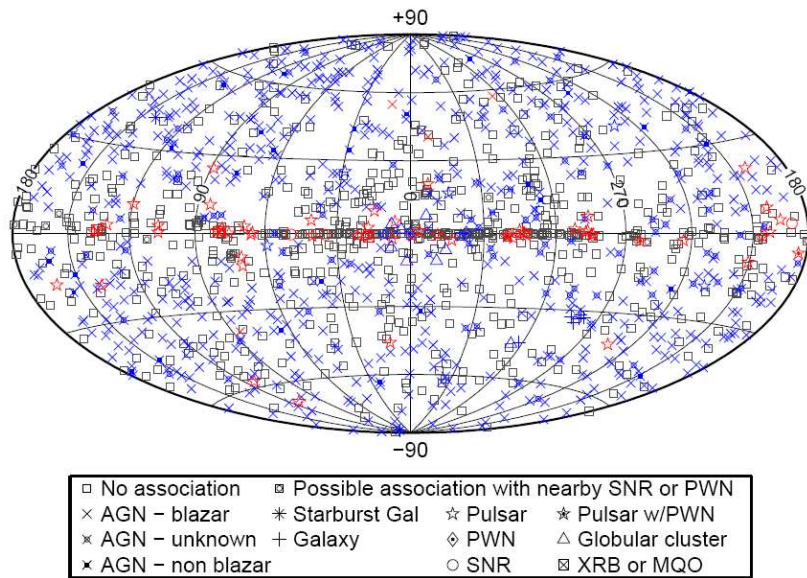
Figure 1.8: *The FERMI/LAT bright source list in galactic coordinates obtained with the first eleven months of survey data. The sky map contains the 1451 catalog sources in the 100 MeV to 100 GeV range [35].*

is a leptonic scenario, where no neutrinos would be produced.

A different scenario to explain the production of high-energetic photons is by means of the decay of neutral pions produced by the interaction of extremely energetic protons with the matter or radiation at the source. This is an hadronic scenario where high energy neutrinos would be also produced from the decay of charged pions and subsequent decays.

The energy spectrum of most of the high-energy photons sources can be explained quite well by the electromagnetic/leptonic processes. In this case, the spectrum shows a double bump shape with one peak in the IR/X-ray band due to synchrotron radiation, and another peak in the gamma range energy due to inverse Compton. The SSC model have successfully explained many blazar spectral energy distributions (e.g. Mk501 [36]). However, recent results have shown some examples as PKS 2155-304 [37] where no clear evidence of flux correlation between the X-ray and the VHE emission components was found.

Moreover, the precise measurements performed with the current IACT detectors of some nearby galactic sources pointed out that the energy spectrum is difficult to be explained by assuming only an electromagnetic contribution. This was observed for the first time by the H.E.S.S. collaboration when they studied the energy spectrum of the shell supernova remnant RX J1713.7-3946 (see Fig 1.9). The shape of its gamma-ray spectrum favours a dominant hadronic scenario [38] [39].

As in the cosmic ray case, some other hypothesis about the production of high energy photons have been formulated. Some of them have a direct relation with "exotic" physics. For instance, photons could appear as a result of the annihilation or decay of very massive or energetic objects such as dark matter candidates, very massive particles at unification scales, primordial black holes, etc.

1.7 High-energy neutrinos

Once high-energy cosmic rays and photons have been detected, the detection of high-energy cosmic neutrinos will complete the "multi-messenger approach", which tries to understand the most energetic processes in the Universe from different points of view. The existence of cosmic rays is a proof that cosmic neutrinos should exist. The question is whether the sources can produce a flux high enough to be detected at the Earth. According to present theoretical models of hadronic acceleration, the expected neutrino flux should be detectable with a 1 km^3 neutrino telescope. A lot of efforts have been made to construct large enough detectors to have a chance for a cosmic neutrino discovery. Therefore, the incoming years will be crucial for the neutrino astronomy field. In this section we will review the main candidates to be high-energy

Chapter 1. Neutrino astrophysics
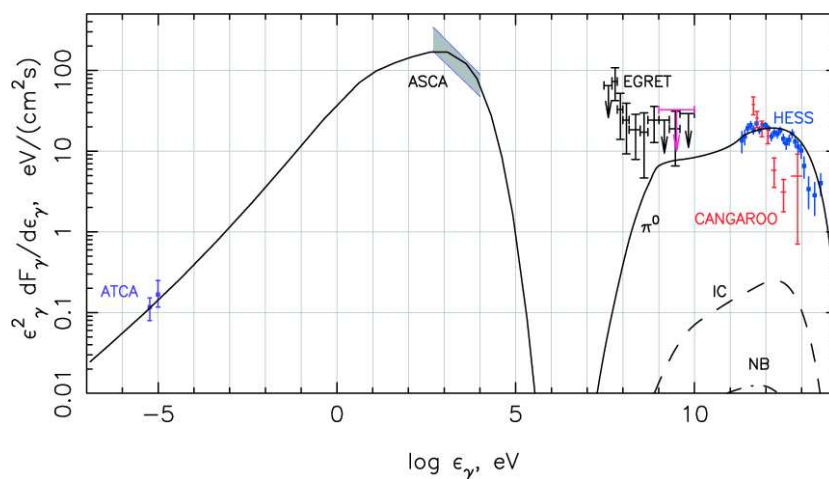
Figure 1.9: *Spatially integrated spectral energy distribution of the SNR RX J1713.7-3946 detected by H.E.S.S. Data from different experiments are shown. The first bump corresponds to the synchrotron radiation, and the second bump above 10^7 eV can have different contributions corresponding to π^0-decay (solid line), inverse Compton (IC, dashed line) and Nonthermal Bremsstrahlung emissions (NB, dash-dotted line) [38].*

neutrinos emitters and which are the predicted fluxes for that sources.

1.7.1 Acceleration and production of cosmic neutrinos

Neutrinos are expected to be produced as a result of the interaction of accelerated protons with matter or background photons in the source. The result are pions (see Eq. 1.12) that decay into gamma rays and neutrinos as it was shown in Eq. 1.2.

$$p\gamma \longrightarrow \Delta^+ \rightarrow p\pi^0/n\pi^+ \qquad (1.12)$$

The decay of particles escaping the source (neutrons and charged pions) will give cosmic rays, gamma rays and neutrinos. Therefore, the expected neutrino sources should produce also high-energy protons and photons. Moreover, if hidden sources were produced by Nature, then we would not have any proof of their existence because of the absorption of the protons and photons at the source. In that case, neutrinos would be the perfect candidates to reveal them.

Once the high energy neutrinos are produced in the astrophysical accelerators, they can travel in straight line from the source to the Earth detectors, and therefore, point back to the source. Astronomers can correlate these sources with astrophysical objects already detected by means of telescopes working with different messengers.

The fraction of the neutrino flavours at the source (ν_e:ν_μ:$\nu_\tau \sim$ 1:2:0) is equalize once they arrive at the Earth (ν_e:ν_μ:$\nu_\tau \sim$ 1:1:1) due to neutrino oscillations.

1.7.2 Cosmic neutrino candidate sources

Being the Sun and the SN1987A the only detected sources of extraterrestrial neutrinos, we can only infer from the cosmic ray and gamma-ray detection which are the more promising candidates to produce cosmic neutrinos. The theoretical predictions are shown in Figure 1.10. However, due to the neutrino properties, objects without other counterparts could also be detected.

The most promising candidates to produce high energy neutrinos, divided in galactic and extra-galactic, are:

Galactic

Thanks to the intense work carried out during the last years by the gamma-ray telescopes, we have now a large number of galactic high-energy gamma sources observed in detail. We know their energy spectrum quite accurately between $\sim$ 100 GeV and a few TeVs, and therefore, we can predict theoretically which should be the neutrino flux emitted by these sources.

Chapter 1. Neutrino astrophysics
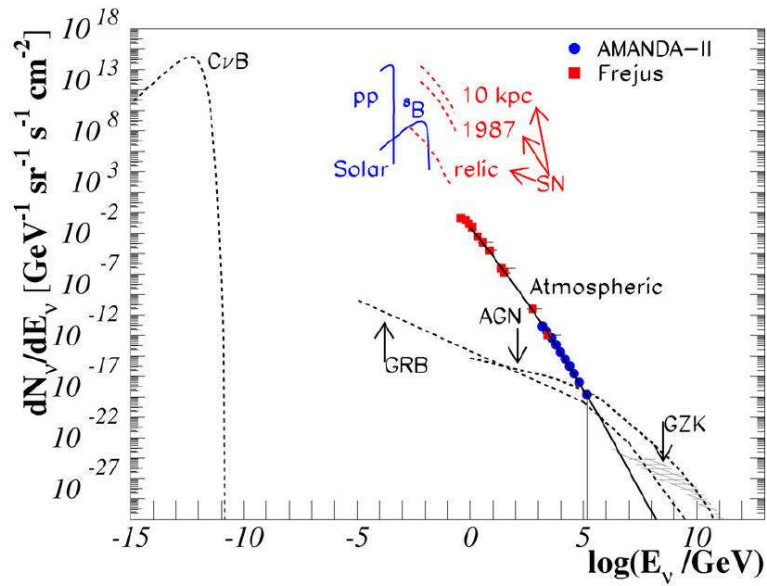
Figure 1.10: *Predicted cosmic neutrino spectrum from the lowest energy due to the Big Bang background to the most energetic processes as AGN or GRB. Data points have been added for the atmospheric neutrinos.*

- **Supernova Remnants (SNRs)**

  We have seen that acceleration of galactic cosmic rays is likely produced by SNRs. Moreover, observations of gamma-ray detectors have confirmed the emission of TeV photons. This photon emission seems to have an important contribution from hadronic acceleration (see section 1.6.1). Therefore, the SNRs have all the ingredients to be also high energy neutrino emitters. However, the predicted fluxes are very low. According to [40], the number of events expected in 5 years in a km^3 detector is of the order of 10 signal events above the TeV range for the most promising cases as RX J1713.7-3946, while the background in this particular case would be around 40 events. The detection of neutrinos from SNR could be the final proof to confirm the emission of pions in the SNR and, therefore, confirm the SNR as the galactic cosmic rays accelerators.

- **X-ray Binary systems**

  Binary systems are composed by two stellar objects orbiting around a common center of mass. The most powerful case is when one of them is a collapsed object such as a white dwarf, a neutron star, or a black hole (e.g. Microquasars). The separation between the objects is small enough so that matter is transferred from the normal star to the compact object through an accretion disk producing mainly X-ray in the process. Neutron stars are known to have very strong surface magnetic fields (10^{12} G) and sometimes millisecond periods. Both the accretion and the magnetic dipole radiation are possible energy sources. The existence of high magnetic fields and plasma flows creates the necessary environment to create of strong shocks waves, and the corresponding particle acceleration. The predictions are of 0.5 events in the TeV range for 5 years in a km^3 neutrino detector [40].

- **Pulsar wind nebulae (PWN)**

  Pulsar wind nebulae (also known as plerions), are extended structures of shocked relativistic particles powered by a pulsar at very high energy. These particles interact with the surrounding media producing gamma-ray emission which has been observed by gamma-ray telescopes. Although gamma-ray emission from PWNs is thought to be produced by inverse Compton scattering, an hadronic contribution for energies in the TeV range has also been suggested [41]. According to theoretical predictions, the PWNs could produce around 10 events (above 1 TeV) in 5 years of a km^3 neutrino telescope, being Vela X and the Crab Nebula the most promising candidates [40].

- **Galactic Centre (GC)**

27

Chapter 1. Neutrino astrophysics

Placed in the Sagittarius constellation, the galactic centre is the most interesting hypothetical source of neutrinos in our galaxy. There, we can find hundreds of white dwarf stars, neutron stars, and a supermassive black hole. All these potential sources and new ones have been already confirmed as gamma ray emitters [42]. However, neutrino emission of individual sources seems difficult. The best chance for detecting neutrinos from GC is to consider the diffuse emission from it. Around 3 events could be detected from GC (above 1 TeV) in 5 years of data taking in a km^3 neutrino telescope [40]. The GC especially has a great interest for a Mediterranean telescope since it is within his field of view.

- **Unknown-No counterpart**

  The results from Fermi have allowed the identification of some of the previous unknown detected sources by EGRET. Likewise, at larger energies, gamma-ray telescopes as HESS or MAGIC have confirmed that there are VHE gamma-ray sources without counterparts in other wavelengths. In this sense, and taking into account that the flux sensitivities beyond ~ 10 TeV for Cherenkov Array Telescopes are significantly reduced, it is not excluded that some sources of energies of the order of ~ 100 TeV and above remain unknown. Neutrino telescopes offer an opportunity to improve our knowledge of such sources, since the effective area of a neutrino telescope increase at high energies (up to ~ 100 PeV).

Extra-galactic

In this subsection we will discuss about the possibility of high energy neutrino emission from extra-galactic sources, and which are the theoretical predictions for their neutrino fluxes.

- **Active Galactic Nuclei**

  As we have seen previously, AGNs are supposed to be steady sources emitting gamma-ray, and therefore, high-energy neutrino emission is also possible. The early theoretical predictions for neutrino emission from AGNs (e.g. [43]) postulated intensities above the Waxman-Bahcall (WB) limit (see Section 1.7.3). However, later results were not so optimistic (e.g. [44]) giving predicted fluxes close to the WB bound. The theoretical predictions can be seen in the cosmic neutrino spectrum plot in Figure 1.10.

  The results published by the AUGER collaboration suggest a correlation between cosmic rays and nearby cosmic sources [27]. This measurement hits the AGNs as high energy cosmic rays sources. Moreover, in the same AUGER data, an excess of events were pointing to Centaurus A within less than 3.1°. This was the closest AGN included in the source list

studied. Theoretical attempts in modelling the sources to infer the flux of neutrinos emitted have immediately arisen. In [45] the author claims that a neutrino detector having 1 km^2 of muon effective area could detect between 0.8 and 0.02 events per year from a source with a index spectral between 2.0 and 3.0, respectively.

- **Gamma Ray Bursts**

  Cosmic neutrino emission is also expected from transient sources as GRBs. Several theories have been postulated during the previous years (e.g. [46]). Waxman and Bahcall [47] stated that neutrinos of $\sim 10^{14}$ eV should be emitted and at least several tens of events detected in a km^3 detector. Currently, with the data already taken by the neutrino telescopes we are close to attain this limit [48]. Therefore, the results that be will provided by neutrino telescopes in the incoming years could represent a turning point for our understanding of GRBs. The main advantage of GRBs is that, being transient sources, they are essentially background free since we can perform a search in a reduced time window where the atmospheric background should be negligible.

- **Starburst galaxies**

  The starburst galaxies are regions with an enormous high rate of star formation when comparing with the rate formation in standard galaxies. In this scenario, it is likely to have neutrino emission as it was suggested by Loeb and Waxman [49]. Synchrotron radiation has been observed in these objects, so relativistic electrons (~ 1 GeV) should be present. Assuming that there are also protons, neutrinos could be produced in pp interactions. According to the authors, the lower limit flux inferred for neutrinos, in the energy range from GeV to 0.3 PeV, is of the order of $E_\nu^2 \Phi_\nu \approx 10^{-7}$ GeV cm^{-2} s^{-1} sr^{-1}. In a km^3 detector, between 10 and 100 events with $E_\nu > 100$ TeV are expected per year.

- **Cosmogenic (GZK) neutrinos**

  GZK neutrinos are the decay product of pions produced by high energy protons which interacts with the CMB [50]. These neutrinos should be in the EeV energy range. If we assume that UHECR are protons coming from AGNs we expect a rate of 1 or 2 events in a km^3 detector per year. The rate is low because the predicted spectrum for GZK neutrinos peaks at ultra high energy (10^8 GeV), where the energy response of the neutrino telescopes decreased because in these cases, the Earth becomes opaque to upward-going vertical neutrinos. In this case, other techniques as acoustic detection seems to be more promising and can complement the neutrino telescope observations.

Chapter 1. Neutrino astrophysics

1.7.3   Diffuse flux of cosmic neutrinos

The neutrino flux predicted is low and difficult to detect. Therefore, discovering a punctual source in the sky will not be trivial. On the other hand, many sources can give a combined signal high enough to be detectable as what is called "diffuse flux". Diffuse flux studies are based on the fact that cosmic neutrinos should have a harder spectra (larger spectral index) than the main background coming from atmospheric neutrinos. Therefore, a significant number of neutrinos above the background is expected at high energies where the atmospheric neutrino flux is highly suppressed (see Fig 1.10). Extra-galactic cosmic rays (protons) and neutrinos should be produced in the same scenarios (AGNs, GRBs, etc.), so a bound between both is expected. With the standard assumption of a injection spectrum of $dE/dN \propto E^{-2}$, as expected from Fermi acceleration, Waxman and Bahcall [51] state that the intensity of high-energy neutrinos produced by photo-meson interaction in a source of size not exceeding the mean free path of proton photo-meson should be: $E^2\Phi_\nu < 2 \times 10^{-8}$ GeV cm^{-2} s^{-1} sr^{-1}. The sensitivity of the IceCube configuration with 40 lines, which has been already reached, is below this limit.

1.8   Other physics topics

Apart from the search of cosmic neutrino emitters, neutrino telescopes cover a wide variety of physics topics. Some of them are reviewed here:

1.8.1   Dark matter search

Apparent deviations from Newtonian dynamics of the cosmological motions have been observed on visible matter (e.g. rotational speeds of galaxies, orbital velocities of galaxies in clusters, etc.) [52]. These gravitational effects cannot be explained by the mass contained in the observed luminous objects, indicating that another kind of non-luminous matter, the so-called dark matter, must exist in the Universe. Experimental results, mainly provided by the WMAP experiment, conclude that about a quarter of the energy density of the Universe consists of non-baryonic dark matter (75% is expected to be dark energy and only 5% accounts for ordinary baryonic matter). The particles known up to now do not fit with the properties required by the dark matter candidates [53]. Neutrinos, which should have mass because they oscillate, are not abundant enough to explain the observations. Moreover, they were relativistic at the stage of the structure formation which would lead to an inconsistent cosmology where galaxies are formed too late. This is the reason why cold dark matter candidates are presently favoured. Among them, the most popular ones are the lightest super-symmetric particle (being the neutralino the best candidate) and the B$^{(1)}$ particle, the first Kaluza-Klein excitation of the B boson in theories
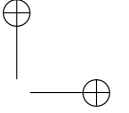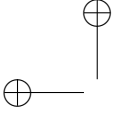
with universal extra dimensions. In both cases, these particles are expected to be gravitationally trapped by heavy mass objects like the Sun or the Earth, where they would annihilate producing neutrinos as final products. These neutrinos could escape from the dense media giving a characteristic signature which could be detected by neutrino telescopes. Therefore, neutrino telescopes could offer an indirect way to detect dark matter.

1.8.2 Monopole search

Magnetic monopoles are predicted by GUT theories. It this scenario and at very high energies, the electromagnetic, gravitational and strong interactions are unified. GUT theories predicts that super heavy magnetic monopoles were created as topological defects on the transition phase of the early Universe. The magnetic monopoles could be accelerated by magnetic fields up to energies of 10^{21} - 10^{24} eV. Therefore, for monopoles of mass below 10^{12}-10^{14} GeV a relativistic behaviour appears and therefore they suffer energy losses.

A moving monopole induces a cylindrical symmetric electric field. When a monopole crosses the matter of our detector, both magnetic and electric field, interact with the medium causing excitation and ionization of the surrounding atoms. The signal induced by a monopole when crossing the detector can be ~ 8500 times higher in light intensity than a muon. In Neutrino telescopes as ANTARES, the signal of a magnetic monopole can be discriminated from other background signals [54].

Other topics that can be studied by neutrino telescopes are: search for Lorentz invariance violation in oscillations of atmospheric neutrinos [55], detection of low energy (MeV) neutrinos from supernovae [56], search for particle emission from cosmic string or topological defects, etc.

1.9 Neutrino telescopes

The neutrino telescope concept was pointed out for the first time by Markov in 1966 [1]. The basic idea is to take advantage of the natural targets in order to get a detection volume large enough to detect the expected cosmic neutrino fluxes. Using an array of photomultipliers (PMTs) embedded in a transparent medium we can detect the Cherenkov light induced by the charged particles produced in the neutrino interaction with the matter. These requirements lead to two options: Antartic ice or ocean/lake water.

According to theoretical predictions, it seems that the natural scale to detect cosmic neutrinos is the km^3 (second generation detectors). Presently, IceCube is the leading neutrino telescope project. It is close to its completion,
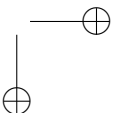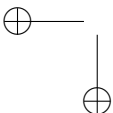
Chapter 1. Neutrino astrophysics

and therefore, near to culminate the first km^3 detection volume. Thus, we are close to have the first answers. In the meantime, since the predictions are quite model dependent, discoveries are not discarded with the available data samples from the current operating detectors (first generation). Actually, as it will be shown, some theoretical models have been already ruled out with the present data.

The ANTARES neutrino telescope will be described and explained in detail in the next chapter. In the following, a brief description of the other neutrino telescope projects is given.

1.9.1 DUMAND

The pioneer project in the construction of a neutrino telescope was DUMAND (Deep Underwater Muon And Neutrino Detection) [57], which started in 1976. It was planned for operate an underwater detector placed at 4800 m depth in the Pacific Ocean off Keahole Point on the Big Island of Hawaii. In December 1993, they were able to deploy a string containing photodetectors and environmental instruments. A junction box was also placed on the ocean bottom and cabled to shore. Unfortunately, this detector was not completed due to the lack of funds and was canceled in 1995. However, it marked the beginning of the neutrino astronomy.

1.9.2 Baikal

The Baikal project, working since 1993, was the first experiment able to operate successfully a neutrino telescope. The detector is located at the Siberian lake Baikal at a depth of 1.1 km. The current detector is the result of several upgrades made during the last years. The first configuration consisted of three strings with 36 optical sensors that was called NT36. The detector was upgraded in April 1998 up to 192 optical sensors distributed in eight strings giving place to the NT200 structure. The last upgrade, NT2000+, took place in 2005 with the addition of three external strings enclosing a volume of 5 M-ton. A review of the status and results of the experiment can be found at [58]. The next activities of the Baikal collaboration point towards the construction of a km^3-scale detector. To this end, a prototype string was deployed in the spring 2008 to test the new technology. The new detector will contain a total of 1300-1700 optical modules, arranged in 90-100 strings with 12-16 OMs each and an instrumented length of 300-350 m.

Results

The analysis of the data taken during the 1998-2003 period have been presented by the Baikal collaboration [58]. Roughly 1000 days of data taking

have been analyzed resulting in the detection of 372 upward going neutrino candidates to compare with the 385 atmospheric neutrinos predicted from Monte Carlo. No extraterrestrial candidate sources were found, being the 90% C.L. upper limit for the neutrino flux (all flavours) of $E^2\Phi < 2.9 \times 10^{-7}$ cm^{-2} s^{-1} sr^{-1} GeV (for 20 TeV $< E_\nu <$ 20 PeV). The experiment has also set upper limits for WIMPs (Weak Interactive Massive Particles) and magnetic monopoles.

1.9.3 AMANDA

The AMANDA (Antarctic Muon And Neutrino Detector Array) detector started in 1992 and was fully operating since 2000. Located at the geographical South pole next to the Amundsen-Scott South Pole Station, it has been taking data independently until 2006 when it was integrated into the IceCube detector, which currently takes advantage of the higher density of AMANDA to be more efficient at low energies. AMANDA-II is the name of the final detector configuration composed by 677 optical modules containing 8" PMTs, distributed in 19 strings embedded in ice at depths between 1500 and 2000 meters as can be seen in Fig 1.11. The resulting instrumented volume was about 15 Mton of ice. In July 2009 AMANDA was finally decommissioned.

Results

A detailed review of the AMANDA results can be found in [59]. The collaboration has presented the analysis of the atmospheric neutrino flux for the data taken on the period of 2000-2003. The observed flux is compatible with the one expected from Monte Carlo and the response of the detector is well understood, however, there is still a 30% of uncertainty on the flux coming from systematics (modelling of the detector and light propagation in ice and from the indetermination of the neutrino energy). Presently, this precision is insufficient to distinguish among the current theories modelling the atmospheric neutrino flux. Concerning the search for astrophysical point sources, AMANDA was able to detect 6595 events in the seven years period (see Fig 1.12). Using an unbinned maximum likelihood search, the maximum significance detected was 3.36 σ before accounting for trial factors. Randomizing the right ascension of the events on the AMANDA sky map to create background maps, they found at least an excess of 3.36 σ in the 95% of the obtained maps. Therefore, the result is compatible with a background fluctuation and there is no evidence of extraterrestrial neutrino sources. Even when they looked at selected sources, no evidence for a neutrino emission was found. In this case, the 90% C.L. upper limits on muon and tau neutrinos is given as $E^2\Phi_{\nu_\mu+\nu_\tau} < \Phi_{90} \times 10^{-11}$ TeV cm^{-2} s^{-1} assuming flavour equality.

Chapter 1. Neutrino astrophysics
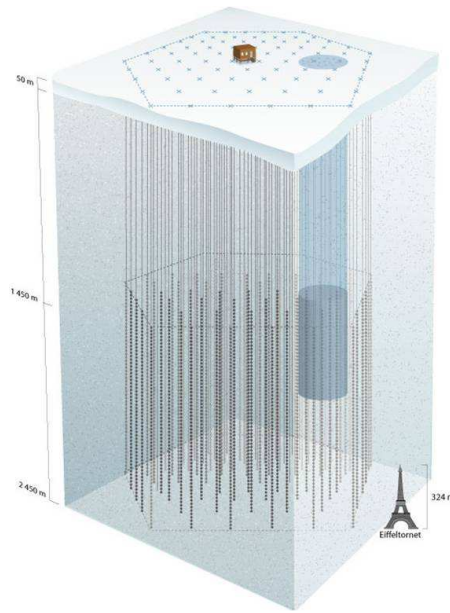
Figure 1.11: *Artistic view of the IceCube neutrino telescope. The AMANDA detector is represented by the solid cylinder within IceCube.*
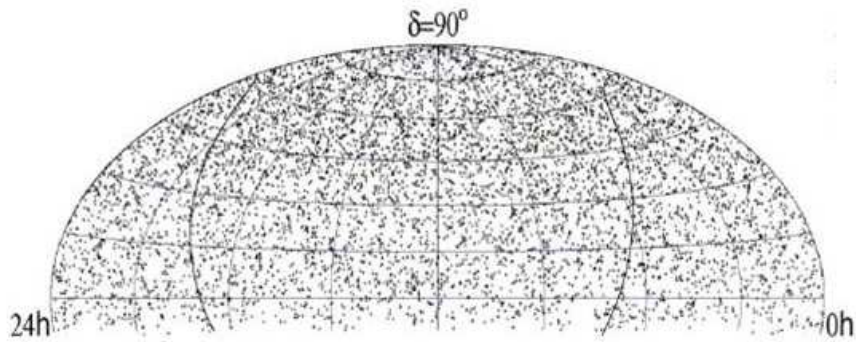
Figure 1.12: *AMANDA sky map in equatorial coordinates with the 6595 neutrino candidates collected during the seven years of AMANDA operation (3.8 live-years).*

Concerning diffuse fluxes of cosmic neutrinos, from the analysis of the data from 2000 to 2003 (807 days of live-time), the number of expected events of high-energy extraterrestrial muon neutrinos was 6.1 in the energy range from 15.8 TeV $< E_\nu <$ 2.5 PeV (with an spectrum of E^{-2}), while 6 events were detected. The corresponding upper limit was E$^2\Phi < 7.4 \times 10^{-8}$ GeV cm^{-2} s^{-1} (see Fig 1.12). With these results no evidence of prompt neutrinos[7] has been found (at 90% C.L). However, the limits obtained by AMANDA are still higher than the WB limit.

In the energy range going from 2×10^5 GeV to 10^9 GeV data from 456.8 days of live-time were analyzed. For such high-energies, the Earth becomes opaque to neutrinos so the search is made for horizontal events. Two events were detected while less than 2.6 background events were expected, which leads to an 90%CL upper limit of E$^2\Phi \leq 2.7 \times 10^{-7}$ GeV cm^{-2} s^{-1} sr^{-1}. Several models which predict neutrino fluxes from AGNs have been preliminarily excluded at the 90% confidence level after these results.

Other studies for physics beyond the standard model, as violation of Lorentz invariance, can be done using atmospheric neutrinos. Small deviations from the theory of relativity are expected to produce measurable neutrino oscillations. However, no indication of that effect was found, and an upper limit has been set. As Baikal, indirect searches for dark matter did not show any evidence.

1.9.4 NEMO

The NEMO (NEutrino Mediterranean Observatory) [60] collaboration studies the possibility of constructing an underwater km^3 neutrino telescope offshore the East coast of Sicily (Italy) in front of Capo Passero at 3500 m depth. The collaboration performed an intense research and development (R&D) activity during the period 1998-2004. In the following years, they tested the main technological solutions developed for the construction of a km^3 scale underwater neutrino telescope. In the so-called Phase-1 a junction box and a prototype tower were deployed at 2100 m depth in December 2006 operating for few months. The connection with the junction box was done by means of a 28 km electro-optical cable. During the Phase-2 the collaboration is constructing a fully equipped 16 storey tower to be deployed at 3500 m depth, and linked with the shore station with a 100 km electro-optical cable. Nowadays, all the activities of NEMO are devoted to the development of instruments for the future KM3NeT detector. For instance, it is foreseen to deploy, a 20-storey KM3NeT tower as well as an ANTARES Mini Line with 4 floors.

---

[7] Atmospheric neutrinos produced from mesons containing charm quarks.

Chapter 1. Neutrino astrophysics

1.9.5 NESTOR

The NESTOR (Neutrino Extended Submarine Telescope with Oceanographic Research) collaboration [61], aimed to construct a neutrino telescope to be deployed offshore the Greek coast in front of Pylos at a depth of 3800 m. The collaboration constructed and deployed a multidisciplinary deep-sea station, at a depth of 4100 m in January 2002. In addition, in March 2003, they successfully deployed a test floor of the detector tower, fully equipped with 12 optical modules, final electronics and associated environmental sensors. It was operating for more than one month. As NEMO the current activities of the experiment are related with the KM3NeT detector design.

1.9.6 IceCube

According to theoretical models, the natural scale to search for cosmic neutrinos is at least the km^3 volume. Therefore, a new generation of neutrino telescopes has started by some collaborations aiming to build such huge detectors. The most advanced project is IceCube, which presently is the biggest neutrino telescope operating in the world. Once completed, it will comprise 4800 ten-inch optical sensors deployed on 80 vertical strings between 1450 and 2450 m under the ice surface at the geographical South pole. For the time being, three quarters of the detector (58 lines) are already deployed. IceCube represents the upgrade of the 0.1 km^2 AMANDA detector which, as has been said, will be embedded inside (Fig 1.11). The detector will detect neutrinos above 100 GeV, and will be able to distinguish among the different neutrino flavours. The expected rate is of 220 neutrinos per day. Moreover, a Deep Core instrumentation is also being constructed (one line already installed) in order to improve the detection sensitivity at low energies ($\sim$10 GeV) for the neutrino properties studies and indirect dark matter searches. In addition, an air shower detector (IceTop) of 300 TeV of threshold helps in the identification of the track. The collaboration has already provided the first results referred to a configuration of 22 lines (IC22). Although still preliminary, results with 40 lines has also been presented in conferences [62]. For 22 lines, 5114 neutrino candidates have been selected in 276 days of live-time. In the analysis of the point-like sources, the highest significant hot-spot detected has a significance of 4.8σ. However, this value (pre-trial) should be corrected by the fact of looking at several directions in the sky (post-trial). After this correction the excess becomes 2.2σ which is not enough for claiming a discovery.

In the preliminary results with 40 lines, and half a year of data taking, there is not any significant excess either (see Fig 1.13). The sky map presented for 40 strings also includes the high-energy down-going reconstructed events selected by energy-sensitive cuts as explained in [63].
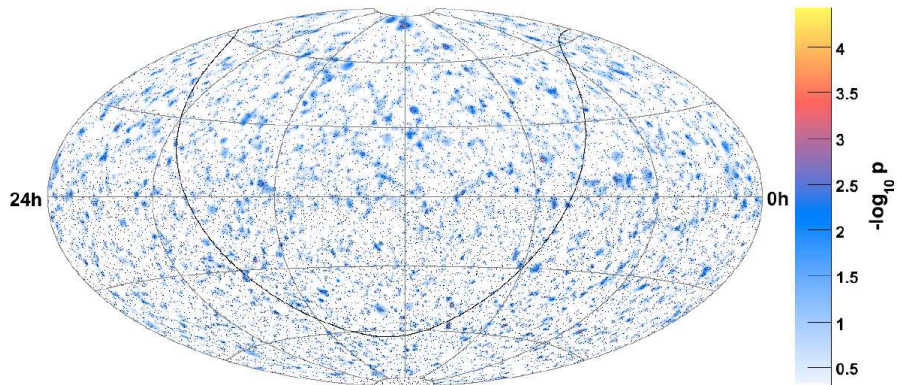
Figure 1.13: *Sky map with 17777 events, 6796 up-going neutrinos candidates (zenith > 90°) in the Northern hemisphere plus 10981 down-going muons rejected to the 10^{-5} level in the Southern hemisphere. The grey tone is related to the probability of the excesses. The maximum significance in the map represents an excess of 7 events. However, after taking into account trial factors, the probability for this event to happen anywhere in the sky map is not significant.*

Chapter 1. Neutrino astrophysics

1.9.7 KM3NeT

Funded by the EU 6th (Design Study) and the 7th (Preparatory Phase) Framework Program, the KM3NeT consortium aims to complete a project for a km^3 scale Neutrino Telescope in the Mediterranean Sea. This collaboration is mainly nourished by physicists and engineers working in the three pilot projects ANTARES, NEMO, and NESTOR. The Conceptual Design Report (CDR) was presented in the spring of 2008, and the preliminary version of the Technical Design Report (TDR) was published in July 2010. KM3NeT will cover the southern hemisphere complementing the observations of IceCube of the northern hemisphere with an overlapping region between both detectors.

The observations of the KM3NeT detector together with the ones from other future projects in the Astroparticle field as the Cherenkov Telescope Array (CTA) project or the Square Kilometre Array (SKA), will extend our knowledge of the Universe detecting the same sources with different messengers.

Chapter 2

The ANTARES neutrino telescope

The ANTARES collaboration has been involved in the construction of an underwater neutrino telescope for more than a decade. Since 2008, this detector is a reality and is taking data smoothly. This chapter summarizes the efforts done by the collaboration to build the telescope and provides a general description of the detector which is the biggest undersea neutrino telescope constructed at present.

2.1 Detection Principle

A neutrino telescope is essentially a three-dimensional array of PMTs embedded in an optically transparent medium, water or ice, enclosing huge matter volumes of the order of km^3. Cosmic neutrinos can cross the Earth which acts as a shield for other particles and arrive at the vicinity of the detector. They can interact with the water/ice or the rock bed and produce, via charge current interaction, a relativistic muon. The Cherenkov light induced by the muon is detected by the photomultipliers and the corresponding time and position information can be used to reconstruct the muon track. Depending on the neutrino energy, the muon track can be taken as the true neutrino direction. For neutrino energies greater than 1 TeV, the muon is aligned with the incident neutrino within a degree (see formula 2.1). At higher energies (above 10 TeV) the kinematics effects start to be negligible and the biggest uncertainty in the direction estimation comes from the calibration (timing and positioning) of the detector.

$$\langle \theta_{\mu\nu} \rangle \approx \frac{0.7^o}{(E_\nu/TeV)^{0.6}} \qquad (2.1)$$

Chapter 2. The ANTARES neutrino telescope

2.1.1 Different neutrino topologies

The reactions that could be produced by a neutrino interacting with matter can be divided into two categories:

$$\nu_l(\bar{\nu}_l) + N \longrightarrow l^-(l^+) + X \qquad \text{charged current (CC)}$$

$$\nu_l(\bar{\nu}_l) + N \longrightarrow \nu_l(\bar{\nu}_l) + X \qquad \text{neutral current (NC)}$$

(2.2)

The CC reactions are weak interactions where a $W^{\pm}$ boson is exchanged and charged particles are created. In the case of NC reactions, it is the Z^0 boson which is exchanged to produce neutral particles. The differential cross section can be written as

$$\frac{d^2\sigma}{dxdy} = \frac{2G_F^2 mE_\nu}{\pi} \left(\frac{M_V^2}{Q^2 + M_V^2} \right)^2 \times [xq_i(x,Q^2) + x\bar{q}_i(x,Q^2)(1-y)^2] \quad (2.3)$$

where G_F is the Fermi constant, m is the nucleon mass, $-Q^2$ is the invariant squared momentum transfer between the incoming neutrino and the outgoing lepton, M_V is the mass of the boson, q_i and $\bar{q}_i$ (i = NC, CC) are the quark and anti-quark distribution functions, and x and y are the Bjorken scaling variables:

$$x = Q^2/2m(E_\nu - E_l) \qquad (2.4)$$

and

$$y = (E_\nu - E_l)/E_\nu \qquad (2.5)$$

A review about the differential cross section for these reactions can be found in [64]. Figure 2.1 shows the CC and NC cross section for energies going from 10 to 10^{14} GeV.

Regarding the CC reactions, events with different topologies can be detected (see Fig 2.2). Muon neutrinos (ν_μ) give a μ which is characterized by the long path travelled before being absorbed (see section 2.1.3). This produces long track events which are suitable for a good reconstruction. Electron neutrinos (ν_e) yield an electron which produces a shower (electromagnetic and hadronic cascade) producing short-track events. The tau neutrino (ν_τ) interaction produces a τ which, if the energy is lower than about one PeV, decays immediately producing a track which can not be separated from the subsequent shower. On the contrary, if the τ energy is greater than about one PeV, the τ can travel several meters before decaying giving a second shower. This produces, for a wide energy range, an identifiable pattern known as *double bang*.
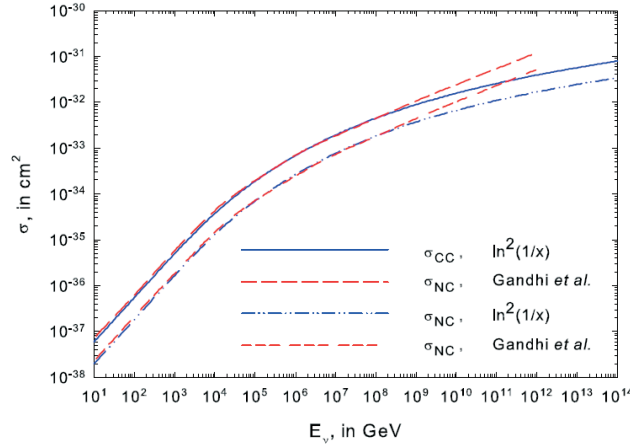
Figure 2.1: *Charged (CC) and neutral (NC) neutrino cross sections as a function of the neutrino energy [64] based on a proton structure function that varies as $ln^2(1/x)$ for small x. The dashed lines refers to previous work based on the CTEQ4-DIS quark distributions.*
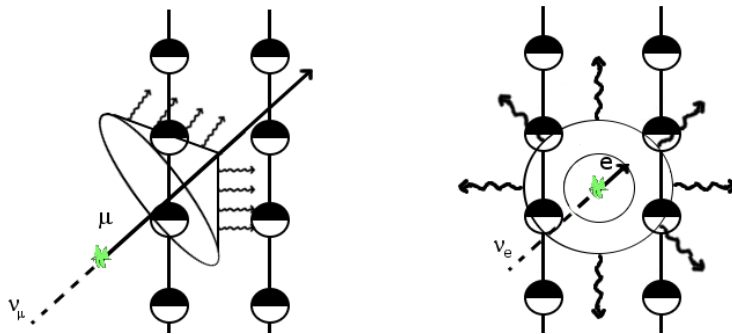
Figure 2.2: *Main event topologies in neutrino telescopes. Left: a track event produced by a muon neutrino. Right: a cascade event produced by an electron neutrino.*

Chapter 2. The ANTARES neutrino telescope

2.1.2   Cherenkov light emission

Cherenkov emission was detected for the first time in 1934, when P. A. Cherenkov observed the emission of blue light from a bottle of water exposed to radioactive bombardment. This radiation appears when a charged particle travels through a dielectric medium at a speed greater than the speed of light in that medium, so the condition for a particle to produce Cherenkov light is $\beta > 1/n$, where n is the refractive index of the medium and β is the particle speed divided by the speed of light in the vacuum. Thus, a fraction of the particle energy is emitted as an electromagnetic shock-wave with low intensity, although, the energy losses due to ionization are 2 or 3 orders of magnitude larger than the energy losses due to Cherenkov emission.

The Cherenkov radiation propagates as a cone whose opening angle depends on the particle velocity as:

$$\cos \theta_C = \frac{1}{\beta n} \tag{2.6}$$

On the ANTARES site, the refraction index is $n \simeq 1.35$ for a wavelength of 450 nm, so $\theta_C \simeq 42°$. The number of photons (N) emitted per unit of length (x) and wavelength (λ) induced by a particle with charge Z and speed β in a medium of refractive index n is given by:

$$\frac{d^2 N_\gamma}{dx d\lambda} = \frac{2\pi \alpha Z^2}{\lambda^2} \left(1 - \frac{1}{\beta^2 n(\lambda)^2} \right) \tag{2.7}$$

As it is shown in the previous equation, the number of emitted photons increases with the frequency. Therefore, most of the photons emitted in Cherenkov radiation are produced in the ultraviolet region of the electromagnetic spectrum.

Integrating the expresion 2.7, it can be shown that around $\sim$100 Cherenkov photons are emitted every cm of flight path in the range from 400 to 500 nm, where the efficiency of the ANTARES PMTs and the water transparency are maximum.

2.1.3   Muon propagation in matter

Muons are able to cross the detector since they lose a small fraction of energy when passing trough matter. Muon energy losses in matter come from ionization and radiative processes (pair production, bremsstrahlung and photonuclear reactions). These energy losses can be parametrized as [16]

$$-\frac{dE}{dx} = a(E) + b(E)E \tag{2.8}$$

where $a(E)$ accounts for the ionization losses and $b(E)$ describes the radiative losses. The critical energy is defined as the energy at which ionization and radiation losses are equal on average, i.e., $E_{\mu c} = a(E_{\mu c})/b(E_{\mu c})$. The critical energies, for water and "standard rock", are ~ 1 TeV and ~ 700 GeV respectively [65].

2.1.4 Physical background

The main background in a neutrino telescope comes from the flux of surviving down-going muons produced by the cosmic ray interactions in the atmosphere. The atmospheric muon flux exceeds the atmospheric neutrino flux by twelve orders of magnitude. In order to reduce, as much as possible, the huge amount of atmospheric muons, neutrino telescopes are buried in water/ice at large depths (typically $\sim$2000 m). Even under such a thick shielding, the down-going atmospheric muon flux is still six orders of magnitude higher than atmospheric neutrinos at a depth of 2300 m water equivalent (Figure 2.3). Therefore, only up-going events are used since only neutrinos are able to cross
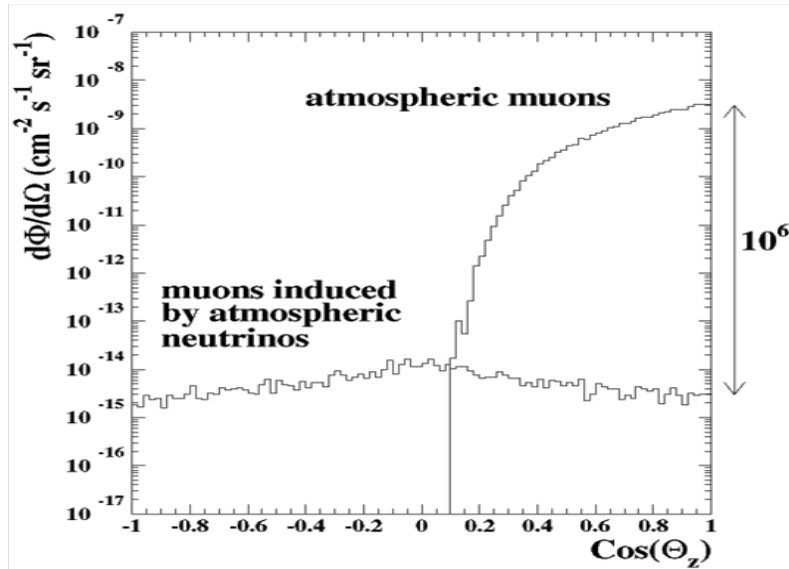
Figure 2.3: *Muon and atmospheric neutrino fluxes at 2300 m water equivalent depth. Even at this depth, the muon flux dominates by six orders of magnitude the neutrino one.*

the entire Earth. With the aim of being more efficient to up-going tracks, the

Chapter 2. The ANTARES neutrino telescope

PMTs of ANTARES are 45° downward oriented. Consequently, ANTARES covers the opposite sight of the sky which would be seen by a conventional optical telescope located in the same place.

The atmospheric neutrino background is more problematic since it is irreducible. However, in the sky map of neutrinos collected by the detector, atmospheric neutrinos are expected to be distributed randomly, whilst cosmic neutrinos should have privileged directions since they are expected to be produced in cosmic sources. Therefore, clusters of events will reveal the existence of cosmic neutrino sources. Figure 2.4 left shows a schematic view of the kind of events seen in ANTARES.
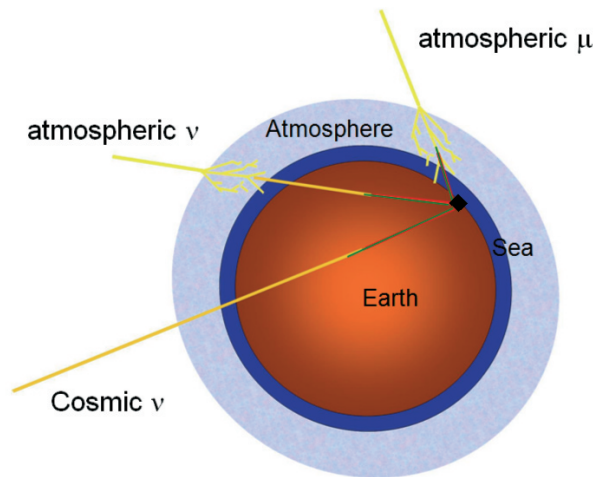
Figure 2.4: *Schematic view of the signal and physical background (atmospheric muons and neutrinos) seen in the ANTARES detector.*

2.2 The ANTARES project

On May 30th 2008, the ANTARES collaboration [2] completed the construction of an underwater neutrino telescope with a surface area of 0.1 km^2 and an instrumented volume of about $180 \times 180 \times 350$ m^3. The detector is located at (42°50'N 6°10'E) at 2475 m depth and 40 km away from Toulon (France) (see Fig 2.5). The final configuration (see Fig 2.6) consists of 885 PMTs distributed along 12 lines. Each line has 25 storeys divided in sectors of 5 storeys. Each storey has a triplet of PMTs with the only exception of the twelfth line, where the upper sector (five storeys) is equipped with acoustic
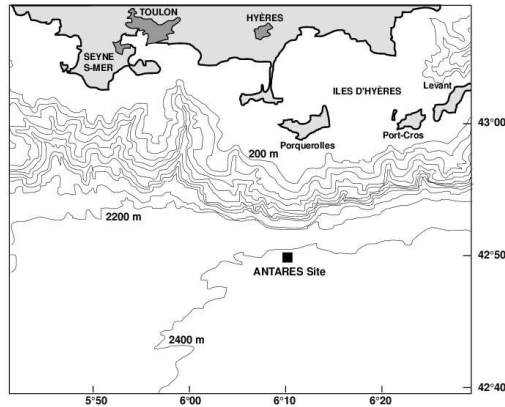
Figure 2.5: *A map of the French region where the detector is deployed.*

devices instead of PMTs. The link to the shore station is done by means of an electro-optical cable which provides the power supply and transmits the data to the shore. This is a unique cable which arrives at the "junction box", where, it is split in thirteen interlink cables, one for each line and one for the instrumentation line. All the data recorded are transmitted to the shore station located at the French ville of La Seyne-sur-Mer. ANTARES is the first submarine neutrino telescope ever built, and as it was said, presenly is the largest neutrino telescope in the northern hemisphere.

2.3 The ANTARES devices

A detector as ANTARES requires a specific instrumentation in order to guarantee a proper operation during the data taking period. This instrumentation is the result of several years of research and development tasks. In this section we describe the main devices of the ANTARES detector.

2.3.1 The Optical Module

The Optical Module (OM) [66] (Figure 2.7) is the basic device of the ANTARES telescope. It contains the PMT which detects the Cherenkov light enclosed in a glass sphere made up of borosilicate, with 41.7 cm of inner diameter and 15 mm of thickness. This sphere is devised to support high pressures of about 260 atm at normal operation and 700 atm on qualification tests. Its refractive index is 1.47 in the 300 - 600 nm range, and light transmission is $>$

Chapter 2. The ANTARES neutrino telescope
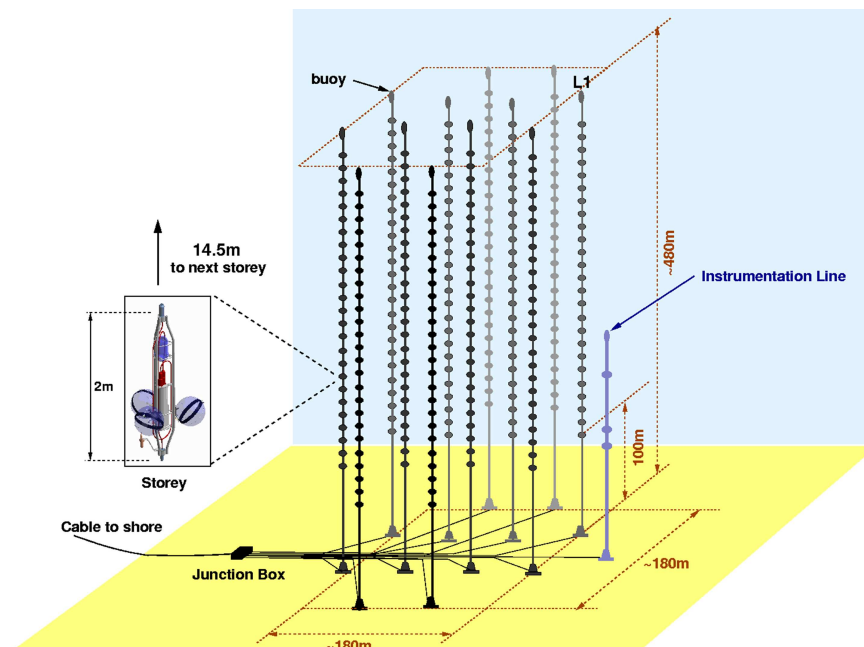
Figure 2.6: *A schematic view of ANTARES where some of the main elements of the detector can be noticed.*

95 % above 350 nm.

The PMT housed in the glass sphere must meet several requirements in order to provide the best performance for physics research. Several PMT models were put under test before the final selection of the Hamamatsu R7081-20 model [67]. This model has a 10" photocathode diameter, a gain $> 5 \times 10^7$ working at high-voltage (< 2000 V), a peak to valley ratio > 2, a transit time[1] spread, TTS < 3 ns (FWHM) and a dark noise rate < 10 kHz for a 0.25 photo-electron (p.e.) threshold.

In order to reduce the influence of the Earth's magnetic field, which can degrade the TTS of the PMT, a μ-metal cage with high magnetic permeability is also included. Fixing the μ-metal and the PMT to the glass sphere, there is an optical gel which is highly transparent and has been devised with an appropriate refraction index to reduce reflection.

Finally, an internal built-in LED placed on the back of the PMT, is used for internal calibration and monitoring of the PMT transit time.
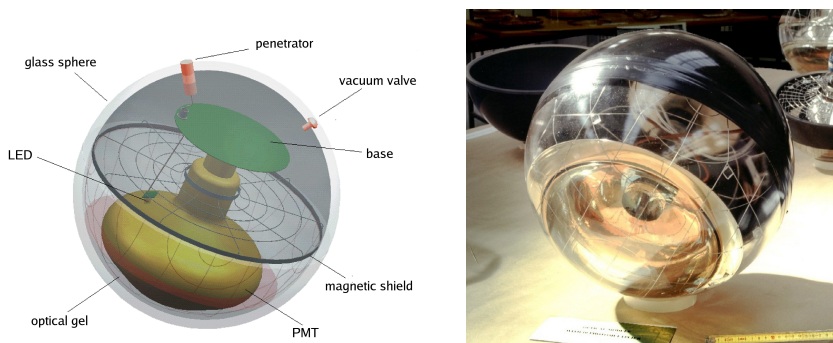
Figure 2.7: Schematic view of the ANTARES Optical Module with its components (left). Picture of an OM used in ANTARES (right).

2.3.2 The Storey

Each storey is composed by a triplet of OMs and a titanium container, the Local Control Module (LCM), which contains and protects the associated electronics from the water pressure. Some storeys have additional instruments: receiving Rx hydrophones (5 per line) devised for the acoustic positioning system, and an LED Optical Beacon (4 per line) for timing calibration purposes.

---

[1]The transit time of the PMT is the time from the light arrival to the photocathode up to the output of the signal in the anode.

Chapter 2. The ANTARES neutrino telescope

The triplet of OMs are equally spaced 120° and facing downward 45° in order to be more efficient for up-going neutrino detection. The LCM is placed at the center of the frame, as can be seen in the Figure 2.8.

All the electronic commands, the clock signal, the slow control, the HV supply and the readout, arrive at the OMs via the electronic boards housed in the LCM. The main electronic board is the Analogue Ring Sampler (ARS) which digitize the signals coming from the OMs, providing information about the amplitude, arrival time and its shape (see section 2.5.1).

Figure 2.8: Picture of a storey being deployed. There are 3 OMs facing 45°downward, and the LCM in the center housing the readout electronic cards. An LED Optical Beacon for timing calibration purposes can also be seen in the top part of the storey frame.

2.3.3   The Line

ANTARES is composed by 12 lines. Each line contains 25 storeys and has a length of $\sim$ 450 m. The lowest $\sim$100 m are not instrumented in order to avoid the fouling and the mud spread out from the seabed by the marive currents. The 25 storeys are 14.5 m equidistant and grouped in five sectors. In each sector, one particular LCM is called the Master Local Control Module (MLCM) which contains the Ethernet switch to concentrate the data traffic coming from the other 4 LCMs and from itself. The lines are anchored to the seabed by the Bottom String Socket (BSS), and held vertically by a buoy at the top of the line. In the BSS, there is the String Power Module (SPM), which provides the power supply to the BSS instruments and to all the LCMs in the string. The electronics required by the slow control system, the clock and the instruments of the BSS are contained in the String Control Module (SCM), which also takes care of the control of the data traffic from the MLCMs. The instruments in the BSS are an acoustic transponder RxTx hydrophone, a
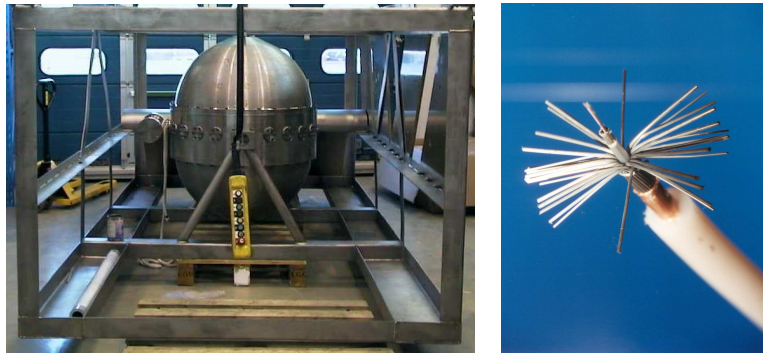
Figure 2.9: *Picture of the junction box (left), and of the main electro-optical cable open (right).*

pressure sensor, and a sound velocimeter. In addition, the BSS of Lines 7 and 8 have a Laser Beacon for timing calibration.

Before the final integration of the lines, some mechanical tests were done with prototype lines as the Mini Instrumentation Line with Optical Modules (MILOM) [68], where the OMs, the Optical Beacons, and some monitoring instruments were tested. A prototype line, the so-called Line 0, was deployed with the aim of studying the leak-tightness of the proposed electronics container scheme and the behaviour of the proposed design for the electromechanical cable [69]. Line 0 also included a prototype of an acoustic detection system.

2.3.4   The Junction Box and the electro-optical cable

The connection between the shore station and the detector is made by the main electro-optical cable (MEOC) which is 42 km long. It has 58 mm of diameter and is composed of 48 monomode pure silica optical fibres. It is designed to provide all the electronic commands, clock, power supply, etc. This cable arrives up to the junction box, an egg-shaped vessel made up of titanium (Figure 2.9) powered at 3700 V. The junction box (JB) splits the signals from the MEOC and distributes them to the lines by means of electro-optical interconnecting link cables. The signals from the junction box are received in the BSS of each line and are sent to the whole line.

Chapter 2. The ANTARES neutrino telescope

2.3.5 Instrumentation Line

Deployed in 2007, the Instrumentation Line (IL) [70] is an update of the previous Mini Instrumentation Line with Optical Modules (MILOM) [68]. The aim of the IL is to monitor the environmental properties of the ANTARES site. The instruments included in the IL are a seismometer, acoustic sensors for calibration purposes, pressure sensors, an Acoustic Current Doppler Profiler (ADCP) for sea current measurements, a light transmission meter (C-Star), a sound velocimeter (SV), a conductivity temperature probe (CT), and an Oxygen-Probe for determining the O_2 concentration, and a BioCam consisting in a camera inside an OM frame.

2.3.6 The AMADEUS system

Acoustic detection has arisen as a promising technique for very high-energy neutrino detection. The technique is based on the detection of the pressure pulse generated by the particle shower produced in a neutrino interaction in water at very high-energies. The ANTARES collaboration has considered this possibility by constructing which is called the AMADEUS (ANTARES Modules for Acoustic Detection Under the Sea) system [71]. The system is integrated in the ANTARES detector being located in the uppermost sector of Line 12 and in the IL. The AMADEUS setup consists of six clusters comprising six acoustic sensors each. This setup allows position reconstruction of acoustic point-sources. It has a dynamic range which goes from $\sim$3 mPa to 10 Pa (RMS) in the frequency range of interest, from $\sim$1 kHz to 100 kHz.

2.4 Site evaluation

A hostile environment as the deep-sea requires a detailed site evaluation in order to check if the detector elements will withstand its hard conditions, and to be sure that these conditions will enable the data acquisition without affecting the detector performance. Some of the most important issues are described here.

2.4.1 Biofouling and sedimentation

Underwater sedimentation and biofouling are natural processes. The former is caused by the gravel accumulation and the latter by the adhesion of microorganisms, mostly bacteria, on the external surfaces. Both effects can spoil the OM transparency. In order to evaluate the loss of light transmission on the ANTARES site, some tests were performed using a mooring line equipped with suitable devices [72].

As it is seen in Figure 2.10, the light transmission in the OM shows a general tendency to decrease with time. However, some recoverings which are correlated with the water current velocity are observed showing that surfaces are fouled by sediments more than by microbial adhesion and growth. Moreover, it seems to stabilize after several months. As it is shown, light transmission is maximum at $\theta = 90^o$ (equatorial) zenith angle, where only a global loss of ~ 2 % is expected after one year of operation.

Average loss sensitivity for the ANTARES OMs is expected to be smaller, since they are downward oriented with a zenith angle of 135˚. Therefore, it is foreseen that during the years of ANTARES data taking, fouling will not entail a considerable problem.
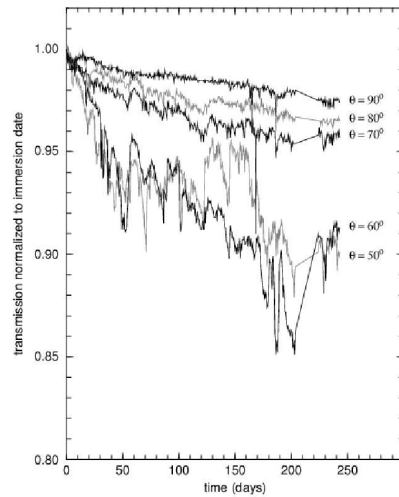
Figure 2.10: *Light transmission decreasing as a function of time. Five angles for OM orientation are considered.*

2.4.2   Optical properties of water

The most important properties which govern the light attenuation in water are the scattering length[2], which affects to the angular resolution, and the absorption length[3], which affects to the optimization of the line separation distances. These parameters depend on the wavelength, and are correlated by the equation:

$$\frac{1}{\lambda_{att}^{(eff)}} = \frac{1}{\lambda_{abs}} + \frac{1}{\lambda_{sct}^{(eff)}} \tag{2.9}$$

---

[2]defined as travel length where the probability of no-suffering any scattering has decayed in a factor e.

[3]defined as travel length where the no-absorption probability has decayed in a factor e.

Chapter 2. The ANTARES neutrino telescope

Wavelength(color)	$\lambda_{\mathbf{att}}^{\mathbf{eff}}$	$\lambda_{\mathbf{abs}}$	$\lambda_{\mathbf{sct}}^{\mathbf{eff}}$
466 nm (Blue)	$46.4 \pm 1.9 \pm 2$	$49.3 \pm 0.3 \pm 2$	$301 \pm 3 \pm 27$
370 nm (UV)	$26.0 \pm 0.5 \pm 1$	$28.9 \pm 0.1 \pm 1$	$133 \pm 3 \pm 12$

Table 2.1: *Results of the study on water optical properties obtained after June 2000 campaign for blue and UV light. The first error is the statistical error and the second is the systematic one.*

where the effective scattering length is defined as:

$$\lambda_{sct}^{(eff)} \equiv \frac{\lambda_{sct}}{1 - \langle \cos\theta \rangle} \tag{2.10}$$

being θ the angle for single scattering.

In a neutrino telescope like ANTARES, the sea water itself constitutes part of the detector. Therefore, the knowledge of the water optical properties is crucial to optimize the design and the detector performance. The ANTARES collaboration measured these optical properties in several sea campaigns using different experimental setups at different sites [73]. The main setup was an isotropic light source (pulsed LEDs) emitting in two different wavelengths (blue and UV). The light was collected by a small PMT of 1" diameter, and the relative separation between the source LED and the PMT could be changed.

Results of the June 2000 campaign are summarized in Table 2.1. The values were taken for blue and UV because these are the wavelengths for which the ANTARES PMTs are more efficient.

Currently, the optical water properties are measured *in situ* using the LED Optical Beacon system [74].

2.4.3 Optical background

The ANTARES underwater location is affected by an unavoidable optical background caused by the decay of the ^{40}K radioactive isotope diluted in water and the biological activity. This background can be described by two main components [75]. The first one is a continuous baseline which component has two sources: the Cherenkov light emitted by the electrons produced in the ^{40}K β-decays and the biological activity due to bacteria colonies. The biological contribution can produce variations in the baseline rate in a long time period. The conclusions from the site evaluation were that there is a typical value of ~ 35 kHz for this baseline[4].

---

[4]This rate depends on the photocathode diameter. In this case, a 8" photocathode was used instead of the 10" ANTARES final photocathode. That means a factor $(10/8)^2$.

The results with the detector lines have shown that the mean rate value is around 60 kHz (see Fig 2.11 top). It is important to realize that bioluminiscence is not a predictable phenomenon. In fact, a few months after the Line 1 connection, an unexpected intense and variable period of bioluminiscence were detected as can be seen in Fig 2.11 on the top plot. This effect lasted for a couple of months reducing the time of data taking. Afterwards, the rate went back to the nominal 60 KHz rate. During 2009 this high bioluminiscence period was reproduced again.

In order to avoid the ageing of the PMTs when high optical background rates are present, a safety threshold is established. If this threshold is exceeded, the PMTs are switched off until a stable low rate is recovered. In the meantime, the rates are monitored by the IL.

The second component of the optical background is composed by short bursts (generally lasting for hundreds of micro-seconds to seconds) which are simultaneously recorded by nearby OMs and are observed superimposed on the constant baseline due to their high rates (20% over the baseline). An example can be found in Fig 2.11 bottom. These bursts are attributed to light-emitting organisms which cross accidentally the detector and, in principle, are not correlated with the continuous component caused by the bacteria colonies. The burst rates can reach values > 200 kHz and, therefore, can produce an appreciable dead time in the acquisition system. A rate dependence on the site, season and undersea current velocity has also been observed.

The optical background can be rejected grouping the OMs in triplets since the electrons produced in the ^{40}K decays are low-energy electrons, they hardly travel a few centimeters in water and, therefore, it is quite unlikely that they can produce a simultaneous signal in the three OMs.

2.5 The Data Acquisition System and readout electronics

The data acquisition system takes care of the PMT signal digitization, data filtering, data transport to the shore, and the storage of the filtered data on disk. A schematic picture of the ANTARES DAQ is shown in the Figure 2.12. This system has been optimized according to the requirements that such underwater location needs. In particular, the PMT signals are digitized off-shore since the analogical transmission can produce information losses due to the long distance between the shore station and the detector.

All storeys are equipped with an LCM which contains the electronics needed for the readout of the 3 PMTs. Each LCM houses several Analogue Ring Sampler (ARS) ASIC[5] chips [76], where the signals coming from the PMTs are digitized. Basically, the ARS digitization provides the time and the integrated

---

[5]Application Specific Integrated Circuit.

Chapter 2. The ANTARES neutrino telescope
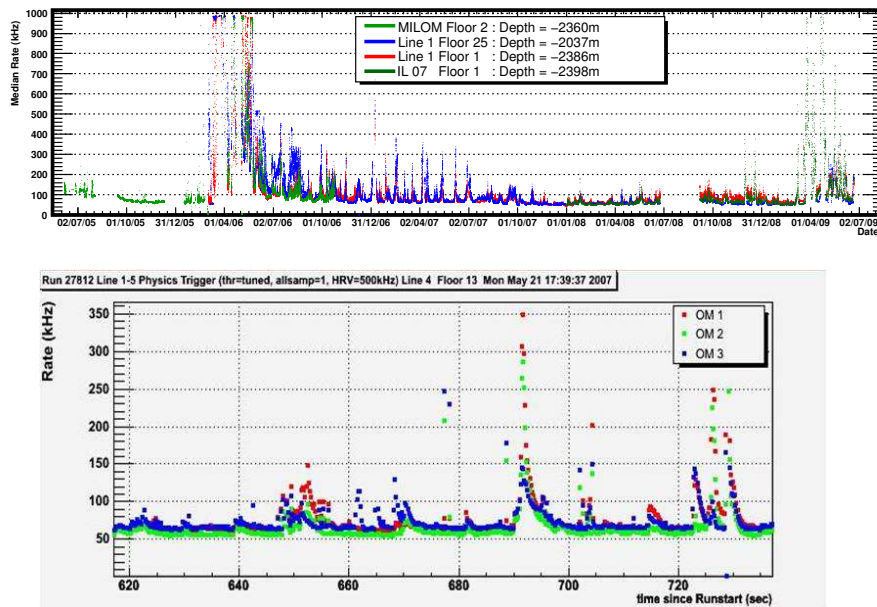
Figure 2.11: *Top: Median rate of the optical background recorded along four years in two storeys of the Line 1, one storey of the IL, and one of the MILOM. A period of 3 months of instability in the baseline rate at the beginning of the plot can be seen. Bottom: Baseline rate for a short time period. Some bioluminiscence bursts can be seen due to a light-emitting organism crossing the detector.*

2.5. The Data Acquisition System and readout electronics
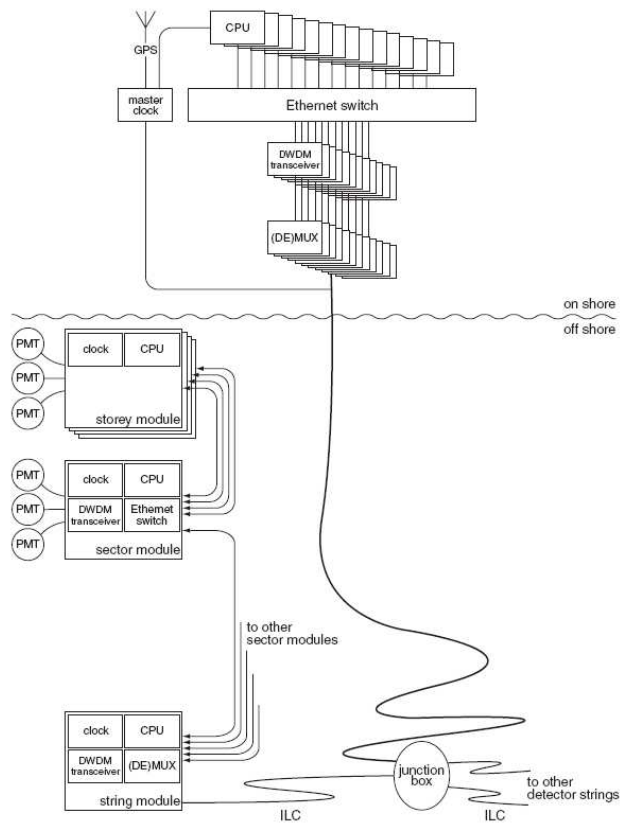
Figure 2.12: *Schematic view of the the DAQ hardware. Each storey has its electronic module (LCM). The information is sent by sectors to the SCM of each line and then to the shore station, at La Seyne-sur-Mer, via the junction box.*

Chapter 2. The ANTARES neutrino telescope

charge of each PMT signal. This combined information defines a Single Photo Electron (SPE) hit. The readout of every PMT is made with 2 ARSs using a token exchange protocol to reduce the dead-time which is about 200 ns due to the limited transfer speed to the analogue pipeline. The LCM of the storeys having an LED Optical Beacon has an additional ARS for the readout of the internal PMT[6].

The information registered by the LCMs is sent via an optical bidirectional 100 Mb/s link to the Master-LCM (MLCM) which merges all the data of the sector into a single Gb/s link thanks to an Ethernet switch. Then, the MLCM data goes to the SCM placed at the line anchor. Afterwards, the data from the whole detector (12 lines + instrumentation line) go to the JB and subsequently to the shore station located at *Institut Michel Pacha* at La Seyne-sur-Mer. The data transport between off-shore and on-shore is made using the Dense Wavelength Division Multiplexing (DWDM) technique, with multiple wavelengths to transmit different streams of data along a single fibre.

ANTARES is operated in an *all-data-to-shore* mode, giving a volume of raw data of 700 MB/s per line. Most of this data are originated from the high background rates caused by bioluminiscence and ^{40}K decay. Because of this very high volume of data, a filtering system is necessary to reduce it. Once the data is on-shore and has been processed, it is written on disk at the shore station and afterwards, sent to "Centre de Calcul de l'IN2P3" at Lyon.

The operation of the complete detector have proven the feasibility of the ANTARES DAQ architecture.

2.5.1   The ARS

Figure 2.13 shows schematically the process followed by a PMT signal in the ARS. With the aim of reducing the dark-current noise of the PMT, an amplitude threshold (L0), whose typical value corresponds to 0.3 photo-electrons, is set. When this threshold is crossed, a time-stamp (TS) and a time to voltage converter (TVC) value are generated providing the time information. Simultaneously, the charge is integrated within a gate of 35 ns long. The sampling frequency can be tuned between 150 MHz to 1 GHz. A Pulse Shape Discriminator (PSD) analyses the pulse shape classifying the signal as single photo-electron (SPE) or waveform (WF). Both WF and SPE modes provide the charge and the arrival time of the hit. In the WF mode, the analogue signal is sampled 128 times every ∼1.6 ns. This mode is very useful in order to do detailed analysis of the signals as calibration and timing parameter calculations. Nevertheless, it produces a big amount of data and currently, only SPE signals are recorded for physics analysis.

In a second step, the pulse information (SPE or WF), charge and time,

---

[6]For the Laser Beacon, there is also a specific ARS in the SCM for its photodiode readout.
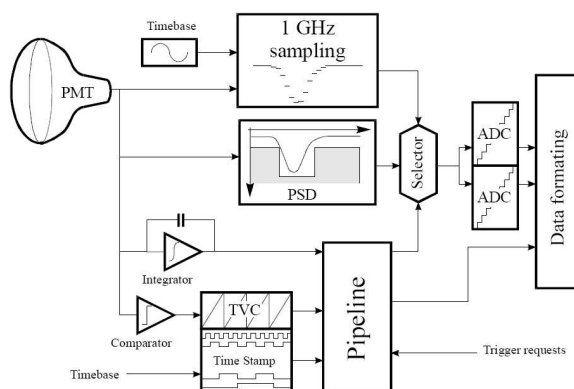
Figure 2.13: *Sketch of the internal ARS processes that takes place when a signal arrives to the PMT.*

is sent to a pipeline memory made up of 16 cells, which is able to handle 16 SPE hits or 4 WF hits. This process releases the ARS in order to acquire new hits without waiting for the precedent hit digitization. The hits in the pipeline memory are digitized by the Analogue to Digital Converters (ADC). The digital values for the charge (AVC) and time (TS + TVC) are generated for the selected hits and sent to the shore station. Afterwards, the pipeline memory is released and remains ready to process new events.

Time measurament

The time information of every hit is provided by the TS (concise time) and the TVC values (fine time). The TS gives the number of half clock cycles (25 ns) from the last reset time stamp (RTS). The TS is referred to the last RTS because the ARS has an internal clock which is reset every RTS. With the last RTS and the TS, it is possible to know the time from the beginning of the run of every recorded hit with an accuracy of 25 ns. Since the clock system is synchronized with the Universal Time, the absolute time can be obtained by assigning the GPS time to the data.

A higher precision is reached with the time to voltage converter (TVC) given by an 8-bit internal ADC in the ARS. This ADC provides a subdivision of the complete clock cycle (50 ns) in 256 parts, therefore, a precision of about 200 ps is attainable. The Figure 2.14 shows how the TVC works. A ramp generator provides a voltage proportional to the time within a clock cycle duration. When a PMT signal crosses the L0 threshold, the ramp voltage is

Chapter 2. The ANTARES neutrino telescope
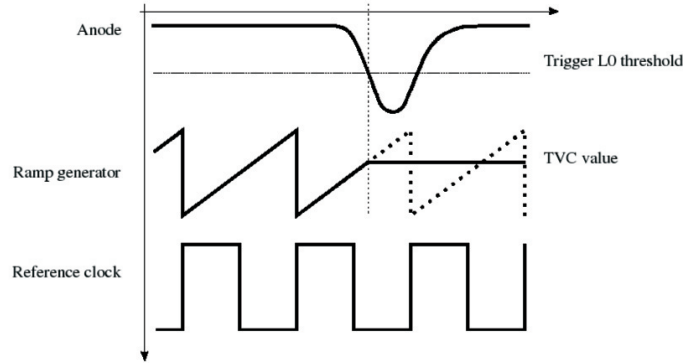
Figure 2.14: *Time measurement procedure in the ARS. A time stamp and a TVC value are generated when the signal crosses the L0 threshold.*

frozen and memorized providing the TVC value. Because of the dead time spent on recovering the ramp shape, a flip-flop system based on two TVC ramps is used.

In the ideal case, the TVC ramps would start synchronized with the clock cycles. However, there is a small shift between them (Figure 2.15). This effect has to be taken into account when computing the hit time, and the TS value has to be corrected to match the real time value.

The value of the TVC units is translated into time by

$$t(ns) = 50 \times \frac{TVC - TVC_{min}}{TVC_{max} - TVC_{min}}, \qquad (2.11)$$

where the TVC_{min} and TVC_{max} are the limits of the real dynamic range of the TVC. Ideally, the TVC range has 256 channels, but in the real case, only around 200 channels are available. The values of the TVC_{min} and TVC_{max} are obtained filling the TVS with a random flat distribution. Then, the TVC_{min} is defined as the first channel exceeding the 10% of the average occupancy, and the TVC_{max} is the last one exceeding this 10% average occupancy.

In Equation 2.11 it is assumed that all the TVC channels are identically wide. However, it is well known that they are different in size. This unequal binning is called Differential Non Linearity (DNL) and has a non-negligible influence on the time measurements [77]. The results show a small effect in such a way that, without correcting by the DNL effect, the error on the TVC measurements is around 0.3 ns (depending on the ARS chip) and once DNLs are corrected, the error is around 0.09 ns. This second order correction is not, at the moment, taken into account in the ANTARES time measurement.

2.5. The Data Acquisition System and readout electronics
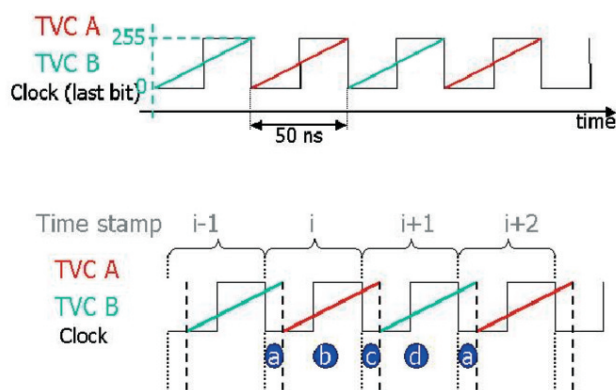
Figure 2.15: *The ideal case (top) and the real case (bottom) of the TVC with respect to clock cycles (TS).*

However, studies to understand and correct the effect are ongoing.

Charge measurement

The PMTs have a nominal gain of 5×10^7 which gives, for a single photo-electron collected in the PMT anode, a signal of about 45 mV (50 Ω load). The charge integration is carried out in three steps in order not to lose any charge. This is done by means of three capacitors (Figure 2.16) working in three different phases: the integration phase (I), where the signal from the anode is integrated, the memorization phase (M), where the integrated charge is recorded in memory, and the charge erasing phase (R), where a reset is done. These phases have an adjustable time cycle duration between 8 and 30 ns, which is on purpose slightly longer than the PMT rise time[7] ($\sim$ 5 ns). When a hit crosses the L0 threshold, the time integration is increased in order to cover all the signal pulse shape. This phase's duration is set between 17 to 50 ns. The charge integrated value is obtained as the sum of the two capacitors in the integration and memorization phase.

After this process, the integrated charge is digitized by an 8-bit ADC called analog to voltage converter (AVC) which provides values from 0 to 255. The conversion from AVC units to charge units (in photo-electrons) has been computed in the laboratory for each specific ARS. The results show that the AVC-charge relation can be considered linear:

---

[7]The rise time is defined has the elapsed time between the 10% and the 90% of the amplitude signal.

Chapter 2. The ANTARES neutrino telescope
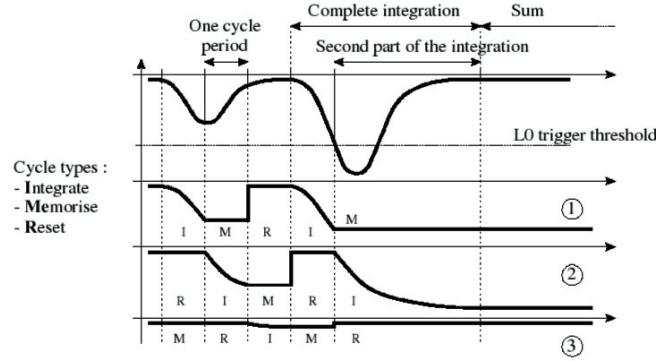
Figure 2.16: *Charge signal integration with 3 capacitors working in different phases. When the L0 is crossed, the ramp voltage is frozen and memorised.*

$$Q_{pe} = \frac{AVC - AVC\_0}{AVC\_1 - AVC\_0} \qquad (2.12)$$

where AVC_0 is the position of the pedestal [78] and AVC_1 is the position of the one photo-electron peak. The AVC_1 and AVC_0 values are calculated for each ARS, and stored in the ANTARES database. The values obtained show important differences among ARSs.

A second order correction known as "cross-talk" effect was found due to the influence of the TVC ramp values in the analog memory of the AVC during the ARS signal digitization (the reciprocal effect, i.e., TVC affected by the AVC, has not been observed). Different AVC values are found for the same charge input depending on the TVC value. This effect increases linearly with the TVC values.

The correction is typically of 4 channels for the complete TVC range. The linear correction to that effect can be written as:

$$AVC_{\mathrm{corr}} = AVC - XT\_\mathrm{slope}(TVC - TVC\_\mathrm{mean}) \qquad (2.13)$$

where $XT\_$slope is the slope (avc bit/tvc bit) of the linear cross-talk effect, and $TVC\_$mean is the centre of the TVC ramp ((TVC_{max} - TVC_{min})/2), where no cross-talk correction is needed, by definition.

In order to obtain the correct value of the charge, the AVC_{corr} value obtained in Equation 2.13 should be used as input (AVC parameter) in Equation 2.12. The expected relative error in the hit charge measurement is smaller than 10%.

The DNL effect also appears in the AVC as a second order correction. According to [77], the error on AVC measurements are around 0.08 p.e. and after the DNL correction are around 0.07 p.e. As in the TVC case, the corrections are difficult to apply and studies are ongoing (e.g. [79]).

2.5.2   The DAQ software

The `RunControl` is the main program used to operate the detector [80]. Controlling all the system processes considered as clients. On every LCM, the `DaqHarness` process organizes the raw data coming from the ARS chips in packets of 13 ms of duration called frames. All the frames belonging to the same time window are sent to a specific PC on shore, and merged into a so-called `TimeSlice`. The `DataFilter` program, running on each PC, processes the TimeSlices looking for `PhysicsEvents` data corresponding to a group of correlated hits in different parts of the detector. The required calibration parameters are obtained from a dedicated database based on the Oracle$^{\copyright}$ database management system [81]. Finally, data are written on disk by the `Datawriter` process. Subsequently, these files are ready for physics analysis and are copied regularly to the computer centre at Lyon, where can be downloaded by authorized users.

The software filtering system

Because of the high rate of bioluminiscence and ^{40}K decays (60 kHz per PMT[8]), the volume of the data produced in ANTARES is too large to be stored. Therefore, a filtering system based on space-time correlations of hits is needed in order to reject a large fraction of background while saving candidate events of expected physics signals.

Although some trigger requirements can be implemented in the off-shore hardware for an on-line data filtering, currently all raw data are processed on shore by the software algorithm, which is called the `datafilter` program, working as a standard hardware trigger system.

The ANTARES collaboration has developed different trigger algorithms depending on the type of physics signal searched. For neutrino source searches the main triggers used are the 3D, 3N and T3 triggers. Both the 3D and 3N [82] are based on the standard 3-dimensional trigger where hits crossing the mandatory L0 threshold in the ARS are tagged as accepted L1 hits if they satisfy at least one the following requirements: they are hits with high charge, typically, 3 photo-electrons or more. This condition can be tuned by the parameter `highThreshold` which optimizes the hit filtering. The second

---

[8]The noise background rate depends on the L0 trigger threshold, with the same environmental conditions, for instance L0 = 0.3 p.e. gives 60 kHz rate, and L0 = 1 p.e. gives 30 kHz rate.

Chapter 2. The ANTARES neutrino telescope
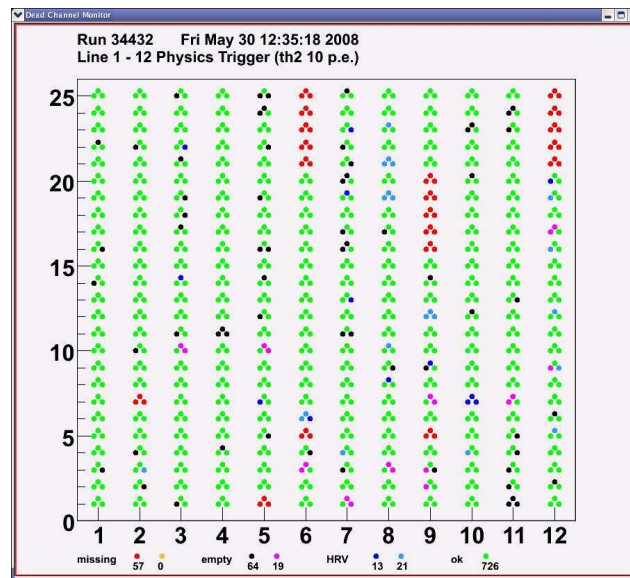
Figure 2.17: *Snapshot of the on-line channel (OM) monitoring. Good channels are marked in green whereas dead channels are marked as red or black (temporaly or permanent dead respectively). In this particular example ~90% of the detector was operational.*

2.5. The Data Acquisition System and readout electronics

requirement implies the hits to be detected in coincidence by more than one PMT in the same storey within a time window of 20 ns (local coincidences). The next trigger level is called L2 and searches for L1 hits on different storeys which are causally connected. The causality requires that two hits recorded with a time difference of $|\Delta t|$ in two different OMs separated a distance $|\Delta x|$ satisfy the relation:

$$\left| \frac{\Delta x}{\Delta t} \right| > \frac{c}{n} \qquad (2.14)$$

where c is the speed of light in the vacuum, and n is the refractive index of the water.

After L2 trigger is performed, a *cluster* with all the causally connected hits is formed from one L1 hit. If this cluster satisfies some requirements as a minimum number of hits (typically five) or a minimum number of storeys involved (typically four), it is considered as an *event*.

The aim of the following trigger level (L3) is to find more hits produced by physics signals that were not included previously in the cluster. To this end, a wider time window called *snapshot* is considered. This snapshot takes the time limits from the actual cluster, and expands the time window to a value about 2.2 μs, since this is the maximum casual time of an event inside the detector diameter (~ 500 m).

This procedure is applied to all the events. The L3 trigger also takes care of merging overlapping events. Two events overlap if the cluster of one event falls in time with the snapshot of another event. The result of two or more merged events is a single cluster with a redefined snapshot. Finally, in the L4 trigger level, all the hits within the snapshot of every event, are saved forming a PhysicsEvent following the ANTARES data format [83].

The difference between the 3D and the 3N triggers is that 3D looks for time correlated hits from a muon coming from any direction, while, the 3N makes a scan of directions and applies the standard one dimensional trigger for each direction. In this case the background is reduced dramatically.

The T3 trigger [84] is based on a "T3 cluster" of hits. A T3 is defined when two L1 hits among three adjacent storeys are in coincidence. The coincidence time window is set to 100 ns when two storeys are adjacent, and to 200 ns in the case of next to adjacent storeys. The trigger logic in this case is to require a minimum number of T3 clusters, typically one or two, within a time window of 2.2 μs, which corresponds to the muon transit time across the detector.

It is important to mention that additional triggers have been developed for specific searches. For instance, there is a directional trigger pointing to Galactic Center. There is also a specially created trigger for search of magnetic monopoles with low velocities, based on 3N trigger but asking for more L1 hit coincidences in the same time window.

Chapter 2. The ANTARES neutrino telescope

2.6 Detector calibration

In order to ensure the best angular resolution attainable, it is important to know precisely the position of each photomultiplier of the detector (positioning), and the arrival times of the Cherenkov photons to the OMs (time calibration) [85]. A good pointing accuracy is needed to discriminate cosmic neutrino events over the isotropic atmospheric neutrino background.

A good estimation of the neutrino energy is also useful (charge calibration) since the energy information is used to get a better rejection of atmospheric neutrinos which are known to have a softer spectrum (rapid decrease of the flux at high-energies) than cosmic neutrinos.

2.6.1 Charge calibration

As it has been seen in section 2.5.1, the charge information is given by the AVC value measured by the ARS chip. The parameters needed for a proper charge calibration are the discriminator threshold used to start the charge integration (*TRIG0_TH* parameter), the pedestal and the photo-electron peak (*AVC_0PE* and *AVC_1PE* parameters), and the cross-talk information (*XT_SLOPE* and *TVC_MEAN* parameters).

The way to measure the discriminator threshold before deployment is to compute the efficiency curve for different input voltage test signals (equivalent to 0, 1, 1.5 photo-electrons). This allows us to know the response function of the dedicated AVC in order to choose the appropriate threshold in mV or p.e. units. Once the lines are installed, the thresholds are recomputed using the signals coming from the background light of ^{40}K, which are basically photo-electron pulses.

The values of pedestal and the one photo-electron peak of the PMT charge spectrum, as well as the parameters for the cross-talk calibration, were measured in the same setup as the threshold tests by means of an external signal. In this case, the pedestal and the photo-electron peak can be inferred from the AVC distribution. As in the previous case, the background light is used as input signal once the lines are deployed

2.6.2 Time calibration

The time calibration of the detector is based on several methods and calibration systems, namely: 1) the echo-based clock system, which enables the measurement of the time delay of the signal from the clock board located on each storey to the shore station, 2) the on-shore dark room calibration system, which allows the measurement of the relative time offsets among PMTs of the same line, 3) the Optical Beacon (OB) system, which sends short light pulses that enable the *in situ* relative time calibration of PMTs, 4) the ^{40}K

calibration method which, as in the case of the OBs, allows a determination of the time differences among PMTs of the same storey, and 5) the internal LED system, which monitors the PMT transit time. We will review extensively the ANTARES time calibration in the next chapter.

2.6.3   Positioning

The relative positioning in ANTARES [86] is done by using two independent systems: an acoustic system which exchanges signals in the 40-60 kHz range, and a set of tiltmeter-compass sensors. The acoustic system is composed by an array of transponders (RxTx) placed at known positions on the seabed, and receiver hydrophones (Rx) distributed uniformly along the lines. The transponders are placed on the anchor of every line and in several autonomous pyramids deployed to this end. The measurement of the travel time of the acoustic signals exchanged between the receiving hydrophones and the emitters fixed at the bottom is measured, allowing a real time localization in space of the Optical Modules by triangulation. In Figure 2.18, the movement of several hydrophones of an ANTARES line for a 20-days period in the XY plane is shown. Hydrophone displacements are followed with an accuracy of a few centimetres. The upper storeys have larger displacements, and a privileged east-west heading of the lines is observed, which can be explained by the Ligurian current.

A good knowledge of the sound velocity is crucial in order to achieve accurate position calculations. In the sea water, the sound velocity depends on the temperature, the salinity and the pressure. All these parameters are measured by the IL.

The second and independent positioning system is composed by a series of tiltmeter-compass sensors located inside all the LCMs. The tiltmeters provide information about the pitch and the roll angles of the storeys with a precision of $\sim$0.2°. The compasses give the heading of each storey defined as the angle between the magnetic north and one OM used as reference. This heading angle is known with a precision better than 1°.

With all this information, i.e., acustics, tiltmeters and compasses, a fit of the line shape is performed which yields a precision of $\sim$10 cm in the OM position.

2.7   Detector performance

2.7.1   Effective area

The effective area is defined as the equivalent surface, perpendicular to the incident particle beam, which is 100 % efficient and detects the same number

Chapter 2. The ANTARES neutrino telescope
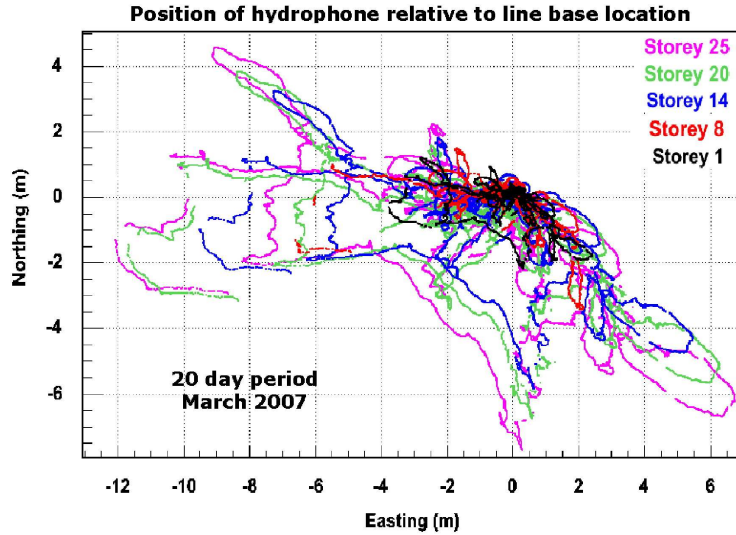
Figure 2.18: *Horizontal tracking of the hydrophones of one particular line in a 20-day period. The hydrophones are located at 100, 202, 289, 376 and 448 m from the sea floor. The measurement precision is ∼10 cm.*

of particles (muons or neutrinos) than the detector. The effective area depends on the energy and the direction of the incident neutrino.

The effective area for neutrinos is much smaller than the muon effective area due to the much smaller neutrino cross-section. Since the cross-section increases with the neutrino energy, so the neutrino effective area does, and becomes greater than 1 m^2 for energies above 100 TeV. Above this energy, neutrinos crossing the Earth at a nadir angle of 0° will probably interact during its travel, because of the long path through the Earth. Therefore, an opacity effect appears depending on the angle. Neutrino events with very high energy are thus expected only for angles close to the horizon.

The formula giving the effective area of a neutrino telescope depends on the energy of the incoming neutrino (E_ν) and its direction (θ_ν, ϕ_ν), i.e. the altitude and azimuth in horizontal coordinates. It can be written as:

$$A_\nu^{eff}(E_\nu, \theta_\nu, \phi_\nu) = \frac{N_{sel}(E_\nu, \theta_\nu, \phi_\nu)}{N_{gen}(E_\nu, \theta_\nu, \phi_\nu)} \times V_{gen} \times (\rho N_A) \times \sigma(E_\nu) \times P_{Earth}(E_\nu, \theta_\nu) \quad (2.15)$$

where N_{gen} and N_{sel} are respectively the number of events generated and reconstructed (after the corresponding quality cuts), V_{gen} is the generation

volume, ρN_A takes into account the nucleon density being N_A the Avogadro's number and ρ the matter density, σ accounts for the cross-section of the neutrino which depends on the energy and finally, P_{Earth} is the probability for a neutrino of energy E_ν and zenith angle θ_ν to cross the Earth up to the interaction point. In Figure 2.19, the neutrino effective area is shown. A distinction based on the neutrino nadir angle direction is made.
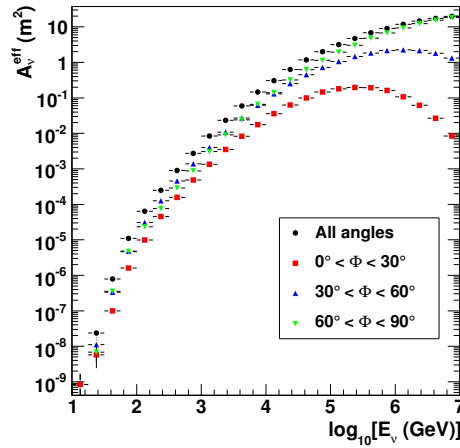
Figure 2.19: *Neutrino effective area averaged over several neutrino angle directions as a function of the neutrino energy. Effective areas for different nadir angles (Φ) are shown. The Earth opacity at high energies can be noticed.*

2.7.2   Angular resolution

One of the most important features of a neutrino telescope is its angular resolution. In ANTARES, the muon (neutrino) angular resolution is defined as the median of the distribution of the angle between the actual muon (neutrino) track and the reconstructed muon track. For the neutrino angular resolution we have to take into account the kinematic angle between the neutrino and the induced muon, as well as the deviation of the muon direction due to multiple scattering. At high energies, the neutrino and the induced muon are essentially aligned. In this case, the pointing accuracy is dominated by errors in the reconstruction of the muon trajectory. The good water properties of the ANTARES site, together with the expected detector resolution (timing calibration, positioning, electronics, etc.), provide an angular resolution better than 0.3° for neutrino events with $E_\nu > 10$ TeV, as can be seen in the Fig-

Chapter 2. The ANTARES neutrino telescope

ure 2.20. A good angular resolution is very important in order to point-back to the cosmic neutrino sources.
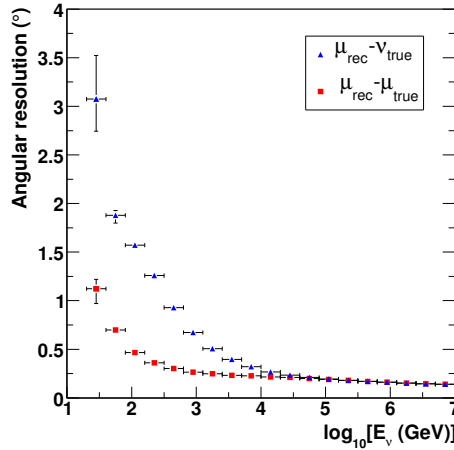
Figure 2.20: *Angular resolution of ANTARES according to a detailed simulation of the detector. The points represent the medians of the angular error distribution for muons and neutrinos. Below 10 TeV the angular resolution is dominated by the kinematic angle between the neutrino trajectory and the muon track. Above 10 TeV, it depends on the quality of the reconstruction (calibration, electronics, etc.)*

2.8   Status of ANTARES detector

The ANTARES detector is working steadily with its final 12-lines configuration since the connection of the last line in May 2008, proving the feasibility of an underwater neutrino telescope. With the detector completed, the most exciting period has started. Several up-going neutrinos are detected every day (e.g. Fig 2.21) and different physics studies and analysis are ongoing.

On March 1st 2009, after almost 1 year of full operation with the full detector, 755 out of 884 channels were operating, which represents the 85 % of the detector. It is important to mention that some problems arose during the detector operation, as it was expected from a experiment deployed in such a hostile environment. In the summer of 2008 a problem in the MEOC prevented the data acquisition for two months, after that period the cable was repaired and the data acquisition was resumed smoothly. During 2009, the line 12 was

redeployed after the on-shore reparation of part of the line. Moreover, the line 10 was reconnected due to a interlink connection problem. Nowadays both are working properly. For 2010 two additional reparations are scheduled. Line 6 and 9 have a large number of dead channels and they are being repaired on-shore. They will be redeployed by November 2010. These facts, even being expected, prove the ability of the collaboration to react quickly to unexpected problems.
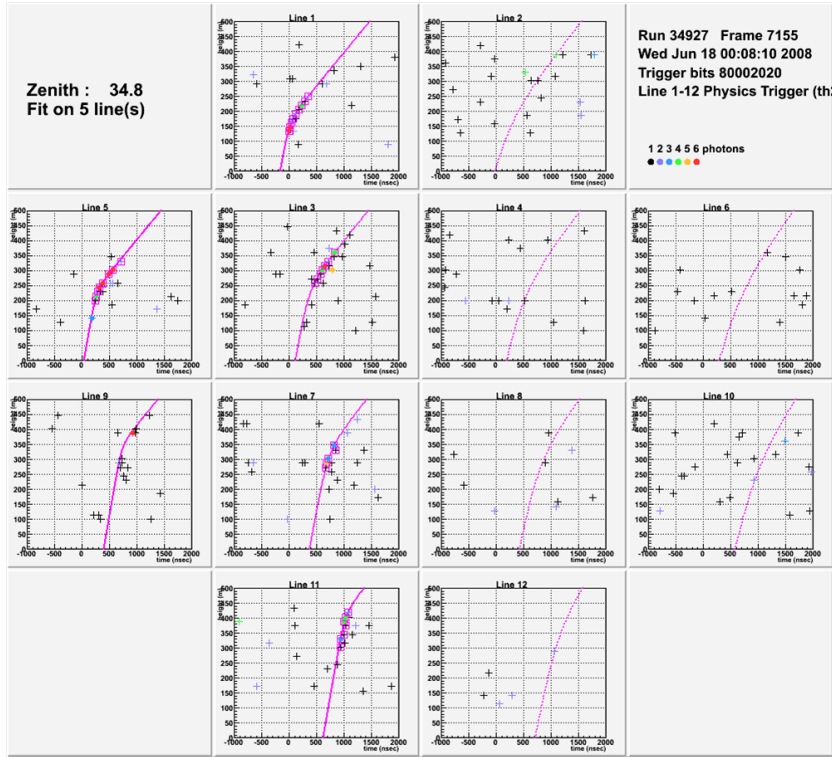
Figure 2.21: *A snapshot of ANTARES event display showing an up-going neutrino recorded in 5 out of the 12 detector lines operating. The event display is composed by a series of 2D plots, one for each detector line. The y-axis is the vertical position of the hit with respect to the seabed and the x-axis shows the arrival time of the hit. The lines represents the fit used to obtain the muon track.*

The elevation[9] distribution of the events collected by the detector up to

---

[9]Elevation is defined as zenith - 90°.

Chapter 2. The ANTARES neutrino telescope

mid-2009 is shown in Fig 2.22 together with the Monte Carlo prediction. This period comprises all the different stages of the detector configuration, i.e. from 5 lines to 12 lines. The number of up-going collected events is 1062 for 341 days of detector lifetime. The population of events with values of elevation (θ) lower than zero comes mainly from atmospheric neutrinos. Above the horizon, atmospheric muon flux dominates. For atmospheric neutrinos, a combined theoretical and systematic error of 30% is assumed, for atmospheric muons the error band is 50%.
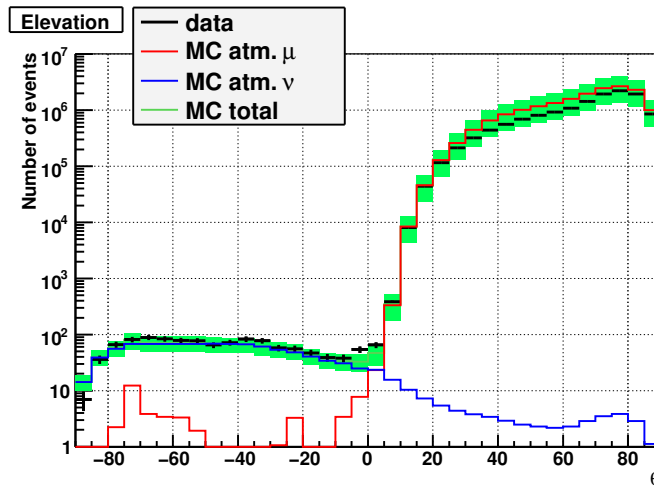
Figure 2.22: *Distribution of the elevation angle for the first 1000 up-going events. The black line represents the data. The other lines represent the Monte Carlo predictions for atmospheric muons and neutrinos.*

Analysis of point-like sources, diffuse flux, Dark Matter searches, atmospheric muons, etc. are being carried out by different groups of the collaboration. The results for 5 Lines of point-like search will be discuss in Chapter 6. The most recent ANTARES neutrino sky map obtained with the data taken from 2007 and 2008 are shown in Figure 2.23. The right ascension of the events has been randomized in order to preserve the blindness of the data.
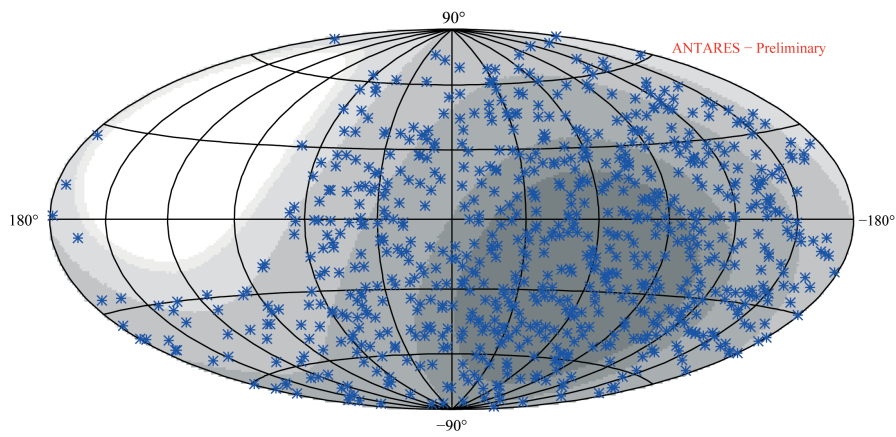
Figure 2.23: *Sky neutrino map in, galactic coordinates, with a pure sample of neutrinos containing 750 multilines candidate events from 2007 and 2008 for a 341 days of detector lifetime.*
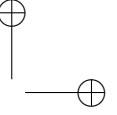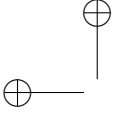
Chapter 2. The ANTARES neutrino telescope
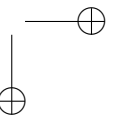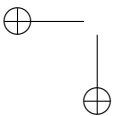
Chapter 3

Time calibration in ANTARES

Angular resolution is crucial for any telescope. For neutrino telescopes is even more important since a low number of events is expected. As a means to achieve the best angular resolution attainable, it is important to know precisely the position of each photomultiplier of the detector (positioning), and to have all the PMTs providing an accurate timing (time calibration). In order to perform the ANTARES time calibration [87], several methods and calibration systems have been conceived. The aim of this chapter is to review all the time calibration systems and methods of ANTARES.

3.1   Introduction

In ANTARES, the expected attainable angular resolution is better than 0.3° for a $E_\nu > 10$ TeV, as long as the positioning and the time calibration precision requirements ($\sim$0.5 ns in relative time resolution and $\sim$10 cm in positioning) are fulfilled.

Concerning the time calibration, we can distinguish between the absolute and the relative time resolution. The absolute time resolution corresponds to the ability of the detector to measure the time of each event with respect to the universal time (UT). This is necessary to obtain correlations with the physics phenomena (e.g. GRB, SN flares, etc.) The required accuracy is of the order of ~ 1 ms. The main uncertainty for the absolute timing in ANTARES comes from the electronic path common to all the OMs. The MEOC, which links the junction box with the shore station, is the principal error source due to its length.

The relative time calibration is the ability of measuring the same time for an identical hit, not depending on which OM hit is recorded. In other words,

2010/11/18 — 18:02 — page 74 — #88

"red.tesis" — 2010/11/18 — 18:02 — page 74 — #88

Chapter 3. Time calibration in ANTARES

to set a common reference for the whole detector. This is essential to achieve the best angular accuracy which is limited by the muon track reconstruction. In order to calibrate the detector, the time offsets of each OM due to its specific PMT transit time and the front-end electronics are measured. The main uncertainties contributing to the relative time resolution come from the transit time spread (TTS) of the signal in the PMTs which gives ~ 1.3 ns of uncertainty, the optical properties of the sea water (light scattering and chromatic dispersion) which gives ~ 1.5 ns of uncertainty for a distance of 40 meters, and the electronics of the system. The later contribution is the only one which can be controlled, and in ANTARES it is required to contribute less than 0.5 ns to the overall relative time resolution, to reach the optimum angular resolution.

3.2   On-shore dark room calibration system

In order to estimate the OM time offsets before the deployment of the lines, the integration sites of ANTARES (CPPM at Marseilles and CEA at Saclay) have assembled a calibration setup consisting in a laser (λ=532 nm) able to send very short (FWHM ~ 0.8 ns) and intense (E $\sim 1\mu$J) pulses of light to the PMTs through a system of optical fibres [88]. The main purpose of this system is to compute the relative time offsets between the OM responses and a synchronous laser signal whose emission time is measured by an internal photodiode. The time of the laser signal arriving at the OM is recorded by the ARS cards. Therefore, the individual PMT offset can be worked out after the correction of the time spent in the optical fibre path and the clock phase[1]. The calibration is performed by sectors of five storeys. The light of the laser pass through an 1-to-16 splitter which provides a synchronous signal to the 15 OMs involved. Taking a particular ARS of a specific OM as a reference, the relative offsets can be inferred for the whole detector. In fact, for each line the ARS0 on OM0 is taken as the reference for the whole line. That gives a small inter-line time incertitude of the order of a single OM time offset. This small offset is corrected *in situ* by the Laser Optical Beacon.

The parameter needed for the physics analysis is the `ARS_T0`[2]. This parameter is defined as the sum of each individual ARS offset and the clock phase of its corresponding storey. The hit time recorded in an OM needs the addition of the T0 in order to know the time spent since the last Reset Time Stamp (RTS) (section 3.3), which will be finally converted to universal time (UT). The expression giving the T0 value using the laser setup can be written down as follows:

---

[1] The clock phase takes into account the different delays in the acquisition starting time depending on the storey and the line.

[2] Hereafter we will refer to it as T0.

3.2. On-shore dark room calibration system

$$T0_{ij} = \langle T_i - T_{PHDj} - \mathrm{Delay_{ij}} \rangle - \mathrm{T_{ref}}, \qquad (3.1)$$

with

$$T_{ref} = \langle T_0 - T_{PHD1} - \mathrm{Delay_{00}} \rangle.$$

The $T0_{ij}$ represents the T0 corresponding to the ARS i in the sector j, T_i is the time read by the i-ARS card, T_{PHD} is the time given by the internal photodiode reading the laser emission time. The $Delay_{ij}$ takes into account the clock phase and the optical fibre length. Finally, a common reference is set by means of the T_{ref} term. The reference used is the ARS0 on the OM0 of the line. The process is repeated in each integration site and the results saved in the ANTARES database. As it will be shown in Chapter 4, once the lines are deployed this calibration is cross-checked and corrected by the LED Optical Beacons in case of drifts.
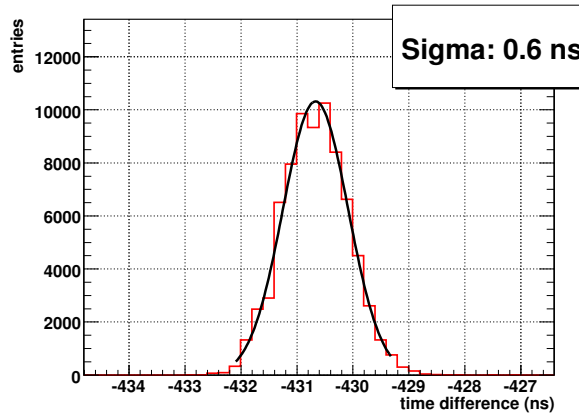
Figure 3.1: *Example of time difference distribution between one of the ARSs of the OM0 on Line 3 (T_i) and the laser photodiode read by the LCM_{ref} (T_{PHD}) before the fibre path and the clock phase correction (*Delay$_{ij}$*).*

The LED Beacons also need to have its internal PMTs calibrated (T0 value) in order to provide an accurate timing. This calibration is also carried out with the same setup, however, due to the lower gain of the small PMT inside the beacon, the laser light arrives to it directly by means of a dedicated fibre to avoid the signal attenuation. The T0 value is obtained in the same way as explained in Eq. 3.1 and the reference used is again the OM0 of the first storey of the line.

Chapter 3. Time calibration in ANTARES

The T0 computation of the internal photo-diode which provides the Laser Beacon emission time is made introducing some changes in the setup. In this case, one LED OB is used as reference since its T0 is already known. Both, the Laser Beacon and the LED Beacon, are located inside the same black box to avoid the background light, and the laser is flashed to illuminate the small internal photomultiplier of the LED Beacon. The T0 of the Laser Beacon is computed from the time difference distribution between the Laser and the LED OB used as reference. More details can be found in [89].

Besides T0 calibration, the laser setup is also used to do the TVC calibration. This calibration takes advantage of the 1 μs uncertainty (jitter) between the arriving clock trigger signal and the laser time emission. Therefore, hits are produced randomly at any of the 255 ADC channels of the 50 ns TVC range. This random distribution equally populates the TVC channels giving a flat distribution (Fig. 3.2). The real dynamic range of the TVC (TVC$_{min}$, TVC$_{max}$), necessary for the conversion from TVC units to time (see Eq. 2.11), can be determined. The gaps and spikes in this distribution are a consequence of the DNL effect (see section 3.8.2). Since this distribution is supposed to be flat it can be used to compute the DNL corrections.
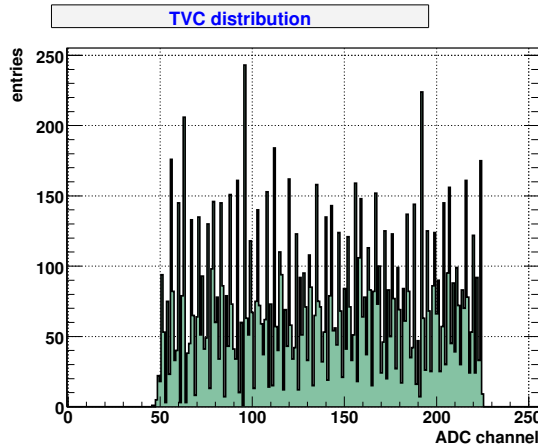
Figure 3.2: *Example of a flat TVC distribution of the ramp B from ARS3, OM2, LCM 1050. The discontinuities in the distribution are due to the DNL effects.*

3.3 Echo-based clock system

The clock system [90] is needed to provide a common signal reference to every ARS of the detector. It consists of a 20 MHz clock generator on shore synchronized with the GPS, a clock distribution system and a clock signal transceiver board placed in each LCM. At regular time intervals[3], the internal clock ARS registers are reset using a common reset time stamp (RTS) signal. The number of RTSs are counted by each LCM and added to the data. The hit time since the beginning of the run is obtained from the number of RTSs. Thanks to this information, the Universal Time (UT) of each hit can be determined afterwards.

A precise knowledge of the relative clock phase offsets of every LCM is necessary to obtain a correct time-stamping of the physics events. In order to calibrate the system, an optical signal is produced on shore by the Master Clock, distributed throughout the detector and sent back by each LCM transceiver as soon as arrives at each LCM. The generated start and stop signals are sent to a time to digital converter (TDC) which measures the round trip delay (Fig. 3.3). This delay is twice the clock phase offset, due to the cables for each individual LCM. All the LCMs are referred to the time of the SCM. This measurement can be done in parallel with the physics data taking. Moreover, the clock is also used to broadcast other signals to the LCMs as for instance, the trigger signal to flash the LED Optical Beacons.

An accurate clock timing is crucial both for absolute and relative time calibration. Considering the time difference between the shore station and the SCM of a line located at the seabed, the whole trip delay takes around 223 μs (Fig. 3.4). The average fluctuation of this value during one year is around 200 ps, which fulfils perfectly well the absolute time calibration requirements ($<$1 ms). Concerning the relative time resolution, the important quantity is the precision in the measurement of the time difference between the anchor (SCM) of a line and each of their storeys (LCM). In this case, the uncertainties are of the order of 15 ps (Fig. 3.5), good enough for our purposes in the relative time resolution ($<$0.5 ns).

3.4 Internal LED system

Every OM has an internal blue (472 nm) LED glued to the back of the PMT which can illuminate, pulsed by the clock, the photocatode from inside the OM (see Figure 2.7 left) at a rate of about 100 Hz. The aim of this system is to monitor the transit time (TT) of the PMTs.

Currently, the transit time is monitored using the stability of the flashing time distribution of the internal LED. In this case, the flashing time is

---

[3]Typically 2^{23} clock cycles

Chapter 3. Time calibration in ANTARES
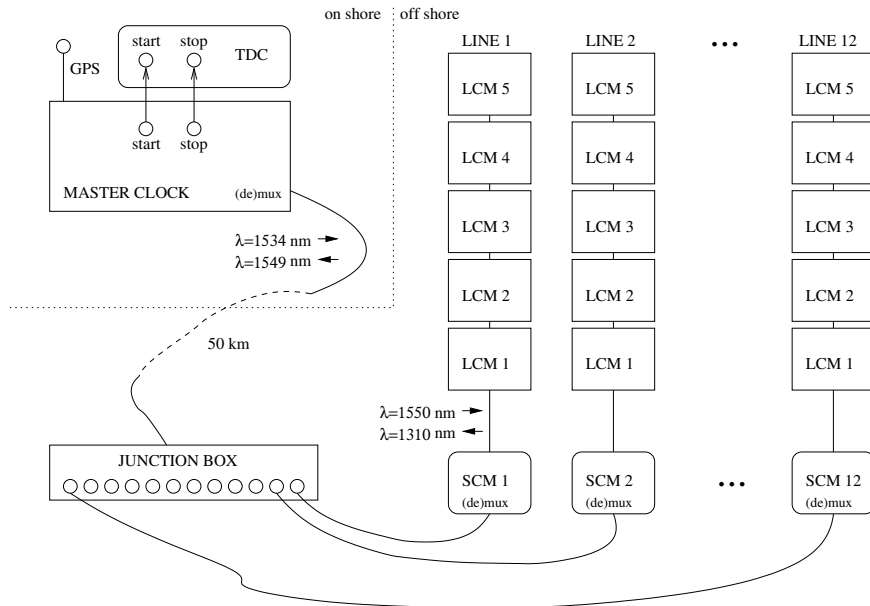
Figure 3.3: *Schematic view of the echo-based clock system with the main elements involved both on shore and off shore.*
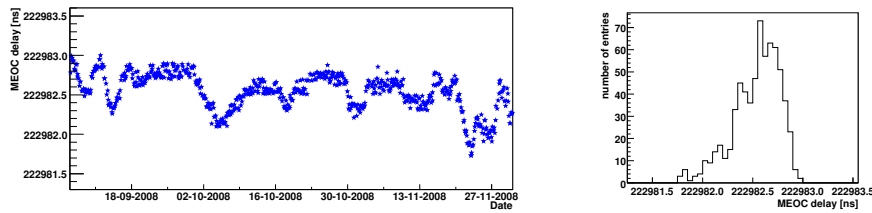
Figure 3.4: *On the left, it is shown the time measurements of the path from shore to a SCM for almost three months. On the right, the projection of the previous plot is shown. Time variations up to 200 ps are observed.*
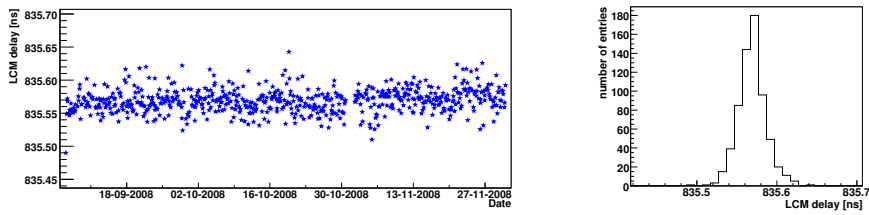
Figure 3.5: *Individual measurements (left) and projection (right) of the time spent by the clock signal along the path from the BSS of Line 11 to a particular storey (10th floor) for a period of almost three months.*
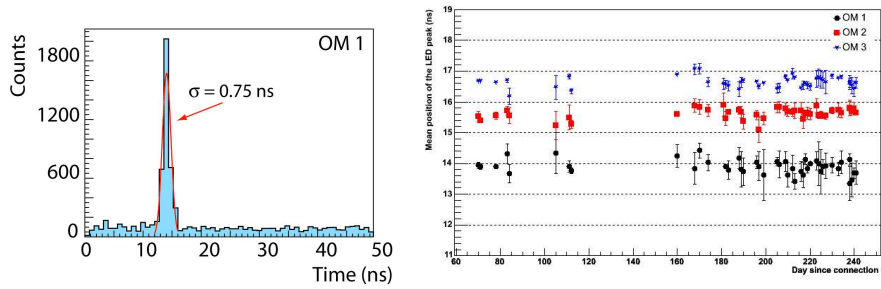
Figure 3.6: *Time stability of the TT of the MILOM OMs for a period of 250 days.*

Chapter 3. Time calibration in ANTARES

taken from the TVC distribution seen by the OM where the internal LED is located (Figure 3.6 left). This distribution shows a clear peak because of the synchronous emission of the internal LED with the clock. This time difference shows that the sigma of the distribution is around 0.8 ns which indicates that the LED intensity is well above the single photo-electron peak.

The results obtained with this system in the MILOM have shown that the transit time of the PMTs is stable within 0.5 ns (Figure 3.6 right). The same result has been reproduced with data from different configurations until the detector completion. Figure 3.7 shows an example for a particular OM.
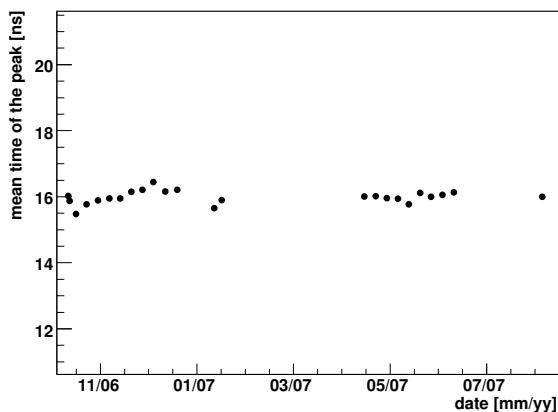
Figure 3.7: *Stability of the transit time of the PMT on the storey 12 of the Line 1 measured with the internal LED for almost one year of detector operation. In the first part of the graph the detector was taking data with one and two lines, and the second part five lines were operating.*

3.5   Optical Beacons system

The Optical Beacons (OBs) [91] are well-controlled sources of pulsed light with a well-known time emission. There are two kinds of Optical Beacons: The LED Optical Beacon and the Laser Optical Beacon. The aim of the OBs is to measure the time resolution and to provide an *in situ* time calibration of the detector by computing the time offsets of all the PMTs. Although the OBs were conceived mainly to perform the detector time calibration, they are also used for different purposes, such as measuring and monitoring the optical water properties of the sea water (absorption and attenuation length), monitoring of

the OM efficiency and cross-checking the positioning system. In this section we give a detailed description of the Optical Beacons features. The performance and results obtained will be explained in detail in Chapter 4.

3.5.1 The LED Optical Beacon

A LED Beacon is an hexagonal prism divided in faces containing 6 blue LEDs (472 nm, spectral FWHM of 35 nm) each one (see Figure 3.8 left), i.e. 36 LEDs in total. Within a face, the top, central and the remaining group-of-four LEDs, can be triggered independently or in combination with the others (see Figure 3.8 right). Each LED is flashed by means of a pulsing circuit based on the Kasputinsky design [92], which was modified for the ANTARES collaboration by the Sheffield group. The circuit is fed with +48V providing a variable DC power supply between 0 and +24 V in order to adjust the light intensity. The LEDs flash in response to the positive-going edge of the trigger pulse provided by the internal ARS clock at a typical frequency of 30 Hz. The clock is able to multiply this flashing rate a factor ten by enabling the "overdrive" option.

Each pulse produces ~ 160 pJ ($\sim 4 \times 10^8$ photons) at maximum intensity. All the components of the beacon are housed in a cylindrical borosilicate glass container which protects them from the deep sea high pressures. The dimensions of the cylinder device are 210 mm for the diameter and 443 mm in length. A standard line of ANTARES contains 4 LED Beacons located at

Figure 3.8: *Left: one of the LED Beacons used for the ANTARES time calibration. The picture shows the hexagonal frame with the 36 LEDs, and the glass container designed to protect the device once has been deployed. Right: a face of the LED Beacon.*

Chapter 3. Time calibration in ANTARES
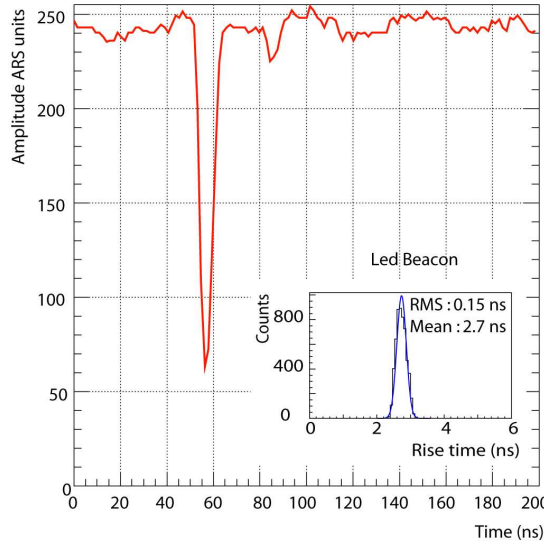
Figure 3.9: *Example of the electronic signal produced by a LED Beacon flash in the ARS of the small LED Beacon PMT readout. Overprinted, the distribution of the rising edges measured during a LED Beacon run is shown.*

the storeys 2, 9, 15, and 21. The main goal of the LED Beacon is to perform the time calibration of the ANTARES OMs. The emission time of the light is known by means of a small photocatode PMT placed inside the frame of the LED Beacon. The readout of the small PMT is done by means of an ARS electronic card specifically devoted to this purpose (see Fig. 3.9).

The voltage of the internal PMT, as well as the intensity of the LEDs, can be varied. A proper choice of these values in combination with the signal threshold is important in order to avoid the noise generated by the associated electronics. The chosen values will depend on the sort of studies to perform. Typically, high intensity runs (the so-called "standard" calibration runs) are used for time calibration (T0 computation), and low intensity runs for optical water parameters studies.

At high intensity, a single LED Beacon can illuminate all the OMs, up to the next LED Beacon in the line with enough light to perform the time calibration. At the beginning of the ANTARES operation, the standard LED Beacon calibration runs were performed once a week and the Beacons were flashing one by one. At present, since the calibration parameters are stable, the standard calibration is performed once a month with the LED Beacons of a given line fired by pairs[4] which seems to be the most efficient flashing

---

[4]One pair is Floor 2 and Floor 15 and the other one is Floor 9 and Floor 21 of the same

strategy.

3.5.2 The Laser Optical Beacon

The Laser Optical Beacon [93] main component is a diode-pumped Q-switched Nd-YAG laser which produces short pulses ($<$ 1ns) of green (532 nm) light with an energy of $\sim 1~\mu$J ($\sim 10^{12}$ photons). The Laser Beacon is fed with +48V which provides a fixed DC power of 12 V. It can be operated in a non-triggered mode at a fixed frequency (around 15 kHz) and in a triggered mode with a variable trigger frequency. In the triggered mode, which is the one used in ANTARES, the laser flashes in response to the positive-going edge of the trigger pulse provided by the internal ARS clock. In this case, the Laser Beacon, as well as the LED Beacon, is triggered by the clock with a maximum flashing rate of ~ 300 Hz in overdrive mode. Since the laser is passively Q-switched, the time delay between the start signal and the light pulse emission is of the order of microseconds and the pulse to pulse fluctuation (jitter) is of the order of a few hundreds of nanoseconds. The time emission of the light pulse is given by a very precise internal photodiode which is read by an ARS card (see Fig. 3.11). The amount of light emitted by the Laser Beacon can be tuned by means of a voltage-controlled optical attenuator resulting from the assembly of a linear polarizer and a liquid-crystal variable retarder [89] (see Fig. 3.10).

All the Laser Beacon components are located inside a cylindrical titanium container whose dimensions are 170 mm in diameter and 705 mm in length. The laser beam is directed towards a lambertian diffuser located in a hole at the centre of the titanium cover. The light is then spread out and leaves the diffuser with an angular distribution proportional to the polar angle as $\cos \theta$. Finally, as the laser points upwards, a quartz rod attached to the titanium frame has being designed to allow the lateral emission of the light in order to minimize the transmission loses due to the sedimentation and biofouling at the seabed (see Fig. 3.12).

As the LED Beacon, the main goal of the Laser Beacon is the to perform the time calibration of the detector. In ANTARES there are 2 Laser OBs attached vertically at the bottom (BSS) of two central lines (Line 7 and 8).

In the standard Laser Beacon calibration run, the beacon illuminates at maximum intensity. This intensity is enough to illuminate up to the tenth floor of all the lines.

---

line. This is repeated for all the detector lines.

Chapter 3. Time calibration in ANTARES
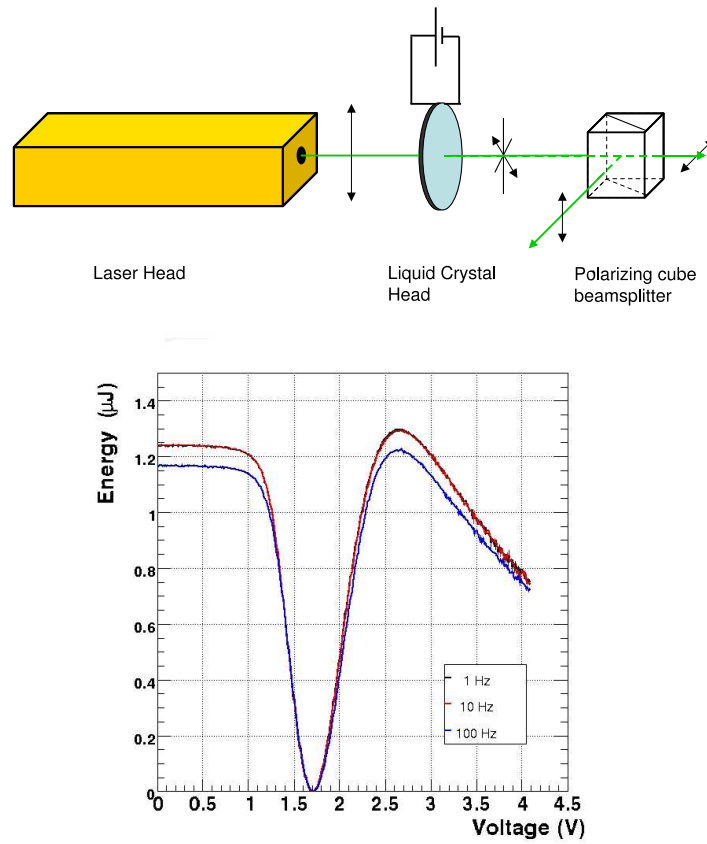
Figure 3.10: *Top: sketch of the laser with the attenuation system for the light emission adjustment. Bottom: energy released by the Laser Beacon as a function of the applied voltage to the crystal-liquid retarder.*
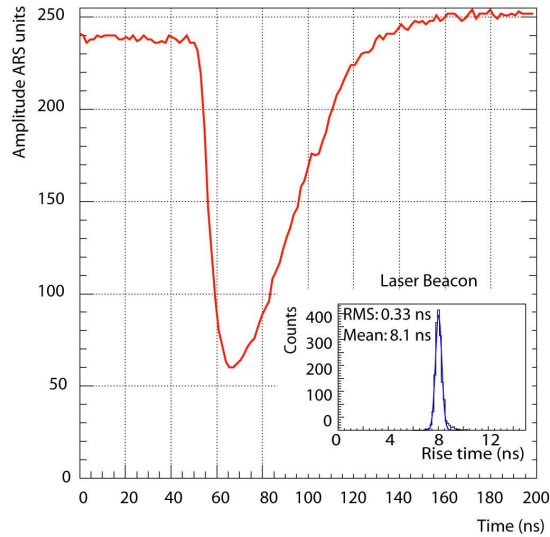
Figure 3.11: *Example of the electronic signal produced by the MILOM Laser OB flash in the ARS of the internal photodiode readout. Overprinted, the distribution of the rising edges measured during a Laser Beacon run is shown.*

Figure 3.12: *Left: one of the Laser OBs used for the ANTARES time calibration, showing the titanium frame, the laser and its electronics. Right: the quartz rod through whose vertical walls spread the laser light to all the detector.*

Chapter 3. Time calibration in ANTARES
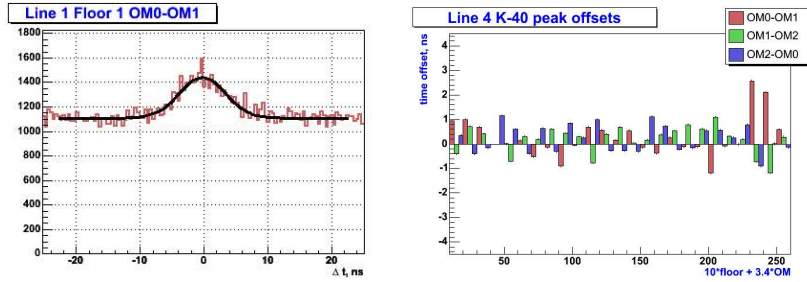
Figure 3.13: *On the left, example of relative time offset difference between two OMs on the same storey computed with the ^{40}K method. This is used to cross-check the ANTARES time offset calibration. On the right, bar histogram of all the intra-storey time differences for a given line. If the calibration were perfect these bars should be essentially 0.*

3.6 Calibration with Potassium 40

The ^{40}K present in the salt water can be used for charge and time calibration taking advantage of the Cherenkov light induced by the relativistic electron generated in the ^{40}K decay. The generated light can illuminate two adjacent OMs at once producing coincidences. The time difference between adjacent OMs in the same storey is known as "intra-storey" time difference. The corresponding distribution should present a bump due to the correlated hits which are detected by two OMs simultaneously (see Figure 3.13 left).

The intra-storey time differences are important for time calibration purposes. They are used as an indirect way to check the T0s of each OM computed previously in the integration sites or *in situ* by the OB system. If the time calibration (T0 values) were perfect, the intra-storey time differences should be 0. Figure 3.14 shows the histogram with all the intra-storey time differences computed for all the OMs of the detector. In this case, the calibration constants (T0) used for the timing computation are the ones obtained in situ by the OB system. The RMS of the distribution is 0.55 ns which value means an improvement with respect to the results obtained with the T0s computed in the laboratory, as we will see in the next chapter. Therefore, the ^{40}K provides an alternative and independent method to cross-checks the LED Beacon results.

Figure 3.14: *Distribution of the intra-storey time differences, for all the OMs of the ANTARES detector, computed at the end of 2008 with the ^{40}K method. The calibration constants (T0 values) used for the timing computation are the ones obtained in situ by the OB system.*

3.7   Atmospheric muons method

The relative time offsets can also be monitored using the thousands of downward atmospheric muons recorded per day in the ANTARES detector. The distribution of the time residuals of the hits[5] are used as a monitoring system which can reveal miscalibrated channels and show whether the offsets used in the reconstruction are accurate enough. However, the ANTARES OMs are downward oriented to enhance the detection of up-going muons, and therefore, the incertitudes in the hit time are large because the induced Cherenkov light does not arrive directly at the OM but after some scattering. Alternatively, up-going muons can be used providing more accurate measurements, however more time is needed since the up-going muon flux is six orders of magnitude lower than the down-going muon flux (see Section 2.1.4). A correct computation of the T0 values will improve the time residuals of the reconstructed tracks as it will be shown in the following chapter.

3.8   Electronic effects in time calibration

The limitations of the analog signal recording in the ARS can distort the hit time information. Two main effects have been considered, the walk effect and the DNL correction.

---

[5]difference between the measured time and the time provided by the track fit.

Chapter 3. Time calibration in ANTARES

3.8.1 Walk effect

Two events which are supposed to arrive to the OMs simultaneously may not produce the same time-stamp because of their analog signals are different in amplitude. Being the discriminator threshold fixed (L0 threshold), the largest signal will cross the threshold before the smallest one. This effect is known as *walk effect*. A schematic picture of the walk effect is shown in the left side of Fig. 3.15.
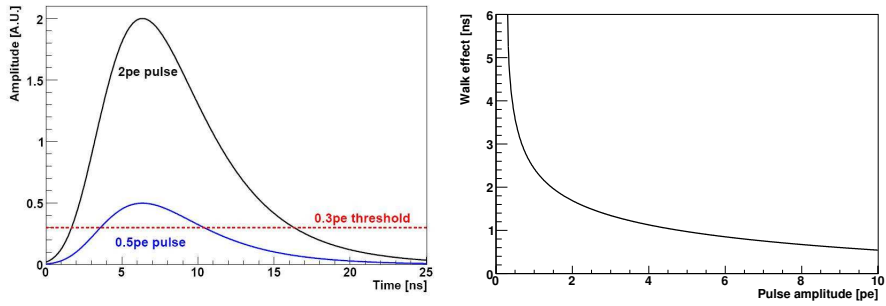
Figure 3.15: *Left: a schematic picture of the walk effect. The biggest the signal the sooner it crosses the discriminator threshold. Right: a graph showing the recorded ARS time as a function of the hit signal amplitude recorded by the PMT.*

In ANTARES, the OM signal hits are produced with different charges. Therefore, a walk effect correction is needed to obtain the most accurate value of the hit time. Some efforts have been done to quantify the walk effect [94]. According to the studies performed in [95], the PMT signal shape does not change event by event except, obviously, by the amplitude. The best walk effect parametrisation is given by:

$$A(t) = a_0 \cdot e^{-\frac{t-a_1}{a_2}} \cdot e^{-e^{-\frac{t-a_1}{a_2}}} \cdot e^{\alpha t 2 - a_3} \cdot Q \qquad (3.2)$$

with $\alpha = 1.31.10^{-2} - 5.1.10^{-3} \cdot a_2$) where A is the pulse amplitude as a function of time t, the a_i are free parameters and Q is the total hit charge.

This parametrisation has been obtained taking data in the WF mode where the pulse signal hits contain 128 samples of 1.5 ns steps. This is the only way to obtain the shape of the signal, since in the SPE mode, only the total charge and the value of the hit time are recorded. The walk effect can be greater than 1 ns when comparing 1 p.e. hits with 10 p.e. hits as it is shown in Fig. 3.15

(right). Therefore, the correction is not negligible and should be applied in the track reconstruction process.

The main source of error in the walk effect correction comes from the charge calibration, that is to say, the use of different sets of charge calibration parameters. However, other effects as multi-pulses (two or more pulses within the ARS integration gate) and the parametrisation of the pulse shape, could also lead to a wrong estimation of the walk effect.

3.8.2   DNL correction

The analysis of the data collected in the ADCs of the ARS chips (TVC and AVC distributions), have shown that the channels are not equal in size. This effect is called Differential Non Linearity (DNL) effect, and is due to an ARS comparator imperfection, when the input analog signal value is converted into an output binary signal [96].

The way to convert the analog signal is by comparison, bit by bit, of the input signal voltage with a reference voltage (V_0). If the signal is higher than the first reference voltage the first bin is set to 1 and the reference voltage is multiplied by a factor $3/2$ for the next comparison. On the contrary, if the signal is lower than the reference, the first bin is set to 0 and the reference voltage is multiplied by a factor $1/2$ for the next comparison. The process is repeated, in a sort of discrimination by bisection, until all the bits are fixed. The DNL effect appears when the reference voltage, growing too slow, sometimes does not reach the final expected value and, therefore, the comparison is not properly done. In this case, if the value is wrongly set to 1 (0), then the remaining bits are set to 0 (1). That gives the overpopulation of some specific channels with respect to the others. The overpopulation effect due to the DNL is clearly visible in Fig. 3.2 where a flat TVC distribution is shown.

As it has been said in Section 2.5.1, the effect in time calibration is assumed to be small (0.3 ns), and although it is not corrected at the moment, studies to take it into account are ongoing.

3.9   Summary

The methods and systems used to perform the time calibration of the ANTARES neutrino telescope have been reviewed in this chapter. They have been successfully tested in the laboratory and once deployed in the sea.

Results confirm that the absolute time resolution required of ~ 1 ms is ensured by the high precision of the clock system. Regarding the relative time resolution (~ 0.5 ns required), there is on the one hand, the unavoidable uncertainty of the transit time of the OMs which can be accurately monitored by the internal LED, and on the other hand, the contributions coming from

Chapter 3. Time calibration in ANTARES

the electronics and the OM time offsets. These later contributions are measured in the integration laboratory before the deployment and once *in situ* by the Optical Beacon system. The results of the Optical Beacon system are presented in the next Chapter. In addition, different calibration methods and systems can be used for cross-checking these results. For instance, ^{40}K measurements complements the LED Beacon results for the OM time offsets. With the ANTARES time calibration working within the specifications, the expected angular resolution, better than 0.3° for high energy neutrinos, can be reached.

Chapter 4

Calibration with the Optical Beacon system

The Optical Beacon (OB) system, composed by LED and Laser Beacons [91], is a system conceived to calibrate the detector by means of a set of pulsed light sources with extremely short width and a very precise emission time. The main goal of the OB system is to perform the relative time calibration of the detector. Moreover, it can be used for other purposes such as the measurement of the intrinsic electronic resolution, the study of the water optical properties [97], the cross-check of the positioning system and the study of the OM efficiencies. All these subjects have been studied carefully from the analysis of the calibration run data. The obtained results are presented and discussed in this chapter.

4.1   Introduction

The relative time calibration implies a precise determination of the time of every hit with respect to a global reference which usually is provided by one specific OM of the detector[1]. In this sense, three main steps can be distinguished in the calibration process. The first one consists in having the three OMs of the same storey properly calibrated, being one OM the reference to the others (*intra-storey* calibration). The second level aims to calibrate all the storeys of the same line with respect to a particular OM used as reference for all the OMs in the line, usually one OM in the first floor of the line (*intra-line* calibration). Finally, the third step refers to the complete calibration of all the lines, choosing one OM as reference to the whole detector (*inter-line*

---

[1] Actually, it is one of the two ARS cards in the OM which is used as reference.

Chapter 4. Calibration with the Optical Beacon system

calibration).

The Optical Beacon calibration system allows us to perform the three afore-mentioned steps. The *intra-storey* calibration is performed by the LED Beacons and validated by the ^{40}K method. The *intra-line* calibration is also performed by the LED Beacons, and the Laser Beacon is used to cross-check the results in the overlapping region of storeys seen both, by the Laser and the LED Beacons. And finally, the *inter-line* calibration is performed by the Laser Beacon. In all these calibration processes, the results from the integration in the laboratory are used as a first estimation of the calibration parameters. In fact, since they are expected not to vary very much, they are used as the input parameters.

After the OB calibration process, all the time calibration constants (T0s) are computed with a precision below the nanosecond. As it has been explained in the previous chapter, the T0 values take into account the information of all the time offsets involved in the signal transmission (individual OM offsets plus clock phase), in such a way that, adding the T0 value to the recorded hit time, we obtain the actual time of the hit.

4.2 Optical Beacon tests at the laboratory

The ANTARES devices are tested first in the laboratory where they are produced and afterwards, in the integration sites before being deployed. In the case of the Optical Beacons, they have been produced and tested at the IFIC laboratory in Valencia. The main tests performed include the verification of the signal stability both in time (jitter between the trigger signal and the light flash) and in charge (amount of emitted light), the synchronization of the light emission, the electronic noise level, and the thermal test. In the integration site laboratory, once the beacons are integrated with their corresponding LCMs, the Optical Beacon signals are re-checked. The calibration constants are computed and the software used for the flashing tested. The detailed results of the integration studies can be found in [98]. Figures 3.9 and 3.11 are examples of the Optical Beacon signals recorded with the beacons already integrated with the detector electronics.

4.3 MILOM Optical Beacon results

The first results of the Optical Beacon system came with the MILOM (Mini Instrumentation Line with Optical Modules) line. The MILOM, composed by only four storeys, had two LED Beacons in two different storeys, and one Laser Beacon attached to the BSS. The Optical Beacons worked well and the first signals from the light flashes were recorded in the OMs confirming the

feasibility of such a calibration system. One of the storeys of the MILOM was a complete ANTARES storey with three OMs. This allowed the *intra-storey* time calibration validating the calibration parameters obtained previously in the laboratory. One of the most important OB results obtained with the MILOM was the first *in situ* measurement of the ANTARES time resolution [68]. This result was obtained by flashing the OMs in the MILOM with a nearby (~ 14.5 m) LED Beacon. Due to the large amount of light received by the OMs, the distribution of the time differences between the LED OB and the OMs distribution (Figure 4.1) depends mainly on the readout electronics. The time resolution can be expressed as:

$$\sigma_{OM}^2 = \frac{\sigma_{TTS}^2}{N_{pe}} + \frac{\sigma_{water}^2}{N_\gamma} + \sigma_{LOB}^2 + \sigma_{elec}^2 \tag{4.1}$$
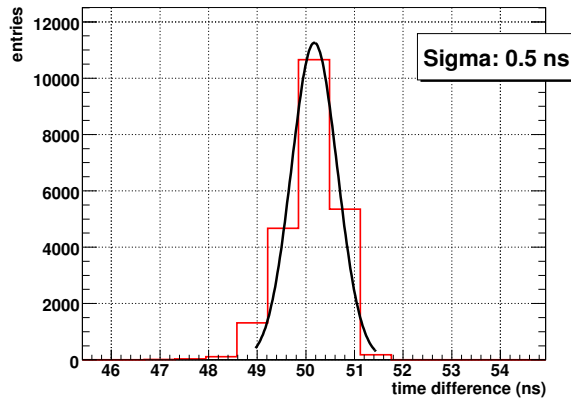
Figure 4.1: *Time difference distribution between an OM on the MILOM and an LED OB placed 14.5 m below. The standard deviation of 0.5 ns can be understood as an estimation of the contribution from the electronics to the ANTARES time resolution. The distribution is not centred at zero because the ARS6 T0 was not computed in the laboratory for the MILOM beacons.*

As a high intensity flash is emitted, the contribution of the PMT TTS (σ_{TTS}), which scales down with the square root of the number of photo-electrons, is negligible. The contribution of the photon dispersion of the light (σ_{water}) is also small since the arrival times will be dominated by the non-scattered photons. Finally, the contribution of the small OB PMT reading the emission time of the signal (σ_{LOB}) is also negligible due to its fast rise time (~ 0.8 ns). Therefore, one can safely assume that the only important con-

Chapter 4. Calibration with the Optical Beacon system

tribution in the Eq. 4.1 comes from the electronics (σ_{elec}). This contribution is ~ 0.5 ns which is compatible with the 0.5 ns required for the relative time calibration.
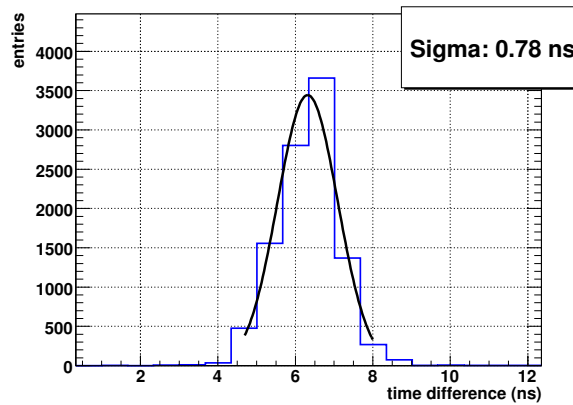
Figure 4.2: *Time difference distribution between two OMs on the MILOM when an LED OB placed 14.5 m below is flashing. The standard deviation of 0.78 ns gives an estimation of the contribution from the electronics to the OM time resolution once it is divided by $\sqrt{2}$. The distribution is not centred at zero because the T0s were not considered for the MILOM OMs.*

Another way to measure the OM time resolution is computing the time difference between two OMs of the same storey with the same configuration (Figure 4.2). Again, the LED OB is flashing at high intensity, and the obtained distribution is the convolution of the time resolutions of the two OMs $\sigma_{OM-OM} = \sqrt{2}\sigma_{OM} \approx \sqrt{2}\sigma_{elec}$, being $\sigma_{elec} \sim 0.5$ ns in agreement with the previous result.

4.4 LED Optical Beacon calibration

The LED Beacons are used in the *intra-storey* and *intra-line* calibration, providing the corrections to be applied to the laboratory T0 values. In this section, the method used to compute the T0 values with the LED Optical Beacon is explained. The results obtained can be compared with the ones computed on-shore in the integration sites thanks to the *intra-storey* time differences. Moreover, the independent calibration method based on the ^{40}K background is used to validate the results. The time evolution of the T0 values is also studied. Finally, other measurements as the optical water properties and charge calibration are explained.

4.4.1   *In situ* ARS_T0 computation

Each ARS card in ANTARES has its specific T0 value. In this section, we present the *in situ* method, as well as the results, for the T0 computation. For the analysis of these runs, we consider only the OMs placed in the same line where the beacons are flashing. *Inter-line* calibration with LED Optical Beacons requires a more detailed study where too many effects (OM orientations, light scattering in water, correction by positioning, etc.) should be taken into account. These effects can be seen in Figures 4.3 and 4.4. In the first case, the OMs are illuminated by an LED beacon placed in the same line considering a very simplified version of the storey where the 3 OMs are considered as single point. As it is seen, the time differences are within 0.6 ns as expected. However, when the calibration is done by an LED beacon located in a different line, the time differences between OMs can differ by several nanoseconds, due manly to position effects. In addition an increase of the sigma of the distribution due to the scattering appears for the cases where the OMs are not directly pointing to the beacon.

The computation of the T0 values is based on the time residuals defined as the difference between the emission time of the LED OB light and the time recorded by the OM when the flash arrives. This quantity is corrected by the time spent by the light to reach the OMs:

$$T^{100} = t_{OM} - t_{LOB} - \frac{d(LOB,OM)}{c_{water}} \qquad (4.2)$$

where t_{OM} and t_{LOB} are the time stamps provided by the ARS reading the OM and the LED OB respectively, d(LOB,OM) is the distance between the LED OB and the OM, and c_{water} is the speed of light in water. Once corrected, the T^{100} should be equal to zero, any difference from zero should be understand as a time offset not considered.

As soon as a calibration run is performed we can obtain the time residual distribution for each LED OB-OM pair. The mean value is obtained after a special fit procedure which is done in two steps. The first step consists of a Gaussian fit from the bin with 20% of the maximum occupancy to the bin with 100%. Then, a second fit is performed taking as reference the mean value of the previous fit. This second fit goes from the bin with 10% of the mean value bin occupancy to the one having a 85% occupancy after the mean. Two examples of how the final fit (after the two steps) looks like can be seen in Figure 4.5 for two different OMs.

In Figure 4.5 left, the time difference (residual) distribution between one LED OB and one particular ARS in an OM two storeys above from the LED OB ($\sim$ 30 m of separation) is shown. In the same figure, the time difference distribution on the right corresponds to one of the ARSs of an OM seven storeys above from the same LED OB ($\sim$ 100 m of separation). Before the

Chapter 4. Calibration with the Optical Beacon system
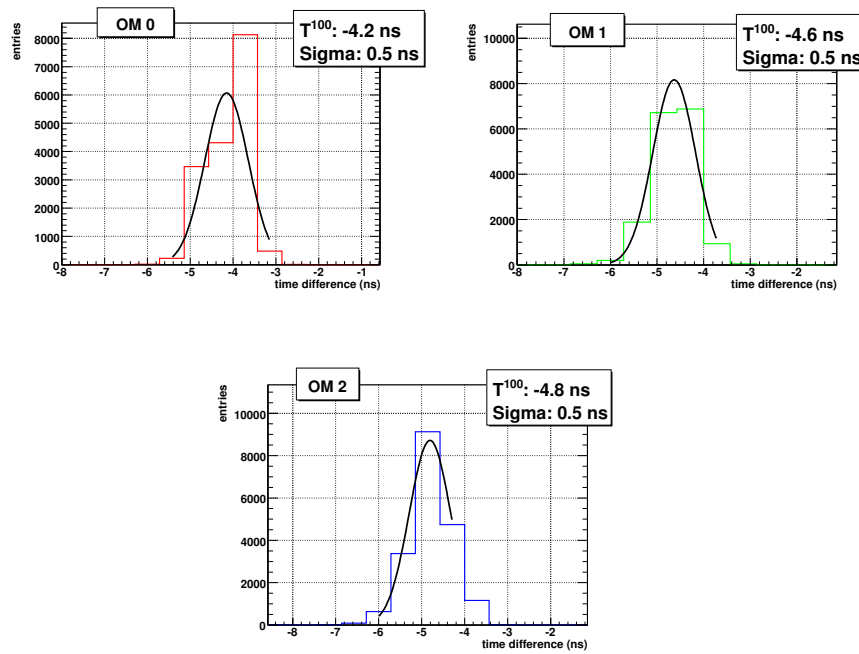
Figure 4.3: *Time residual distributions of the three OMs on the 3rd floor of Line 2 when the LED OB on the 2nd floor of the same line is flashing. The three values are within 0.6 ns.*

4.4. LED Optical Beacon calibration
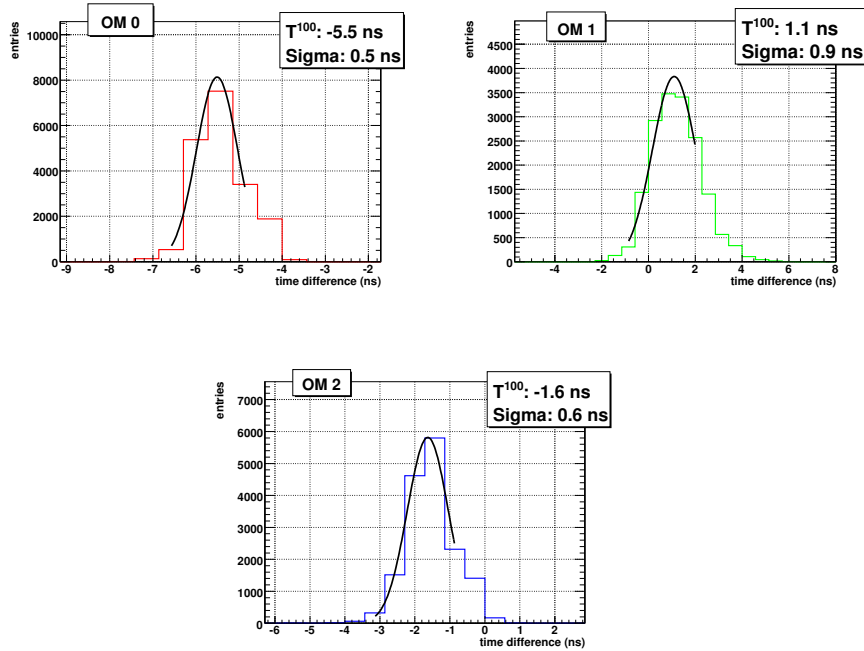
Figure 4.4: *Time residual distributions of the three OMs on the 3rd floor of Line 2 when the LED OB on the 2nd floor of the Line 6 is flashing. Unlike the previous example, there are discrepancies among the T0 values up to 6 ns due to the different orientation of the OMs. For the OM1, which is not pointing in the beacon direction, the sigma of the distribution is larger due to the contribution of the scattered photons.*

Chapter 4. Calibration with the Optical Beacon system
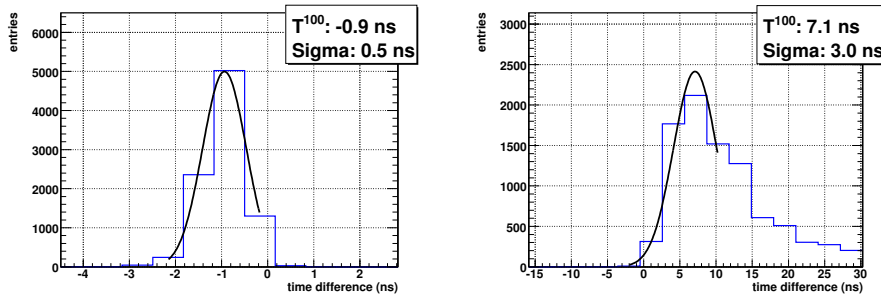
Figure 4.5: *Two examples of the fits over the time residuals. On the left, final fit for a single ARS in a OM placed two storeys above the flashing beacon. On the right, final fit for a single ARS in a OM placed seven storeys above the same flashing beacon. The more distant the OMs, the wider the distribution due to the late-arrival scattered photons.*

two-step fit, the binning is properly chosen with regard to the statistics of the distribution. As expected, the distribution for the closest ARS (OM) is very narrow and has a width close to the expected relative time resolution coming from the electronics which is < 0.5 ns. The distribution for the farthest ARS (OM) is wider ($\sigma \sim 3$ ns). In this case, the amount of late-arriving photons due to scattering is not negligible and has an important contribution to the tail of the distribution. The reason to perform the residual fits only up to 85% after the mean value of the distribution is to avoid this tail which does not follow a Gaussian distribution.

The T0 values used in the residual computation, for each OM and LED OB PMT, are the ones computed at the integration sites before the deployment of the line. Therefore, we expect the mean values from the residual distribution fits to be centred at zero. Any shift of the residuals from zero, should come from variations in the sea (temperature effects, etc.) or from miscalibration in the laboratory.

Representing these time residuals of the storeys in the same line, we realize that the mean values are not well centred at zero. In fact, an additional delay appears in each storey as we go farther away from the flashing LED OB (see Figure 4.6 left). This additional delay follows quite well a straight line as a function of the LED OB-OM distance. The walk effect is unable to explain by itself the total delay and, even after the walk correction, there is a linear trend for the T^{100} values (see Figure 4.6 right).

This behaviour can be understood as originated by the "early-photon" ef-
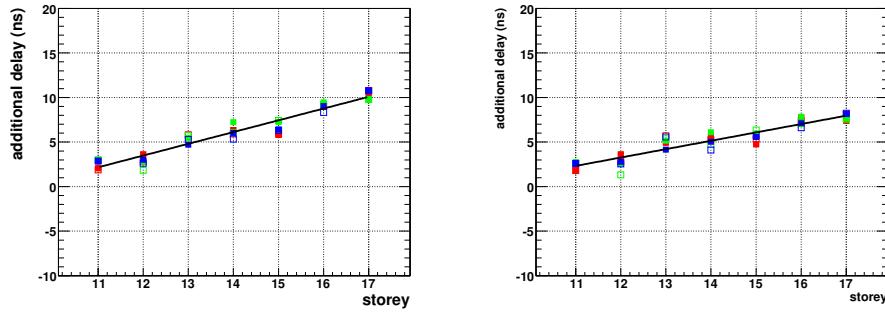
Figure 4.6: *On the left, fit over the time residuals (each point) for all the ARS along 7 storeys. On the right, the same fit with the residuals but after applying the walk effect correction.*

fect. The "early-photon" effect is a consequence of the inability of the PMTs to resolve multiple photons arriving from the same LED OB flash very close in time. Due to the big amount of light emitted by the LED OB, the PMTs next to the beacon record the time of the first arriving photons of the LED OB pulse. For the most distant PMTs, this effect is reduced and therefore, the residuals are shifted to delayed values[2].
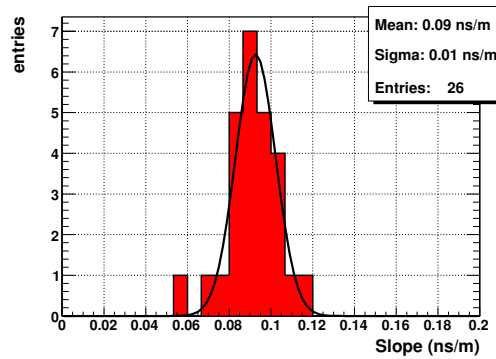
Figure 4.7: *Distribution of the slope values obtained from the fits of the 10 lines.*

The effect shown in the previous example on Figure 4.6 is reproduced all

---

[2]for an statistical description of the effect see [99].

Chapter 4. Calibration with the Optical Beacon system

over the detector. The distribution of the slope values obtained after the linear fits performed with the LED Beacon runs is shown in Figure 4.7. The mean value is 0.09 ns/m and the width of the distribution is 0.01 ns/m. Indicating that the "early-photon" law neither depends on the LED OB nor on the line.

Since this behaviour is reproduced in a stable way through all the detector, the deviations of each ARS from the fitted straight line can be used to obtain the correction to be applied to the calibration used in the time residual computation.

Considering that there are series of LED OB time calibration runs performed once a month, we can compute a new full set of calibration constants monthly. As the T0s are supposed to be stable in time, a new set is only re-computed when the detector goes through major changes in its configuration. In this work, we present the detailed procedure applied to the runs performed on 18th February 2008 (the complete list of runs can be found in the Appendix A). At that moment the detector configuration was of 10 lines. The T0 computation procedure for the whole 12-line detector is the same.

For every LED OB calibration run, the time differences of all the ARSs of the OMs placed above the LED OB on the same line are computed with respect to the LED OB. The first floor used for the linear fit is the second closest to the beacon. Too much light arrives to the OMs of the first storey just above the LED OB, this point deviates from the linear trend. The last storey used in the fit is chosen to be the eighth starting from the LED OB location (e.g. OMs on the 10th floor being flashed by the LED OB on the 2nd floor). For longer distances, the error in the fit used in the time residual distributions is too large, due to a substantial increase of scattered photons and to the lack of statistics[3]. In addition, the light intensity arriving at these distant OMs reaches the photo-electron level, where the "early-photon" effect vanishes. In these cases, as there are 4 LED OB per line, a closest beacon to these OMs can be used for the time calibration. The same procedure is followed for all the OMs on the line.

Once the fit is performed, the new T0 values are inferred from the deviations from the straight line fit which is taken as the common reference. The fit is revised to check if there are bad points due to faulty OMs which can spoil the goodness of the fit. In order not to be biased by these points, we proceed in an iterative way. In each step, the points having a deviation from the fit larger than 2 ns are not taken into account and the fit is repeated. Moreover, the fit is performed only if there are at least 4 active storeys. Otherwise, large errors can be introduced in the fit, and hence, in the T0 correction. The removed points are then corrected according to this final fit.

If there are not enough points to perform the fit, other available systems, as the Laser Beacon, are used for this calibration. If there is no way to correct

---

[3]Alternative fits are being studied to extend the linear fit to more storeys.

this part of the detector, then the values from the previous calibration data set, e.g. from laboratory, are kept[4].

Due to the distribution of the beacons along the detector, there are some OMs which are not optimally corrected by the method: storeys 1, 2 and 3, because they are not above the beacon (1st and 2nd) or too close (3rd). In addition, a linear fit of the OMs on floors 24th and 25th is not optimal since there are too few points to perform a fit with the LOB on floor 21 and they are too distant to be included in the fit corresponding to the previous LED OB (15th floor). However, the OMs on floors 2nd, 3rd, 24th and 25th can be indeed calibrated, at least at the *intra-storey* level.

The 1st floor as it will be shown can be calibrated with the Laser Beacon. Therefore, the combination of Laser and LED OBs gives as a result the complete relative time calibration of the whole telescope.

Figure 4.8 shows the correction to be applied to the laboratory T0 values according to the *in situ* measurements using the LED Optical Beacon calibration runs taken on February 2008. The change of these offsets with respect to the measured values in the integration sites were not very large since only the 15% of the PMTs needed a correction greater than 1 ns, as can be seen in Figure 4.8.

These results reflects, on the one hand, the need to measure *in situ* the T0 corrections of the cases where the differences are large and, on the other hand, means a validation of the measurements in the laboratory.

Binning effect and fit errors

The process to perform the T0 computation relies on a correct time residual fit. Due to the DNL effect in the TVC ramps, it is found that some regions of the time residual distributions are not correctly populated and the Gaussian shape is distorted. This can mislead the double Gaussian fit performed giving an incorrect mean value. The easiest way to avoid this effect is making a proper rebinning of the histogram which would produce a smooth distribution. In principle, a specific rebinning should be necessary for every ARS time residual, that means to choose a specific binning for a thousand of histograms. This is a cumbersome task which needs a huge human intervention. An alternative solution consists in choosing a common binning automatically as a function of the distance LOB-OM, i.e., for common floors. This solution works fine for the nearby storeys where a non optimal choice of the bin does not entail big errors, since the time residual distributions are quite narrow ($\sigma \sim 0.5$ ns). However, because of the scattered photons, the more distant the OM is (w.r.t. the LED OB) the wider the distribution becomes (see Fig. 4.5). Therefore, the error in

---

[4]One data set contains all the values which fills one table of the database. A new data set is released when an update of the calibration is done.

Chapter 4. Calibration with the Optical Beacon system
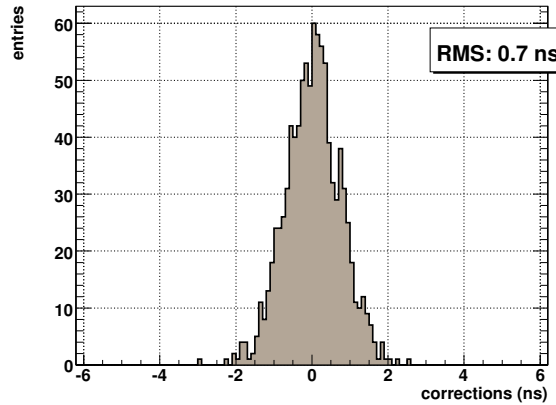
Figure 4.8: *Distribution of the corrections to be applied to the offsets computed in the integration sites. These corrections were obtained in situ by the Optical Beacons for 10 lines*

the mean value estimation is larger in these cases. In the worst scenario, this effect can be around 2 ns for the most distant OMs.

The impact of choosing an appropriate binning for the time residual histograms can be seen in Fig. 4.9. This is a comparison between the different T0 corrections obtained when an automatic binning is performed and when a carefully rebinning is carried out. The changes are typically small with only 4% of the corrections larger than 1 ns (19 % larger than 0.5 ns). The biggest corrections correspond to the most distant OMs which, as we have explained before, are the cases where an unsuitable binning selection have more impact.

The error associated to the residual fit is discussed elsewhere in [99]. The main contribution to the error comes from the bin size in the time residual distribution: $\sigma_{bin} = \Delta_{bin}/\sqrt{12}$. For the most distant case, i.e., LED OB on F2 illuminating OMs on F9, the width bin used is almost 3 ns which means around 0.8 ns error. In this case, this contribution dominates in the T^{100} determination. For the closest OMs (e.g. OM on floor 4) this error is reduced to less than 0.3 ns and, unlike the precedent case, the dominant contribution comes from the electronics (0.5 ns).

4.4.2   *Intra-storey* time differences

One way to check the validity of a set of T0 values is to work out the so-called *intra-storey* time differences, which are evaluated computing the time
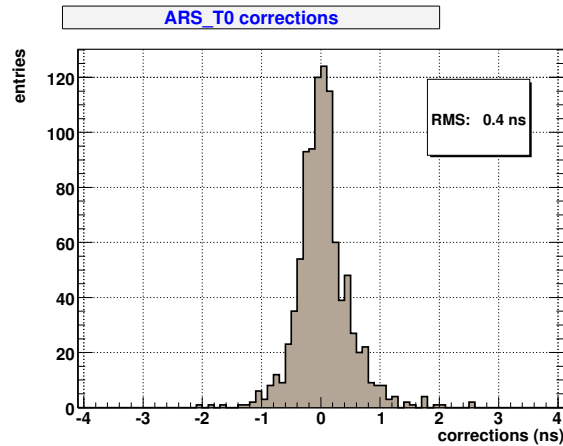
Figure 4.9: *Distribution of the changes in the T^{100} of the time residuals when using the automatic binning fit or an optimal fit after a proper rebinning. The corrections are in general small. Only the more distant OMs to the LED Beacon have, in some cases, corrections larger than 1 ns.*

difference between OMs being on the same storey and placed above the flashing LED OB. There are 3 possible *intra-storey* time differences for the same storey (combination of 3 elements taken by pairs). If the T0 values used for the computation of the *intra-storey* time differences are the correct ones, the distribution must be centred at zero.

We can compute the *intra-storey* time differences of all the OMs placed above each LED beacon and also the OMs located in the same storey of the beacon which, although being below it, they receive enough light. Therefore, we can check the OMs from the 2nd storey to the 25th.

In Figure 4.10 left, we show the *intra-storey* time differences of Line 2 computed using the T0 data set values from the laboratory. In the X-axis the number of the OM-OM time difference is represented starting from the OM0-OM1 time difference of 2nd floor, and going through all the three possible OM-OM time differences of each floor of the whole line up to the OM2-OM0 time difference of the 25th floor. In the Y-axis, the value of the OM-OM time difference is represented. This value is extracted from a Gaussian fit of the OM-OM time difference distribution going from the bin with the maximum occupancy before the mean to the bin with the 20% after.

As can be seen, there are discrepancies up to ~ 1.5 ns. If we project the bar diagram into a histogram, as in Figure 4.10 right, the values are distributed according to a Gaussian shape well centred at zero and with a RMS ~ 0.6 ns.

Chapter 4. Calibration with the Optical Beacon system
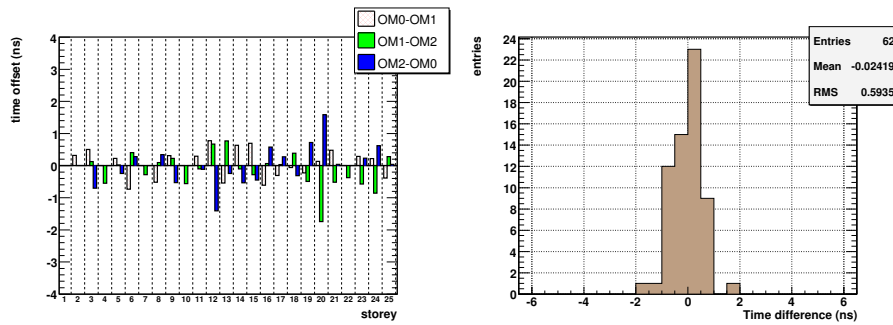
Figure 4.10: *On the left, bar diagram with the the time differences of adjacent OMs on the same storey for a complete line. On the right, the previous values projected into a histogram. The example corresponds to Line 2.*

This cross-check can be done for each calibration day and for all the lines. Considering the 10 lines configuration, we obtain a distribution centred at 0 with RMS $\sim$ 0.72 ns (Fig. 4.11). Therefore, the validity of the laboratory values is confirmed. However, we can improve the offsets with the *in situ* calibration and check the *intra-storey* time differences using the new offsets.

Using the method explained to compute the T0s *in situ*, the results of the *intra-storey* cross-check should improve. When we observe a big *intra-storey* discrepancy it comes from some particular miscalibrated OM. This is also observed as a point which is away from the linear fit of the residuals. One clear example can be seen in Figure 4.12. On the left, the linear fit of the residuals of Line 1 from the 17th to the 23rd floor is shown. As can be seen, storeys 20 and 21 have some points clearly out of the fit. If we observe the same storeys in the *intra-storey* time difference bar diagram (Figure 4.12 right) large discrepancies are also found. In Figure 4.13, an example of *intra-storey* time differences for the Line 3 is shown when we use the laboratory T0s (left) and the values obtained *in situ* (right).

In general, there is a great improvement for most part of the line. As can be seen, the largest bars (discrepancies larger than 2 ns) are corrected. As it was mentioned before, storeys 2 and 3 (*intra-storey* of 1st storey can not be computed with the LED OB) and the storeys 24 and 25 are not corrected by the method, therefore, the values for these storeys do not change. It is also important to notice that sometimes, the more distant storeys from the flashing LED OB, have a less precise correction, as it is reflected in the storeys 15 and 16 of Figure 4.13 right. Doing a systematic study of the first 10 lines deployed, we see that the correction goes in the expected direction. In the Table 4.1 we

4.4. LED Optical Beacon calibration
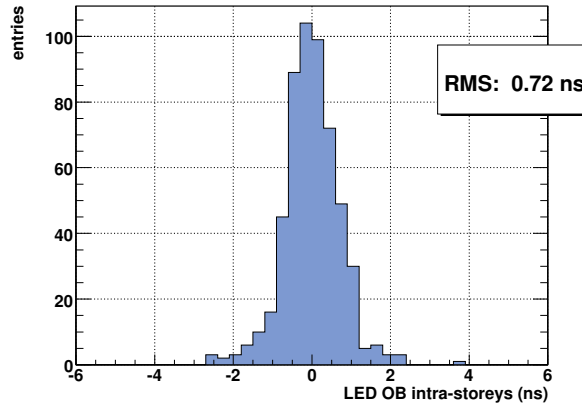
Figure 4.11: *Distribution of the intra-storey time differences of adjacent OMs for 10 lines using the time calibration constants (T0s) obtained in the laboratory.*
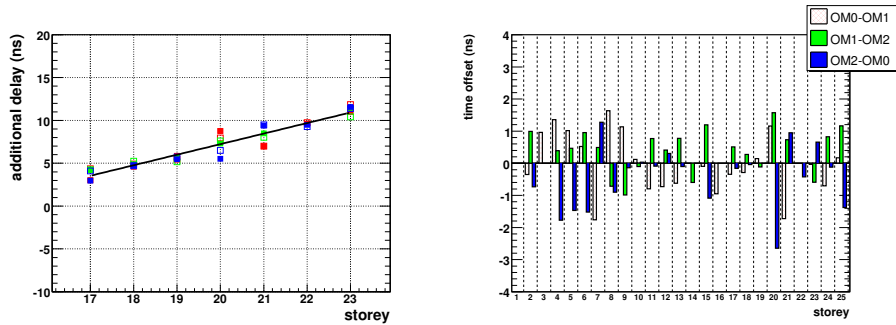
Figure 4.12: *On the left, example of a linear fit over the time residuals for a fraction of the Line 1 (from the 17th to the 23rd floor). On the right, bar histogram for the whole Line 1. As can be seen, large discrepancies in the linear fit (floors 20 and 21) are seen as large discrepancies in the intra-storey values for the same floors.*

Chapter 4. Calibration with the Optical Beacon system
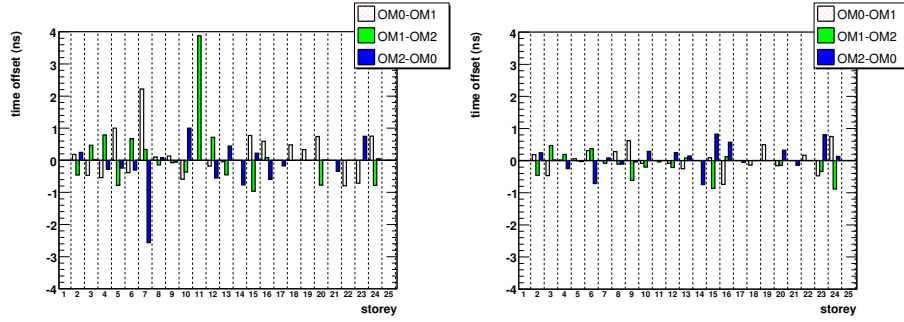
Figure 4.13: *On the left, example of the bar histogram for Line 3 computed using T0s from the laboratory. On the right, the same bar histogram using the new in situ T0 data set. A nice improvement because of the T0 correction is observed.*

present a summary of the results of the *intra-storey* time differences for each individual line taking into account the laboratory and the *in situ* T0 values.

Line	entries	Laboratory T0s		*in situ* T0s	
		μ(ns)	RMS(ns)	μ (ns)	RMS (ns)
1	64	-0.02	0.92	0.00	0.49
2	62	-0.03	0.55	0.00	0.33
3	56	0.05	0.85	-0.03	0.40
4	66	0.01	0.77	-0.01	0.59
5	53	0.02	0.83	0.02	0.51
6	52	0.02	0.63	0.00	0.50
7	51	0.00	0.60	0.00	0.47
8	70	0.00	0.63	0.00	0.54
9	28	-0.02	0.61	0.00	0.51
10	44	-0.03	0.62	0.00	0.35

Table 4.1: *Summary of the intra-storey results using the LED OBs for the 10-lines detector configuration using the offsets computed in the laboratory and in situ. The table contains the mean values and the RMS of the distribution for both cases.*

As can be seen, the distributions become narrower using the new *in situ* values, as expected. When all the modules in the 10-line detector are consid-

ered (546 entries), the RMS goes from ~ 0.72 ns to ~ 0.48 ns. This means a 33% linear improvement or, in other words, we can say we have substracted an error of 0.54 ns added in quadrature. When only the OMs with the T0 offsets corrected by the method (448 entries) are considered, the RMS goes from ~ 0.72 ns to ~ 0.41 ns, that means a 40% of improvement, or the substraction of an error of 0.59 ns added in quadrature. Notice, though, that each miscalibrated OM enters into two OM differences, so there is a sort of double counting.

Time stability of the *intra-storey* time differences

The evolution of the RMS of the relative time offset distribution gives an indirect way to check the stability of the T0 values. The more miscalibrated the detector, the bigger the RMS of the distribution. In Fig. 4.14 left, the RMS as a function of time for the whole 2008 and 2009 period is shown. A slightly increasing of the RMS with some values out of the trend can be noticed. In these cases, the larger RMS increases are not due to a global effect of the whole distribution but due to a few OMs. A detailed analysis has shown that these spoiling OMs needed a retuning of their high voltages (HV). This retuning was performed in August 2009 and, the T0 values were recomputed as it will be explained in Section 4.4.4. Afterwards, the RMS of the *intra-storey* went back to the 0.6 ns accuracy (last point in the Fig. 4.14 left).

Apart from the RMS, the distribution gives also information about the validity of the T0 values. If no systematic errors are present, the mean value of the distribution should be centred at zero. The graphic of the Fig. 4.14 right shows that the mean value is very stable in time and, indeed, centred at zero.

The errors in the RMS plot are computed as follows:

$$\epsilon(RMS) = \frac{1}{2\sqrt{s^2}} \sqrt{V(s^2)} \tag{4.3}$$

where $s^2 = \frac{1}{N-1}\sum(x_i - \bar{x})^2$, and $V(s^2)$ is the variance of the sample variance, which is given by $V(s^2) = \frac{1}{n}(\mu_4 - \frac{n-3}{n-1}\mu_2^2)$ being μ_i the central moment of the order i [16]. The error in the mean value shown on Fig. 4.14 right is the RMS value divided by the root square of the number of entries.

4.4.3 Cross-check with the ^{40}K method

The ^{40}K present in the salt water can be used for charge and time calibration using the Cherenkov light cone induced by the electron coming from the ^{40}K decay. This light cone can illuminate two OMs in coincidence so that the *intra-storey* time difference can also be estimated in a similar way as it is done with the LED OB. Although both sources have different intensities, *intra-storey* time differences should be equal.

Chapter 4. Calibration with the Optical Beacon system
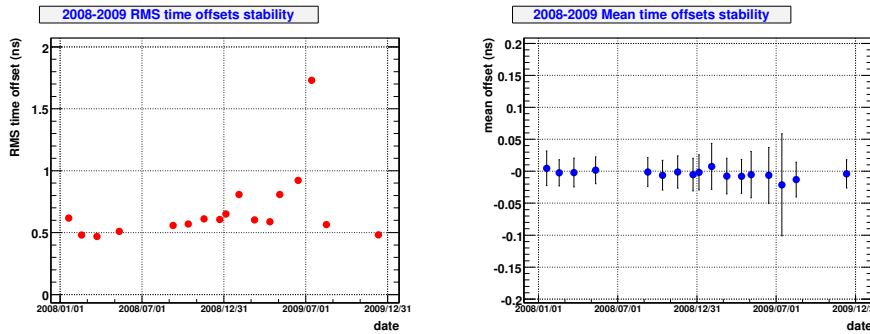
Figure 4.14: *Time evolution of the RMS (left) and the mean value (right) of the intra-storey time difference distribution obtained with the LED Beacon. After the HV tuning of some OMs performed in August 2009 the linear trend is recovered.*

There are several ways to show the correlation between the ^{40}K and LOB *intra-storey* time differences. For instance, comparing the result of the ^{40}K time coincidences using the T0 values from the laboratory and the ones computed *in situ* by the LOBs. The detailed results of each individual line are summarized in Table 4.2.

For the 10-lines detector configuration, the 627 ^{40}K *intra-storey* time differences are distributed with a RMS of ~ 0.72 ns when the laboratory T0s are used. This value decreases up to ~ 0.57 ns (see Fig. 4.15) if the *in situ* T0 values computed by the OB system are used instead, what means a 20% of improvement. Considering only the OMs whose offsets have been corrected by the *in situ* OB calibration (442 entries), the RMS moves from ~ 0.71 ns to ~ 0.50 ns, being a 30% improvement.

It is clear that using the T0 values computed with the LOBs improves the ^{40}K time coincidences, reducing the RMS of the distribution to less than 0.6 ns.

Another way to show the correlation between the ^{40}K and LOB *intra-storey* time differences is by direct comparison using the same set of T0s, for instance, the laboratory values. This is shown in Fig. 4.16, the plots show the correlation (left) and the difference (right) between the *intra-storey* time differences computed with the ^{40}K method (Fig. 4.15 left) and the LED OBs (Fig. 4.11). According to the results, the differences between both methods are distributed with a RMS ~ 0.5 ns, fulfilling our timing calibration requirements.

It is worthy to emphasize that the ^{40}K calibration is a completely independent method used for the cross-check of the T0 computation. Indeed, the

Line	entries	Laboratory T0s		*in situ*	
		μ(ns)	RMS(ns)	μ (ns)	RMS (ns)
1	67	0.18	0.98	0.21	0.58
2	65	0.11	0.72	0.14	0.55
3	67	0.24	0.93	0.19	0.84
4	70	0.22	0.69	0.21	0.61
5	56	0.19	0.64	0.14	0.53
6	55	0.20	0.62	0.19	0.45
7	54	0.22	0.46	0.22	0.45
8	72	0.17	0.65	0.17	0.51
9	53	0.16	0.44	0.17	0.41
10	68	0.17	0.72	0.19	0.58

Table 4.2: *Summary of the intra-storey time differences with the ^{40}K method using the T0s computed in the laboratory and the T0s computed in situ by the OB system. The ^{40}K data used to obtain these results is cumulative data up to May 2008 [100].*
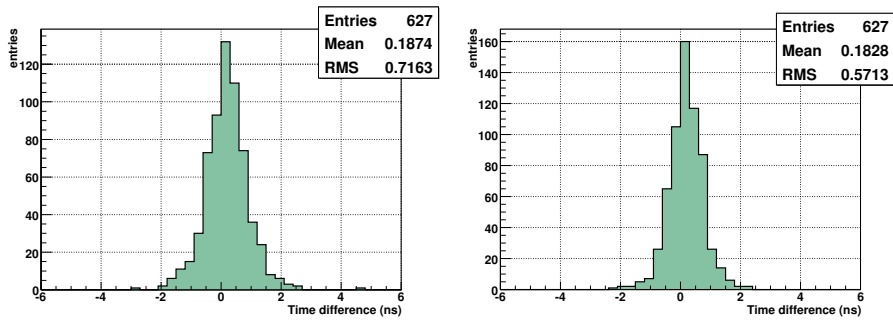
Figure 4.15: *The intra-storey time differences obtained with the ^{40}K method. On the left, computed with the default T0s from the integration at the laboratory. On the right, computed with the corrected T0s values provided by the LED Optical Beacon system in situ. The overall distribution shows a good improvement.*

Chapter 4. Calibration with the Optical Beacon system
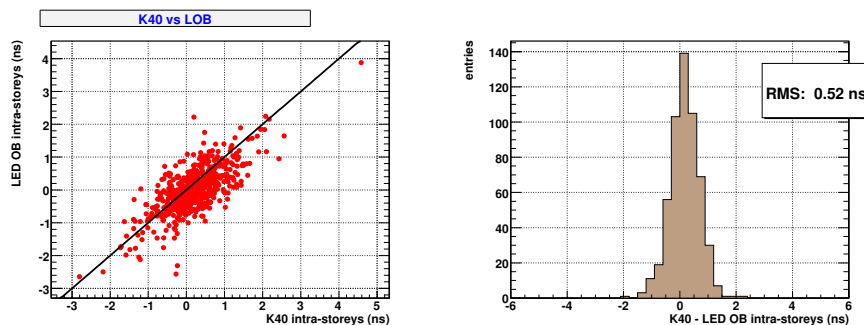
Figure 4.16: *On the left, correlation between the intra-storey time differences computed with the ^{40}K method and the LED OBs. The straight line represents the perfect agreement. On the right, the distribution of the differences between the intra-storeys computed with the LED OB and with the ^{40}K method.*

^{40}K is a "moving", low intensity light source relatively close to the OMs while the LED OB is a fixed, high intensity light source relatively far from the OMs. The cross-check performed increases the confidence in our method and thus, in the calibration of the detector, making it very robust at the *intra-storey* level.

4.4.4   Update of the T0 values and time stability

One important feature to monitor is the stability in time of the T0 values. As it has been presented, this stability is controlled observing the evolution of the *intra-storey* time difference distribution. The RMS of this distribution is stable in time, and deviations from this behaviour provide hints of small drifts in the OMs whose HV need to be retuned. The first update of the in situ T0 values which were computed on February 2008, came after the retuning of the high voltages of the OMs done in August 2009. Thanks to the LED OB, a complete set of T0 values were recomputed. The differences between the new and the previous set of T0s can be seen in Fig. 4.17. The distribution has a Gaussian shape with a small positive tail due to the increase of the previous T0 values.

Fig. 4.18 shows the changes made on the T0 values versus the changes made on the OM HVs. A clear correlation is seen between both. However, this correlation does not go across the (0,0) point meaning that even with no HV correction, a T0 change is present. Since this effect is not expected to be a consequence of the HV tuning, it seems to point in the direction hinted by
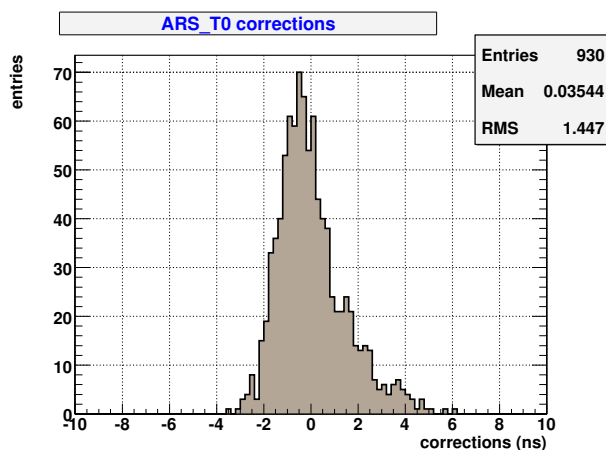
Figure 4.17: *Difference between the T0 values computed in August 2009, after the HV retuning, and the old ones computed in February 2008.*

the *intra-storey* time differences (Fig. 4.14 left), where the T0s drift slowly in time before the HV tuning. The points lying on the X-axis, are the OMs not corrected by the LED OB, therefore, there is no change in the T0 values even with a HV change.

The *intra-storey* time difference cross-check has been also used in order to assess the impact of the HV tuning in the T0 values. The Fig. 4.19 shows the resulting distributions obtained with an LED OB calibration run taken with the new HV values, using the T0 values previous to the HV tuning (left) and using the updated T0 values (right). As it can be seen the RMS of the distribution is back to ~ 0.5 ns as expected from a proper calibration.

4.4.5   Other calibration using the LED Optical Beacon system

As it has been mentioned, the LED OB is a very versatile device which can be used, not only to perform the relative time calibration, but also to obtain useful information about the performance of the detector. In this regard, it is possible to estimate and monitor the optical properties of the water and, in addition, to monitor the OM efficiencies which have been computed using the ^{40}K method [101].

Chapter 4. Calibration with the Optical Beacon system
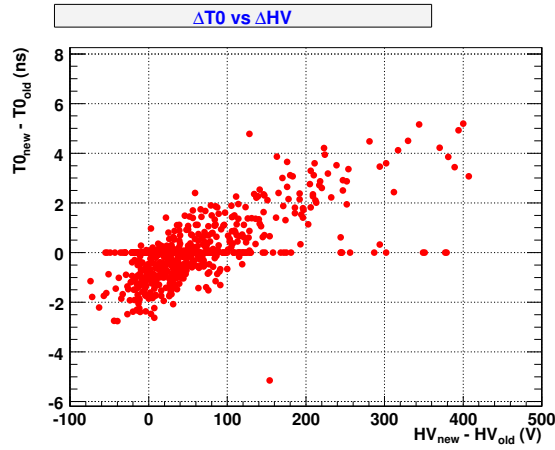
Figure 4.18: *Correlation between the T0 value changes with respect to the OM HV changes. The greater the size of the HV correction, the larger the change in the T0. The fact that the points do not cross the origin could be understood as a global drift in time of the T0 values independently of the HV.*
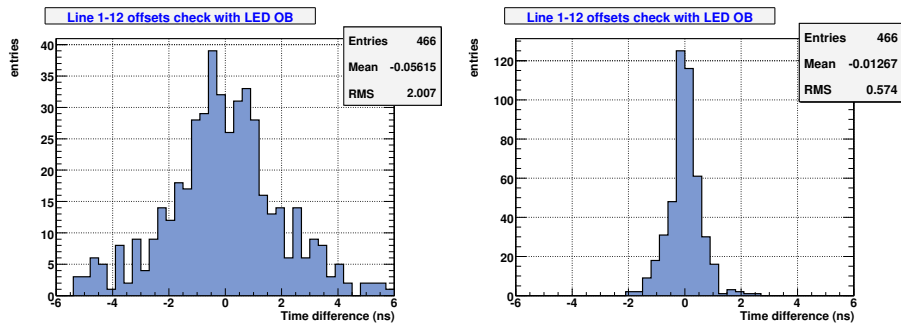
Figure 4.19: *Intra-storey time difference distributions for the LOB calibration runs taken with the new HV settings. On the left, the distribution is computed using the previous T0 values. On the right, the same distribution but with the updated T0 values. The RMS of ∼ 0.5 ns is restored.*

Optical water properties

The water optical properties are of crucial importance in the Monte Carlo simulation. A first estimation of the absorption length has been computed [?] based on the exponential fit of the total signal hits collected by the OMs. In order to avoid the losses due to the dead time in the charge integration, these measurements have to be done when the OMs work below the photoelectron level. Thanks to the experience gained with the Optical Beacon system when performing time calibration, as well as the tests carried out in the integrations of the laboratory, the light intensity of the beacons can be tuned with an optimal configuration, i.e., a configuration allowing the beacon to illuminate the OMs of a line at the photoelectron level. Currently, further studies are under way to incorporate the arrival time information to study the influence of the scattering light.

OM efficiency monitoring

One important feature of the LED Beacon is the stability in the emitted amount of light (see [98]). The evolution of the collected charge by the OMs in an LED Beacon run during a long time period can be used to check the OM efficiency.

In the left part of Fig. 4.20 the evolution of the charge recorded by the three OMs of the storey 6 in Line 1 for half a year time period is shown, This picture clearly hints that the OM0 is losing efficiency. From the analysis performed with the ^{40}K method, the loss of efficiency is seen as a decrease in the rate of coincidences of the OM0 with the two other OMs.
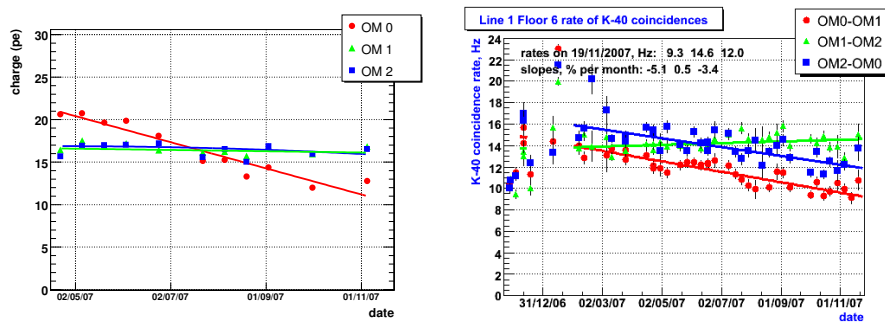
Figure 4.20: *Left, charge evolution in time of the three OMs on Line 1 floor 6 for a 6 months period. Right, the ^{40}K coincidence rate for a period which comprises the previous one. From both plots, it is clear that the OM0 is losing efficiency during this period.*

Chapter 4. Calibration with the Optical Beacon system

The evidence is clear in the overlapping time period. The knowledge of the OM efficiency is very important for the studies where the measurement of the collected charge is needed. This has a clear impact in the analysis of the optical water properties. Apart from the time calibration, OM efficiency monitoring and optical water properties studies are currently the most relevant ongoing analysis with the OB system.

4.5   Laser Optical Beacon calibration

The Laser Beacons are used to carry out either *intra-line* and *inter-line* calibration. With the LED Beacons, we have been focused on the calibration of the OMs which are on the same line where the beacon is located. This simplifies considerably the analysis because of the symmetry of the setup. The calibration with Laser Beacons, being placed at the bottom of some lines, is affected by additional effects as the OM angular acceptance, delayed scattered photons, line movements, etc. All these effects lead to an increase of the incertitude in the time resolution. In order to estimate the influence of the OM acceptance and the photon scattering, a Monte Carlo simulation has been produced [102]. In addition, the position of the lines has been corrected according to the positioning systems (see Appendix B). The walk effect is also corrected and, the time residual distributions are fitted to the convolution of a Gaussian and an exponential function in order to reproduce the scattering tail. Finally, an increase of the statistics of the Laser Beacon runs helps to minimize the errors. The present analysis has been carried out with 12 Laser Beacon runs taken from February to May 2008 (the complete list of runs can be found in the Appendix A).

4.5.1   *Inter-Line* time calibration

Due to their fixed location in the detector, the Laser Beacons are the most suitable devices to compute and monitor the time delay between lines. The analysis has been performed using the Laser Beacon on Line 8 (see Fig. 4.21). There is also a second Laser located at the anchor of the Line 7 but it does not work because of a power supply failure.

The method to perform the time calibration with the Laser Beacon is based, as in the LED OB case, on the time residuals between the beacon and the OMs as defined in Fig. 4.22. Since the intrinsic offsets of the OMs and the laser beacon are known from the laboratory time calibration performed before the deployment, the residual distribution should be roughly centred at zero. In any case, as the aim of the Optical Beacon system is the relative time calibration, any systematic time offset of the beacons shifting slightly the distribution, is not critical for our time calibration purposes.
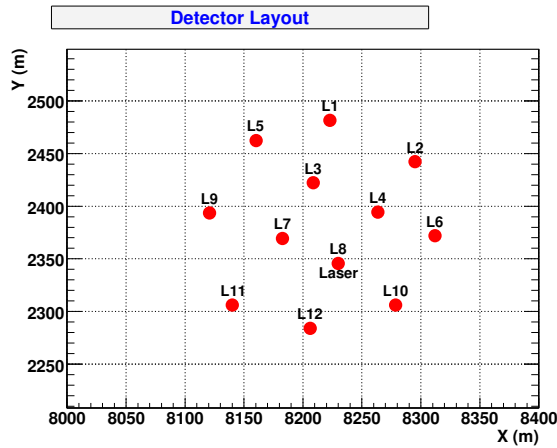
Figure 4.21: *Layout of the twelve lines of the complete ANTARES detector. The Laser Beacon used in the analysis is installed in the BSS of Line 8.*

The time residuals are corrected by the walk effect, the actual position of the OMs is used and the delay from the propagation of the green light in water is subtracted. Also, in order to decrease the incertitude, several runs were taken during a period where there were not important updates in the detector as an OM HV tuning. Moreover, in order to minimize the effects due to the orientation of the OM, only OMs pointing to the Laser within a 40° cone were chosen. An example of how the residual fit for a particular OM looks like can be seen in Fig. 4.22.

The fit of the time residuals is performed for the first storeys of all the lines and the maximum of the fitted function (T^{100}) for each storey is obtained. Then, we compute the average values of the twelve runs.

Fig. 4.23 shows the average T^{100} values as a function of the average Laser OB-Storey distance. The range goes from the distance where the OMs are illuminated at the photo-electron level (> 160 m) up to the region where the errors in the time residual computation are too large because of the lack of statistics (> 240 m).

A flat distribution for each line is shown in agreement with what is expected at the photoelectron level, since in this case, there is not "early-photon" effects[5]. This distribution can be compared with the MC simulation shown in (Fig. 4.24). The MC simulation takes into account the different effects of the absorption and scattering on the time residuals for all the lines. The OM po-

---

[5]Even though the laser pulse is very narrow the scattering makes it wider, leading to a small "early-photon" effect for the high intensity regime.

Chapter 4. Calibration with the Optical Beacon system
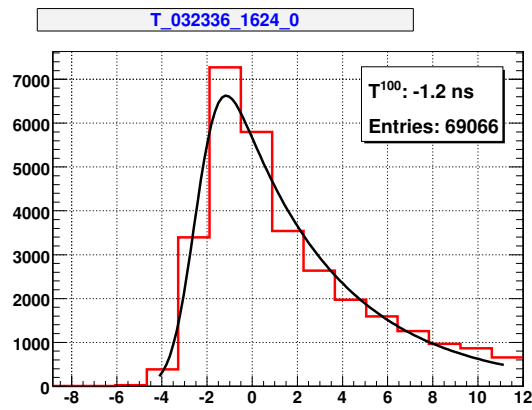
Figure 4.22: *Time difference distribution between an ARS of the 1st floor of Line 1 and the Laser Beacon located at the BSS of the Line 8.*
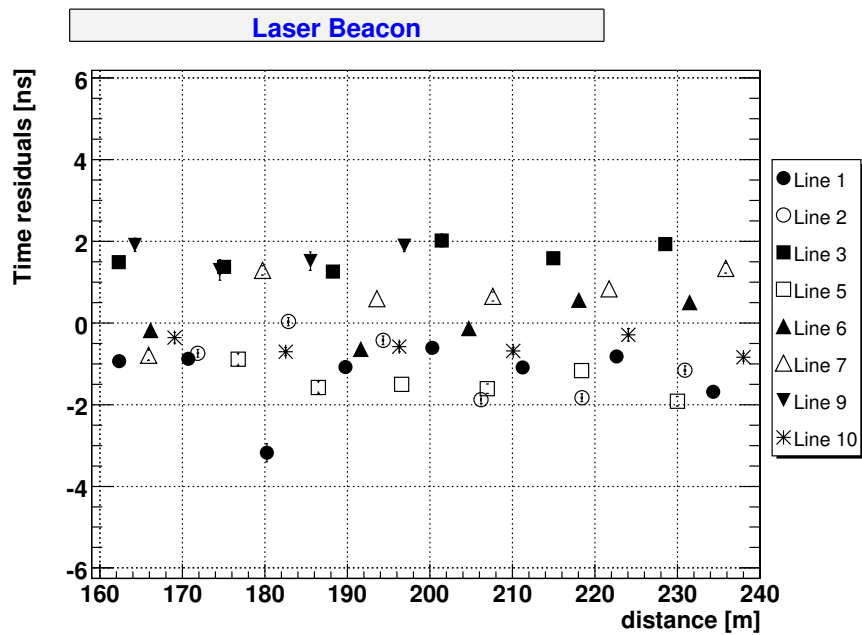
Figure 4.23: *Averaged T^{100} values for each storey (one point) as a function of the distance to the Laser Beacon. Only the selected range of distances is shown.*

sitions are inferred from the real data in order to reproduce the real distances and positions of the OMs.
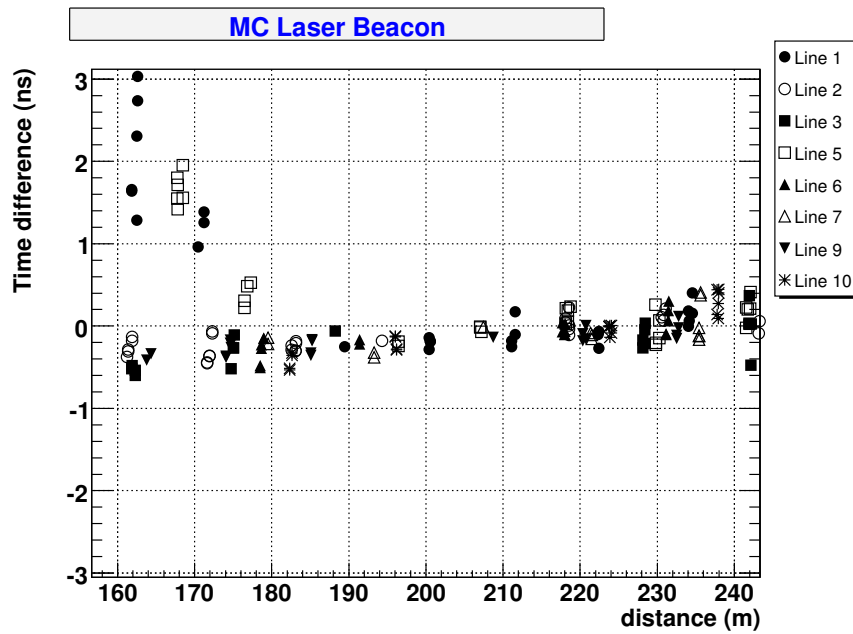
Figure 4.24: *MC simulation with the T^{100} for each ARS (one point) with respect to the distance to the Laser Beacon. Although the MC needs some fine tuning, the trend of the points is compatible with the flat distribution observed in data.*

The MC simulation shows that all the lines should have the same value for the time residuals, basically zero, with a very small slope compatible with a flat distribution. This small slope can be assumed as a combination of two effects. The incertitude in the exact amount of emitted light by the laser which could means that the photoelectron level is still not reached in the whole range in the graph. And in addition, the influence of the light scattering which causes a sort of early-photon effect. Another noticeable effect is that some points clearly deviates from the linear trend. They correspond to the first OMs on lines 1 and 5. This effect comes from the simulation of the emitted light trough the laser rod which is not accurately simulated. In fact, the emission angle for these OMs are over the critical emission angle for the simulated rod. As a consequence, these OMs do not see direct light but only scattered.

The MC confirms the flat distribution observed in data. Therefore, the observed time shifts among lines should be real time offsets among them. The

Chapter 4. Calibration with the Optical Beacon system

inter-line calibration is performed by selecting a common reference for all the lines. The zero value is chosen arbitrarily as the common reference. It is important to notice that this choice has no effect in the relative time calibration.

Finally, the obtained offsets are added to the T0s of the corresponding line completing the relative calibration of the detector. Fig. 4.25 shows the distribution of the Laser Beacon corrections.
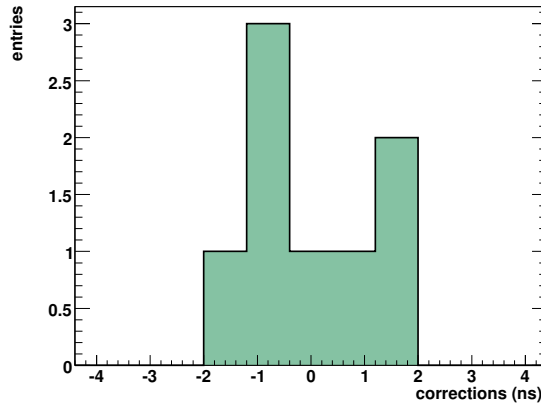
Figure 4.25: *Inter-line time offsets computed with the Laser Beacon.*

4.5.2   Intra-Line time calibration

Although the main goal of the Laser Beacon is to perform the *inter-line* calibration, it can also be used to calibrate some parts of the detector where the LED OBs can not reach its best performance. In addition, it can also be used to cross-check those parts where Laser and LED overlap and both perform well. This calibration will be in most cases a cross-check of the LED OB calibration. Having a look to Fig. 4.23, a correct *intra-line* calibration means that all the values (T^{100}) of a given line must lie on a horizontal line. In principle, most of the storeys represented in the plot are compatible with this horizontal behaviour. However, there is one storey at 180 m that clearly differs from this tendency. That floor correspond to the 3rd storey on Line 1. This discrepancy is difficult to detect with the LED OBs because, as it was explained in the LED OB section, the *intra-line* calibration for this storey is not possible since is does not follow the linear trend of the "early-photon effect" fit. Therefore, this storey must be corrected by the Laser Beacon being moved to the horizontal level of its line.

4.5.3   Positioning cross-check

The fixed location of the Laser Beacon at the anchor of the line is also useful to perform cross-checks of the positioning system. This cross-check is done computing the mean value of the time residuals of a given floor, for a long time period. This is shown in Fig. 4.26 left for the first floor on Line 7 in a period of 75 days. The points spread with a RMS of 1.9 ns for the whole period. These time residuals are computed assuming the nominal alignment (detector made with rigid straight lines). The distribution of the T^{100} values improves significantly when the real positions provided by the positioning system are considered. In this case, the T^{100} values are distributed with a RMS of 0.5 ns (Fig. 4.26 right). This is of the order of magnitude of the relative time and positioning resolution, both of 0.5 ns[6].
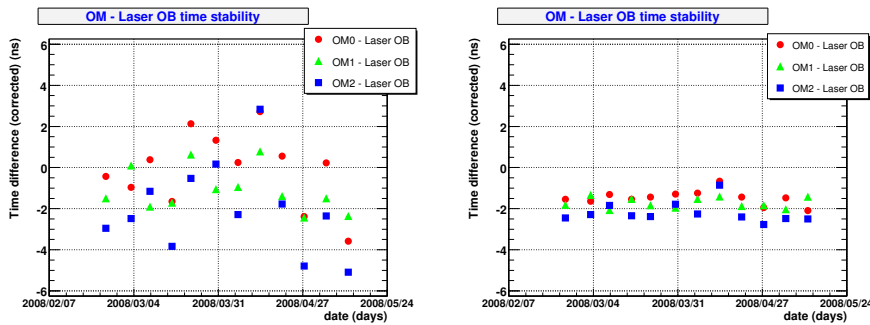
Figure 4.26: *The Laser-OM time differences for Line 7 Floor 1 during almost three months. On the left using the nominal alignment and on the right using the actua positions of the OMs.*

4.5.4   Impact on the time residuals of the reconstructed events

Like the *intra-storey* calibration, the *intra-line* and *inter-line* calibration can be tested using the physical background signals of the experiment. In this particular case, we can use the time residuals of the reconstructed muon tracks. The distribution of these time residuals depends on the TTS of the PMTs, the light propagation in water, the readout electronics and the calibration constants. Since the detector was previously calibrated in the laboratory and the correction of the calibration constants are, in general, not much larger than one nanosecond, the improvement on the tracks residual distribution using

---

[6]The 10 cm precision of the positioning system can be translated into 0.5 ns time precision considering the speed of light in water ~ 20 cm/ns.

Chapter 4. Calibration with the Optical Beacon system

different sets of T0 values is going to be small. In order to stand out the effect of the T0 corrections we have applied some specific cuts when computing the time residual distribution of the muon tracks. Only well reconstructed tracks (good quality tracks), and whose orientation does not differ more than 1° when computed with both T0 sets are selected. These time residuals have been computed for all the reconstructed tracks in a ten-days period of data taking and using two different sets of T0 values (laboratory and *in situ*). Finally, we have considered only the hits on the OMs where the T0 values from both sets differ more than than 3 ns. After these cuts, the time residual distributions of the reconstructed tracks have the shape shown in Fig. 4.27.
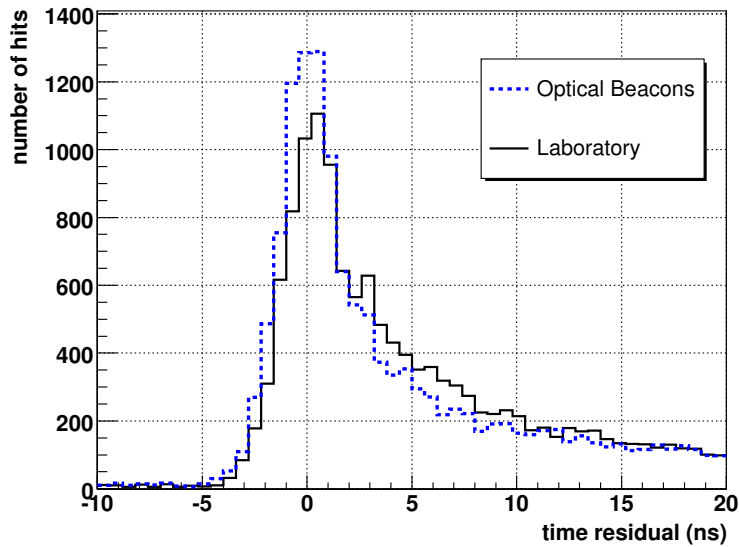
Figure 4.27: *Time residual distributions of a 10 days real physics event sample containing well reconstructed tracks (good quality fit parameter) for the OMs with larger corrections. The distributions are obtained using the calibration constants from the laboratory (dashed line) and the final calibration constants after the Optical Beacon corrections (solid line).*

As it is expected, the population of the central bulk grows at expenses of the tails when the T0s computed with the OBs are used instead of the laboratory calibration constants.

4.6 Conclusions

The Optical Beacon system has been designed mainly to perform the *in situ* relative time calibration of the detector in its three steps: *intra-storey*, *intra-line* and *inter-line* calibration. The *intra-storey* calibration is achieved thanks to the LED OBs and is confirmed with good agreement by an independent analysis based on ^{40}K. The *intra-line* calibration is performed mainly by the LED OBs. The Laser OBs are used to verify these results and to correct the cases in which the OMs are not properly illuminated by the LED OBs. Finally, the relative time calibration is completed with the calibration at the *inter-line* level, which is performed by the Laser OBs. The validity of the *intra-line* and *inter-line* has been tested by looking at the time residuals of the reconstructed atmospheric muon tracks. The time residuals distribution improves using the calibration constants (T0s) computed with the Optical Beacon system.

The OB system has confirmed the electronics resolution of ~ 0.5 ns required to perform the relative time calibration. Moreover, the OB system allows the *in situ* time re-calibration of the detector with great accuracy in case of changes due to a re-calibration of the detector or time drifts of the calibration constants.

The time calibration obtained plays a key role in the detector performance and guarantees the expected angular resolution.

In addition, the Optical Beacon system has been used for other studies as the measurement of the optical water parameters, OM efficiencies and cross-check of the positioning system. These are issues that have been started in this thesis but they will be studied in detail in future works.

Chapter 4. Calibration with the Optical Beacon system

Chapter 5

Monte Carlo simulation and data processing

The ANTARES detector has been taking data since the deployment and connection of the first line in February 2006. The detector became fully operational in May 2008 with the connection of the final lines completing the scheduled twelve lines. During this period, the detector went through different configurations. The data collected with one and two line configuration was mainly used for environmental measurements and for the first atmospheric muon studies [103]. The connection of the following three lines took place in January 2007 and set a 5-line detector configuration (375 PMTs) which lasted until the end of 2007. The operation of this configuration provided enough statistics to perform some physics analysis and in particular, the search for point-like sources which is one of the subjects of this thesis. The data selection carried out for this analysis and the comparison between data and Monte Carlo are reviewed in this chapter.

5.1 Monte Carlo simulation

Monte Carlo (MC) simulation is required in any high energy physics experiment to take into account all the known information about the detector (physics processes, electronics response, etc.) It allows us to understand the performance of the detector by trying to reproduce the actual experimental conditions. The Monte Carlo chain in ANTARES can be divided into four main parts:

Chapter 5. Monte Carlo simulation and data processing

- **Generation of the physics signal**

  Two kind of physics signals can be produced in ANTARES. Firstly, the up-going events produced by either atmospheric or cosmic neutrinos. Secondly, the down-going atmospheric muons whose flux at the ANTARES depth is still six orders of magnitude larger than the up-going neutrino flux. The generation of **neutrinos** is done with the GENHEN [104] programme[1] which takes into account the interaction of neutrinos with the Earth for both interaction channels (NC and CC) and considers the three neutrino flavours.

  The energy of the generated events ranges from 10 GeV to 10 PeV following a power law with a spectral index of $\gamma = 1.4$ (see Eq. 1.3). This value is taken to obtain enough statistics at high energies. This is reweighed afterwards to different spectral indexes in order to account for the atmospheric flux (included in the generation package) or cosmic sources. In the case of neutrino sources, a spectral index of $\gamma = 2.0$ is assumed.

  The generated events are selected by the interaction vertex and the target nucleon. The selected events have a vertex inside a predefined volume of about 2.5 times the attenuation length of the light in water at the ANTARES site from the instrumented volume. This volume, which contains the detector, the so-called *can*, is approximated by a cylinder of 480 m height and 100 m of radius.

  The CC neutrino interaction is reproduced by LEPTO [105], the parton density functions are included in the CTEQ6 [106] software, and the hadronisation in PHYTIA/JETSET [107]. Finally, the propagation of the induced muon is simulated by MUSIC [108].

  The atmospheric **muon** flux is produced in the hadronic showers after the primary cosmic rays interaction with the atmosphere. Their simulation is done by CORSIKA [109]. The energy range is $1\text{-}10^5$ TeV per nucleon. The program takes into account the propagation of the muons up to the sea surface while the propagation inside the sea water up to the can is simulated by the MUSIC package as in the case of neutrinos.

- **Tracking and Cherenkov light emission**

  Once the muons resulting from the physics generator arrive at the can surface, their tracking is simulated by GEASIM [110] and KM3 [111]. GEASIM is a program which simulates the generation of Cherenkov light by a particle in water, including light from any secondary particles. Physics processes involved like energy losses, multiple scattering, radiative processes and hadronic interactions are also included. This

---

[1]GENHEN is a subprogram of the GENNEU main program.

program is based based on GEANT 3.21 software. KM3 take into account the detector simulation including the OM angular acceptance, the water optical properties of the ANTARES site as light absorption and scattering.

- **Optical Background noise simulation**

  It is known that the environment where the ANTARES detector is located has a considerable optical background produced mainly by the ^{40}K decay and the biological activity. According to the previous sea campaigns and the current data taking, this unavoidable optical background produces a rate of around 60 kHz per OM. The ^{40}K can be simulated assuming that it produces a constant rate. The bioluminescence is obtained from the data itself. The `SummaryTimesliceWritter` program [112] allows us to generate the counting rates for all the detector using a sub-system of it.

- **PMT response**

  The `TriggerEfficiency` program [113] simulates the effect of the electronics on the data. It takes into account the main features of the PMT and the ARSs as the dead time or the walk effect. Starting from the true number of Cherenkov photons, an analogue Gaussian pulse is simulated. Then all the processes (charge integration time window, time-stamp from the threshold crossing, etc.) are simulated providing a final hit with the same information as in the real data acquisition.

5.2   Event reconstruction algorithms

One of the aims of a neutrino telescope is the precise reconstruction of the muon tracks from their induced Cherenkov light. The direction and the energy information obtained from the reconstruction are the basis for the physics analysis because they are directly correlated with the direction and energy of the primary neutrino.

5.2.1   Track reconstruction

For a muon track at a given time (t_0), the expected arrival time (t_{exp}) to the OM of the Cherenkov photons induced by the muon track can be written as (see Fig 5.1):

$$t_{exp} = t_0 + \frac{1}{c}\left(l - \frac{k}{\tan\theta_c}\right) + \frac{1}{v}\left(\frac{k}{\sin\theta_c}\right), \qquad (5.1)$$

Chapter 5. Monte Carlo simulation and data processing
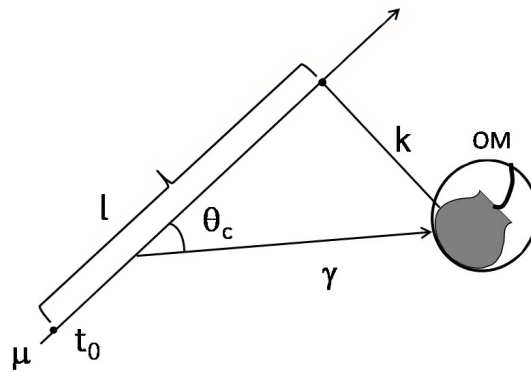
Figure 5.1: *Schematic view of a muon track. The parameters used in the reconstruction are shown.*

where l is the distance from the starting point t_0, to the point of closest approach. The k parameter is the distance from the OM to the point of closest approach, θ_c is the Cherenkov angle, and v is the group velocity of the light in water. The second term corresponds to the muon propagation and the third one to the Cherenkov photon propagation.

The ANTARES collaboration has developed several reconstruction algorithms of the muons tracks. All of them are based on the PDF distribution of the time residuals, defined as the time difference between the measured arrival time and the expected time of a direct photon to the OM ($r \equiv t_{mea} - t_{exp}$).

The way of finding the best muon track can be performed by maximizing the likelihood function $\log L = \sum_{i=1}^{N_{hits}} \log P(r_i)$, where $P(r)$ is the residual PDF, or by minimizing a quantity like $\chi^2 = \sum_{i=1}^{N_{hits}} r_i^2$. In both cases, since the equation to compute the residuals is non-linear, the minimization/maximization is performed in an iterative way. Currently, two algorithms are used for data analysis in ANTARES:

Offline Strategy

The algorithm used in the Offline Strategy [114] performs a sequence of different fitting procedures in order to maximize the likelihood function. These fitting procedures are linked together in such a way that each fit produces the input of the following fit, except for the first one which is a linear pre-fit. The PDF of the residuals ($P(r)$) is obtained from MC simulation using a detailed parametrization. The track reconstruction process is based on a *maximum-*

likelihood algorithm used to construct a statistic

$$\Lambda = log(L)/N_{DOF} + 0.1(N_{comp} - 1), \qquad (5.2)$$

able to estimate the quality of the track parameters. The term, which contains the number of compatible solutions (i.e. solutions within 1° with respect to the preferred track) found by the reconstruction algorithm, improves the discrimination between "good" and "bad" reconstructed tracks, so that, the badly reconstructed tracks are eliminated by selecting the appropriate cut on the Λ value.

The Offline Strategy is included in the current software package used for track reconstruction in ANTARES: CalReal (see [115] and references therein). Moreover, CalReal allows the calibration and/or track reconstruction of the raw data recorded in the ANTARES runs. The program takes automatically the best calibration set which contains the most suitable calibration constants (charge, time, position) for the specific run analysed.

The output of the program is written in a `ROOT` format file, which contains the complete information (e.g. track parameters) needed for the data analysis.

Online Strategy

The second algorithm used in the track reconstruction is the so-called Online Strategy [116]. Although this algorithm was conceived to obtain a quick online fit of the track to monitor the detector performance (e.g. Fig 2.21), it can also be used for offline data analysis. The algorithm is based on the minimization of a defined χ^2-like function which takes only a high purity fraction of signal hits, direct Cherenkov photons, and merges the hits of the three OMs in the same floor using the centre of the storey as the hit position for the fit. Two kinds of fits can be performed. The particle track fit, which considers the track as a straight line in the space, and the bright point fit, where Cherenkov photons are emitted by a point light source in a single flash at a given moment. Moreover, the algorithm does not use the information of the positioning systems, considering the detector as made up of rigid straight lines. As a consequence of these simplifications, the algorithm does not reach an optimal angular resolution as good as the previous Offline Strategy does. However, this strategy is less dependent on our knowledge of the detector, which makes the strategy very robust. This is very important in the first data analysis, where some tuning is still needed for sophisticated algorithms in order to get a good agreement between data and MC. In this work we have chosen the Online Strategy for the data track reconstruction.

Chapter 5. Monte Carlo simulation and data processing

5.2.2   Energy reconstruction

The neutrino energy reconstruction in ANTARES relies on the energy reconstruction of the induced muon, and the energy reconstruction is based on the energy losses when the muon crosses the matter surrounding the detector (see Section 2.1.3). However, events not completely contained are frequent, which makes difficult a good energy estimation. The $\log_{10} E^{\mu}_{rec}/E^{\mu}_{gen}$ distribution is well-centred around 0, and has a sigma value about 0.3 in the energy range from 500 GeV to 1 PeV, which means a knowledge of the muon energy within a factor 2-3 [117]. For our analysis of point-like source searches, the energy selection, as we will see, comes implicit in the reconstruction quality cut.

5.3   Data processing

After the track reconstruction process, the output files, both real data and MC, are re-processed in order to translate the horizontal coordinates, azimuth and elevation[2], to equatorial coordinates, right ascension (RA) and declination, using a program based on the Slalib libraries [118].

5.3.1   Blinding policy

In all the experiments, but specially in those were low statistics signals are expected as in the case of neutrino telescopes, a blinding policy helps to reduce the human bias in the results of the analysis. In this sense, part of the data information is blinded until the selection criteria (quality cuts) are optimized. Otherwise, minor changes in the selection criteria of the data could significantly modify the results obtained. The rules of the blinding policy must be clearly defined before the analysis process. These rules could differ from one analysis to another.

In the point-like source analysis, all the parameters and selection cuts applied to the data sample should be fixed before looking at the real position of the events in the sky map (RA, declination). In order to estimate the background from real data a scrambling of the RA coordinates will be enough to not violate the blinding policy. Once the analysis is approved by the Collaboration, the data is unblinded.

---

[2]instead of the most commonly used coordinate which is the altitude, in ANTARES is used the elevation coordinate, defined as the angle between the object and the observer's local horizon.

5.3.2 2007 data taking period

The 2007 data taking period comprises from January 27th to December 4th, 2007. Taking away the time spent on human interventions, sea operations, calibration runs and sporadic data taking problems of the detector (see Fig 5.2), this period is equivalent to 244.8 active days of live-time. For our analysis a good data quality is required, therefore, some selection criteria are applied. The first criterion is based on the active number of OMs. An OM is considered to be active when its counting rate exceeds a threshold of 40 kHz, which is well below the lowest value measured baseline rate ($\sim$ 60 kHz). The minimum number of active OMs in our data selection must be the 80%, which means at least 300 OMs out of the total 375 comprising the 5-line configuration.

The second criterion is based on the optical background conditions. Runs with baseline rates above 120 kHz and burstfraction[3] larger than 40% are excluded. These criteria reduces the active number of days to 167.7. Finally, a trigger inefficiency found in the final data sample reduced the effective live-time to 140 days of data taking.

Figure 5.2: *Amount of data taking time (in seconds) distributed along the 24 hours of a day, divided in slots of one hour. Noticeable effects are: small dips due to human interventions during the morning and the afternoon, some recovery at lunch time and evening, and smooth running along the night with a slight decrease.*

---

[3]The burstfraction is defined as the fraction of time with a rate above 1.2 $\times$ baseline rate.

Chapter 5. Monte Carlo simulation and data processing

5.3.3 2007 data calibration

The first calibration parameters of ANTARES were obtained at the integration sites. These parameters were recomputed *in situ* and are updated regularly. In ANTARES, all the calibrations parameters needed for the data analysis are grouped in calibration sets. Each set contains the most updated parameters of all the calibration tables involved for a specific day. For the 2007 data taking period, the four different sets created are summarized in the following table (Table 5.1). The 0pe and 1pe refers to the position of the pedestal and the one photo-electron peak respectively, and the T0 refers to the time calibration constants.

Calib. set	start date	end date	T0 id	1pe id	0pe id
2007:L5:V4.0	31/01/2007	10/05/2007	10746202	4954763	4954257
2007:L5:V4.1	16/05/2007	01/10/2007	10746202	5394630	5394610
2007:L5:V4.2	01/10/2007	29/11/2007	10746202	32572635	5394610
2007:L10:V5.0	29/11/2007	04/12/2007	16703026	7707892	7707846

Table 5.1: *Summary of offline calibration sets used, containing the name of the set, the start and stop date for which the set is valid, the T0, 1pe and 0pe set of values used in this particular set.*

The `highThreshold` parameter (c.f. Section 2.5.2) was changed from 10 p.e. to 3 p.e. in June 2007. The 10 p.e. threshold was used at the beginning in order to be more restrictive in the data selection. Afterwards, it was moved to 3 p.e. Although the effect in the detector performance is small, it is taken into account in the analysis by weighting each period with its corresponding live-time.

5.4 Data-MC comparison

In order to understand the performance of an experiment, a comparison between real data and Monte Carlo is required. MC simulation aims to take into account all the known processes which are involved in the experiment, from the generation of the physics signal up to the recording of the hits in the OMs. A good agreement between both means that physics behind the experiment is well understood. In this section, a selection of the most relevant plots showing data-MC comparisons will be presented. Based on these plots, quality cuts can be established in order to select a high purity data sample for the point-like source analysis.

Data sample selection

The main quality cuts are applied to obtain the final data sample to be used in the analysis. The first cut is applied in elevation. The way to reject the large number of atmospheric muons consists in selecting only the up-going reconstructed events. Since the Earth shields the detector from atmospheric muons, only neutrino events should survive to this cut. However, mis-reconstructed down-going muons can sometimes lead to an up-going track reconstruction, so a cut based on the quality of the reconstruction is needed to clean significantly the sample. Moreover, we ask for some additional requirements:

- Only events reconstructed by at least two lines are considered in order to avoid events with a high error in the reconstructed angle (in particular in the azimuthal direction).

- Tracks must have more than 5 hits.

- If the Online Strategy fit stops at the boundary condition for the elevation angle, i.e., at +90° and -90° angles, the events are excluded to avoid cosine angles greater than 1 during the fitting procedure.

- The bright point fit quality parameter (χ^2_B) is fixed to be larger than 1.8. For the point-like source analysis this election is not crucial since choosing a different value has a negligible impact.

Figure 5.3 shows the elevation distribution before applying any cut for data and MC. In the plot the number of real data events are 7.79×10^6 while the number of MC background events are 7.22×10^6. Therefore, there is a 7% deficit of MC events in our sample. From this distribution, we could take all the events fulfilling the upward reconstructed criterion (elevation $< 0°$). However, we can see that most of the up-going reconstructed tracks are composed mainly by atmospheric muons (doted line) which have been mis-reconstructed. In the case of atmospheric neutrinos it can also be noticed a small tail for elevation angles larger than 0° which is composed by atmospheric neutrinos reconstructed as down-going (faint line) since only the up-going component of the background has been simulated.

Since the track reconstruction of the Online Strategy is done using the χ^2-like quality track parameter, a proper selection based on this parameter will clean up the sample of mis-reconstructed muons.

Figure 5.4 shows the quality track parameter distribution before applying any cut in elevation. The data-MC agreement is observed all along the distribution except a small discrepancy at low χ^2 values.

Figure 5.5 shows again the elevation distribution but only for those tracks having a χ^2 parameter value lower than 1.8, which will be the final data selection cut used for the point-like source analysis. In the plot the number of

Chapter 5. Monte Carlo simulation and data processing
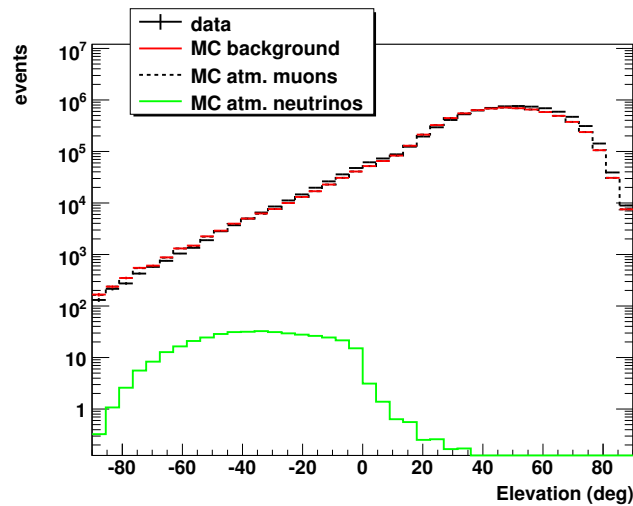
Figure 5.3: *Elevation distribution of the reconstructed events during the 2007 data taking period. Data are compared to the MC background coming from atmospheric muons and neutrinos. The total background, and the muon and neutrino contribution are shown separately.*

real data events are 1.81×10^6 and the number of MC background events are 1.82×10^6 confirming the good agreement between both samples.

It can be seen that the agreement between data and MC is still good once the quality criteria has been applied. Moreover, the upward and downward regions are clearly distinguished. We can also see an accumulation of muon-like events close to the horizon, probably due to some remaining mis-reconstructed events. The number of these mis-reconstructed events is difficult to estimate so that, in order to get rid of this muon contamination, **a cut in elevation $<$ -10° is established as default cut**. As we will see in the next chapter, the sensitivity is not significantly affected by the rejection of these events. This default cut in elevation will be applied in the following steps of our analysis and in the subsequent figures.

The distributions shown in Figure 5.5 contains only events having a $\chi^2 < 1.8$. Changing this cut, leads to different purity in terms of muon-neutrino proportion. In principle, a high purity sample with only neutrinos and not muons is desirable. However, the election of the cut depends on the analysis to be performed. In this case, the election is done based on the sensitivity, i.e., we choose the cut that minimizes the average flux upper limit (sensitivity). The computation of the sensitivity will be explained in the next chapter where we will introduce the point-like search method used for this work. In the follow-
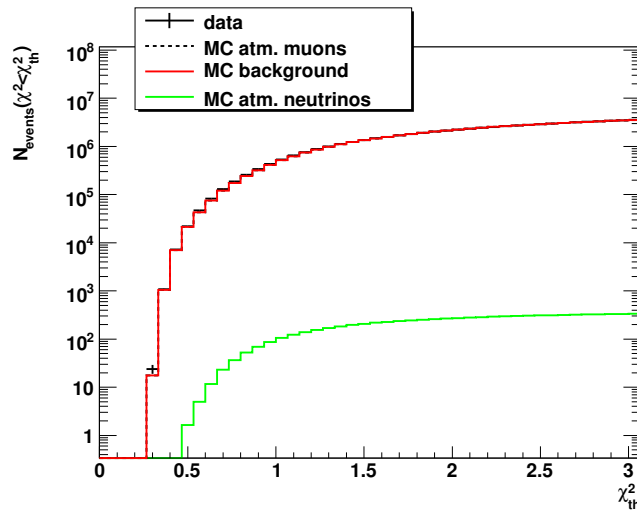
Figure 5.4: *Cumulative distribution of the χ^2 parameter for real data and MC obtained from the track reconstruction with the Online strategy. The discrepancy appears in the region of low values of the χ^2, while for high χ^2 values there is a very nice agreement data-MC.*

ing, the track quality cut $\chi^2 < 1.8$ is used and it will be justified in the next chapter.

In Fig. 5.6, the χ^2 fit quality parameter distribution is shown. The agreement data-MC is not so good for values of χ^2 below 1.1, where there is an overestimation of the atmospheric neutrino MC contribution.

The results shown in the previous figures have been summarized in Table 5.2. The number of events predicted by MC for muons and neutrinos is shown, as well as how it is compared with the data and the corresponding muon contamination for different χ^2 parameter cuts. According to this table, a lower χ^2 cut would provide a smaller sample but this will be cleaner. After the two quality cuts, the final selected data sample for the point-like source analysis has 314 remaining data events which means a daily rate of 2.2 neutrinos. The discrepancy with respect to MC estimation is of 12%.

Other interesting distributions

In addition to the elevation distribution, there are other distributions which can provide valuable information. In Figure 5.7 the other horizontal coordinate, the azimuth, is presented. This distribution present some bumps which are supposed to come from the detector asymmetry due to the 5-line configu-

Chapter 5. Monte Carlo simulation and data processing
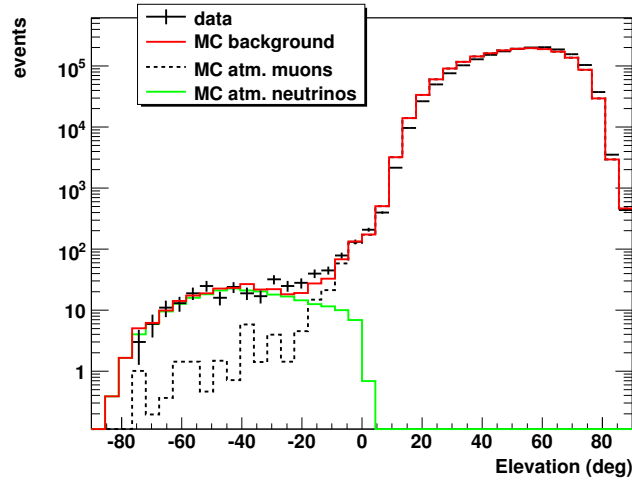
Figure 5.5: *Elevation distribution for a specific cut on the quality parameter ($\chi^2 < 1.8$). The agreement is quite good both for up-going and down-going reconstructed events. It is important to notice that the errors presented are only statistical.*

χ^2 cut	Data	Total bg. events	μ	ν	Cont.(%)
1.3	130	155	0	155	0
1.4	153	175	0.6	174	0.3
1.5	173	191	1	190	0.5
1.6	208	207	4	203	2
1.7	244	236	21	215	9
1.8	314	277	52	225	19
1.9	417	371	137	234	37
2.0	600	498	255	243	51
2.1	877	817	566	251	69

Table 5.2: *Number of survival data and MC events after applying different χ^2 cuts. The last column gives the muon contamination in the sample. The elevation cut at -10° is applied as default.*
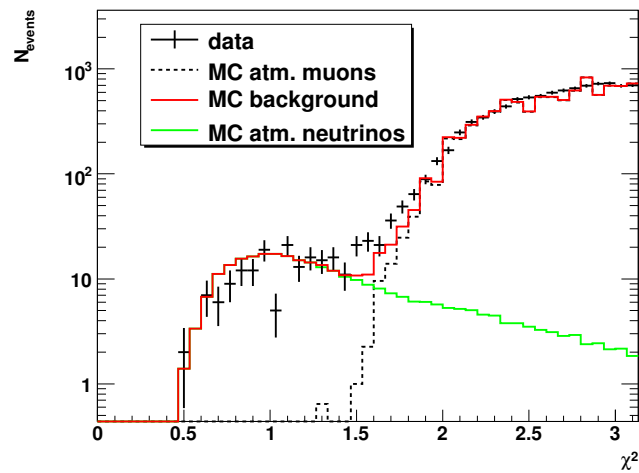
Figure 5.6: *Distribution of the χ^2 fit quality parameter once the events above -10° of elevation have been rejected. As it can be seen the agreement data-MC is good in the region above 1.1 with a slight discrepancy for lower values of χ^2. The cumulative of this plot can be used to estimate the percentage of contamination in the atmospheric neutrino data sample coming from the atmospheric muon events.*

Chapter 5. Monte Carlo simulation and data processing
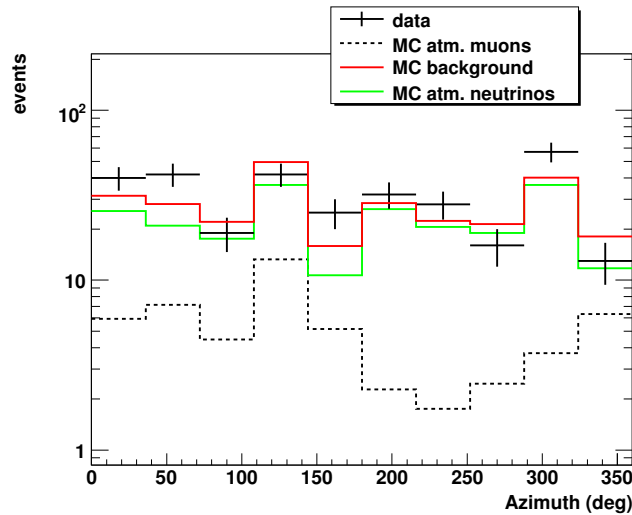
Figure 5.7: *Azimuth distribution of the final 314 events data sample. The flatness of the distribution comes from the isotropic flux of atmospheric neutrinos.*

ration. The data-MC agreement is good once the two default cuts in χ^2 and elevation are applied.

The data analysis will be performed with equatorial coordinates since the cosmic source catalogs are usually presented in this form in order to be independent of the event time. After the conversion from horizontal coordinates, the resulting declination distribution can be seen in Fig. 5.8.

Due to the location of the ANTARES detector in the Earth, the Southern hemisphere in the celestial sphere is seen the most part of the time (-90° to 0°). In addition, the detector can also detect neutrinos coming from the Northern hemisphere during a fraction of time. This region is very important since can be used to cross-check with current experiments looking at this sky region, as IceCube does. The instantaneous overlapping is of 0.6π sr and of 1.5π sr considering the time-integrated fields of view of both experiments.

The right ascension distribution is shown in Fig. 5.9. This distribution is supposed to be flat due to the Earth rotation.

Fig. 5.10 shows the distribution of the number of hits for the reconstructed tracks of the 314 events of the data sample. The agreement is better for the events having many hits (i.e. high energy events). For very high energies the distribution is dominated by the statistical fluctuations due to the few number of events. The excess of events with small number of hits present in this plot should be due to having more muons in the sample as it was hinted in Fig. 5.5.
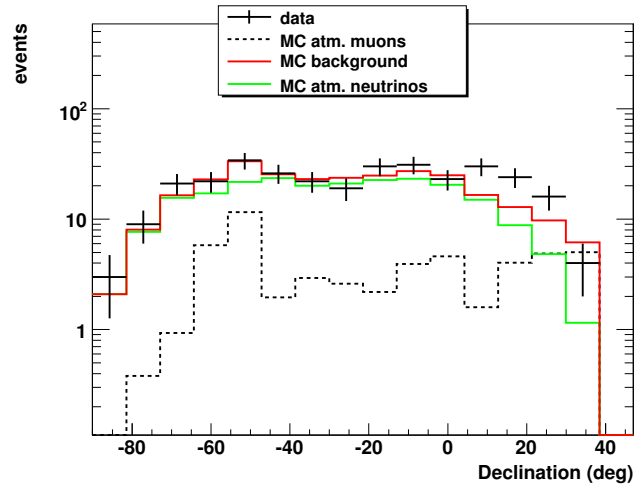
Figure 5.8: *Declination distribution of the 314 events selected for the point-like source search analysis.*
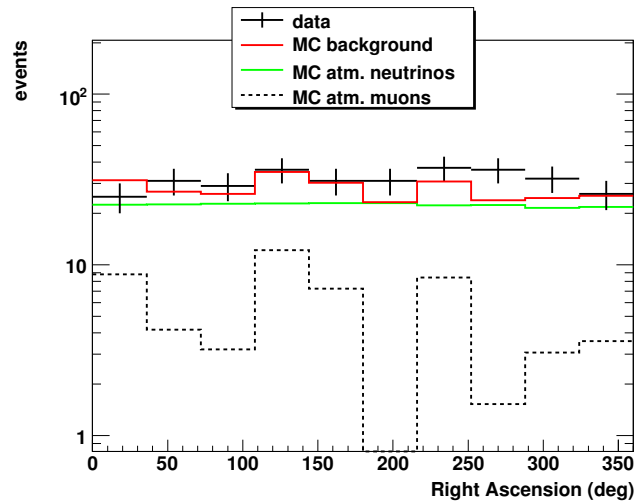
Figure 5.9: *Plot showing the flat distribution in right ascension of the 314 selected events.*

Chapter 5. Monte Carlo simulation and data processing
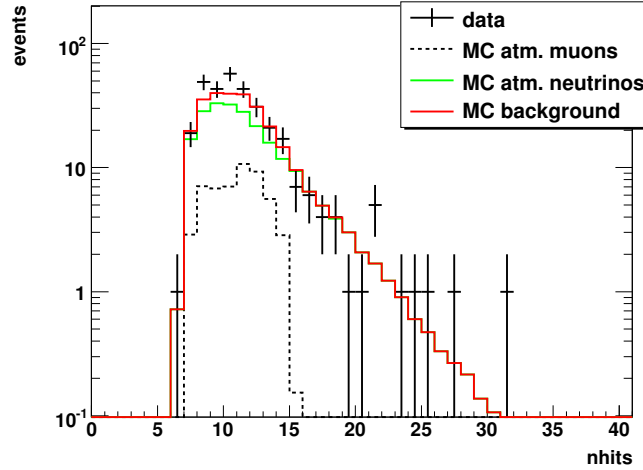
Figure 5.10: *Number of hits used in the track reconstruction for all the 314 selected events.*

Finally, we can also plot the elevation distribution with the neutrino and anti-neutrino contributions separately (Fig. 5.11). As it is shown in this plot the anti-neutrino contribution is a factor $\sim$3 smaller than the neutrino contribution.

5.5 Detector performance

The two more important pieces of information for the analysis of point-like sources are the angular resolution and the effective area. In order to estimate both quantities the signal from the source is simulated assuming a power law $\frac{d\Phi_\nu}{dE_\nu} \propto E_\nu^{-\gamma}$, where the spectral index is expected to vary from 2 to 3 [28]. As it has been previously said, in this work we assume a value of $\gamma = 2$.

5.5.1 Angular resolution

The angular distribution of the neutrino events coming from a given source is known as the Point Spread Function (PSF) of the telescope. This is related to the angular resolution which is defined as the median of the distribution of the angle between the reconstructed muon track and the actual neutrino direction. According to Monte Carlo (MC) simulations, the attainable angular resolution with the 5-line configuration of ANTARES is better than 3° for a
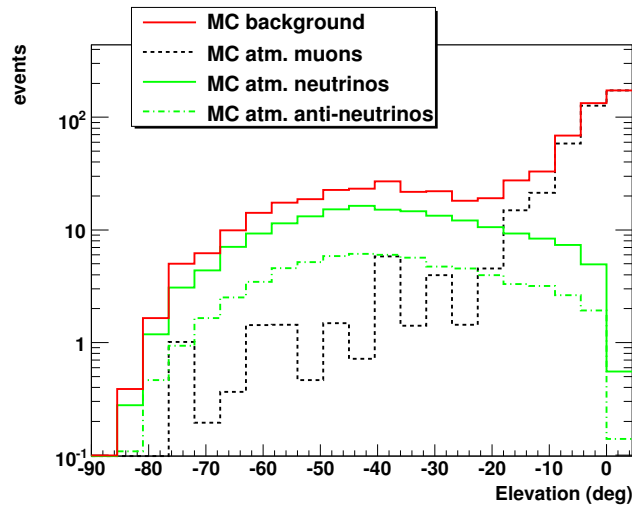
Figure 5.11: *Elevation distribution using $\chi^2 < 1.8$ as the quality cut. The neutrino and anti-neutrino contributions predicted by MC are shown separately.*

$E_\nu > 100$ TeV and a $\chi^2 < 1.8$ cut, as can be seen in Figure 5.12 (top).

Drawing the angular resolution as a function of the declination angle, and averaging over the energy range 10 GeV - 10^7 GeV, Figure 5.12 (right), it can be seen that the graph shows a U-shape, being the worst angular resolution at the edges. This feature seems to has its origin in the 5-line detector anisotropy, which affects mainly to the tracks coming from certain directions. This feature disappears when a 12-line symmetric detector is considered.

The track reconstruction algorithm is based on the time residual distribution. As it was explained previously, this time residual PDF is computed by simulation which means that a good agreement data-MC for the time residual distribution is mandatory in order to rely on our angular resolution. Figure 5.13 shows the time residuals from data and neutrino MC. The muons background has not been considered and the neutrino MC has been renormalized to fit with the data.

5.5.2 Effective area

The second main piece of information in the analysis is the effective area. As it was explained in Chapter 2, the effective area is defined as the 100% efficient surface which detects the same number of events than the real detector. This magnitude allow us to link the event rate detected with the flux of the

Chapter 5. Monte Carlo simulation and data processing
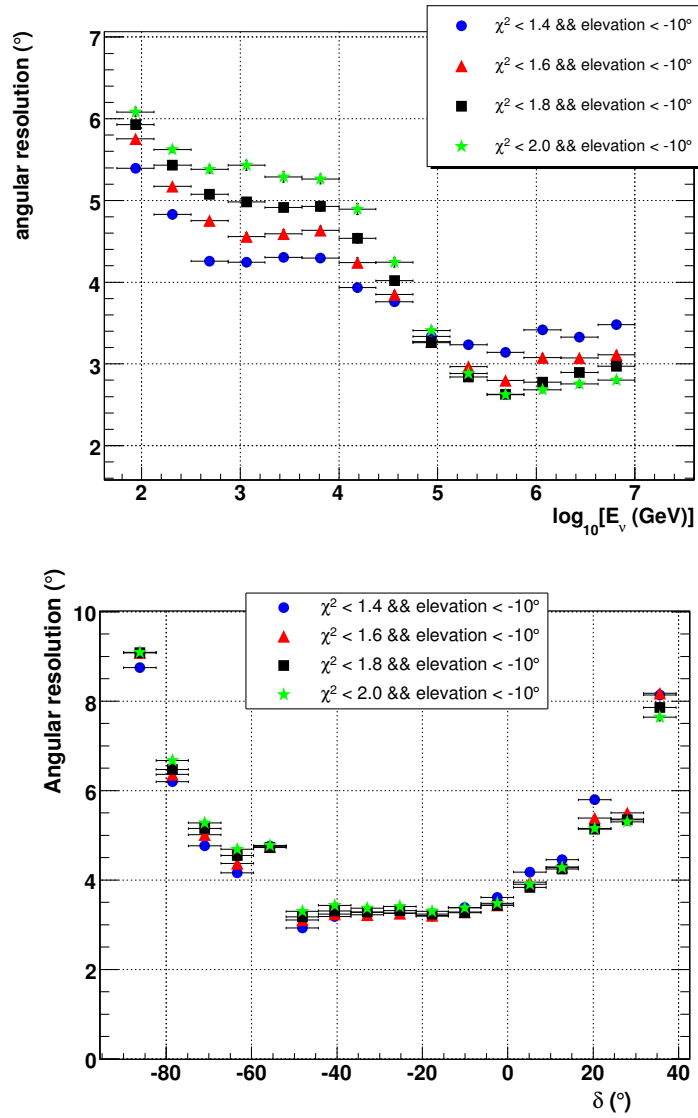
Figure 5.12: *Angular resolution for the 5-line configuration as a function of the energy (top) and declination (bottom) for different χ^2 cuts. Points represent the medians of the angular error distribution for neutrinos.*
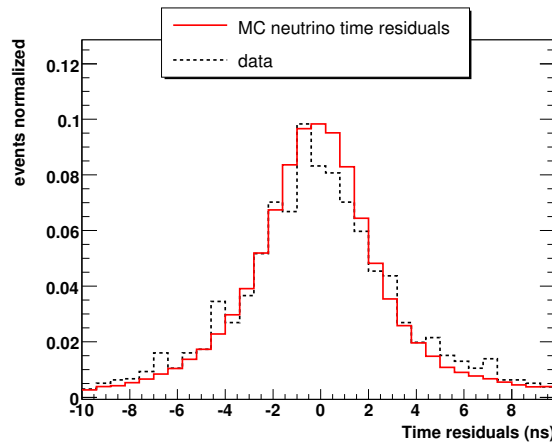
Figure 5.13: *Time residual distribution (i.e. the measured time minus the direct propagation time) of the 314 selected events for the point-like source analysis (dashed line) compared with Monte Carlo simulation (solid line).*

source. The effective area increases with the neutrino energy because of the increasing neutrino cross section and the muon range. For the 5 lines configuration the ANTARES neutrino effective area becomes greater than 1 m^2 for $E_\nu > 100$ TeV. Above the PeV range the Earth becomes opaque to neutrinos and, as a consequence, the effective area decreases. Figure 5.14 shows the dependence of the effective area on the selection cut chosen. In this case, the full elevation range is considered. Although the effective area does not change significantly when comparing the 10 pe and 3 pe periods, an average effective area considering the two different periods was computed.

The effective area as a function of the declination is computed averaging the energy range between 10 GeV and 10^7 GeV.

Finally, Figure 5.15 shows the detector response for the atmospheric neutrino flux and the E^{-2} spectra for the cuts used in the analysis ($\chi^2 < 1.8$ and elevation $< -10°$).

5.6   Error estimation

The distributions presented in this chapter were computed considering only statistical errors. The main uncertainties in the measurements are expected to come from the limited knowledge of the quantum efficiency, the angular acceptance of the optical modules and the optical water parameters. These uncertainties are supposed to affect less than a 30% in the measurements. All

Chapter 5. Monte Carlo simulation and data processing
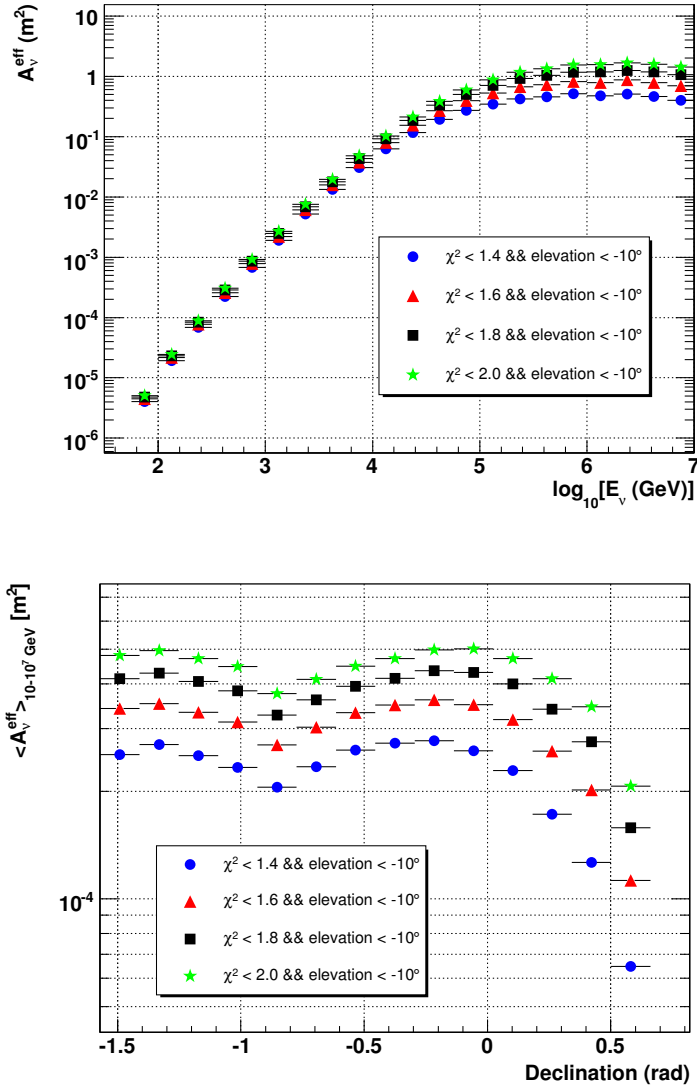
Figure 5.14: *Effective area with the 5-line configuration for different χ^2 cuts. As a function of the energy (left), and depending on the declination (right).*
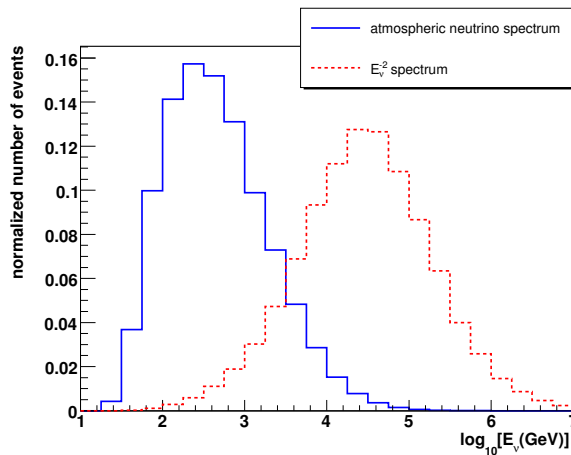
Figure 5.15: *Detector response for the atmospheric neutrino flux (solid line) and the E^{-2} spectrum (dashed line) using the default cuts.*

the distributions presented in this chapter comparing data and MC have an agreement better than this 30%.

The performance of the detector, angular resolution and effective area would be affected by these uncertainties. Therefore, the sensitivities and the limits obtained will be also affected. The impact of these effects will be estimated in the next chapter.

5.7   Summary

In this chapter, we have defined the selection criteria for the data processing with the aim to obtain the best data sample to be used in the point-like source search analysis. In this process, a data-MC comparison has been carried out to understand the performance of our collected data. The reconstruction strategy chosen for the data processing was the Online Strategy, because presently, it provides the better data-MC agreement. This strategy provides robust and reliable results since it uses a very simplified version of the detector, where each storey represents a single point, and the lines are considered as rigid and straight.

Two main cuts were chosen. The first one is based on the elevation and rejects all the events reconstructed with a elevation angle higher than -10°. This cut rejects the tracks reconstructed close to the horizon where there is a high degree of contamination coming from to the mis-reconstructed up-going muons. The second cut is based on the track reconstruction quality parameter.

Chapter 5. Monte Carlo simulation and data processing

In our case, we ask for the cut giving the best sensitivity for a binned method based on a cone-shaped search. That prompted to the election of a $\chi^2 < 1.8$ cut. The results for the sensitivity will be obtained in the next chapter once the method will be introduced. All the required data-MC comparisons presented in this chapter have used these two selection cuts.

At the end, the amount of surviving events are 314. According to the MC simulations this sample has an atmospheric muon contamination of less than 20%.

Chapter 6

Flux limits for point sources

One of the most exciting topics in high-energy neutrino astronomy is the search for neutrino sources in the sky map. The detection of high-energy neutrinos coming from cosmic objects like AGNs, GRBs or SNRs is crucial in order to understand the most energetic processes of the Universe as was reviewed in Chapter 1. A positive result would mean a tremendous breakthrough in the cosmic rays origin studies and also in the understanding of the γ-ray production processes at high energies. Moreover, the detection of unknown sources invisible with other techniques is not discarded.

Due to its relevance, the search for point sources has been one of the first physics analysis performed with the 2007 data of the ANTARES detector. As it has been discussed in the previous chapter, 314 events survived the cuts applied to the data sample chosen for our analysis. The results obtained searching for point sources using a binned technique are presented in this chapter.

6.1   Point source search methods

The reconstructed and selected events in our sample are supposed to come from an isotropic flux of atmospheric neutrinos, with a small fraction of atmospheric muon contamination, and (potentially) from diffuse cosmic fluxes. Drawing all those events in a sky map they lead to an approximately isotropic distribution. Embedded in this sky map there could be accumulations of events coming from fixed positions in the sky corresponding to cosmic neutrino emitters. Due to the small number of expected events, it is of the utmost importance to have an efficient method able to point out accumulations of events coming from the cosmic neutrino sources. In this sense, different search algorithms were implemented by the collaboration in order to extract the max-

Chapter 6. Flux limits for point sources

imum information from the data. The search methods for point sources can be divided into binned and unbinned methods.

6.1.1 Binned methods

The binned methods are based on the counting of events inside a particular region or bin (n_{obs}). Typically, two approaches are followed in the binned method analysis: grid and cluster. In the grid method, the sky is divided in a grid of bins using the declination and right ascension coordinates. Accumulations of events are searched in each bin of the grid. In the cluster approach, the search for an excess of events is made using cones of a given size centered around each of the events of the sample. A point source can be claimed, within a certain confidence level, if there is a significant excess of events inside a cone or a bin with respect to the background. The number of background events inside a bin follows a Poisson distribution with mean n_b. Therefore, the probability to observe n_{obs} events in the same bin where the background is n_b is given by:

$$P(n_{obs}, n_b) = \frac{n_b^{n_{obs}} e^{-n_b}}{n_{obs}!} \qquad (6.1)$$

From this test statistic we can obtained the so-called p-value. By definition, the p-value is the probability of obtaining a result compatible with the one actually obtained, under the assumption of the hypothesis that all the observed events are background events. In the binned methods it means the probability to find n_{obs} events or more from background inside the search bin. The binned search analysis of the ANTARES data presented in this work is made using cones of a given size. This size and the location in the sky of the cone center depends on the analysis performed (fixed list or all-sky) as it will be explained in the following sections.

Other binned techniques as for instance those based on a grid are extensively described in [119].

6.1.2 Unbinned methods

The unbinned methods take advantage of all the available information such as energy and space distribution of the events, as well as any other relevant information to discriminate the signal with respect to the background. This makes them more powerful and sensitive than the binned methods. In the unbinned methods, both signal and background events have an associated probability distribution. The compatibility of the data is evaluated with two hypothesis, only background and background plus signal. The methods maximize the likelihood, and use a continuous test statistic, which is often a sort of likelihood ratio. As in the binned methods, this test statistic gives the probability of a cluster to be produced by the background.

146

Currently two unbinned methods are used for the analysis of the ANTARES 2007 data. One method is based on the Expectation Maximization (EM) algorithm [120] which is a pattern recognition algorithm that maximizes analytically the likelihood in finite mixture models. These mixture models are different groups of data described by different density components (data and background). The EM uses a pre-clustering algorithm in order to find a set of candidate clusters that exceed a given number of events. The algorithm is applied to these pre-selected clusters. The other unbinned method is based on the maximization of a likelihood ratio. This method was studied extensively for the ANTARES in [114]. Two point source analyses have been performed with the 2007 data sample, one based in a selected source of sources which are good candidates to be cosmic neutrino emitters. And the other analysis does not considers any assumption in the source location, therefore, it is a full sky search.

6.2 Fixed point sources search

The first analysis consists in searching neutrinos coming from fixed directions in the sky where, according to the observation of a luminous source in other counterpart messengers (gamma, X-ray, proton, etc.), are good candidates for neutrino emission. As in the cut selection of the final data sample, the analysis procedure has been carried out following a blinding policy and the list of potential cosmic neutrino emitters has been chosen *a priori*.

6.2.1 Blind analysis

In order to perform the analysis optimization, the only piece of information needed from real data is the declination coordinate of each event since keeping the right ascension coordinate unknown, the blindness is preserved. In this way, the cone size optimization is computed without bias. Once the analysis optimization is performed, the data are unblinded and the distribution of the neutrino events collected in the real data sample is compared with the source list in order to check if an excess within a certain confidence level is present.

Flux limits

Assuming that we know the predicted neutrino flux from a source, $\Phi(E, \alpha, \delta)$, our effective area is given by $A_{eff}(E, \alpha, \delta)$ and the duration of our data sample is $T(\delta)$, we can obtain the predicted number of events (n_s) with the simple equation:

$$n_s = \Phi(E, \alpha, \delta) \times A_{eff}(E, \alpha, \delta) \times T(\delta) \times \epsilon(\alpha, \delta) \qquad (6.2)$$

Chapter 6. Flux limits for point sources
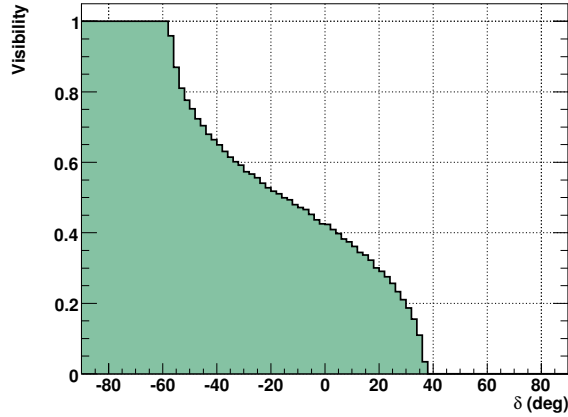
Figure 6.1: *Visibility for the 2007 data period as a function of the declination angle once the cut on elevation has been applied.*

where E represents the neutrino energy and α, and δ are the equatorial coordinates (right ascension and declination) of the source location. The dependence of the time on the source declination ($T(\delta)$) comes from the visibility, which means the fraction of time a sky position can be seen from a given location in the Earth. Finally, the reconstruction method efficiency term, $\epsilon(\alpha, \delta)$, accounts for the probability that the muon track will be reconstructed in the same cone than the original neutrino.

The final visibility for our analysis is shown in Fig. 6.1. Due to the elevation cut applied at -10° to our selected data sample, the visibility of ANTARES is reduced.

Once the experiment is performed, the number of events detected (n_{obs}) is compared with the number of events expected from background (n_b) in the same period of time. In the case that no discovery may be claimed, a flux upper limit is set. Comparing the values of n_{obs} and n_b, an upper limit in the number of events ($\mu_{90}(n_{obs}, n_b)$) can be computed following the Feldman-Cousins unified approach [121]. In this case, the 90% CL limit on the source flux is given by:

$$\Phi(E, \alpha, \delta)_{90\%} = \frac{\mu_{90}(n_{obs}, n_b)}{\epsilon(\alpha, \delta) A_{eff}(E, \alpha, \delta) T(\delta)} \tag{6.3}$$

By means of the Equation 6.2, 90% CL the flux limit can be written as a function of the source flux using the expected number of events n_s:

$$\Phi(E,\alpha,\delta)_{90\%} = \frac{\mu_{90}(n_{obs},n_b)}{n_s}\Phi(E,\alpha,\delta) \qquad (6.4)$$

Thus, the factor $\mu_{90}(n_{obs},n_b)/n_s$ constrains the source flux emission. This can only be calculated once the experiment has been performed. Therefore, in order to optimize the selection cuts of the analysis we should use an equivalent factor which does not depend on the observed data and could be used *a priori*. This factor is the so-called Model Rejection Factor (MRF) in which the upper limit in the number of events $\mu_{90}(n_{obs},n_b)$ is replaced by the average upper limit ($\bar{\mu}_{90}$), also known as sensitivity [122], which is the average of all the possibles upper limits weighted by their Poisson probability.

$$\bar{\mu}_{90}(n_b) = \sum_{n_{obs}=0}^{\infty} \mu_{90}(n_{obs},n_b)\frac{n_b^{n_{obs}}e^{-n_b}}{n_{obs}!} \qquad (6.5)$$

Therefore, the MRF definition can be written as:

$$MRF = \frac{\bar{\mu}_{90}(n_b)}{n_s} \qquad (6.6)$$

Cone size optimization

The cone size optimization is based on the minimization of the MRF, i.e., the selected cone size for a given source location will be the one providing the minimum MRF. We have seen that the two pieces of information involved in the MRF are the $\bar{\mu}_{90}$, and the expected signal from the source (n_s). The $\bar{\mu}_{90}$ depends only on the background events (Eq. 6.5) which is obtained directly from our sample for each declination. Figure 6.2 shows the declination distribution of the data sample selected after applying a $\chi^2 < 1.8$ cut. In order to minimize the statistic fluctuations a polynomial fit to the distribution has been performed.

The estimation of the signal is obtained from the point spread function (PSF), i.e., the angular resolution. In Figure 6.3 (left) the PSF with respect to the declination angle is shown in a 3D graph. The PSF for each declination angle is taken as the corresponding slice of this 3D graph. An example for a declination of -28.4° is shown in Fig. 6.3 (right). This plot shows that the 50% of the tracks have an angular error better than 1°. A more restrictive cut in the number of lines considered in the reconstruction, cleans up the second peak.

The MRF is computed for ten different declination bands ranging from -90° to 47°. However, due to the lack of background statistic in the boundaries for the background and to the bad angular resolution at these declinations (see Figure 5.12), the plots are only shown in the range from -76° to 20° . As we will see later all the sources in the list are within this range.

Chapter 6. Flux limits for point sources
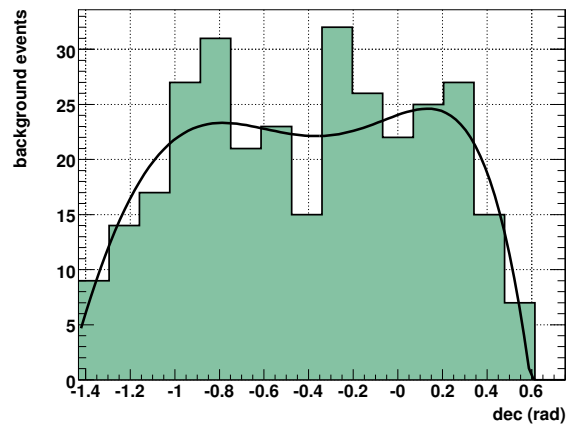
Figure 6.2: *The declination distribution of the remaining data events after applying the $\chi^2 < 1.8$ and elevation quality cut. A polynomial fit is superimposed.*
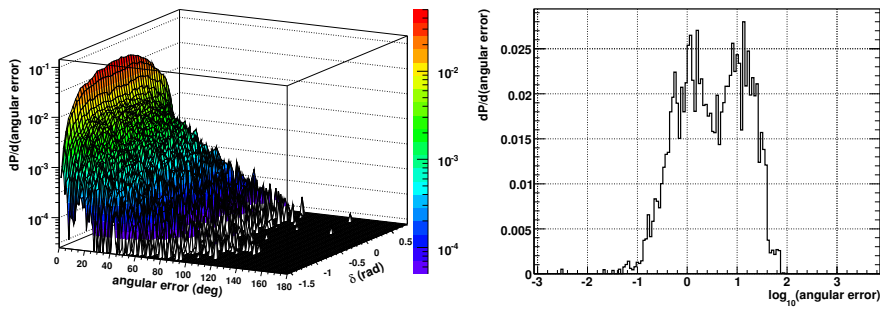
Figure 6.3: *On the left, the point spread function (PSF) for different declinations in a 3D graph. On the right, a slice of the PSF plot for a given declination, δ=-28.4˚.*

The expected number of background and signal events depends on the size of the cone as is shown in Fig. 6.4. On the left, the number of background events included in the cone as a function of the cone size is shown. The figure on the right shows the fraction of signal events contained in the same cone. The cone size changes from 0° to 10° in 0.2° steps. The MRF obtained
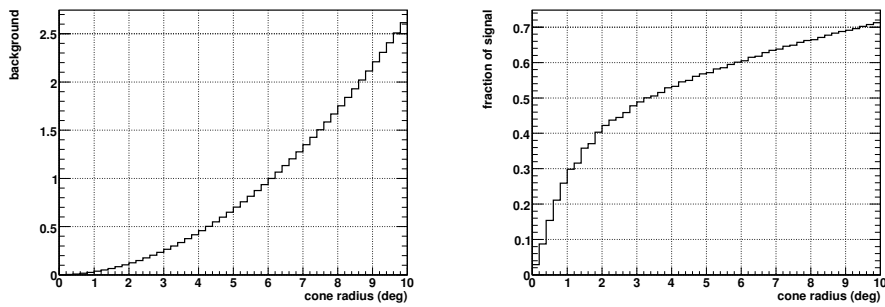
Figure 6.4: *Number of background events (left side) and fraction of signal events expected inside a search cone as a function of the cone radius. In both cases, the declination is δ=-28.4°.*

in the example of Fig. 6.4 can be seen in Fig. 6.5. The best cone size is the one providing the minimum MRF, $\sim$ 4.8° in this case. The minimum MRF obtained for all the declinations bands analyzed are shown in Fig. 6.6. Finally, the optimum cone size obtained for every declination angle is shown in Fig. 6.7. The size of our search cone ranges from 4° to 5° . The expected number of background and signal events inside the optimum cone as a function of the declination is shown in Fig. 6.8. An average of 0.6 events are expected depending on the declination.

Cone method sensitivities

Once we have computed the optimum cone size for each declination band, we can obtain the sensitivity for different cuts based on the χ^2 figure of merit (see section 5.2.1). Moreover, comparing the sensitivities for these different χ^2 cuts, we can find out the χ^2 cut which provides the best sensitivity. Figure 6.9 shows the computed sensitivity as a function of the declination for different χ^2 quality cuts. These sensitivities have been computed using the averaged effective area presented in the previous chapter, therefore the flux shown in the plot has been integrated for energies ranging from 10 GeV to 10 PeV. Unlike the sensitivity plots presented in this subsection, the final upper limit results,

Chapter 6. Flux limits for point sources
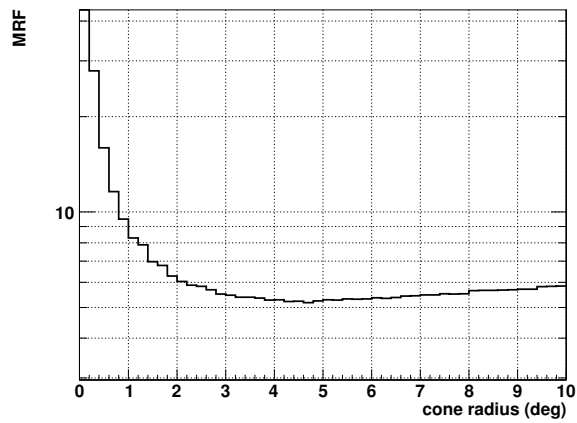
Figure 6.5: *The computed MRF as a function of the cone size for a particular declination angle δ=-28.4°. The best cone is found to be ∼ 4.8°.*
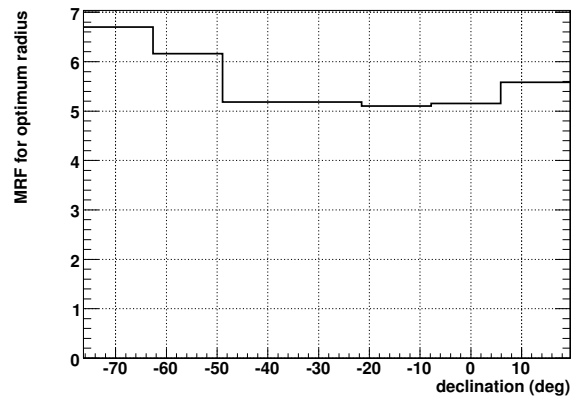
Figure 6.6: *Minimum MRF obtained for the different declination bands used in the analysis.*
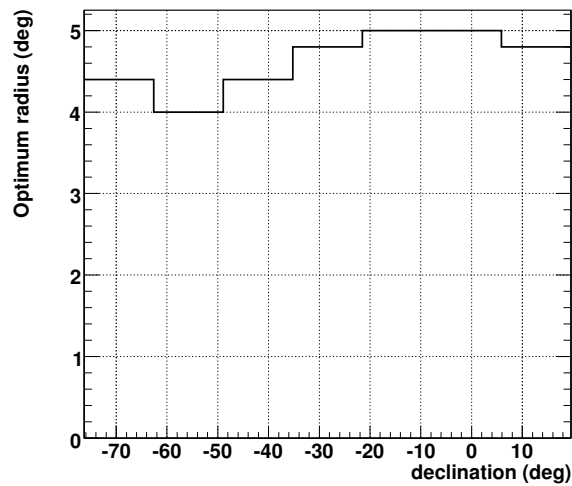
Figure 6.7: *Best search cone size for the different declination bands used in the analysis. The average search cone size is $\sim 4.5°$.*
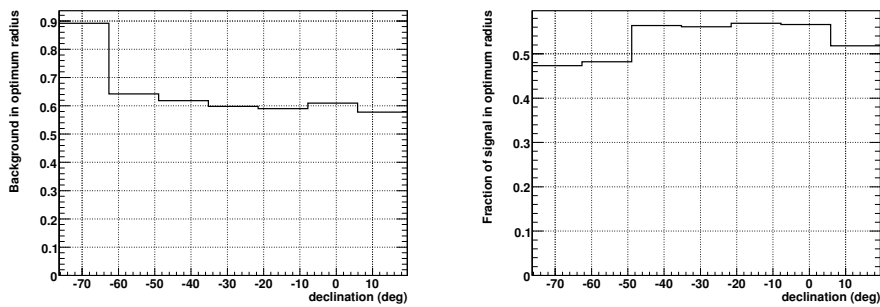
Figure 6.8: *Expected number of background events (left) and fraction of expected signal (right) inside the optimum search cone for the different declination bands.*

Chapter 6. Flux limits for point sources
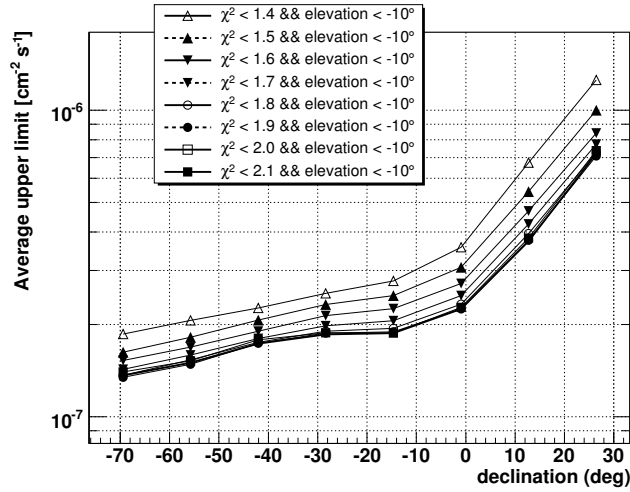
Figure 6.9: *Sensitivity, as a function of the declination angle, for different cuts on χ^2. The sensitivity improves up to a cut on 1.8-2.0 and then it starts to get worse. The final cut selected for our analysis is $\chi^2 < 1.8$.*

with the data already unblinded, will be presented as differential flux in order to be compared with other experiments.

The chosen cut is the one providing the best sensitivity. According to the Fig. 6.9, the sensitivity improves up to a cut on 1.9 and it is getting worse for cut values higher than 2.1. Therefore, the best cut should be in the interval ranging from 1.8 to 2.0. As we will see, for the all-sky search analysis the optimum χ^2 quality cut is $\chi^2 < 1.8$. Therefore, for the sake of simplicity it was agreed to choose the same cut for both fixed source and all-sky search analysis. As we have discussed previously, the chosen cut gives a final sample of 314 events.

Systematic error estimation

In the previous subsection, we have computed the sensitivities for the binned method without taking into account the uncertainties in the signal efficiency and in the background estimation. These uncertainties can be included modifying the probability density function (PDF) describing the statistical processes of interest, in our case, the probability to obtain a given number of events inside a cone for a given expected background. Following the treatment

presented in [123] the modified PDF becomes:

$$q(n)_{s+b} = \frac{1}{2\pi\sigma_b\sigma_\epsilon} \int_0^\infty \int_0^\infty p(n)_{b'+\epsilon's} \times e^{-(b-b')^2/2\sigma_b^2} e^{-(1-\epsilon')^2/2\sigma_\epsilon^2} db'd\epsilon', \quad (6.7)$$

where b represents the background and ϵ the efficiency, being $p(n)$ the prior PDF. The error distribution is described by a Gaussian function.

The systematics uncertainties due to a non-perfect knowledge of the detector have been described in detail for muons in [124]. For our analysis we have considered the following contributions. Firstly, there is the uncertainty on the light absorption length in water which is assumed to be $\pm 10\%$ over the whole wavelength spectrum, leading to a $\pm 20\%$ uncertainty in the number of expected events. Secondly, the detection efficiency of the PMTs. The acceptance for Cherenkov photons impacting the PMT at small angles with respect to the PMT axis is determined with an uncertainty of $\pm 15\%$. Thirdly, the theoretical model uncertainty is assumed to be 20%. Finally, the data-MC discrepancy is of the order of 10% as it was shown in the previous chapter. Taking into account all the pieces of information we considered an overall uncertainty of 30% in the signal detection efficiency. The background uncertainty is supposed to have a much smaller effect since it is estimated from the data itself, so it has not been considered. The sensitivities computed taking into account the systematic errors using the public routines published in [123] are shown in Figure 6.10. As it can be noticed, an uncertainty of 30% in the signal efficiency has an impact of 10% in the sensitivity.

In order to check the robustness of our sensitivity estimation, a further test including the uncertainty in the angular resolution has been performed. First, we have assumed an angular resolution 10% worse than the prediction from the MC, based on the small differences in the data and MC time residual distributions. Second, we have also considered a more extreme case of 50% worsening. Figure 6.11 shows the sensitivities for the predicted angular resolution and the modified ones. The impact is negligible using a 10% worse angular resolution, and in the 50% case, the predicted sensitivity only changes by a 10%. The absolute pointing precision is estimated to be about 0.2 degrees according to studies based on the measurements of line positions and orientations using GPS.

In addition, it has been also estimated the effect of the elevation cut (elevation $<$ -10°) taken as default in the analysis. According to the Figure 6.12 even removing a significant number of events the sensitivity is not worsened significantly.

Considering all the aforementioned facts, the final limits presented in this chapter will take into account the combined effect of 30% in the signal detection efficiency plus 10% in the angular resolution, which can be considered as conservative.

Chapter 6. Flux limits for point sources
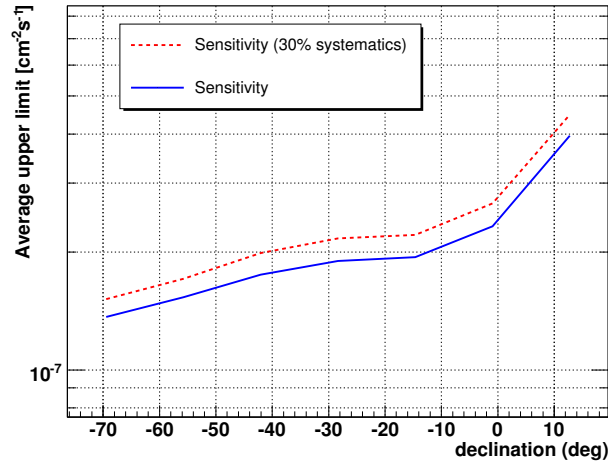
Figure 6.10: *Sensitivity as a function of the declination computed with (dashed line) and without (solid line) taking into account a systematic error on the efficiency of 30%. In both cases, the cut on the quality parameter is $\chi^2 < 1.8$. The influence is of the order of $\sim 15\%$.*
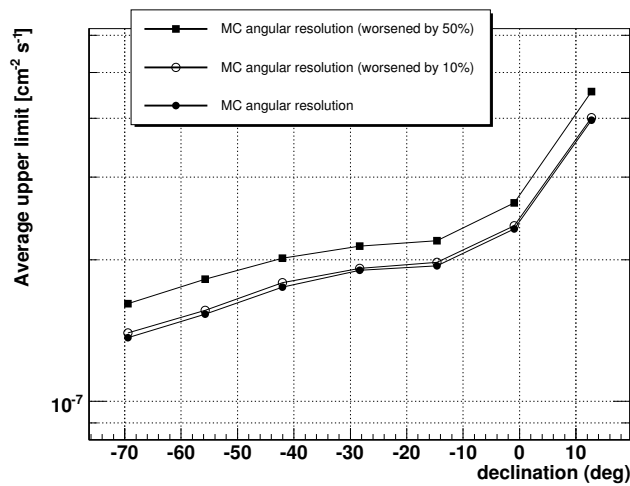
Figure 6.11: *Sensitivities computed with a 10% and 50% worsen angular resolution. The chosen cut is again $\chi^2 < 1.8$.*
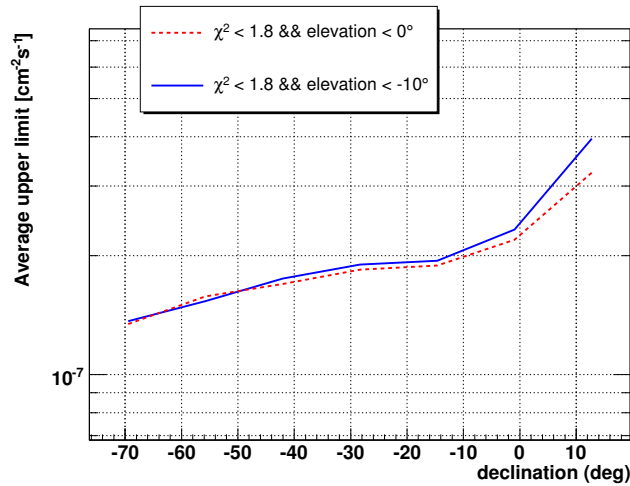
Figure 6.12: *Sensitivities computed with different elevation cuts.*

6.2.2   List of potential sources

The sources chosen for the 2007 data analysis are the result of a specific selection extracted from a more extensive list elaborated for the complete 12-lines detector [125]. The three main criterion for the full-detector selection were: the selected sources have VHE γ-ray emission (i.e. E > 0.1 TeV) and is well explained by the hadronic models. The sources must be seen as up-going for ANTARES. The angular separation between sources should not be smaller than the ANTARES angular resolution (0.3° at 10 TeV). This last condition was slightly modified for the 2007 data analysis fixed source list. In this case, the criteria is having sources with an angular distance larger than 3° which is the expected angular resolution with the Online Strategy at high energies. The sources are considered only as one location in the sky keeping the coordinates of the most promising candidates.

Finally, a total of 24 candidates sources (galactic and extragalactic) were selected as the most promising candidates to be detected with the 2007 data sample. The 24 sources are listed in the Table 6.1.

Data challenges

Once the optimization process has been performed, there is still room to carry out some cross-checks before unblinding the data. A standard test consist in the so-called "data challenges" test, where a simulated sample is used in order

Chapter 6. Flux limits for point sources

to test the developed software tools to obtain the unblinded results. Several data challenges has been performed. In this section, we mention one of them which uses a random sample of 314 events. It is formed by events with the real declination but scrambled in right ascension using a uniform distribution from -10° to 10° centred on the real coordinate. Using this kind of tests, we can look for accumulations caused by the background and estimate the trial factors to be considered when the real data will be unblinded.

In this example, the most significant source has a p-value of 0.026, with three events observed in the cone. This is the so-called pre-trial p-value, since we still have not taken into account the fact that we are looking at more than one source. This value can be corrected in order to estimate which is the probability of obtaining a given p-value at least in one cone, when using several search cones. This corrected probability is the so-called post-trial p-value. It is usually computed using simulations of many experiments reproducing the original one. In the cases where the pre-trial p-value is very small, for instance, when a source candidate is detected, we can assume that the probability of detecting more than two excesses in the same sample is negligible and then, a good approximation of the post-trial p-value can be easily obtained multiplying the pre-trial p-value by the number of search cones used.

For the data challenge case we have performed a simulation in order to assess the significance of the generated sample. The simulation took into account the real expected background, i.e., inside each cone the events were simulated according to a Poisson distribution using the expected number of background events computed in the analysis as the mean of the distribution.

The results obtained are compatible with the background fluctuations.

6.2.3 Results

After the data unblinding, the true equatorial coordinates of the 2007 data sample become available. The resulting sky map showing the real coordinates of the 314 selected events is shown in Figure 6.13. The software tools previously tested are used now with the real data sample. The results are summarized in Table 6.1. The table shows the list of sources with its position in the sky (δ, α), the number of background events expected in the optimum search cone (n_b), the number of observed events inside the cone (n_{obs}), the p-value (p) and the corresponding upper limit at 90% C.L. (ϕ_{90}) obtained with the binned method. The upper limit value is the normalization constant of the differential muon-neutrino flux assuming a E^{-2} spectrum (i.e. $E^2 d\phi_{\nu_\mu}/dE \leq \phi_{90} \times 10^{-2}$ GeV m^{-2} s^{-1}).

It is important to notice that after the data unblinding, the n_b is computed from the real data and not from a fitted function. The procedure is done in the following way. In order to avoid a bias in a case a source signal is present in the cone, the number of expected background events is computed from the total
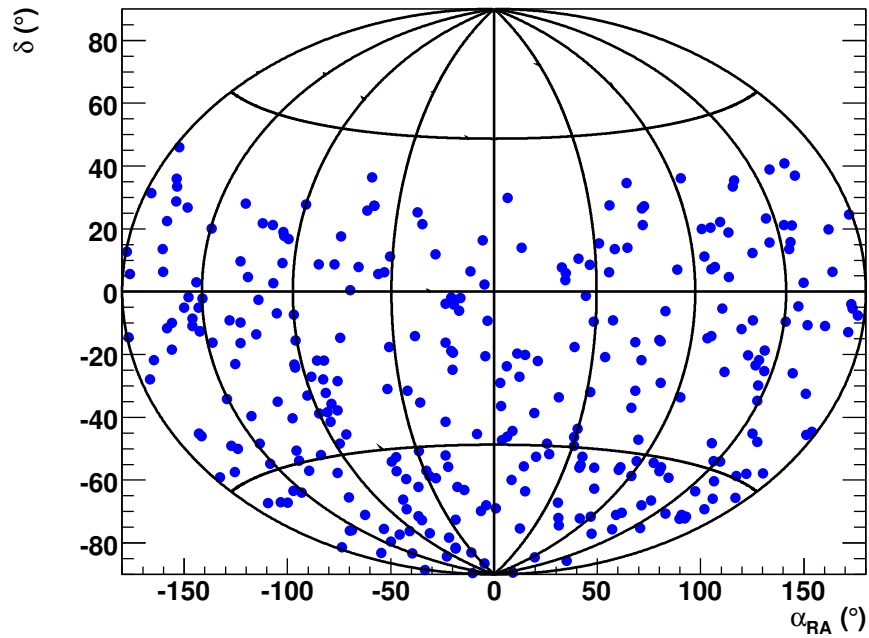
Figure 6.13: *Sky map in equatorial coordinates (right ascension vs declination) with the 314 events selected for the point source analysis from the 2007 data sample.*

Chapter 6. Flux limits for point sources
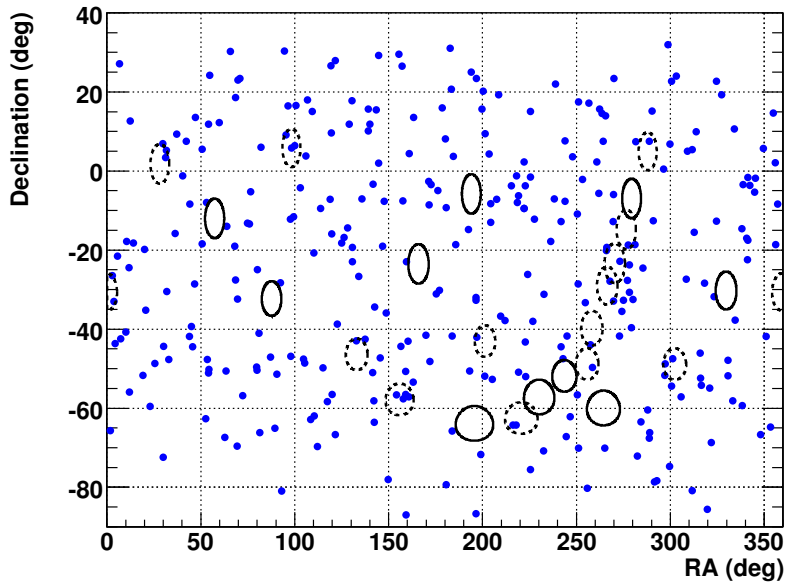
Figure 6.14: *Unblinded sky map with the cones used by the bin method. The cones containing some events inside are plotted with a discontinuous line.*

number of events within the corresponding declination band, but subtracting the events inside the cone.

The number of events inside the 24 cones is 22 while the average expected from the background is 17. Therefore, this is suppose to happen in 14% of the simulated experiments.

It is important to notice that the p-values presented in the table are "pre-trial" values which should be corrected in order to provide a proper evaluation of the observed excess. The lowest p-value obtained correspond to the HESS J1023-575 source with a p-value of 0.0015. Performing 10^4 experiments the probability of obtaining this p-value or better in any of the sources of the list is 3.3% which means a significance of 2.1σ. The second lowest p-value is obtained in the HESS J0632+057 source with 0.026.

The final sky map including the search cones centered in the source list locations is shown in Fig. 6.14. The size of the cone comes from the MRF optimization explained in section 6.2.1.

Not having found any significant excess, the upper limits for all the sources in the list are computed. The systematic uncertainties (30% in the signal

Source name	δ (°)	α(°)	n_b	n_{obs}	p-value	ϕ_{90}
PSR B1259-63	-63.83	195.70	0.96	0	1	0.86
RCW 86	-62.48	220.68	0.59	2	0.12	2.87
HESS J1023-575	-57.76	155.83	0.47	4	0.0015	4.85
CIR X-1	-57.17	230.17	0.70	0	1	0.95
HESS J1614-518	-51.82	243.58	0.81	0	1	1.38
GX 339	-48.79	255.70	0.87	1	0.59	2.33
RX J0852.0-4622	-46.37	133.00	0.73	1	0.52	2.58
RX J1713.7-3946	-39.75	258.25	0.62	1	0.46	2.67
PKS 2155-304	-30.22	329.72	0.65	0	1	1.35
Galactic Center	-29.01	266.42	0.66	1	0.49	2.7
W28	-23.34	270.43	0.71	1	0.51	2.64
LS 5039	-14.83	276.56	0.76	1	0.54	2.64
HESS J1837-069	-6.95	279.41	0.77	0	1	1.51
SS 433	4.98	287.96	0.65	1	0.48	3.9
HESS J0632+057	5.81	98.24	0.62	3	0.025	7.72
ESO 139-G12	-59.94	264.41	0.92	0	1	0.87
PKS 2005-489	-48.82	302.37	0.84	2	0.21	3.61
Centaurus A	-43.02	201.36	0.56	1	0.43	2.71
PKS 0548-322	-32.27	87.67	0.51	0	1	1.41
H 2356-309	-30.63	359.78	0.65	1	0.48	2.64
1ES 1101-232	-23.49	165.91	0.71	0	1	1.36
1ES 0347-121	-11.99	57.35	0.85	0	1	1.41
3C 279	-5.79	194.05	0.83	0	1	1.52
RGB J0152+017	1.79	28.17	0.56	2	0.11	5.54

Table 6.1: *List of the 24 cosmic neutrino source candidates with their corresponding location in the sky. The results given are the number of expected background events inside the cone (n_b), the number of detected events (n_{obs}), the p-value, and the normalization constant of the differential muon-neutrino flux assuming a E^{-2} spectrum (i.e. $E^2 d\phi_{\nu_\mu}/dE \leq \phi_{90} \times 10^{-2}$ GeV m^{-2} s^{-1}).*

Chapter 6. Flux limits for point sources
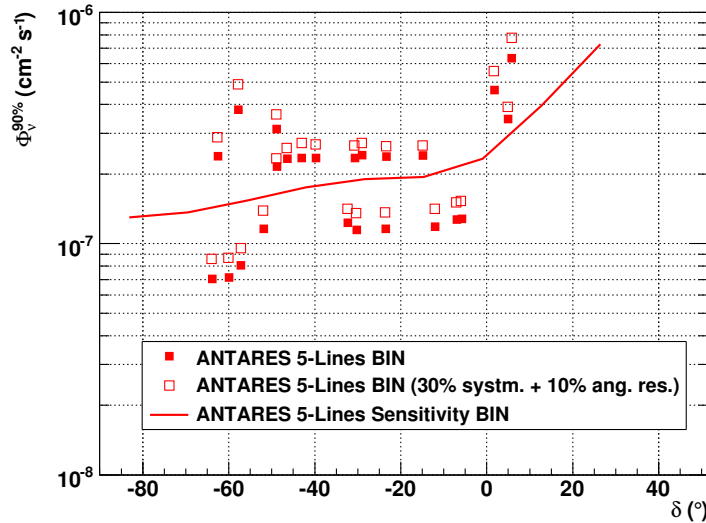
Figure 6.15: *Upper limits obtained with the 2007 data sample using the binned method. The solid squares are the limits without errors. The empty squares are the upper limits considering the systematic uncertainties. The line represents the sensitivity previously computed.*

detection efficiency plus 10% in the angular resolution) have been taken into account when computing these upper limits. The effect of the systematic errors can be seen in Figure 6.15.

In order not to depend on an arbitrary integration energy range, unlike the previous plots presented, the final limits compared with other experiments are presented as differential fluxes in Figure 6.16. As can be seen in this plot, the limits obtained with the 2007 ANTARES data are comparable with those provided by previous experiments also looking at the Southern sky. This is mainly because of the large effective area of ANTARES for high energies (10 - 100 TeV). A significant improvement is expected with the complete detector (solid line).

6.3   All-sky scan

The second point binned search analysis with the 2007 data performs an all-sky scanning where no assumption about the source location is considered. In this case, the main advantage is that any neutrino source can be detected
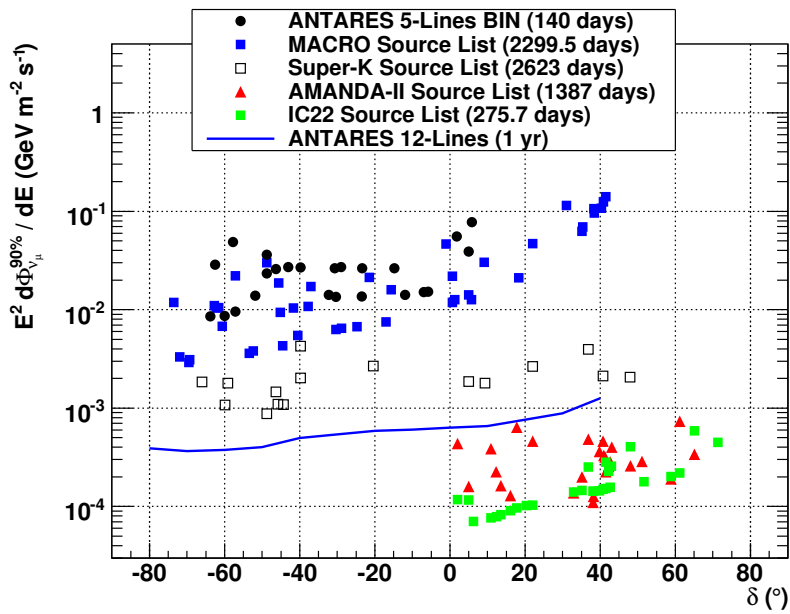
Figure 6.16: *Upper limits obtained with the 2007 data sample (5 lines, 140 days of live-time), compared with the expectation of 1 year with the complete detector (12 lines), and with the results from other experiments.*

Chapter 6. Flux limits for point sources

including unknown sources without counterparts in other emissions. The main drawback is that more significance is needed in order to claim for a discovery since, as we will see, we have to pay the price of a larger trial factor penalty.

6.3.1 Blind analysis

As it was done in the fixed source search, the all-sky analysis also requires a blind process for the optimization of the selection cuts *a priori*. Instead of looking at a few location in the skymap, the search algorithm for a all-sky survey looks at every locations where there is a detected event. Due to the number of events and the size of the cones, the overlapping among several cones is possible. In case of overlapping, we chose the cone with the largest significance in terms of p-value. The optimization of the cone size is based on the discovery potential rather than on the MRF, in order to be more efficient to a source discovery. The selection cut providing the lowest discovery flux will be chosen as the final cut for the analysis. As we have explained before, we are going to use the same data sample of 314 events which has been used for the fixed point source search.

Discovery potential

In an all-sky search, a number of observed events higher than the expected background for a given location in the sky is needed in order to claim for a discovery. In the cone search method, once the experiment is performed, the probability to observe a number of events n_{obs}, or higher from the background is given by the p-value computed for each cone. In this analysis we can fix the minimum probability (p-value) to claim for a discovery and then, optimize the best cone search size in order to minimize the required signal to have such a discovery.

This minimum number of events is n_{crit} which must fulfill that the cumulative Poisson probability (p-value) of detecting n_{crit} or more events if the average background is given by n_b should be lower than a given probability α. This α, or confidence level (CL), is typically expressed in terms of standard deviations (two-sided) of the normal distribution. For instance 3σ and 5σ leads to 2.7×10^{-3} and 5.73×10^{-7} probability, respectively.

Let's assume now that the number of observed events n_{obs} is composed by both background (n_b) and signal (n_s). Then, the strength of the observed signal should be large enough so that $n_b + n_s$ produce the desirable n_{crit} with certain probability. This probability is known as the statistical power (SP). The minimal signal needed to reach the required SP is called the least detectable signal (n_{lds}). In the optimization for a discovery this n_{lds} plays the role of the average upper limit in the MRF computation. By using the n_{lds} we obtain the model discovery potential [126].

All-sky discovery flux

The discovery flux is defined as the minimum flux needed to claim for a point source discovery. It is computed using Eq. 6.3 replacing the 90% CL upper limit by the number of required signal events to reach the discovery threshold. This required number of signal events is obtained from the n_{lds} weighted by the cone efficiency.

The definition of discovery depends on the confidence level and the statistical power. In this work we have chosen a confidence level of 3σ, i.e., the background probability to produce the observed number of events is smaller than 2.7×10^{-3}. We will also include the CL of 5σ for comparison. The statistical power chosen is 50%, which means the odds of being over the CL threshold when using our selection cuts.

The confidence levels must take into account the number of cones used in our analysis. To this end, we divide the $n\sigma$ probability by the number of cones used in the search (N_{cones}). As we are using N_{cones} cones in our search we expect $N_{cones} \times 2.7 \times 10^{-3}$ bins with an excess of 3σ. Therefore, our discovery threshold should be set as $\dfrac{n\sigma}{N_{cones}}$.

Cone size optimization

The cone size optimization is based on the minimization of the discovery factor. The process is analog to the optimization for the fixed source analysis, i.e., the cone size is increased in steps of 0.2° for ten different declination bands ranging from -90° to 47°. Due to the lack of statistics at high declinations, we restrict our search range from -84° to 33°. For each declination band, the discovery potential is computed as it is shown in Fig. 6.17. The minimum of this graph indicates the best cone for the all-sky survey of this declination band. The jumps in the discovery potential are due to discreet behaviour of the n_{crit} value. The result obtained for the whole range of declinations are shown in Fig. 6.18. As can be seen, the average optimum radius is around 2° for most of the declination bands. The cone sizes are smaller than in the case of the fixed source search analysis. Being the cone radius smaller, the number of expected background events inside is also smaller (Fig. 6.19). This value is around 0.1 depending on the declination. It is important to notice that all the plots presented in this subsection have the default quality cut of $\chi^2 < 1.8$ which, as we will see in the next subsection, is the optimum cut for the all-sky analysis.

Discovery flux optimization

We can compute the discovery flux for different values of the χ^2 parameter looking for the lower source flux needed to claim for a discovery. This is shown

Chapter 6. Flux limits for point sources
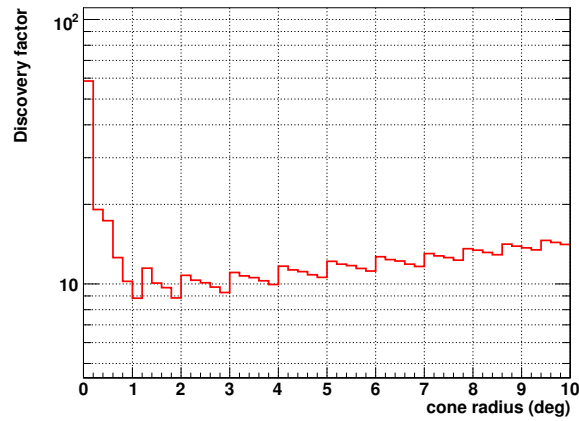
Figure 6.17: *Example of the discovery potential as a function of the cone radius for a particular declination (-28.4°). According to the graph, the optimum cone should have a radius of ∼ 1°, for this particular declination.*
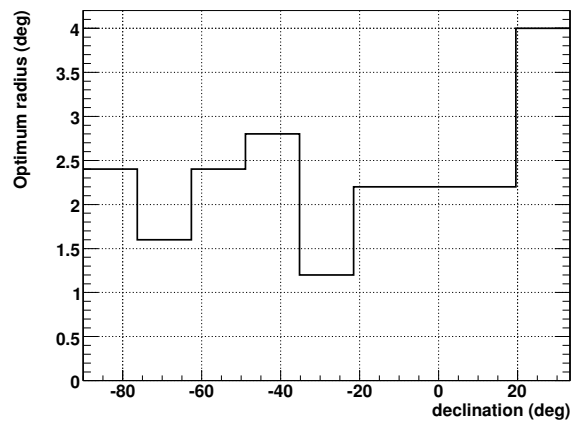
Figure 6.18: *Optimum cone size to be used in an all-sky search for different declinations.*
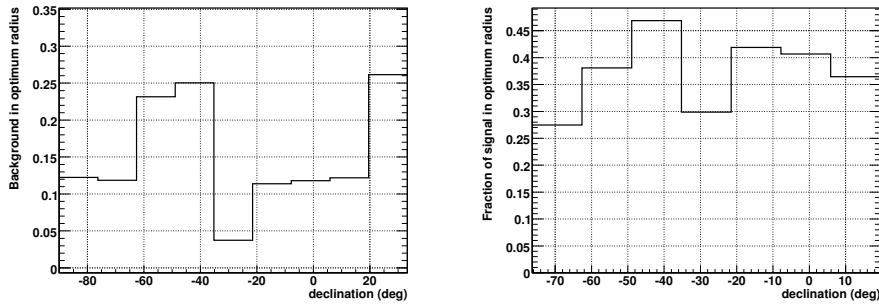
Figure 6.19: *Expected number of background events (left) and fraction of signal (right) expected, inside the optimum cones in all-sky search for different declinations bands.*

in Figure 6.20. The lower flux is reached when taking a cut on the quality parameter as $\chi^2 < 1.8$. Again, the flux has been computed using the averaged effective area presented in the previous chapter, therefore the discovery flux presented in the plot has integrated the E^{-2} spectrum over the 10 GeV - 10 PeV energy range.

Once we have fixed the quality cut for our analysis, we can estimate the number of events inside the optimum search cone required to obtain a discovery for a given declination. This is shown in Fig. 6.21 where according to the plot, for a CL of 3σ and a SP of 50% we need at least 3-5 events inside the cone to produce such an excess. In case of choosing a CL of 5σ then, 6-7 events are needed. In case of a 3σ excess, we will refer to it as an "evidence" while a 5σ excess will be considered as a "discovery". Moreover, we have to take into account that not all the neutrino events emitted by the cosmic source will be inside the search cone because of the cone efficiency, which comes from the non-optimal angular resolution of the reconstruction strategy used. After corrections by the cone efficiency. The number of neutrino events emitted by the source needed to claim for a discovery ranges from 9-13, considering a CL of 3σ, and 14-20 considering a CL of 5σ, as it is shown in Figure 6.22

We can also compare the sensitivity (flux limit) obtained in the fixed source searches with the discovery fluxes obtained in this analysis. This is shown in Fig. 6.23. As expected, the discovery fluxes should not be lower than the sensitivity since the sensitivity has been optimized to be as low as possible. Therefore, a source emitting with a flux so that the flux arriving at the Earth is lower than the detector sensitivity will not be visible. On the contrary, if this flux is between the sensitivity and the discovery flux, will be considered

Chapter 6. Flux limits for point sources
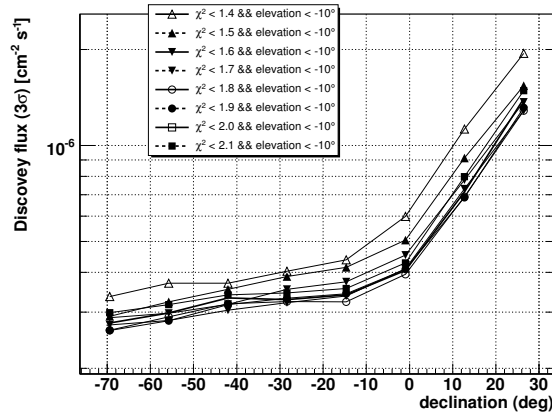
Figure 6.20: *Discovery flux as a function of the declination for different cuts on χ^2. The lower flux is reached for the quality cut $\chi^2 < 1.8$.*
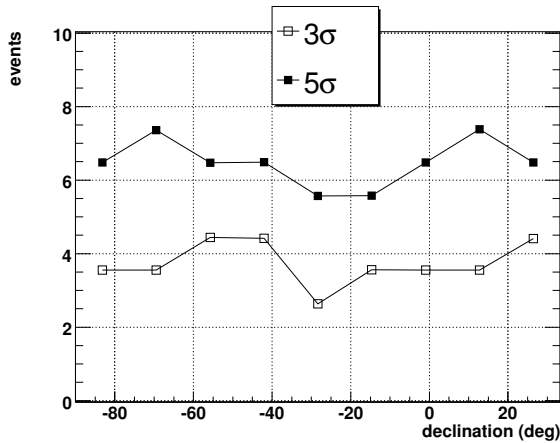
Figure 6.21: *Number of events inside the optimum search cone required to obtain a discovery for a CL of 3σ and 5σ as a function of the declination angle. The SP has been fixed to be 50%.*
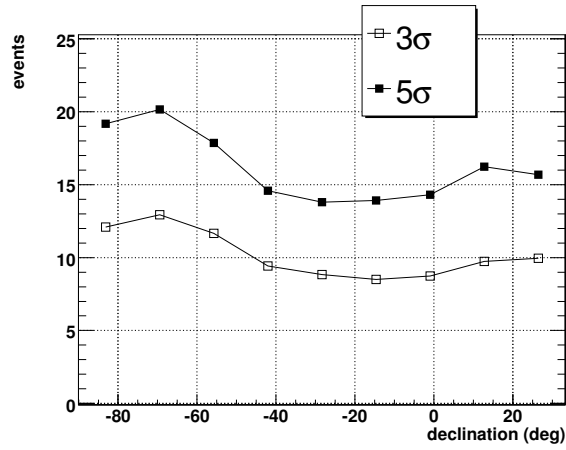
Figure 6.22: *Number of events emitted by the cosmic source required to obtain a discovery for a CL of 3σ and 5σ as a function of the declination angle. The SP has been fixed to be 50%.*
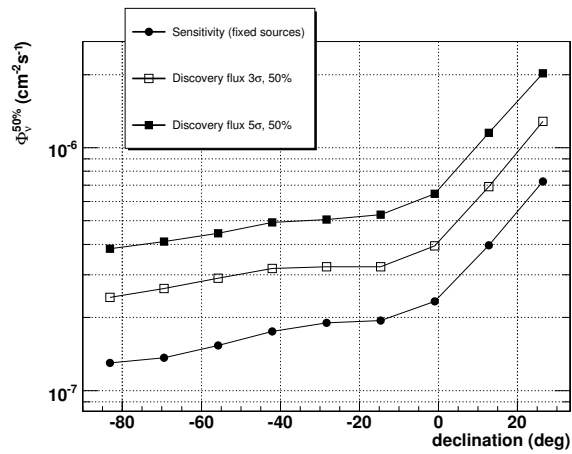
Figure 6.23: *Comparison between the flux limits (sensitivity) and discovery fluxes for a CL of 3σ and 5σ and a SP of 50%.*

Chapter 6. Flux limits for point sources

as candidates. Finally, if the flux from the source is higher than the discovery flux will be considered as a discovery with a certain CL and SP.

Data challenges

As in the fixed source search, we can test our software tools before unblinding the data. In this case, the data challenge consists of simulating a source signal embedded in a random sample. The cone sizes used in this test are the ones obtained from the optimization procedure. It is important to remark that including a source *a posteriori* in our sample is going to change a little bit the declination distribution leading to slightly different values for the optimum cones. In any case, the entailed changes are small and are not relevant for the aim of the test.

The generated sample included a source emitting 10 events at a location of (-10.0, 195.7), which according to Fig. 6.22 is enough to lead for an evidence (3σ excess). The software tools found a cluster of 4 source events at (-10.22, 196.5) which led to a 3σ excess in agreement with Fig. 6.21.

6.3.2   Results

In the all-sky scan we do not make any *a priori* assumption about the source location in the sky. The search is performed looking at all the events. The most significant excess is found at (δ = -57.7°, α = 157.8°). That cone contains 3 events apart from the one used to define the center of the cone. These are the same events that have been found in the fixed source search. The p-value obtained in that case was 0.0015. In this case, as we are looking at several locations in the sky the trial factor is higher and the post trial p-value becomes 0.34 which corresponds to less than 1σ excess, being compatible with the background fluctuations. The sky map is shown in Fig. 6.24, and a zoom of the most significant cone is shown at Fig. 6.25.

Finally, the unblinded sky map is presented as a significance map in Figure 6.26. The map is divided into grids of 1°× 1°, and the significance, defined as $S = -log_{10}(p-value)$, is given using a color code. The hottest spot is found at (δ=-56°, α=157°) with a significance of roughly 4.0, in agreement with the previous results.

6.4   Conclusions

The ANTARES neutrino telescope has been completed and is taking data smoothly. The first analysis searching for point cosmic sources has been performed with the 2007 data sample where 5 out of the total 12 lines were taking data. A sample of 314 events were selected after the optimization of the cuts
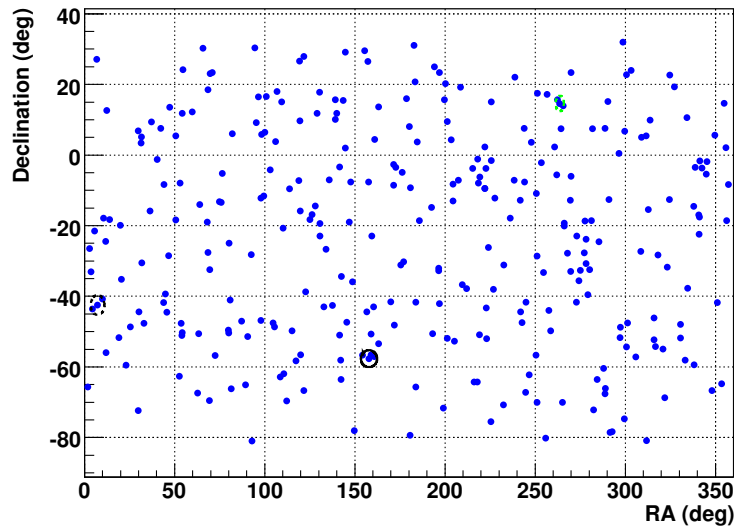
Figure 6.24: *The plot shows the sky map obtained after the all sky analysis with the final unblinded data. The most significant cone gives a pre-trial p-value of 0.0015 which, after post-trial, is compatible with background fluctuations.*
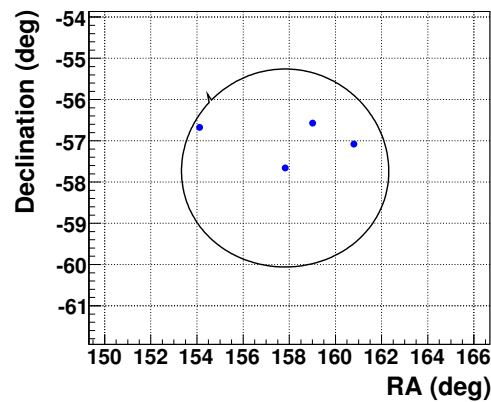
Figure 6.25: *The plot shows a zoom of the most significant cone which contains 3 events apart from the one used to define the cone.*

Chapter 6. Flux limits for point sources
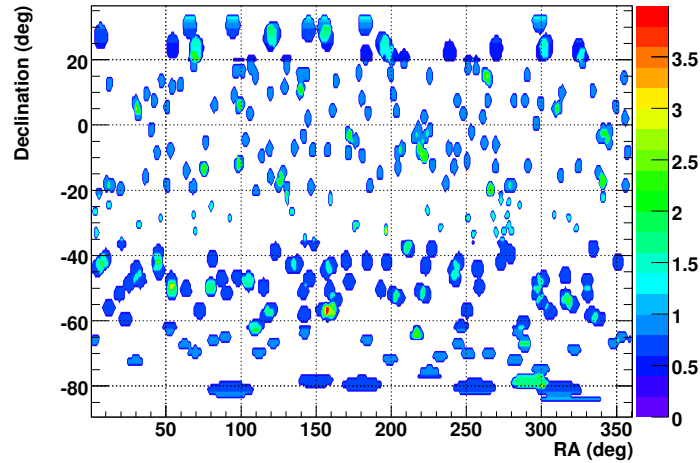
Figure 6.26: *Significance sky map with the 314 events data sample. The most significant spot is found at (δ=-56°, α=157°).*

on a blinded data. We have performed the search by a binned method based on cone shaped bins. Two analyses were performed. In the first one a list of potential candidate sources were selected. No significant excess was detected for any of them, being the most significant one the HESS J1023-575 with a pre-trial p-value of 0.0015 which post-trial becomes a 2.1σ (double sided) significance. With this result, the corresponding flux limits where obtained taking into account the systematic uncertainties due to a non-perfect knowledge of the detector. These limits were compared with the results from previous experiments.

The second analysis consisted in all-sky search being the most significant excess found at (δ=-57.7°, α=157.8°), with a post trial p-value of 0.34 corresponding to less than 1σ, excess which is compatible with the background fluctuations.

Finally, although none of the two analyses have shown any evidence for cosmic neutrino sources, it is important to point out that the incoming data already with the complete ANTARES detector will improve the present limits or make a discovery.

Conclusions

During the last years the development of the neutrino astronomy has been impressive. The leading project, IceCube, is almost finished and KM3NeT is foreseen to be ready in the incoming years. Both of them will reach the critical km^3 volume detection in order to be sensitive to the predicted neutrino fluxes. This milestone will open a new window to explore the Universe using cosmic neutrinos. The physics topics to be studied are many and very challenging. Among them, one of the most exciting is the search for neutrino point sources. The observation of a cosmic neutrino source in combination with other messengers as photons or cosmic rays will help to understand the high-energy processes involved and to clarify the origin of the most energetic cosmic rays. The main candidates to be a cosmic neutrino source are the AGNs and GRBs which are known to be the most powerful accelerators in the Universe. However, hidden sources without any other cosmic messengers as counterparts are also possible, and their discovery would mean an important impact in the astrophysics field. The ANTARES neutrino telescope has been completed and is currently working with its final twelve lines configuration since 2 years. The first data have been already analyzed and in this work we present the analysis corresponding to the search for point sources.

The work presented in this thesis has been divided into two main parts. The first one is dedicated to the ANTARES time calibration system and it is specially focused in the results provided by the Optical Beacon system. A proper time calibration is crucial to achieve the desired angular resolution of the detector which is supposed to be of 0.3° for neutrino energies of $E_\nu > 10$ TeV.

In the second part, once we have confirmed the pointing capabilities thanks to the time calibration, a point source search analysis using the data taken during 2007 with the 5-line configuration is presented.

Time calibration with the Optical Beacon System

The time calibration systems of ANTARES has been reviewed in the Chapter 3. We can distinguish between absolute and relative calibration. The first

Conclusions

one refers to the detector capability to measure precisely the time of each hit with respect to the UT. The second refers to the detector capability to synchronize all the OMs in time at the nanosecond level. The relative time calibration is performed *in situ* mainly by the Optical Beacon system. This system consists in a series of pulsed light sources with a well-known emission time. Taking the difference between the hit time recorded by an OM and the time when the light pulse is emitted, the relative time offsets of all the OMs can be computed. The calibration results provided by the OB system have been presented in Chapter 4, with the following conclusions:

- The time resolution of the OM has been proven to be of the order of 0.5 ns using a direct way (OM-LED OB time difference) and an indirect way (OM-OM time differences).

- The individual time offsets (T0s) can be computed with the LED OBs, based on deviations from the empirical linear "early-photon" law. The corrections with respect to the calibration constants computed in the laboratory are small, not being greater than 1 ns for the 85% of the OMs.

- The indirect cross-check of the T0 validity (OM-OM time differences), obtained by means of the LED OB system and by the ^{40}K method, agrees within 0.5 ns.

- The OB calibration system has shown the capability of recomputing all the calibration constants up to the 0.5 ns level after a major upgrade of the detector as the HV retuning of the OMs.

- The Laser Beacon has been used to synchronize the time of the different lines and, in addition, it has helped to calibrate the lower storeys of the lines.

- Taking advantage of the fixed location of the Laser Beacon, a cross-check of the positioning system has been performed with an agreement of 0.5 ns.

- The improvement of the calibration constants obtained using the Optical Beacon system ameliorates the time residuals of a sample of reconstructed muon tracks.

Search for point sources with 5-line data

The search for point sources in ANTARES has been performed using a sample of data taken in 2007 when the detector was composed by five out of

the total twelve detection lines. The selection process of the final data sample has been explained in Chapter 5 where the chosen reconstruction strategy and the final quality cuts used have been justified. In Chapter 6, a point source search analysis using a bin has been presented. This method consists in the search for accumulation of events coming from a cosmic neutrino source in a sky map mainly populated by atmospheric neutrinos and muons by means of a cone shape binned technique. Two kinds of analysis has been performed. The first one uses a list of fixed sources which are catalogued as good candidates for neutrino emission according to the high-energy gamma-ray and cosmic ray observations. The second analysis consists in an all-sky survey where no *a priori* assumption about the source location has been made. The conclusions are the following:

- After applying the corresponding quality cuts, a final sample of 314 events has been selected for the analysis of the 2007 data. This sample has been optimized on the basis of best sensitivity.

- A binned method with a cone shape was used. The size of the cone was chosen in order to exclude as much as possible the background events maximazing then the signal-background ratio. Thanks to that optimization a better upper limits can be settled and discoveries need less events in order to be claimed.

- The analysis with a list of fixed sources has not shown evidences of cosmic neutrino emitters, being the most significant cluster the one corresponding to HESS J1023-575 (δ=-57.76°, α=155.83°) with 4 events inside the search cone. This cluster has a pre-trial p-value of 0.0015 which post-trial becomes a 2.1σ (double sided) significance. The probability of this cluster of being produced by background fluctuations is of 3.3%. The corresponding upper limits have been computed and compared with the previous results from other experiments as it is shown in Figure 6.27. These limits take into account the 30% of the systematic uncertainties.

- The all-sky survey analysis has not shown any significant excess either. The most significant cluster was found at the same location of the cluster found by the candidate list analysis as the most significant one. It corresponds to a cone containing 3 events apart from the one used to define the cone. The p-value obtained in that case was 0.0015, being compatible with the background fluctuations since, according to the simulations the chance of being produced by the background is of 34%.

- Although the results presented in this work did not show any evidence of cosmic neutrino sources, the incoming analysis will be performed with a optimazed reconstruction strategy, a more powerful search method and,

Conclusions
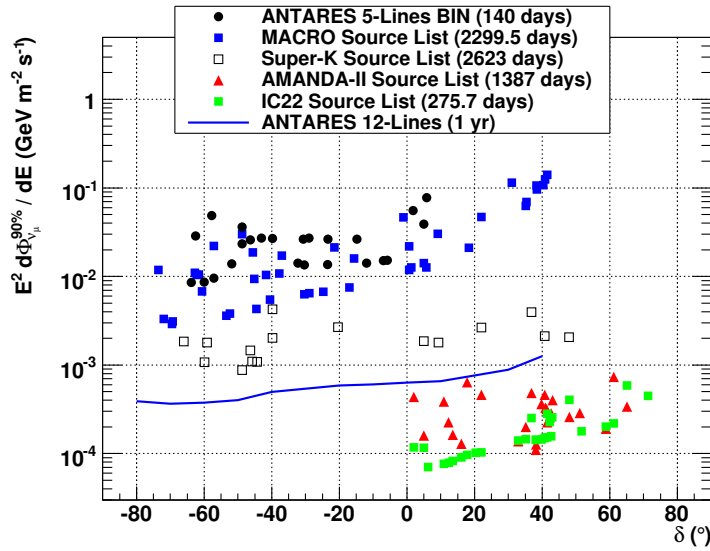
Figure 6.27: *Upper limits obtained with the 2007 data sample (5 lines, 140 days of live-time), compared with the expectation of 1 year with the complete detector (12 lines), and with the results from other experiments.*

the most important thing, more statistics. Therefore, it is expected a great improvement in the upper limits or maybe the first discovery of a cosmic neutrino source.

Calibratge temporal i cerca de fonts puntuals amb el telescopi de neutrins ANTARES

Hem viscut per salvar-vos els mots,
per retornar-vos el nom de cada cosa.
Salvador Espriu.

Introducció

Astronomia de neutrins

La major part de la informació que tenim hui en dia del nostre Univers s'ha obtingut mitjançat l'observació i detecció de la llum, és a dir, dels fotons provinents de diferents tipus d'objectes còsmics, com ara els estels, galàxies, etc. Gràcies als grans avanços tecnològics i desenvolupament científic, els experiments actuals han aconseguit ampliar el rang d'energies detectable dels fotons fins a l'oldre dels TeV. A més a més, la detecció d'altres tipus de partícules apart dels fotons, com ara les que constitueixen els raigs còsmics, han permès augmentar els nostres coneixements en el camp de la física de partícules i l'astrofísica. L'astronomia de neutrins és una nova forma de fer astronomia de recent aparició que pretén complementar aquestes observacions utilitzant com a missatger còsmic el neutrí. Segons les teories actuals aquestos neutrins serien emesos per les mateixes fonts emissores de fotons i raigs còsmics, encara que no està descartada l'emissió per part d'objectes invisibles a altres tipus de detecció.

El concepte de telescopi de neutrins naix arran de l'idea presentada per Markov en 1966 on proposava utilitzar una matriu de fotomultiplicadors submergida en un medi òpticament apropiat, com ara aigua o gel, per tal de detectar el pas dels muons relativistes produïts per la interacció d'un neu-

Resum

trí amb la matèria, gràcies a la llum Cherenkov emesa per aquestos muons.
L'avantatge d'utilitzar neutrins com a missatger còsmic ve del fet que el rang
d'energies que es pot abastar és major que el dels fotons, els quals tenen un
recorregut lliure mig molt menut a energies majors del TeV, per tant l'Univers
esdevé opac. Els neutrins, al ser partícules neutres, també poden apuntar di-
rectament a les fonts d'on són emesos, cosa que en el cas dels raigs còsmics
no passa, perquè al ser partícules carregades perden la seua direccionalitat, i
només a molt altes energies (EeV o majors) són capaços d'apuntar a la font
que els produeix.

Fonts de neutrins

Actualment existeixen només dues fonts extraterrestres de neutrins con-
firmades. Una d'elles és el Sol, que produeix neutrins de baixa energia, de
l'ordre del MeV, com a producte de les reaccions de fusió que es produeixen
al seu nucli. L'altra font coneguda fou la supernova SN1987A, que explotà
en 1987 molt pròxima a la terra ($\sim$50 kpc). Els neutrins produïts en aque-
sta explosió foren detectats per tres experiments diferents, acumulant un total
de 24 esdeveniments amb energies de l'ordre dels 10 MeV. A més d'aquestes
dues fonts emissores de neutrins, també comptem amb un fons irreductible de
neutrins produïts després de la interacció dels raigs còsmics amb l'atmosfera.
Aquesta interacció produeix mesons que tenen els neutrins com a producte de
desintegració.

L'objectiu dels telescopis de neutrins és detectar neutrins d'origen còs-
mic molt energètics, expandint així el coneixement que es té actualment de
l'Univers a altes energies. Pel que respecta a fonts d'origen galàctic, els prin-
cipals candidats per a emetre aquests neutrins són les fonts còsmiques d'alta
energia com els romanents de supernova (SNRs), sistemes binaris de raigs X,
pulsars, el centre galàctic i altres fonts desconegudes sense contrapartida. Pel
que fa a fonts d'origen extra-galàctic tenim els nuclis de galàxia actius (AGNs)
i les explosions de raigs gamma (GRBs) com als candidats més prometedors.
Els models actuals de AGNs, diuen que estan composats de un forat negre
supermassiu al seu interior amb un disc d'acreció on s'acumulen pols i gas.
Durant l'acreció de la massa pel forat negre, es produeix l'emissió d'un jet[1]
des del seu centre. La classificació dels AGNs es fa atenent a la seua orientació
respecte a l'observador (Galaxies Seyfert, Quasars, Blazars, etc.). Les GRBs
són fonts transitòries extremadament lluminoses de radiació electromagnètica.
Actualment es creu que les explosions que emet estan molt focalitzades i per
tant l'emissió és menor a la que se'ls suposava quan foren descobertes. Les
seues emissions de raigs gamma són de durada curta (des de milisegons fins a
minuts). Aquestes emissions solen estar acompanyades per emissions de raigs

---

[1]doll de partícules.

X i radio dies després.

Per a la major part de candidats, tant galàctics com extra-galàctics, s'espera que hi haja una correlació entre l'emissió de fotons i neutrins sempre que s'assumisca que la producció de fotons es d'origen hadrònic. Aquestos fotons serien produïts pels pions neutres productes de la reacció. De la mateixa manera, la producció de neutrins s'explicaria com a producte de desintegració dels pions carregats presents en la mateixa reacció. En qualsevol cas no es descarta l'emissió de neutrins per part de fonts desconegudes.

Telescopis de neutrins

Actualment hi han diversos projectes immersos en la construcció i pressa de dades amb telescopis de neutrins. Entre ells podem destacar AMANDA/ IceCube. AMANDA fou un telescopi de neutrins que estigué funcionant des de 2000 fins a 2006 quan va ser integrat dins del nou detector IceCube. Aquest nou projecte pretén aconseguir per primera volta un telescopi de neutrins amb un volum de detecció d'1 km^3. IceCube s'està acabant d'instal·lar al pol Sud i es preveu que estiga complet en 2011. Actualment la presa de dades es fa de manera continua amb la part del detector ja operatiu. La principal característica d'aquest experiment és que el medi òptic utilitzat per a la detecció dels neutrins és el gel. També recentment han començat la incorporació d'una estructura central de detecció més densa que la resta del detector, anomenada *Deep Core*, que pretén ampliar el rang de detecció a energies menors del GeV.

Apart de AMANDA/IceCube també tenim 2 detectors més actualment funcionant. Per una banda Baikal, que està actiu des de 1993 i que continua prenent dades en l'actualitat. L'altre projecte operatiu és ANTARES que porta des de 2006 acumulant dades i des de 2008 està completament operatiu. Aquesta col·laboració junt als projectes NEMO i NESTOR, han unit esforços per a construir un detector de almenys 1 km^3 que complementarà les observacions d'IceCube ja que estan situats en diferents hemisferis. Les primeres dades de KM3NeT estan previstes per a 2014 amb l'instal·lació de la primera part instrumentada del detector, per tant, es preveu que els pròxims anys siguen fonamentals per al desenvolupament de l'astronomia de neutrins.

El telescopi de neutrins ANTARES

ANTARES (Astronomy with a Neutrino Telescope and Abyss environmental RESearch) és un col·laboració europea que ha construït un telescopi de neutrins completament operacional des del 30 de maig de 2008. El detector està situat a 2500 metres de profunditat al fons del mar mediterrani a 40 km de distància de la costa de Toló (França). Està composat per 12 línies de 450 m de llargària equipades amb 25 fotomultiplicadors cadascuna, formant una xarxa

Resum

tridimensional que permet la detecció de la llum Cherenkov induïda pel muó generat en la reacció del neutrí amb la matèria que envolta al detector.

El medi hostil en el que es troba el detector fa necessària una adequada instrumentació capaç de suportar les condicions extremes de l'entorn. És per això que els fotomultiplicadors estan protegits per una espècie d'esfera feta de borosilicat amb unes dimensions de 41.7 cm de diàmetre intern i 15 mm de gruix dissenyada per a aguantar pressions de 260 atm. Dins d'aquesta esfera trobem també una gàbia de μ-metal i gel òptic per a unir la part de borosilicat amb el fotocàtode per tal de reduir les pèrdues per reflexió. Finalment, trobem a més un LED intern que s'utilitza per al calibratge temporal. Tot el conjunt d'esfera, fotomultiplicadors, gàbia μ-metal, gel òptic, etc. constitueix el que s'anomena mòdul òptic (OM).

Els OMs estan disposats de tres en tres, en una estructura anomenada pis (*storey*). En aquesta estructura els OMs estan espaiats 120° mirant cap avall 45°. El pis compta, a més, amb un mòdul de titani que conté les targetes electròniques per a l'alimentació i transmissió de les dades dels OMs. El pis compta també en cert casos amb instruments addicionals com hidròfons (cinc per línia) i/o balises òptiques (quatre per línia). Els pisos estàn units formant l'anomenada línia (*line*). Ancorada al fons marí mitjançant l'ancora (*anchor*) que la manté lligada a terra i dos boies la mantenen rígida. La part de l'ancora s'encarrega d'alimentar la línia mitjançant el SCM². Apart, junt a una línia específica d'instrumentació (IL), té també instruments amb un objectiu més interdisciplinari. Per exemple, aparells per a mesurar la salinitat, corrents marines o fins i tot un sismòmetre. Finalment les dotze línies es connecten a l'estació de control a la platja mitjançant la caixa d'unió (*junction box*) i un cable electro-òptic que permeten la transmissió de dades i l'alimentació de tots els elements del detector.

Tenint en compte que l'objectiu és detectar neutrins d'alta energia ($> \mathrm{PeV}$) els quals tenen un recorregut de l'ordre de km, la traça deixada una vegada reconstruïda permet obtindre una molt bona direccionalitat de l'esdeveniment registrat, per tant el detector compta amb una molt bona resolució angular, actuant així com a telescopi.

L'ubicació del detector en les profunditats marines està justificada per tal d'eliminar al màxim el fons irreductible de muons atmosfèrics. Encara que cal tindre en compte que la reducció no és total i a les profunditats on està situat el detector, el flux de muons atmosfèrics és encara sis ordres de magnitud major que el flux de muons produïts per neutrins atmosfèrics. Per tal d'aconseguir un millor rebuig en la selecció d'esdeveniments només es consideren els muons reconstruïts en direcció ascendent. D'aquesta manera queda garantit que els muons detectats han sigut produïts per un neutrí, ja que és l'única partícula capaç de travessar tota la terra sense interaccionar. A més a més, per tal

---

²De l'anglès String Control Module.

d'augmentar l'eficiència de recol·lecció en aquest cas, els fotomultiplicadors estan orientats 45° cap avall. Encara que és molt més abundant, el fons de muons atmosfèrics té l'avantatge de que el podem rebutjar simplement exigint traces ascendents. Els esdeveniments que romanen, encara que són produïts per neutrins, en la seua majoria tenen el seu origen en la interacció dels raigs còsmics amb l'atmosfera. En aquest cas l'única forma per a separar neutrins atmosfèrics dels còsmics és mitjançant algoritmes de cerca, com veurem més endavant.

A banda del fons físic que acabem d'explicar, també tenim un fons òptic irreductible degut a la ubicació submarina del detector. Aquest és degut principalment a la llum produïda per éssers vius (bioluminescència) i al fons de potassi 40 present en la sal marina. El sistema de selecció d'esdeveniments (*trigger*) és capaç de rebutjar aquest fons aplicant restriccions de causalitat.

Una de les parts fonamentals del detector és el sistema d'adquisició i com s'estructura. Bàsicament cada OM té dues targetes electròniques associades, per tal de reduir el temps mort, anomenades ARS[3] que s'encarreguen de mesurar el temps i la càrrega d'aquells esdeveniments recollits pel fotomultiplicador que hagen superat el llindar en càrrega de 0.3 fotoelectrons (L0[4]). Aquesta informació una volta digitalitzada, s'arreplega per a cada pis amb 6 ARSs (un més si el pis conté una balisa òptica) que es troben al LCM[5] corresponent. L'informació de cada LCM és enviada en grups de 5 pisos (sector) a un Master-LCM (MLCM) que junta tota la informació i l'envia al SCM a la base de la línia i posteriorment a la caixa d'unió des d'on serà enviada finalment a l'estació de control en la costa. No hi ha sistema de *trigger* previ a la recepció de les dades en l'estació de control, sinó que és *a posteriori* quan es seleccionen les dades que s'utilitzaran per a l'anàlisi. Aquesta selecció és fa a diferents nivells, el nivell 0 el dóna el llindar en càrrega d'adquisició del OM. Després al 1r nivell (L1) romanen sols si tenim un esdeveniment d'alta càrrega i/o tenim una coincidència multiple al mateix pis. En el 2n nivell (L2) busquem tots els hits[6] connectats causalment amb l'esdeveniment generador del L1. Finalment al 3r nivell (L3) la finestra per a cercar esdeveniments s'amplia de manera que els esdeveniments provinents de senyals físiques poden ser inclosos també. A més a més es poden desenvolupar diferents tipus de *trigger* canviant la cerca depenent de la direcció del muó o canviant la finestra temporal per a acceptar més esdeveniments.

Per a un funcionament òptim el detector necessita d'un correcte calibratge tant en temps com en posició. La part temporal serà explicada en detall més avant, al ser un dels temes principals d'aquesta tesi. Pel que respecta a la part

---

[3] Analogue Ring Sampler.

[4] Lx designa diferents nivell del *trigger*, en aquest cas utilitzem el zero al no ser pròpiament un nivell de *trigger*.

[5] De l'anglès Local Control Module.

[6] Cada senyal detectada en un OM.

Resum

de posicionament, ANTARES compta amb un sistema acústic composat per una matriu de transpondedors, és a dir, emissor i receptor a la vegada situats en les bases de cada línia, i de hidròfons que actuen de receptors situats al llarg de cada línia. Mitjançant la mesura del temps que tarda el senyal acústic en recórrer el trajecte que separa els aparells permet una localització espacial dels OM per triangulació en temps real. Junt a aquest sistema acústic, una targeta electrònica fent les funcions de brúixola i d'inclinòmetre permeten el càlcul de la direcció del pis i els angles de balanceig i caboteig amb una precisió de 1° i 0.2° respectivament. La combinació d'aquest sistema i l'acústic permeten determinar la posició dels OMs amb una precisió de l'ordre de 10 cm.

Actualment, el detector porta prenent dades des de maig de 2008 amb les 12 línies finals, amb sols una interrupció durant 2 mesos degut a un trencament parcial del cable electro-òptic. A més cal assenyalar que s'han realitzat operacions de manteniment reparant i/o reconnectant les línies més danyades, garantint així la maxima eficiència per a la presa de dades.

Objectius

Aquest treball de tesi doctoral té dues parts diferenciades, que a la volta estan relacionades. D'una banda el treball ha consistit en l'estudi del sistema de calibratge temporal del detector ANTARES i l'anàlisi dels resultats obtinguts amb el sistema de balises òptiques desenvolupades a l'Institut de Física Corpuscular a València. Com veurem aquest sistema proporciona una gran precisió en la mesura del temps i per tant la qualitat de la traça reconstruïda és bona, i com a conseqüència la resolució angular dels esdeveniments també ho és. L'objectiu en aquest cas és aconseguir precisions en la mesura del temps de l'ordre del nanosegon.

L'altra part s'ha centrat en l'anàlisi de les dades recollides durant tot el 2007, per a fer una cerca de fonts puntuals mitjançant un mètode de bin. Al tractar-se de la primera anàlisi de fonts puntuals realitzat amb dades reals del detector, l'estratègia de reconstrucció utilitzada no està completament optimitzada per donar la millor resolució angular i s'ha preferit utilitzar l'aproximació més conservadora que considera un detector rígid i els triplets de OMs d'un mateix pis com a un punt. Aquestes simplificacions fan que l'estratègia siga molt robusta i l'accord amb el Monte Carlo molt bo. L'objectiu d'aquesta part és dur a terme una primera cerca de fonts de neutrins per tal de veure algun excés significatiu en la distribució d'esdeveniments enregistrats o pel contrari posar limits en l'emissió de neutrins còsmics.

Calibratge temporal del detector

Amb el calibratge temporal d'un telescopi de neutrins es pretén obtindre primer de tot, una precisió temporal relativa menor del nanosegon. Açò significa que coneguem el temps d'enregistrament dels esdeveniments pels OMs amb aquesta precisió, o el que és el mateix, els OMs estan sincronitzats entre ells dins d'1 nanosegon. Exigint açò, es reconstrueix la traça amb gran exactitud, i per tant ens dóna una bona resolució angular del nostre esdeveniment. A més a més, també es necessita una precisió absoluta menor del microsegon, de manera que puguem correlacionar l'esdeveniment vist amb objectes còsmics detectats amb altres tècniques, com per exemple detectors de raigs gamma.

La part de calibratge temporal presentada en aquesta tesi conté un ampli resum del mètodes utilitzats per a calibrar temporalment el detector. Aquests mètodes són el fruit de molt anys de treball de la col·laboració amb una aportació molt significativa del grup de València. Els mètodes són els següents:

Calibratge al laboratori

Amb el calibratge al laboratori es pretén tindre una primera estimació de les constants de calibratge del detector, és a dir, mesurar tots els desfasaments temporals introduïts pels camins elèctrics que recorre el senyal de rellotge, així com els desfasaments intrínsecs de cada OM degut al fet de ser diferents entre ells. Açò s'aconsegueix mitjançant un muntatge experimental que consisteix en enviar un senyal de làser a 15 OMs utilitzant una fibra òptica en la propagació del senyal. Com l'emissió del làser és coneguda i la llargària de les fibres òptiques també ho és, poden saber el desfasament temporal intrínsec de cada OM.

Sistema de rellotge

El sistema de rellotge és necessari en ANTARES per tal de proporcionar una senyal comú de referència en tots els ARSs del detector. El rellotge consisteix en una senyal de 20 MHz de freqüència síncrona amb el GPS, que es transmet de la costa a tot el detector. El camí fins a aplegar a l'ARS s'anomena fase del rellotge (*clock phase*). La mesura d'aquesta quantitat es fa mitjançant un sistema d'eco on la senyal s'envia a cada ARS i torna al lloc on s'ha generat, la mesura del temps d'anada i tornada dividit per 2 ens dóna el valor de la fase del rellotge corresponent. La suma de la fase del rellotge més el desfasament temporal intrínsec de cada OM constitueix la constat de calibratge anomenada T0 que serà el paràmetre a utilitzar posteriorment en les anàlisis.

Resum

Balises òptiques

Aquest sistema està dissenyat amb la finalitat de realitzar el calibratge temporal del detector amb una precisió millor que el nanosegon una vegada instal·lat en l'aigua. Hi han dues classes de balises òptiques, les Làser i les LED. Les dues són essencialment fonts emissores de llum polsada de la qual coneguem amb gran precisió el seu temps d'emissió. La finalitat principal d'aquest sistema és poder mesurar els desfasaments temporals de tots els OMs del detector. A més a més, les balises òptiques poden tenir utilitats addicionals com mesurar les propietats òptiques de l'aigua, verificar el posicionament acústic o mesurar les eficiències dels OMs.

- Balisa LED.
  Amb forma de prisma hexagonal, la balisa LED està composta per 36 LEDs individuals distribuïts en grups de sis LEDs per cara. En cada cara es distribueixen un dels LEDs apuntant cap a dalt mentre que la resta apunten radialment. Els LED emeten en la regió del blau de l'espectre visible (λ=472 nm, FWHM=35 nm) amb una energia màxima de 160 pJ (4×10^8 photons) per cada pols emès. L'emissió es produeix amb un circuit polsador alimentat amb 48 V i disparat per la senyal del rellotge a una freqüència màxima de $\sim$300 Hz. El temps d'emissió del pols es conegut gràcies a un fotomultiplicador menut ubicat dins de l'estructura de la balisa LED. Finalment tota l'estructura amb les targetes electròniques corresponents estan ubicades dins de un cilindre de borosilicat de dimensions 210 mm de diàmetre i 430 mm de longitud que el protegix de les altes pressions submarines.

- Balisa Làser.
  Basat en un diode polsat de Nd-YAG, la balisa Làser produeix polses curts ($<$ 1 ns) de llum verda (λ=532 nm) d'energia d'1 μJ aproximadament ($\times 10^{12}$ photons). Al igual que la balisa LED, la llum és disparada utilitzant la senyal del rellotge. El temps d'emissió en aquest cas es coneix mitjançant un fotodíode intern de gran precisió. La quantitat de llum emesa pel Làser pot ajustar-se amb un sistema compost d'un polaritzador lineal i un retardador variable fet de cristall líquid. El Làser junt a la seua electrònica associada està ubicat dins d'un contenidor cilíndric de titani de 170 mm de diàmetre i 705 mm de longitud.

LED intern

Dins de la estructura que forma l'OM hi ha un LED que il·lumina el fotocàtode des de darrere amb una freqüència d'uns 100 Hz. Aquest sistema permet monitoritzar el temps de transit de cada fotomultiplicador.

Potassi 40

Com s'ha explicat una de les parts que contribueixen al fons òptic durant la recollida d'esdeveniments es el potassi 40 present el la sal de l'aigua marina. Aquests fons pot ser utilitat de manera intel·ligent per tal de calibrar temporal-ment el detector. L'idea és utilitzar la llum Cherenkov produïda per l'electró generat en la desintegració del potassi 40 per tal de veure coincidències temporals en OMs adjacents. Com veurem, aquest mètode pot ser utilitzat com a comprovació dels resultats obtinguts pel sistema de balises òptiques. A més a més el potassi 40 s'utilitza per a la mesura d'eficiències dels fotomultiplicadors.

Muons atmosfèrics

Els desfasament temporals poden també ser monitoritzats utilitzant les traces dels milers de muons descendents que creuen contínuament el detector. Aquest sistema permet validar les constants temporals obtingudes pel sistema de balises òptiques.

Cerca de fonts puntuals de neutrins

Un dels temes d'investigació més interessants en un telescopi de neutrins és la cerca de fonts puntuals. El descobriment d'una font puntual emissora de neutrins tindria implicacions directes tant si prové d'una font ja coneguda mitjançant altres emissors (e.g. fotons), com si prové d'un lloc on no es tenia constància de cap emissió còsmica. A l'hora de fer l'estudi de fonts puntuals primer de tot s'ha fet una selecció dels esdeveniments que seran utilitzats a l'anàlisi. Aquestos esdeveniments han sigut reconstruïts amb una estratègia que fou concebuda en un principi per a la ràpida reconstrucció *on-line* que degut a la seua robustesa i simplicitat ha sigut la que s'ha triat per a la primera anàlisi de fonts puntuals de neutrins.

Per a l'anàlisi de cerca de fonts puntuals, degut a la baixa estadística d'aquest tipus d'anàlisi, s'ha aplicat una política de *blinding* que consisteix sim-plement en optimitzar els talls de selecció *a priori* per tal d'evitar l'influència de factors humans externs. Açò s'aconsegueix simplement ocultant part de la informació que es té i realment no és necessària durant la fase d'optimització dels talls de selecció. Per al cas concret de la cerca de fonts puntuals, el *blinding* s'aconsegueix simplement evitant conèixer la informació temporal de l'esdeveniment, que traduint a coordenades equatorials és fer l'optimització sense utilitzar la coordenada de l'ascensió recta.

La selecció de dades s'ha fet utilitzant talls de selecció basats en l'optimització

Resum

de la sensitivitat (promig del limit superior[7]) i del flux de descobriment segons el tipus d'anàlisi. Açò ha portat a triar dos talls de selecció com talls per defecte. Primer, el paràmetre de qualitat de la reconstrucció de traces en l'estratègia *on-line* (χ^2) ha de ser menor que 1.8. Un valor de χ^2 menor vol dir que major és la puresa de la mostra, per tant, en el nostre cas estem exigint que la mostra d'esdeveniments siga molt pura en neutrins.

El segon tall consisteix en rebutjar els esdeveniments reconstruïts quasi horitzontals, ja que en aquest cas, la discriminació de muons és més difícil. Per tal d'aconseguir-ho, es rebutgen els esdeveniments reconstruïts amb l'angle elevació menor que -10°, on el 0 és l'horitzó.

S'ha fet una comparació de les dades i el Monte Carlo primer per a estudiar quin impacte té el tall fet en χ^2 en la puresa de la mostra, i després considerant els 2 talls de qualitat per tal de comprovar que s'enten el nombre d'esdeveniments enregistrat estudiant diferents paràmetres com l'elevació, azimut, declinació, ascensió recta, etc.

Les prestacions del detector amb l'estratègia de reconstrucció i els talls de selecció escollits, proporciona una resolució angular de 3° per a esdeveniments d'energia de l'ordre dels 100 PeV o major. L'area efectiva[8] per als mateixos talls de selecció i mateix rang d'energies, aplega a 1 m^2.

Discussió dels resultats

Calibratge amb el sistema de balises òptiques

Com hem vist el temps d'emissió de la llum en les balises òptiques es coneix amb gran precisió per tant podem calibrar temporalment el detector.

Les primeres proves foren de funcionalitat, i es realitzaren en els laboratoris primer a València i després a Marsella. Estes proves serviren per a comprovar l'estabilitat del senyal elèctric, sincronització de l'emissió de llum, nivell de soroll electrònic, test tèrmics, etc. Després vingueren el primers tests *in situ* amb el desplegament de la primera línia d'instrumentació (MILOM) que incloïa dues balises LED i una Làser. Els resultats obtinguts demostraren que es podien calcular les constants de calibratge (T0) comprovant els valors que es mesuraren prèviament al laboratori. A més, per primera vegada es va poder demostrar que la contribució de l'electrònica a l'incertesa en la resolució temporal era de l'ordre de 0.5 ns utilitzant tant diferències temporals entre la balisa LED i un OM, o entre OMs dins d'un mateix pis.

---

[7]En anglès average upper limit.

[8]Superfície d'eficiència de recolecció del 100% que detecta el mateix nombre d'esdevenimets que aquest.

Resum

Balises LED

Las balises LED s'utilitzen principalment per al calibratge dins del mateix pis (*intra-storey*) i entre pisos només de la mateixa línia (*intra-line*). Les raons de calibrar els OMs amb un LED situat en la mateixa línia són d'una banda, la simplicitat donat l'alt grau de simetria entre a balisa LED i els tres OMs que composen el pis. D'altra banda, degut principalment a l'acceptància dels OMs, el *scattering* de la llum en l'aigua i l'incertesa en la posició (uns 10 cm segons el sistema de posicionament), les mesures temporals son més imprecises. Per al calibratge entre línies (*inter-line*) s'utilitza normalment la balisa Làser i la LED serveix de comprovació. El calibratge *intra-storey* i *intra-line*, s'obté mesurant els residus temporals. Aquest residus estan definits com la diferència entre l'emissió de la llum de la balisa menys el temps de l'esdeveniments vist per l'OM corregint pel temps que tarda la llum en arribar al OM. Amb aquesta definició, el residu temporal per a cada OM, una vegada considerades totes les constants temporals de calibratge, hauria de ser igual a zero. En canvi els resultats mostren que aquesta quantitat varia en funció de la distància, de manera que als pisos més propers pareix que la llum arribe abans del que s'esperaria. Aquest efecte (*early-photon effect*) és degut a que els OMs son incapaços d'enregistrar múltiples fotons que apleguen a la mateixa vegada al fotomultiplicador provinents d'un flash de la balisa. En aquest cas solament es guarda el primer esdeveniment en temps. L'efecte es va suavitzant a mesura que l'intensitat (distància) és menor (major), fins aplegar a un punt en el que només arriba un fotó per cada flash de la balisa, que és el que es coneix com a nivell del fotoelectró. Simulacions Monte Carlo han mostrat que en una certa regió prèvia al nivell del fotoelectró aquest efecte es pot modelitzar senzillament com a un efecte lineal. Per tant, una vegada coneguem el valor del residu temporal, mitjançat un ajust gaussià a la distribució, podem representar tots els residus dels OMs més propers a la balisa LED en funció de la distància, i ajustar-los a una línia recta. La recta ajustada s'utilitza de referència i per tant, tots els OMs poden ser calibrats relativament a eixa recta. Posteriorment, es mesuren les correccions a les constants de calibratge, i amb els resultats es calculen unes noves constants de calibratge.

El càlcul de les constants temporals amb les balises LED han mostrat que aquestes no canvien gaire una vegada s'han instal·lat els OM *in situ*. De fet, les correccions fetes a les constants mesurades al laboratori han sigut menors d'1 ns en el 85% dels OMs.

La part de calibratge *intra-storey* pot ser comprovada utilitzant el mètode de calibratge basat en la desintegració del potassi 40. Els resultats mostren que les diferencies OM-OM obtingudes per les balises LED són molt semblants a les obtingudes pel potassi 40. De fet, si es recalculen les diferencies OM-OM amb les noves constant obtingudes amb la balisa LED, aquestes milloren significativament.

Resum

L'evolució temporal de les constant de calibratge es poden mesurar estudiant com canvien les diferencies *intra-storey* durant un cert període de temps, ja que un descalibratge general del detector propiciaria que aquestes diferencies anaren augmentant. El que s'ha observat és que l'evolució és lenta i només és significativa si hi han gran canvis en la configuració del detector, com ara, un canvi en els voltatges d'alimentació dels OMs. Aquest canvi implica un canvi en les constants temporals. Gràcies a les balises LED les constants temporals poden ser recalculades, tornant als nivells de precisió inicials.

Balises Làser

Las balises Làser s'utilitzen principalment per al calibratge entre pisos de la mateixa línia (*intra-line*) i entre línies (*inter-line*). Al igual que amb la balisa LED, el mètode per a calibrar utilitzant la balisa Làser està basat en el càlcul de residus temporals. De igual manera, es calcula la diferència temporal balisa respecte OM i es corregeix pel temps que tarda la llum en recórrer la distancia que els separa. Els residus en aquest cas inclouen la correcció per posició i *walk effect*[9]. També amb la finalitat de reduir al màxim l'efecte de l'orientació dels OM respecte del Làser, sols es consideren aquells que formen un angle menor de 40° amb la direcció que uneix la balisa Làser i el centre del pis. L'histograma obtingut s'ajusta a una convolució d'una funció gaussiana i una exponencial i es pren el valor del màxim de la funció. La dependència d'aquest valor amb la distància segueix molt bé una línia recta sense pendent una vegada s'aplega al nivell del fotoelectró. La repetició del procés per a tot el detector permet per una banda comprovar el calibratge *intra-line* si hi ha algun valor que no seguisca la tendència lineal, i per altra fer el calibratge *inter-line* si les rectes no són coincidents per a cada línia del detector.

A més la balisa Làser, degut a que esta fixada a l'ancora de la línia 8, la seua posició es coneguda amb gran precisió. Per tant, es pot utilitzar per a verificar el sistema de posicionament. Per exemple, s'han calculat els residus temporals per a un període de tres mesos per a dos casos diferents, en un es consideren les posicions reals de cada OM segons ens diu el sistema de posicionament, en l'altre cas es considera la línia simplement com a rígida. Els resultats mostren que l'acord en el primer cas és millor de 0.5 ns, mentre que en el segon cas és de l'ordre de 2 ns.

Finalment les constants temporals calculades amb la combinació de resultats de les balises òptiques, tant LED com Làser, s'han utilitzat per a calcular els residus temporals d'una mostra de muons atmosfèrics i s'han comparat amb els residus temporals obtinguts amb les constant del laboratori. Aquesta prova s'ha fet per a un grup de OMs amb una correcció major de 3 ns en els T0s. Els

---

[9]Avançament en la mesura del temps d'un senyal elèctric degut a la seua amplitud, que fa que creue el llindar de discriminació avanç del que s'esperaria.

resultats mostren una millora de la distribució amb les constant tretes amb les balises òptiques, per tant, el reajust dels T0s *in situ* ha sigut satisfactori com es mostra a la figura 6.28.
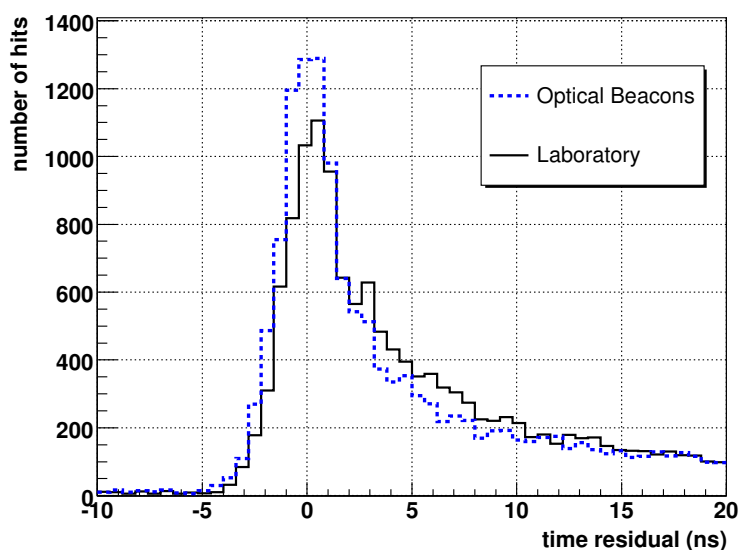
Figure 6.28: *Distribució de residus temporals per a una mostra de 10 dies de muons atmosfèrics ben reconstruïts (bon paràmetre de qualitat del fit) on els OMs utilitzats han tingut correccions majors a 3 ns en els seus T0s. Les distribucions s'han obtingut utilitzant les constants de calibratge del laboratori (línia discontinua) i les calculades amb les balises òptiques in situ (línia continua).*

Cerca de fonts puntuals mitjançant un mètode de bin

El mètode de cerca de fonts puntuals triat per a aquest treball de tesi ha sigut un mètode de bin, on l'exploració del cel es fa mitjançat un con centrat en una posició concreta del mapa celeste en el qual s'han dibuixat tots els esdeveniments enregistrats pel detector. Aquest mètode està basat en el comptatge d'esdeveniments dins del con triat. Sabent el nombre d'esdeveniments que esperaríem tindre dins del con provinents dels fons, podem estimar quina es la probabilitat de que el nombre observat siga degut a una fluctuació estadística assumint que es segueix una distribució Poissoniana. Si la probabilitat és molt menuda aleshores podem afirmar que hi ha una acumulació deguda a la presencia de neutrins còsmics. Aquesta probabilitat sol expressar-se o bé en

Resum

percentatge, o bé utilitzant directament el valor de probabilitat entre 0 i 1, en aquest últim cas es sol anomenar com *p-value*.

Els mètode bin es menys potent que els mètodes *unbin* els quals trauen més informació a la distribució dels esdeveniments en el mapa celeste. Els mètodes *unbin* s'han tractat en un treball paral·lel, demostrant ambdós mètodes la seua compatibilitat en quant a resultats.

Amb les dades de 2007, que equivalen a 140 dies de presa de dades, s'han recollit milers d'esdeveniments dels qual sols 314 han passat tots els talls de selecció. Dues anàlisis s'han fet amb aquesta mostra de dades. Primer una anàlisi utilitzant una llista de fonts seleccionades i després una cerca en tot el cel.

Finalment, abans de presentar els resultats, s'han testat el software utilitzat fent proves (*data challenges*) amb mostres que contenen esdeveniments ficticis, a les quals, per exemple, se'ls han inclòs esdeveniments provinents d'una font inventada.

Llista de fonts seleccionades

En la primera anàlisi s'ha fet una cerca utilitzant una llista de fonts candidates preseleccionades. Aquestes fonts s'han escollit per haver mostrat una emissió en altres formes de missatgers còsmics (raigs gamma, raigs X, protons, etc.). La llista final conté 24 fonts que estan separades almenys per 3° per a evitar solapaments. Per a l'anàlisi es dibuixa un con de cerca centrat exactament en les coordenades de cada font.

L'optimització del tamany del con es fa en vistes d'aconseguir el millor limit superior en el flux d'emissió de la font candidata. Per a cada declinació es busca el tamany del con que done la millor proporció entre la senyal detectada i el fons. Com el nombre d'esdeveniments observats no es coneix *a priori*, es fa una mitja pesada amb una distribució de Poisson. El fons el podem extraure directament de les dades i la senyal de la simulació Monte Carlo de la resolució angular.

El resultats obtinguts d'aquesta anàlisi mostren a la font HESS J1023-575, amb 4 esdeveniments dins del con de cerca, com a la millor candidata a ser emissora de neutrins. Aquest excés té una probabilitat de 3.3% de ser produïda pel fons. No havent cap excés significatiu, es poden extraure els limits superiors d'emissió, en flux, de cada font seleccionada.

És important assenyalar que els resultats presentats dels limits en els fluxes consideren un error sistemàtic del 30% degut principalment a l'incertesa en l'absorció de la llum en l'aigua (20%), l'aceptància dels fotomultiplicadors (15%) i discrepàncies de les dades amb el MC (10%).

Els resultats finals estan recollits en la taula 6.2.

La comparació gràfica dels resultats amb resultats d'altres experiments es mostra a la figura 6.29.

Nom de la font	δ (°)	α(°)	n_b	n_{obs}	p-value	ϕ_{90}
PSR B1259-63	-63.83	195.70	0.96	0	1	0.86
RCW 86	-62.48	220.68	0.59	2	0.12	2.87
HESS J1023-575	-57.76	155.83	0.47	4	0.0015	4.85
CIR X-1	-57.17	230.17	0.70	0	1	0.95
HESS J1614-518	-51.82	243.58	0.81	0	1	1.38
GX 339	-48.79	255.70	0.87	1	0.59	2.33
RX J0852.0-4622	-46.37	133.00	0.73	1	0.52	2.58
RX J1713.7-3946	-39.75	258.25	0.62	1	0.46	2.67
PKS 2155-304	-30.22	329.72	0.65	0	1	1.35
Galactic Center	-29.01	266.42	0.66	1	0.49	2.7
W28	-23.34	270.43	0.71	1	0.51	2.64
LS 5039	-14.83	276.56	0.76	1	0.54	2.64
HESS J1837-069	-6.95	279.41	0.77	0	1	1.51
SS 433	4.98	287.96	0.65	1	0.48	3.9
HESS J0632+057	5.81	98.24	0.62	3	0.025	7.72
ESO 139-G12	-59.94	264.41	0.92	0	1	0.87
PKS 2005-489	-48.82	302.37	0.84	2	0.21	3.61
Centaurus A	-43.02	201.36	0.56	1	0.43	2.71
PKS 0548-322	-32.27	87.67	0.51	0	1	1.41
H 2356-309	-30.63	359.78	0.65	1	0.48	2.64
1ES 1101-232	-23.49	165.91	0.71	0	1	1.36
1ES 0347-121	-11.99	57.35	0.85	0	1	1.41
3C 279	-5.79	194.05	0.83	0	1	1.52
RGB J0152+017	1.79	28.17	0.56	2	0.11	5.54

Table 6.2: *Llista de les 24 fonts candidates de neutrins còsmics amb la seua localització en el mapa celeste. Els resultats donats són el nombre d'esdeveniments de fons esperats dins del con (n_b), el nombre d'esdeveniments detectats (n_{obs}), el p-value i la constant de normalització del flux diferencial de neutrí muonic assumint un espectre que va com E^{-2} (i.e. $E^2 d\phi_{\nu_\mu}/dE \leq \phi_{90} \times 10^{-2}$ GeV m^{-2} s^{-1}).*

Resum
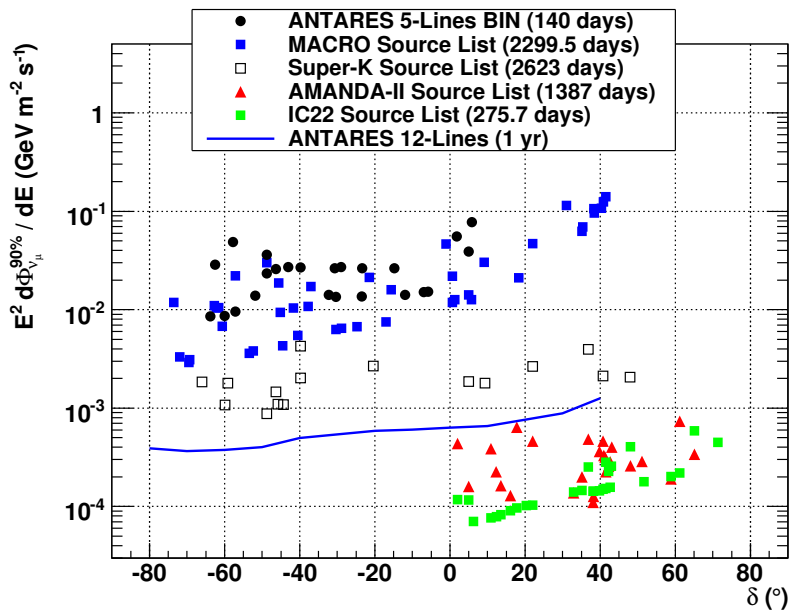
Figure 6.29: *Limits superiors obtinguts amb la mostra de dades de 2007 (5 linies i 140 dies de presa de dades), comparats amb el que s'espera amb un any amb el detector complet i amb els resultats d'altres experiments.*

Cerca en tot el cel

En aquesta anàlisi s'ha fet una cerca sense cap suposició sobre l'emplaçament de les fonts de neutrins. L'avantatge en aquest cas és que qualsevol font pot ser detectada sense necessitat de haver sigut detectada prèviament. El desavantatge és que necessitem més esdeveniments en el con de cerca per a poder afirmar que s'ha descobert una font.

En aquesta anàlisi l'optimització del tamany del con es fa amb l'idea d'obtindre un descobriment amb el menor nombre possible d'esdeveniments. Açò implica, per norma general, que el tamany del con de cerca és menor. Aquest con de cerca estarà centrat en cadascun dels esdeveniments enregistrats, en aquest cas l'esdeveniment utilitzat com a centre del con no es tindrà en compte. En cas de solapament romandrà el con amb major significància.

Per a aquesta anàlisi l'excés més significatiu el dona de nou la font HESS J1023-575, amb 4 esdeveniments dins del con sent un d'ells el centre del con. En aquest cas la probabilitat d'aquest excés de haver estat produït pel fons és del 34%.

Conclusions

Durant els últims anys el desenvolupament de l'astronomia de neutrins ha sigut impressionant. El projecte referència, IceCube, està quasi acabat i el projecte KM3NeT està en fase de desenvolupament i està previst que estiga apunt per als pròxims anys. Aquestos projectes arribaran al km^3 de volum de detecció cosa que els farà sensibles als fluxes de neutrins predits pels models teòrics actuals. Açò possibilitarà l'exploració de l'Univers utilitzant neutrins còsmics per primera vegada. Els temes de física a cobrir son variats i molt prometedors. Entre ells està la cerca de fonts puntuals de neutrins. La combinació d'esta cerca junta a la que es fa utilitzant altres missatgers com fotons o raigs còsmics ajudarà a entendre els processos d'alta energia involucrats, així mateix clarificarà l'origen dels raigs còsmics més energètics. Els principals candidats per a ser fonts de neutrins còsmics són els AGNs i els GBRs dels quals es sap que són els acceleradors més potents en l'Univers. Tanmateix, també és possible detectar fonts amagades sense altres emissors com a contrapartida. El seu descobriment tindria especial rellevància en el camp de les astro-partícules. El detector de neutrins ANTARES està completament construït i porta prenent dades més de dos anys. Les primeres dades han sigut ja analitzades.

El treball presentat en esta tesi ha estat dividit en dues parts. La primera està dedicada al sistema de calibratge temporal d'ANTARES, centrant-se sobretot en els resultats obtinguts amb el sistema de balises òptiques. Un correcte calibratge temporal és important per tal d'obtenir la millor resolució angular possible del detector. En la segon part es presenta l'anàlisi corresponent a la

Resum

cerca de fonts puntuals de neutrins amb les dades recollides durant 2007 on 5 de les 12 línies total del detector estaven funcionant.

Calibratge temporal amb balises òptiques

- S'ha comprovat que la resolució temporal del OM és de l'ordre de 0.5 ns tant de manera directa amb les diferencies temporals entre la balisa LED i els OMs, com de manera indirecta amb les diferencies entre OMs del mateix pis.

- Els desfasaments temporals (T0s) poden ser calculats amb les balises LED, basant-se en les desviacions respecte a la llei lineal empírica basada en l'efecte de l'*early-photon*. Les correccions respecte les constant de calibratge obtingudes en el laboratori són menudes i en el 85% dels casos menor del nanosegon.

- La comprovació indirecta de la validesa de les constants temporals (T0s) calculades mitjançant els sistema de balises LED i pel mètode de potassi 40, tenen un accord de 0.5 ns.

- El sistema de balises òptiques ha demostrat ser capaç de recalcular totes les constant de calibratge temporal fins a una precisió de 0.5 ns després de actualitzacions en el detector, com per exemple un recalibratge dels voltatges d'alimentació.

- La balisa Làser s'ha utilitzat per a sincronitzar el temps de diferents línies i, a més, ha ajudat a calibrar els primers pisos de les línies.

- Aprofitant la posició fixa de la balisa Làser, s'ha fet una comprovació del sistema de posicionament obtenint un accord millor de 0.5 ns.

- Els residus temporals d'una mostra de muons atmosfèrics calculats amb les constant de calibratge del laboratori milloren quan s'utilitzen les constants temporals calculades pel sistema de balises òptiques *in situ*.

Cerca de fonts puntuals amb dades de 5 línies

- Després d'aplicar els corresponents talls de selecció, la mostra final conté 314 esdeveniments per a l'anàlisi de les dades de 2007. Aquesta mostra ha sigut optimitzada basant-se en una òptima sensitivitat.

- S'ha utilitzat un mètode de bin, on la forma triada per a la cerca ha sigut un con. El tamany del con s'ha ajustat per tal de rebutjar al màxim el fons i maximitzar així la relació senyal/fons. Açò permet obtindre

millors limits, per al cas en que s'utilitza una llista de fonts candidates, i
els descobriments poden fer-se amb menor nombre d'esdeveniments, per
al cas de fer una cerca en tot el cel.

- L'anàlisi utilitzant una llista fixa de fonts candidates ha mostrat que
  no hi han evidències de emissors de neutrins còsmics. L'agrupació més
  important d'esdeveniments correspon a la font HESS J1023-575 (δ=-
  57.76° α=155.83°) amb quatre esdeveniments dins del con de cerca. Açò
  dóna un valor *pre-trial* del *p-value* de 0.0015 que esdevé 2.1σ de sig-
  nificància, que vol dir que la probabilitat de que aquesta agrupació
  d'esdeveniments vinga com a conseqüència de les fluctuacions estadís-
  tiques del fons és del 3.3%. Els limits corresponents han sigut obtinguts
  i es mostren en la figura 6.29. Aquestos límits incloUEN els errors sis-
  temàtics del 30%.

- En l'anàlisi de cerca de fonts en tot el cel, tampoc s'ha vist ningun excés
  significatiu. L'agrupació amb més significància fou trobada en el mateix
  lloc on estava la de la llista fixa. En aquest cas el con de cerca contenia
  3 events apart del que s'utilitza per a definir el con. El *p-value* és 0.0015
  que és compatible en les fluctuacions del fons ja que segons les simulacions
  fetes el 33% dels casos tenen una agrupació d'esdeveniments amb eixa
  significància.

- Encara que els resultats presentats no mostren pel moment cap evidència
  clara de fonts còsmiques de neutrins, les següents anàlisis comptaran amb
  una estratègia optimitzada, un mètode de cerca més potent i, el que és
  més important, amb molta més estadística. Per tant, s'espera una millora
  important dels limits presentats o tal vegada el primer descobriment
  d'una font còsmica de neutrins.

Resum

Bibliography

[1] A. M. Markov. In *Proceedings of the Rochester Conference*, New York, USA, 1960.

[2] J. Carr for the ANTARES collaboration. Data from the ANTARES Neutrino Telescope. *J.Phys. Conf. Ser.*, 136:022047, 2008.

[3] Jr. C.L. Cowan, F. Reines, F.B. Harrison, H.W. Kruse, and A.D. McGuire. Detection of the Free Neutrino: A Confirmation. *Science*, 124:103, 1956.

[4] Jr. R. Davis, D.S. Harmer, and K.C. Hoffman. Search for neutrinos from the Sun. *Phys. Rev. Lett.*, 20:1205, 1968.

[5] J. N. Abdurashitov et al. (SAGE collaboration). Solar-neutrino results from sage. *Physics of Atomic Nuclei*, 63:943–950, 2000.

[6] T. A. Kirsten. Gallex solar neutrino results. *Progress in Particle and Nuclear Physics*, 40:85–99, 1998.

[7] R. Svoboda. *Nuclear Physics B (Proc. Suppl.)*.

[8] Q.R. Ahmad et al. (SNO Collaboration). Direct Evidence for Neutrino Flavor Transformation from Neutral-Current Interactions in the Sudbury Neutrino Observatory. *Phys. Rev. Lett.*, 89:011301, 2002.

[9] Y. Fukuda et al. (Super-Kamiokande Collaboration). Evidence for Oscillation of Atmospheric Neutrinos. *Phys. Rev. Lett.*, 81:1562, 1998.

[10] K. Abe et al. (Super-Kamiokande Collaboration). A Measurement of Atmospheric Neutrino Flux Consistent with Tau Neutrino Appearence. *Phys. Rev. Lett.*, 97:171801, 2006.

[11] K. Hirata et al. Observation of a Neutrino Burst from the Supernova SN1987A. *Phys. Rev. Lett.*, 58:1490, 1987.

BIBLIOGRAPHY

[12] R.M.Bionta et al. Observation of a Neutrino Burst in Coincidence with Supernova 1987A in the Large Magellanic Cloud. *Phys. Rev. Lett.*, 58:1494, 1987.

[13] E.N. Alekseev, L.N. Alekseeva, V.I. Volchenko, and I.V. Krivosheina. Detection of the neutrino signal from SN 1987A in the LMC using the INR Baksan underground scintillation telescope. *Physics Letters*, B 205:209, 1988.

[14] B. Pontecorvo. Inverse Beta Processes and Nonconservation of Lepton Charge. *Zh. Eksp. Teor. Fiz.*, 34:247, 1958.

[15] V. F. Hess. Über Beobachtungen der durchdringenden Strahlung bei sieben Freiballonfahrten. *Phys. Z.*, 13:1084, 1912.

[16] C. Amsler et al. Review of Particle Physics. *Physics Letters*, B667:1, 2008.

[17] T. Antoni et al. KASCADE measurements of energy spectra for elemental groups of cosmic rays: Results and open problems. *Astropart. Phys.*, 24:1, 2005.

[18] A. M. Hillas. Cosmic Rays: Recent Progress and some Current Questions. 2006.

[19] D. R. Bergman and J.W. Belz. Cosmic rays: the Second Knee and beyond. *J. Phys. G: Nucl. Part. Phys.*, 34:R359–R400, 2007.

[20] T. Wibig and A. W. Wolfendale. At what particle energy do extragalactic cosmic rays start to predominate? *J. Phys. G: Nucl. Part. Phys.*, 31:255–264, 2005.

[21] V. Berezinsky, A. Gazizov, and S. Grigorieva. On astrophysical solution to ultrahigh energy cosmic rays. *Phys. Rev.*, D74:043005, 2006.

[22] M. Lemoine. Extra-galactic magnetic fields and the second knee in the cosmic-ray spectrum. *Phys. Rev.*, D71:083007, 2005.

[23] K. Greisen. End to the cosmic ray spectrum? *Phys. Rev. Lett.*, 16:748, 1966.

[24] G. T. Zatsepin and V. A. Kuzmin. Upper limit of the spectrum of cosmic rays. *Sov. Phys. JETP Lett.*, 4:78, 1966.

[25] V. Berezinsky, M. Kachelrieβ, and A. Vilenkin. Ultra-high energy cosmic rays without GZK cutoff. *Phys. Rev. Lett.*, 79:4302–4305, 1997.

[26] J. Abraham et al. (AUGER Collaboration). Correlation of the highest-energy cosmic rays with the positions of nearby active galactic nuclei. *Astropart. Phys.*, 29:188–204, 2008.

[27] J. D. Hague. Correlation of the Highest Energy Cosmic Rays with Nearby Extragalactic Objects in Pierre Auger Observatory Data. 2009.

[28] E. Fermi. On the origin of the cosmic radiation. *Phys. Rev.*, 75(8):1169, 1949.

[29] G. M. Webb. First order and second order Fermi acceleration of energetic charged particles by shock waves. *Astrophys. J.*, 270:319–338, 1983, July 1.

[30] `http://www.nasa.gov/centers/goddard/news/topstory/2007/active_galaxy.html`.

[31] E. Nakar. Short-Hard Gamma-Ray Bursts. *Physics Reports*, 442:166–236, 2007.

[32] S.E. Woosley and J.S. Bloom. The Supernova-Gamma-Ray Burst Connection. *Ann.Rev.Astron.Astrophys*, 44:507–556, 2006.

[33] T. Piran. Gamma-ray burst and the fireball model. *Physics Reports*, 314:575–667, 1999.

[34] A. De Rujula. An introduction to Cosmic Rays and Gamma-Ray Bursts, and to their simple understanding. 2007.

[35] `http://fermi.gsfc.nasa.gov/ssc/data/access/lat/1yr_catalog/`.

[36] J. Albert et al. (MAGIC collaboration). Variable very high energy γ-ray emission from Markarian 501. *Astrophys. J.*, 669:862–883, 2007.

[37] F. Aharonian et al. (HESS collaboration). Simultaneous observations of PKS 2155-304 with hess, *FERMI*, *RXTE*, and ATOM: spectral energy distributions and variability in a low state. *Astrophys. J.*, 696:L150–L155, 2009.

[38] E. G. Berezhko and H. J. Völk. Theory of cosmic ray production in the supernova remnant RX J1713.7-3946. *Astronomy & Astrophysics*, 451:981, 2006.

[39] F. Aharonian et al. (HESS collaboration). Primary particle acceleration above 100 TeV in the shell-type supernova remnant RX J1713.7-3946 with deep HESS observations. *Astronomy & Astrophysics*, 464:235, 2007.

BIBLIOGRAPHY

[40] A. Kappes, J. Hinton, C. Stegmann, and F. A. Aharonian. Potential neutrino signals from galactic γ-ray sources. *Astrophys. J.*, 656:870, 2007.

[41] D. Horns et al. Nucleonic gamma-ray production in Vela X. *Astronomy & Astrophysics*, 451:L51, 2006.

[42] F. Aharonian et al. (HESS collaboration). Discovery of very-high-energy γ-rays from the Galactic Centre ridge. *nature*, 439:695, 2006.

[43] F. Halzen and E. Zas. Neutrino Fluxes from Active Galaxies: A Model-Independent Estimate. *Astrophys. J.*, 488:669, 1997.

[44] J. Alvarez-Muñiz and J. Meszaros. High energy neutrinos from radio-quiet active galactic nuclei. *Phys. Rev.*, D70:123001, 2004.

[45] F. Halzen and A. O'Murchadha. Neutrinos from Auger Sources. 2008. astro-ph/0802.0887v2.

[46] J. K. Becker et al. Coincident GRB neutrino flux predictions: Implications for experimental UHE neutrino physics. *Astropart. Phys.*, 25:118, 2006.

[47] E. Waxman and J. Bahcall. High energy neutrinos from Cosmological Gamma-Ray Burst Fireballs. *Phys. Rev. Lett.*, 78:2292–2295, 1997.

[48] A. Achterberg et al. (IceCube Collaboration). The Search for Muon Neutrinos from Northern Hemisphere Gamma-ray Bursts with AMANDA. *Astrophys. J.*, 674:357–370, 2008.

[49] A. Loeb and E. Waxman. The cumulative background of high energy neutrinos from starburst galaxies. *J. Cosm. and Astr. Phys.*, 05:003, 2006.

[50] R. Engel, D. Seckel, and T. Stanev. Neutrinos from propagation of ultrahigh energy protons. *Phys. Rev.*, D64:093010, 2001.

[51] E. Waxman and J. Bahcall. High energy neutrinos from astrophysical sources: An upper bound. *Phys. Rev.*, D 59:023002, 1998.

[52] G. Bertone, D. Hooper, and J. Silk. Particle dark matter: evidence, candidates and constraints. *Physics Reports*, 405:279–390, 2005.

[53] G. Bertone. *Particle dark matter: observations, models and searches.* Cambridge University Press, 2010.

[54] B. van Rens. *Detection of Magnetic Monopoles below the Cherenkov Limit*. PhD thesis, Amsterdam university- Amsterdam, The Netherlands, 2006.

[55] D. Morgan et al. Neutrino telescope modelling of lorentz invariance violation in oscillations of atmospheric neutrinos. *Astropart. Phys.*, 29:345–354, 2008.

[56] F. Halzen, J.E. Jacobsen, and E. Zas. Ultratransparent Antarctic ice as a supernova detector. *Phys. Rev.*, D53:7359, 1996.

[57] J. Babson et al. (DUMAND Collaboration). Cosmic-ray muons in the deep ocean. *Phys. Rev.*, D42:3613, 1990.

[58] A. Avrorin et al. (BAIKAL collaboration). Status of the BAIKAL neutrino experiment. 2009.

[59] The icecube collaboration: contributions to the 30th International Cosmic Ray Conference (ICRC 2007). arXiv:0711.0353v1.

[60] A. Capone et al. Recent results and perspectives of the NEMO project. *Nucl. Instr. and Meth. Phys. Res. A*, 602:47–53, 2009.

[61] P. A. Rapidis. The NESTOR underwater neutrino telescope project. *Nucl. Instr. and Meth. Phys. Res. A*, 602:54–57, 2009.

[62] A. Karle. IceCube. 2009.

[63] R. Abbasi et al. (IceCube collaboration). Extending the Search for Neutrino Point Sources with IceCube above the Horizon. *Phys. Rev. Lett.*, 103:221102, 2009.

[64] E. L. Berger et al. Ultrahigh energy neutrino scattering. *Phys. Rev.*, D77:053007, 2008.

[65] D. E. Groom, N. V. Mokhov, and S. I. Striganov. Muon stopping power and range tables 10 MeV-100 TeV. *Atomic Data and Nuclear Data Tables*, 78:183–356, July 2001.

[66] P.Amram et al. (ANTARES collaboration). The ANTARES optical module. *Nucl. Instr. and Meth. Phys. Res. A*, 484:369, 2002.

[67] J. A. Aguilar et al. (ANTARES collaboration). Study of large hemispherical photomultiplier tubes for the ANTARES neutrino telescope. *Nucl. Instr. and Meth. Phys. Res. A*, 555:132–141, 2005.

BIBLIOGRAPHY

[68] J.A. Aguilar et al. (ANTARES collaboration). First results of the Instrumentation Line for the deep-sea ANTARES neutrino telescope. *Astropart. Phys.*, 26:314–324, 2006.

[69] M. Ageron et al. (ANTARES collaboration). Studies of a full scale mechanical prototype line for the ANTARES neutrino telescope and tests of a prototype instrument for deep-sea acoustic measurements. *Nucl. Instr. and Meth. Phys. Res. A*, 581:695–708, 2007.

[70] R. Lahmann. Description of the Instrumentation Line 2007 (IL07). ANTARES Technical note, 2007. 3-INS-07-01-A.

[71] R. Lahmann. Deep-sea acoustic neutrino detection and the AMADEUS system as a multi-purpose acoustic array. *Nucl. Instr. and Meth. Phys. Res. A*, 602:255–261, 2009.

[72] P.Amram et al. (ANTARES collaboration). Sedimentation and Fouling of Optical Surfaces at the ANTARES Site. *Astropart. Phys.*, 19:253–267, 2003.

[73] J. A. Aguilar et al. (ANTARES collaboration). Transmission of light in deep sea water at the site of the Antares neutrino telescope. *Astropart. Phys.*, 23:131–155, 2005.

[74] H.Yepes-Ramirez. Water absorption length measurement with the ANTARES optical beacon system. *Nucl. Instr. and Meth. Phys. Res. A*, page doi:10.1016/j.nima.2010.04.124, 2010.

[75] P.Amram et al. (ANTARES collaboration). Background light in potential sites for the ANTARES undersea neutrino telescope. *Astropart. Phys.*, 13:127–136, 2000.

[76] D. Lachartre. Ars1 Analogue Ring Sampler & ARS_CONV Users Manual Version 1.9. ANTARES Internal note, 2000. ANTARES-Elec/2000-6.

[77] E. Delagnes et al. Ars : tests, settings and performances for physics. ANTARES Internal note, 2006. ANTARES-Elec/2004-001.

[78] E. Carmona. Estudio de fotomultiplicadores de gran fotocátodo para el telescopio submario de neutrinos ANTARES. Master's thesis, Universitat de València, Spain, 1999.

[79] S. Loucatos. Correction of the differential non-linearity of the ADC's. ANTARES Internal note, 2007. ANTARES-Elec/2005-002.

[80] J. A. Aguilar et al. (ANTARES collaboration). The data acquisition system for the ANTARES neutrino telescope. *Nucl. Instr. and Meth. Phys. Res. A*, 570:107–116, 2007.

[81] Oracle Corporation. `http://www.oracle.com`.

[82] M. de Jong. The ANTARES Trigger Software. ANTARES Internal note, 2005. ANTARES-SOFT/2005-005.

[83] M. de Jong. Antares data formats. ANTARES Internal note, 2004. ANTARES-SOFT/2004-006.

[84] J. Carr, S. Escoffier, and D. Zaborov. Proposition for an alternative trigger based on the t3 cluster trigger. ANTARES Internal note, 2007. ANTARES-SOFT/2007-016.

[85] F. Salesa. Calibration system of antares neutrino telescope. In *Proceedings for the 20th European Cosmic Ray Symposium (ECRS)*, Lisbon, Portugal, 2006. `http://www.lip.pt/events/2006/ecrs/proc/ecrs06-s0-188.pdf`.

[86] M. Ardid. Positioning system of the ANTARES neutrino telescope. *Nucl. Instr. and Meth. Phys. Res. A*, 602:174–176, 2009.

[87] F. Salesa. ANTARES time calibraton. *Nucl. Instr. and Meth. Phys. Res. A*, 602:72–75, 2009.

[88] S. Karkar. *Détection de microquasars et calibration en temps du télescope à neutrinos ANTARES*. PhD thesis, Université de la Méditérranée- Aix Marseille II, Marseille, France, 2004.

[89] F. Salesa, V. Roca, and J. Zuñiga. A new laser beacon with voltage-controlled light intensity. ANTARES Internal note, 2007. ANTARES-CALI/2007-004.

[90] Ch. Olivetto and F. Réthoré. Numerical clock distribution for antares. ANTARES Technical note, 2000. 3LCM 03-01/C.

[91] M. Ageron et al. (ANTARES collaboration). The ANTARES optical beacon system. *Nucl. Instr. and Meth. Phys. Res. A*, 578:498–509, 2007.

[92] J.S. Kapustinsky et al. A fast timing light pulser for scintillation detectors. *Nucl. Instr. and Meth. Phys. Res. A*, 241:612–613, 1985.

[93] J.A. Aguilar et al. Specifications and design of the laser beacon. ANTARES Technical note, 2007. 3-INS-04-02-A.

[94] G. Lambard. Walk Effect Correction. ANTARES Internal note, 2006. ANTARES-CALI/2006-004.

[95] G. Guillard. Walk Effect: the WaveForm approach. ANTARES Internal note, 2009. in preparation.

BIBLIOGRAPHY

[96] Antares internal wiki page. `http://antares.in2p3.fr/internal/dokuwiki/doku.php?id=dnl_correction`.

[97] J.A. Aguilar. Measurements of the attenuation length in ANTARES with the Optical Beacon system. ANTARES Internal note, 2007. ANTARES-Site/2007-001.

[98] F. Salesa. Integration and First Results of the Optical Beacon Calibration System of the ANTARES Neutrino Telescope. Master's thesis, Universitat de València, Spain, 2006.

[99] J.A. Aguilar. *Analysis of the Optical Beacon system and search for point-like sources in the ANTARES neutrino telescope*. PhD thesis, Universitat de València, Spain, 2008.

[100] K40 analysis personal page. `http://antares.in2p3.fr/users/zaborov/internal/k40`.

[101] D. Zaborov. In *Proceedings for the Rencontres de Moriond 2008*, La Thuile,Aosta valley, Italy, 2008.

[102] C. Bigongiari. Calibob status. Oral presentation, 2008. ANTARES Collaboration meeting.

[103] M. Ageron et al. (ANTARES collaboration). Performance of the first ANTARES detector line. *Astropart. Phys.*, 31:277–283, 2009.

[104] K. Kuzmin et al. Genhen v6r3: implementation of the Glashow resonance and of the MUSIC transport code. ANTARES Internal note, 2004. ANTARES-SOFT/2004-012.

[105] G. Ingelman et al. LEPTO 6.5: A Monte Carlo generator for deep inelastic lepton-nucleon scattering. *Comput. Phys. Common*, 1997.

[106] J. Pumplin et al. New generation of parton distributions with uncertainties from global QCD analysis. *JHEP*, 07:012, 2002.

[107] T. Sjostrand. PHYTIA 5.7 and JETSET 7.4 physics and manual. *Comput. Phys. Common*, 1994.

[108] P. Antonioli et al. A three-dimensional code for muon propagation through the rock: MUSIC. *Astropart. Phys.*, 7:357–368, 1997.

[109] D. Heck et al. CORSIKA: A Monte Carlo code to simulate extensive air showers. Technical Report FZKA 6019.

[110] J. Brunner. ANTARES Internal documentation. `http://antares.in2p3.fr/internal/software/geasim.html`.

BIBLIOGRAPHY

[111] D. J. L. Bailey. KM3 v2r1: User Guide. ANTARES Internal note, 2002. ANTARES-Soft/2002-006.

[112] M. de Jong. The Summary Timeslice Writter program. ANTARES Internal note, 2005. ANTARES-SOFT-2005-006.

[113] M. de Jong. The `TriggerEfficiency` program. ANTARES Internal note, 2009. ANTARES-SOFT-2009-001.

[114] A. Heijboer. *Track reconstruction and point source searches with ANTARES.* PhD thesis, Universiteit van Amsterdan, 2004.

[115] C. Reed. Physics and Real (CalReal) Release v2r0. ANTARES Internal note, 2008. ANTARES-SOFT/2008-006.

[116] J. Brunner. The BBfit reconstruction algorithm. ANTARES Internal note, 2009. ANTARES-SOFT-2009-012.

[117] J. D. Zornoza. *Sensitivity to Diffuse Fluxes and Energy Spectrum Reconstruction in the ANTARES Neutrino Telescope.* PhD thesis, Universitat de València, Spain, 2005.

[118] SLALIB - Positional Astronomy Library. `http://www.starlink.rl.ac.uk/star/docs/sun67.htx/sun67.html`.

[119] E. Carmona. *Study of the event reconstruction and expected performances for the point-like sources of the future ANTARES neutrino telescope.* PhD thesis, Universitat de València, Spain, 2003.

[120] J. A. Aguilar and J. J. Hernández-Rey. The expectation-maximization algorithm applied to the search of point sources of astroparticles.

[121] G. J. Feldman and R. D. Cousins. Unified approach to the classical statistical analysis of small signal. *Phys. Rev.*, D57:3873, 1998.

[122] G.C. Hill and K. Rawlins. Unbiased cut selection for optimal upper limits in neutrino detectors: the model rejection potential technique.

[123] F. Tegenfeldt and J. Conrad. On Bayesian treatment of systematic uncertainties in confidence interval calculation. *Nucl. Instr. and Meth. Phys. Res. A*, 539:407–413, 2005.

[124] J.A. Aguilar et al. (ANTARES collaboration). Zenith distribution and flux of atmospheric muons measured with the 5-line antares detector. *accepted for publication in Astroparticle Physics.*

[125] S. Toscano. Golden-list for a point source search in antares. ANTARES Internal note, 2009. ANTARES-PHYS-2009-012.

BIBLIOGRAPHY

[126] G.C Hill et al. Examining the balance between optimising an analysis for best limit setting and best discovery potecial. 2005.

[127] G. Lelaizant. Geometric constants synthesis for the MILOM and line 1. ANTARES Internal note, 2006. ANTARES-CALI-2006-002.

[128] F. Cassol. Alignment algorithms and software. ANTARES Internal note, 1999. ANTARES-Slow/1999-001.

Appendix A

LED Beacon calibration runs

This Appendix summarizes the runs used for the Optical Beacon analysis.

Table A.1 contains the list of LED OB runs taken on 18th February 2008, used for the analysis in this thesis.

Runnumber	Date (day/moth/year)
32336	25/02/2008
32568	04/03/2008
32666	10/03/2008
32809	17/03/2008
33035	23/03/2008
33276	31/03/2008
33415	07/04/2008
33558	14/04/2008
33666	21/04/2008
33839	28/04/2008
34006	05/05/2008
34178	12/05/2008

Table A.2: *List of Laser OB runs used for the analysis.*

Table A.2 contains the list of Laser OB runs taken from 25th February 2008 to 12th May 2008, used for the analysis in this thesis.

Optical Beacon calibration runs

Runnumber	LED OB flashing
32116	L1-F9+L1-F21
32115	L1-F2+L1-F15
32118	L2-F9+L2-F21
32117	L2-F2+L2-F15
32120	L3-F9+L3-F21
32119	L3-F2+L3-F15
32122	L4-F9+L4-F21
32121	L4-F2+L4-F15
32126	L5-F9+L5-F21
32123	L5-F2+L5-F15
32129	L6-F9+L6-F21
32127	L6-F2+L6-F15
32132	L7-F9+L7-F21
32131	L7-F2+L7-F15
32134	L8-F9+L8-F21
32133	L8-F2+L8-F15
32114	L9-F9+L9-F21
32112	L9-F2+L9-F15
32137	L10-F9+L10-F21
32136	L10-F2+L10-F15

Table A.1: *List of LED OB runs used for the analysis.*

Appendix B

Positioning transformations

Unlike the intra-line LED OB runs, where there is a high level of symmetry in the OM arrangement, for the Laser OB runs analysis the position of the OM must be known with a high level of accuracy in order to correct the effect of the movement of the adjacent lines with respect to the fixed position of the Laser since these movements can delay or advance the arrival time of the beacon light. Moreover, the orientation of the OMs which affects the amount of photons detected due to the scattering and the angular acceptance of the PMT.

Thanks to the positioning system of ANTARES, each 6 minutes the position of the storey r_{storey} = (x, y, z) and the three Euler angles (α, β, γ) are written in the database.

Since a Laser Beacon runs last for only a couple of minutes only one set of positioning values is used. In particular, it is chosen the closest in time with respect to the starting time of the Laser Beacon run.

The coordinates of an OM are obtained by means of a rotation in the storey reference system plus a translation to the absolute position in the detector as follows:

$$\vec{r}_{final} = R \times \vec{r}_{storey} + \vec{r}_{trans} \tag{B.1}$$

where r_{storey} gives the position of the geometrical centre of the OM with respect to a reference system whose XY plane is defined by the plane containing the three OM. The X direction is given by the OM0 and the Z direction is given by the vertical line direction (rigid lines). The values for the geometrical distances for the OMs and LED OB are obtained from [127] assuming that the three OMs are 120° separated:
OM0 = (0.437, 0, 0) m,
OM1 = (-0.218, -0.378, 0) m,

Positioning transformations

OM2 = (-0.218, 0.378, 0) m,

LED OB = (0, 0, 1.003) m.

The R is the rotation matrix which contains the Euler angles which can be written as [128]:

$$\begin{pmatrix} \cos\gamma\cos\alpha - \sin\gamma\cos\beta\sin\alpha & -\cos\gamma\sin\alpha - \sin\gamma\cos\beta\cos\alpha & \sin\gamma\sin\beta \\ \sin\gamma\cos\alpha + \cos\gamma\cos\beta\sin\alpha & -\sin\gamma\sin\alpha + \cos\gamma\cos\beta\cos\alpha & -\cos\gamma\sin\beta \\ \sin\beta\sin\alpha & \sin\beta\cos\alpha & \cos\beta \end{pmatrix}$$

Finally, the r_{trans} translates the OM coordinates to the absolute reference system of the detector.